Flow and Heat Transfer Intensification by Elastic Turbulence

Guice Yao

Submitted in accordance with the requirements for the degree of
Doctor of Philosophy

The University of Leeds
School of Chemical and Process Engineering

December, 2019

The candidate confirms that the work submitted is his/her own, except where work which has formed part of jointly-authored publications has been included. The contribution of the candidate and the other authors to this work has been explicitly indicated below. The candidate confirms that appropriate credit has been given within the thesis where reference has been made to the work of others.

Parts of this thesis are based on work as follows which has been either published in academic journals or submitted in reviewing:

Yao, G., Zhao, J., Ramisetti, S.B. and Wen, D., 2018. Atomistic Molecular Dynamic Simulation of Dilute Poly (acrylic acid) Solution: Effects of Simulation Size Sensitivity and Ionic Strength. *Industrial & Engineering Chemistry Research*, 57(50), pp.17129-17141.

GuiceYao, JinZhao, HaieYang, Haruna, M.A. and DongshengWen. 2019. Effects of salinity on the onset of elastic turbulence in swirling flow and curvilinear microchannels. *Physics of fluids*, **31**(12), p123106.

Yao, G., Zhao, J., Shen, X., Yang, H. and Wen, D., 2020. Effects of rheological properties on heat transfer enhancements by elastic instability in von-Karman swirling flow. *International Journal of Heat and Mass Transfer*, 152, p.119535.

Guice Yao, Haie Yang, Jin Zhao and Dongsheng Wen. 2020. Experimental Study on Flow and Heat Transfer Enhancement by Elastic Instability in Swirling Flow*. International journal of thermal science*. Under review.

As co-author, the candidate also provided modelling processing, data collection, result analysis and evaluation for the following papers:

Zhao, J., Yao, G., Ramisetti, S.B., Hammond, R.B. and Wen, D. 2018. Molecular Dynamics Simulation of the Salinity Effect on the n-Decane/Water/Vapor Interfacial Equilibrium. *Energy & Fuels*. 32(11), pp. 11080-11092.

Zhao, J., Yao, G., Ramisetti, S.B., Hammond, R.B. and Wen, D. 2018. Molecular dynamics investigation of substrate wettability alteration and oil transport in a calcite nanopore. *Fuel*. 239, pp 1149-1161.

Zhao, J., Yao, G. and Wen, D. 2018. Pore-scale simulation of water/oil displacement in a water-wet channel. *Frontiers of Chemical Science and Engineering*. pp. 1-12.

Yang, H., Yao, G. and Wen, D., 2019. Experimental Investigation on Convective Heat Transfer of Shear-thinning Fluids by Elastic Turbulence in a Serpentine Channel. *Experimental Thermal and Fluid Science*, p.109997.

Acknowledgement

First and foremost, I would particularly like to express my great thanks to my supervisor Professor Dongsheng Wen for allowing me to join his research group, for his support, kindness, encouragement and always devoting time in his very busy schedule. Professor Wen does me a lot favour at the beginning of my PhD career, especially when I was new to the elastic turbulence. His rich experiences and knowledge always inspire me and guide me out of trap from the issues or difficulties. I am so grateful for his supporting to allow me conduct experiments in Beihang University. The advanced equipment there helps a lot for my PhD subjects. I cannot forget Professor Wen's encouragement when I failed to get the expected results or when my manuscript was rejected by the journal. His kindness and patience are always the ones touch me and motivate myself to keep moving. I cannot have finished this PhD research without his support. The support and mentoring I received from him is something I will remember always in my future life.

I would also appreciate my beloved family: my parents and my elder sister. Their comprehensive understanding and supporting through all my PhD study really give me power and confidence to come across this tough but fruitful period. With their stand behind me, I can focus on my study without distractions.

Much appreciation to all my officemates and our research group members (past and present). It has been a pleasure to be a member of this research group, which has a collaborative and vibrant environment that has led to much friendship and enjoyment. I would specially like to acknowledge the help, comments and great friendship from Dr Srinivasa Ramisetti and Dr Jin Zhao. Collaboration with them provided valuable insight into a wide range of techniques. I would also show my appreciation to the colleagues when I met in Beihang university. With their support, I could do the heat transfer experiments smoothly.

I would also like to specially thank my former Master supervisors, Prof Zhaoliang Wang at China University of Petroleum (UPC) for his ongoing care, encouragement and great support.

Apart from the academic side, I would like to thank my friends in my daily life. Their accompany in Leeds makes me feel at a big family. Playing, drinking, and even having food together is really a fantastic memory for me.

Last, I would appreciate myself for commemorating the couple of working night.

Abstract

Elastic instability is proposed as a promising method to intensify heat transfer of a polymer solution at a very low Reynold number. However, the onset of elastic instability highly relies on the rheological properties of the polymer solution, whose concomitant effects on the heat transfer side have not been revealed. Besides, most of the studies adopted passive techniques to induce the elastic turbulence, the active control of polymer motion and thereby induce the elastic turbulence has not been investigated. To address these limitations, this work aims to conduct a systematic study to reveal the effects of polymer rheological behaviours on the flow and heat transfer performance and to probe the potential for the active control of elastic turbulence, which could improve the understanding of mechanism of elastic turbulence and its potential application in heat transfer intensification.

At the bulk level, the effects of polymer sensitivities such as polymer concentration and salinity on the rheological properties of hydrolysed polyacrylamide (HPAM) solutions were first investigated experimentally. It showed that with the increase of polymer concentration or the reduction of the salinity, the viscosity of polymer solutions could be increased significantly, showing stronger shear-thinning behaviours. The different mechanisms were interpreted by microscopic HPAM morphology by molecular dynamics simulation (MD). The salt cations shielding the polymer electronic repulsion leaded to the collapse of the polymer molecules, reducing the viscosity consequently. The effects of polymer solution on the onset of elastic turbulence and heat transfer were conducted in two experimental setups, i.e., a swirling flow between two parallel plates and a curvilinear microchannel. The polymer solution either with a high concentration or a low salinity was capable of inducing elastic instability easily, which was consistent with the mixing performance in curvilinear microchannel. However, this salinity-based rheology effects could not be described by the interpretation for the effects of polymer concentration, which is mainly ascribed to the additional shielding effects. A similar trend was observed in heat transfer experiment. For a given flow velocity, polymer solutions with a higher concentration and a low salinity exhibited much significant convective heat transfer enhancement. The salinity effects became weak as the swirling flow velocity continually increased. The maximum enhancement seemed to be independent on salinity, which could be also demonstrated by the fact that a salinity independent power-law exponent at a value of -4.3 was observed in fully developed elastic regime for all of the polymer solutions. When the polymer solutions were normalised by the polymer

relaxation, the polymer concentration was no longer influenced the heat transfer performance. Whilst high salinity captured better heat transfer capability than low salinity due to the existence of the dramatic shear-thinning phenomenon.

Microscopically molecular dynamics (MD) simulations were conducted to exam the HPAM morphology variation under external electric field to investigate the possibility of active control /induction of elastic turbulence. It showed that with the external electric force field applied on the flow passages or channels, the salinity effects on the polymer rheology became insufficient due to the attraction between charged wall and cations, which would modify the onset of elastic instability. It seems to be possible to control the motion of ions to change the polymer conformation, thereby inducing the elastic instability at even lower Re and Wi,

The work advances our understanding of the flow and heat transfer of polymer solutions from both bulk and microscale, and could open a new window of opportunity for elastic turbulence applications.

Keywords: elastic turbulence, polymer, non-Newtonian flow, rheology, heat transfer, molecular simulation

Table of Contents

List of Tables

List of Figures

Chapter 1
Introduction

This chapter discusses the background, motivation and outline for the research described in this thesis. Section 1.1 gives a brief background of high demand in heat transfer intensification and its limitations when applied in industry. The motivations of the research are demonstrated as followed, highlighting the necessity of the further investigations on heat and flow enhancement based on elastic turbulence. At last, a full structure outline of this thesis is provided in section 1.3.

1.1 Research background: high demand of efficient heat transfer

Energy has been regarded as one of the most important issues among the humanity development in the next few decades, especially under the consideration with the challenge of mitigating carbon emission and global warming (Smalley, 2005). Saving energy and securing clean energy seems to be the only efficient method to solve these problems. Among all the forms of energy we are using today, over 70% are generated or transferred by heat. In many industrial conditions, heat is desirable to be removed immediately. Otherwise, the accumulation of the heat could affect the working performance of the equipment and even may cause serious accidents somehow. In fact, the heat transfer performance limits the development of industries to some degree, including nuclear fission, fusion, micro/nano electronics mechanical systems (MEMS/NEMS), and chemical engineering, etc. Considering the rapid increase in energy demand, or the high compacted degree of the small electronic devices, intensifying the heat transfer process and reducing energy loss due to ineffective use have become an increasingly important task.

The natural mechanism of heat and mass transported within fluids are the molecular diffusion and thermal conduction. While the heat removal between fluids and walls relies on thermal convection. These mechanisms, however, lead to inefficient heat transfer performance in micro scale due to the flow is always confined to laminar regime in such conditions. A classical and efficient cooling method employs the turbulent circulation of fluids around the wall to increase the heat transfer coefficients. Many great efforts have been developed to carry out the transition from laminar to turbulence, including vortex promoters, periodic expansion–constriction structure, rough wall

surface and boundary layer redevelopment. The common purpose of these methods is to disturb the low-velocity flows and to enlarge the contact interfaces between fluids and walls. However, these alternatives are expensive and challenging when applied on small scale, and the performance cannot be satisfactory.

It is well known that for Newtonian fluids, turbulence occurs when the Reynolds number is large. However, in micro scale, the Reynolds number is normally very small because of the small characteristic length and low flow velocity. As a result, the flow in micro scale keeps laminar state, leading to inefficient heat and mass transfer without any modifications. Unlike Newtonian fluids, in such a case, viscoelastic fluids can exhibit irregular flow patterns and large velocity fluctuations because of the polymer stretching. This turbulent-like phenomenon is called elastic turbulence (Larson, 2000a).

1.2 Motivation

Since the elastic turbulence was experimentally proposed in 2000 (Groisman and Steinberg, 2000), it has attracted many scholars' attentions due to its potential applications. For example, elastic turbulence has already been verified to benefit the flow and heat transfer intensification, which can be used in aerospace engineering, biochemical engineering, computer science engineering and etc. Besides that, elastic turbulence may become the key point to explain the mechanism of chemical enhanced oil recovery in petroleum engineering. Although many experimental and theoretical investigations about elastic turbulence have been conducted so far, an exact mechanism leading to flow instabilities is still blurred. For example, the interaction between the onset of elastic turbulence and the polymer responding is not completely clear. The elastic turbulence is dependent on polymer coil-stretch transition while the polymer conformation is sensitive to pH, salinity or other effect parameters with specific functional groups bonded. Thus the polymer sensitivities will, absolutely, affect the onset of elastic turbulence. In addition, in most experiments, the elastic turbulence was induced passively either by inserted obstacles or the curvature. The active control of polymer coil-stretch transition and thereby to induce elastic turbulence have not been considered by previous research. If using the external forces such as electric and magnetic fields to actively trigger elastic turbulence, then the applications of elastic turbulence will be widely extended and the flow and heat transfer will be enhanced at specific required situations.

Due to these limitations, this project will first aim to study the polymer sensitivity to polymer concentration, salinity and other effect factors; then actively control polymers to induce the elastic turbulence for flow and heat transfer intensification. Both experiments and simulations will be conducted to probe the rheology and conformation of polymer molecules under various conditions. The thermal properties of polymer solution and the heat transfer performance with different polymer responding will be ultimately measured and analysed. And the method for actively inducing elastic turbulence will be carried out.

1.3 Outline of this thesis

This project mainly contains four parts. Firstly, the polymer sensitivities will be investigated. Both experiments and MD simulations were used to reveal the effects of salinity and polymer concentration on polymer rheology and morphology. Secondly, the variations of the onset of elastic turbulence by polymer responding in swirling flow will be conducted and a mixing performance in a curvilinear channel will be adopted as a validation. Thirdly, the effect of polymer sensitivities on the heat transfer performance by elastic turbulence will be conducted. Finally, The last part will focus on the active control of polymer to induce elastic turbulence.

Overall, this project will provide additional mechanism of the effect of polymer responding on elastic turbulence. The related flow and heat transfer performance will be measured and discussed consequently. What's more, an original method will be developed to induce elastic turbulence. This may make the elastic turbulence have more practical applications. The Figure 1.1 gives a clear outline of this thesis.
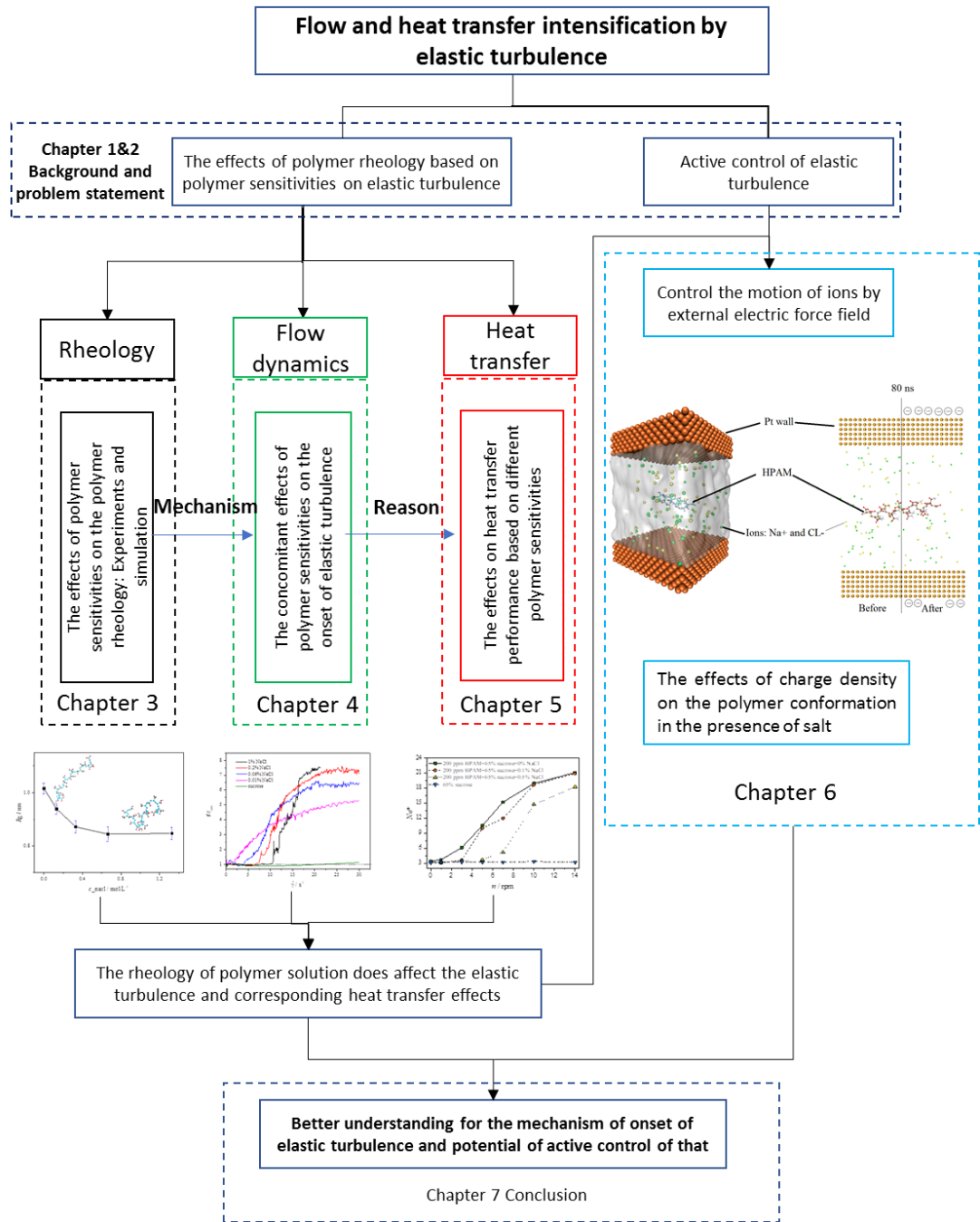
Figure 1.1 Outline structure of the thesis

Chapter 2
Elastic turbulence for heat transfer applications: background and development

This chapter provides related literature review on the heat transfer enhancement by elastic turbulence from three different aspects. Firstly, conventional methods of enhancement in heat transfer are introduced. The present techniques seems to be insufficient for the heat transfer intensification at low Reynolds number (*Re*), where the elastic turbulence has been regarded as a promising approach. Secondly, the development of the understanding of the elastic turbulence is reviewed. Most of the works are focused on the onset condition of elastic turbulence since the contribution of elastic turbulence is highly dependent on its onset conditions for any potential application. Finally, the effects of polymer sensitivities on polymer rheology and conformation are demonstrated. Due to the limitation of rheology effects driven by solution chemistry on the elastic turbulence, how such polymer sensitivities affect the polymer rheology are discussed and will provide mechanism for the future study.

2.1 Conventional methods of flow and heat transfer intensification

The heat and mass transfer efficiency is highly dependence on the thickness of thermal boundary between the wall and the fluid . The existence of thermal boundary significant increases the thermal resistance and reduces the heat transfer in between. To reduce the thickness of the thermal boundary, various investigations have been undertaken and can be classified into three main groups: passive techniques, active techniques and the compound methods .

The passive methods enhance the heat transfer mainly by modifying the surface geometry, or fluid properties and by promoting liquid-vapour phase-change process. These techniques are briefly discussed in the following paragraphs.

2.1.1 Surface modification

Surface modification is one of the most widely used methods. Several classic modifications are surface roughness modification, surface coating and surface structure medication, the aim of which is to promote turbulence and improves the mixing of the fluids, weakening the thickness of thermal boundary layer (Léal et al., 2013). However, the improvement or modification of surface roughness is not significant in laminar natural convection because the

roughness does not cause major perturbations. Generally speaking, the roughness improvement and surface coating are applied for further improvement under the condition that the surface structure modification has been conducted. In terms of surface structure modification, it produces a desirable heat transfer increase based on the following mechanisms: (1) boundary layer development disruption as well as the increase of intensity of turbulence; (2) heat transfer areas enlargement; (3) chaotic flow or secondary flow generation.

Many different structures were conducted to fulfil these requirements, such as twisted tape, wire coil (Bergles, 1969; Uttarwar and Raja Rao, 1985; Ravigururajan and Bergles, 1996; Kalinin and Dreitser, 1998; Manglik and Bergles, 2003; Dewan et al., 2004; Promvonge, 2008), fins (Bontemps et al., 1994; Cavallini et al., 1999) or porous medium (Miscevic et al., 2006; Poniewski and Thome, 2008). Those structures are capable of intensifying the heat transfer performance to some degree but do have their own adaptable regime. The twisted tape was proved to be more effective for small Prandtl number fluids whereas the wire coil was reported to be good with high Prandtl number fluids, as discussed by Wang and Sunden (Wang and Sunden, 2002), and Manglik and Bergeles (Manglik and Bergles, 1993). This is because the twisted tape perturbs the bulk fluid while the wire coil mixes the flow in the viscous sublayer near the wall. Therefore, for a laminar flow, the dominant thermal resistance is not only limited the thin layer near the wall but also extend over the entire cross-section, where the twisted tape is probably effective. In contrast, the dominant thermal resistance relies on the thin viscous sublayer near the wall in a turbulent flow, where the wire coil is more effective.

Indeed, by coupling different structures a further enhancement could be reached (Promvonge and Eiamsa-ard, 2007b; Promvonge and Eiamsa-Ard, 2007a; Promvonge, 2008). However, this coupling configuration always comes across a challenge that to design an optimized structure with excellent heat transfer rate as well as acceptable pressure drop. Actually, although the complicated surface modification could lead to high heat transfer efficiency, the dramatic increase of pump power cannot be achieved sometimes. In addition, with the development of electronic devices tends to micro scale, the manufacture becomes more challenging, which makes many ideal structure unrealistic.

2.1.2 Phase-change method

Another way to enhance the heat transfer is to use the liquid-vapour phase change, which is the subjects of amounts of works (Berenson, 1962; Wayner, 1999; Zalba et al., 2003; Kim, 2009; Chu et al., 2012; Viskanta, 2018). When the fluids change phase around the wall, a significant intensification of the concomitant heat transfer performance is observed, which is mainly ascribed to the disruption of the thermal boundary layer by the nucleation sites and the detachments of bubbles at the wall. Intensification is then observed due to the increase of the numbers of nucleation phenomenon and the motion of the detachment of numerous bubbles. Nowadays, the phase-change heat transfer has been regarded as one of the most efficient methods for heat transfer augment in spite of the detailed mechanism has not been illustrated clearly. Some results obtained in similar geometry are scattered and hard to predictable.

2.1.3 Modification of fluid properties

The surface modification and the phase-change method are based on the modification of the surface structure and the working conditions. Unlike those two methods, there is an additional approach to enhance heat transfer by changing the thermal properties of working fluids. Water as a most common used working fluid possesses relatively higher thermal conductivity among all the fluids we use today, in spite of which amounts to merely around 0.6 $W \cdot m^{-1} \cdot K^{-1}$. Such value is several orders lower than most metals or metal oxides. A concept of adding certain solid particles into a base liquid to increase its thermal conductivity has been practiced for a long time. A so called nanofluid (Choi and Eastman, 1995) is introduced by suspending functionalized nanoparticles with diameters smaller than 100nm for the heat transfer applications. The addition of nanoparticles into base liquid could affect the thermal conductivity, heat capacity, viscosity and density thereby influencing the effectiveness of heat transfer. The mechanism for its enhancement is still unclear and potential interpretations include interfacial layering, Brownian motion, ballistic transport of energy carriers and the structure effect (Keblinski et al., 2002; Eapen et al., 2007; Philip et al., 2008).

Indeed, the contribution of nanofluids to the convective heat transfer is not expectedly significant. Some investigations even indicated that the increase of the thermal conductivity could be offset by the increased viscosity (Pak and Cho, 1998; Buongiorno, 2006). However, combing with nanofluids and phase-change method, significant boiling heat transfer enhancements has been reported (Witharana, 2003; Wen and Ding, 2005; Wen et al., 2005; Liu et al.,

2007b; Park and Jung, 2007b; Park and Jung, 2007a). The improvement of the boiling behaviour might be ascribed to the interaction of nanoparticles with heat surface and subsequent modification of surface properties.

It is shown that coupled methods do play an efficient role for the heat transfer enhancement. Through the surface coating to change the wettability of the liquid on the wall could lead to the augmentation of the nucleation site number and will increase the boiling heat transfer (Khan et al., 2004; Phan, 2010). Besides, the modification of surface structure could optimize the contact angle of the bubbles and contribute the detachments, which results in high boiling heat transfer rate (Bontemps et al., 1994; Phan et al., 2010).

2.1.4 Active methods with external force fields

Apart from the passive methods mentioned above, there are many active techniques which can further intensify the heat transfer by means of external force fields. Among them, the electric field (Allen and Karayiannis, 1995; Carrica et al., 1996; Cipriani et al., 2004; Laohalertdecha et al., 2007; Omidvarborna et al., 2009), magnetic field (Sparrow and Cess, 1961; Pirmohammadi and Ghassemi, 2009; Lajvardi et al., 2010; Sheikholeslami et al., 2014; Sheikholeslami et al., 2015; Sheikholeslami et al., 2016) and acoustic wave (Fand, 1965; Li and Parker, 1967; Loh et al., 2002; Hyun et al., 2005) are three popular techniques to control the motion of the working fluids and to achieve the heat transfer efficiency required. A basic aim of such method is to convert external energy into kinetic energy thereby making chaotic motion in the radial direction of the flow which disrupts the thermal boundary layer (Fernández and Poulter, 1987). Despite the complexity in design for the usage of external force field, with the increase growth of demand for heat transfer these years, passive techniques solely are insufficient to reach the required performance sometimes, which makes the use of active techniques become necessary to meet the requirement of heat removal.

In fact, the methods discussed above are all widely used in the industries. It's hard to identity which one is better. One should consider their own requirements to determine which method is adaptable. It should be noted that most of techniques are conducted in the condition with high Reynolds number (Re). Even for passive technique with twist-tape, most of investigations were studied at Re larger than 100. The heat transfer intensification at low Reynolds number seems to be blank. Otherwise, a complicated configuration or costing external force field generators are required. What's more, in many practical cases, due to the size limitation of the geometry (such as porous structures in

rock), the flow stays in laminar state because of the extremely low Re and the heat transfer is insufficient.

One of the proposed approaches for flow intensification at a very low Reynolds number is to use viscoelastic fluids, which are usually formed by adding small amount of high-molecular-weight polymer into a pure Newtonian solvent (Bird et al., 1977). This viscoelastic fluid exhibits dramatic flow instability in the presence of elastic nonlinearity, which is characterized by a normalized Weissenberg number, defined as $Wi=\dot{\gamma}\cdot\lambda$, where $\dot{\gamma}$ is the shear rate applied to the flow and λ is the polymer relaxation time. In particular, when the inertial effects are unimportant at vanishing Reynolds number, the viscoelastic fluids are pronounced to induce purely elastic instability at $Wi > 1$ (Muller et al., 1989; Larson et al., 1990; Groisman and Steinberg, 1998), and with further increase of the value of Wi, the flow is excited to a so-called elastic turbulence regime (Vinogradov and Manin, 1965; Larson, 2000a). Such turbulent-like flow behaviour weakens the thermal boundary layer and has been proved to benefit the heat transfer performance both in macroscale and micro size level (Traore et al., 2015; Whalley et al., 2015; Abed et al., 2016; Li et al., 2016a; Li et al., 2017), which provides the potential for the heat transfer intensification at low Reynolds number. However, the understanding of this area is quite limited due to few studies concerning this topic. Further works have to be investigated to reveal the heat transfer dependence on elastic turbulence and its mechanism. What's more, due to the flexibility of the polymer, it's much easier by control of the polymer motion with external force field to change the flow motion, which is not a common principle for conventional working fluids such as water. The limitation of the understanding and the potential application of elastic turbulence on heat transfer forms the motivations of this project. Before the ultimate goals are reached, the overview of the development of elastic turbulence and concomitant mechanism is introduced below, which, in return, absolutely provides guidance for the future works.

2.2 State-of-the-art of the elastic turbulence

2.2.1 Introduction of elastic turbulence

In fluid dynamics, laminar flow occurs when a fluid flows in parallel layers with no disruption between layers (Batchelor, 2000).There are no perturbations to the direction of the flow, nor eddies and swirls of the fluid. The motion of laminar flow is very orderly and the streamlines are smooth.

Turbulent flow is a flow regime in contrast to the laminar flow with irregular flow patterns, vortexes of fluid and strong velocity fluctuations (Tennekes and Lumley, 1972). It is difficult to give an accurate definition of turbulence, but there are some common features in turbulence: random streamlines in spatial and temporal domains, high dissipation rate, multiscale eddies and unstable velocity field; see Figure 2.1 for an illustration.

(a) Laminar   (b) Turbulence
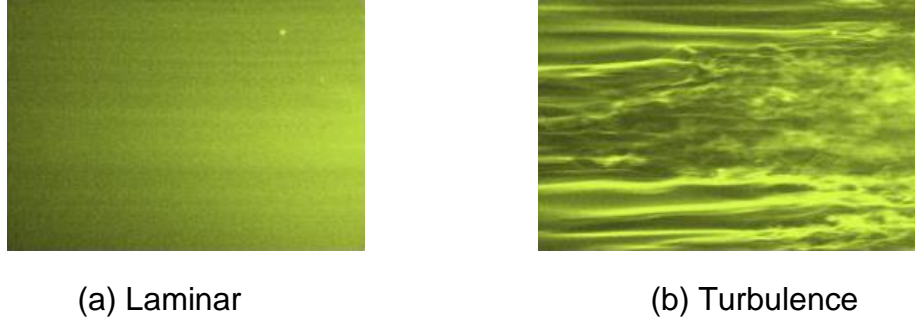
Figure 2.1 Visualization of laminar and turbulence of Newtonian fluids in a flat-plate flow (Matsubara and Alfredsson, 2001)

It is well know that for Newtonian fluids the transition from laminar to turbulent occurs when the velocity of flow is high, kinematic viscosity of the fluid is low and the characteristic length is large. The motion of Newtonian fluid is followed by Navier-Stokes equations (Landau and Lifshitz, 1987):

$$\frac{\partial \vec{V}}{\partial t} + (\vec{V}\nabla)\vec{V} = -\frac{\nabla P}{\rho} + \eta \Delta \vec{V} \tag{2.1}$$

where $\vec{V}$, η are the velocity and kinetic viscosity of the fluid respectively, P is the pressure and the ρ is the density of the fluid. In equation (2.1), there are a nonlinear term $(\vec{V}\nabla)\vec{V}$ and a viscous dissipative term $\eta\Delta\vec{V}$. The Reynolds number, $Re = \vec{V}L/\eta$, defining the ratio of the nonlinear term to the dissipative term, is the criterion to balance flow state. When Re is high enough, the nonlinear effects are strong and the fluid shows turbulent features (Tritton, 1988).

The conventional Navier-Stokes equations cannot characterise the viscoelastic fluids since the addition of polymer provides additional elastic effects on the base flow. In such case, the motion of the viscoelastic fluid can be governed by modified equation (2.2) (Bird et al., 1977):

$$\frac{\partial \vec{V}}{\partial t} + (\vec{V}\nabla)\vec{V} = -\frac{\nabla P}{\rho} + \left(\frac{\eta_s}{\rho}\right)\Delta\vec{V} - \frac{\nabla\tau_P}{\rho} \tag{2.2}$$

Where η_s is the viscosity of Newtonian solvent and τ_p is the additional elastic stress term to describe the polymer effects. A simple model describing the τ_p is the Maxwell-type

$$\tau_p + \lambda \frac{D\tau_p}{Dt} = -\eta_p \left[\nabla \vec{V} + \left(\nabla \vec{V}\right)^T\right] \tag{2.3}$$

where $D\tau_p/D_t$ represents the upper-convected derivative defined by

$$\frac{D\tau_p}{Dt} = \frac{\partial \tau_p}{\partial t} + \left(\vec{V}\nabla\right) \cdot \tau_p - \left(\vec{V}\nabla\right)^T \cdot \tau_p - \tau_p\left(\nabla\vec{V}\right) \tag{2.4}$$

it can be found that the elastic nonlinear terms are all the order $\lambda\left(\vec{V}/L\right)\tau_p$. The ratio of the elastic nonlinear terms to the linear relaxation term, τ_p, is called Weissenberg number, $Wi = \lambda\left(\vec{V}/L\right)$. Similar with the function of Reynolds number in viscous nonlinearity, the Weissenberg number represents the degree of the elastic nonlinearity. When the Wi is larger than a critical value, the mechanical properties of viscoelastic fluids become notable elastic nonlinear. One famous example is the hoop stress (Weissenberg effect) (Weissenberg, 1947).

As mentioned above, the viscoelastic fluid exists two different nonlinear terms: inertial and elastic. Different values of Re and Wi lead to different hydrodynamic phenomena. Although there is no specific explanation for how the inertial nonlinear and elastic nonlinear contributes to the flow instability, it can be qualitatively classified into four flow regime (Burghelea, 2005). Figure 2.2 shows a sketch of the four hydrodynamic stabilities. (1) If both Wi and Re are smaller than threshold values, the flow is stable. No eddies and fluctuations occur and the flow is totally in laminar regime. (2) If Wi is too small to be negligible, $Wi < Wi_c$, the flow fluctuates only when the inertial nonlinearity is large compared to the viscous dissipation. Thus if Re exceeds critical value, $Re > Re_c$, the flow turns into inertial turbulence. (3) If Wi and Re are both higher enough than critical value, both nonlinearities cause the flow perturbations. In this regime, the addition of polymers causes a significant reduction of flow resistance. This remarkable hydrodynamic phenomenon presented by Tom (Toms, 1948) is called drag reduction. Since the drag reduction allows oil to be transported at lower pump power, it attracts many attentions in petroleum engineering soon.

(4) When the Re is small while Wi exceeds the threshold value, the flow undergoes elastic instabilities and ultimately evolves turbulent-like flow as Wi increases. This chaotic dynamic state is solely driven by nonlinear elastic stresses. Although the chaos occurs in the absence of inertial nonlinearity, it exhibits same features of inertial turbulence, such as random flow patterns, large velocity fluctuations and the significant increase of flow resistance. This turbulent-like flow is called elastic turbulence (Larson, 2000b), which was first experimentally reported by Groisman and Steinberg in 2000 (Groisman and Steinberg, 2000).
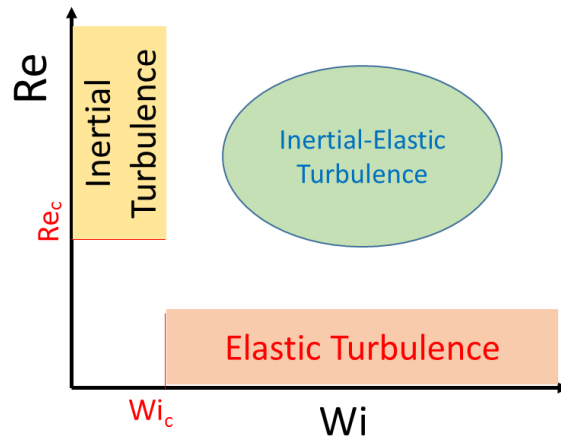
Figure 2.2 Sketch if hydrodynamic stability diagram

2.2.2 Development of elastic turbulence

The first experiment of elastic turbulence was conducted by Groisman and Steinberg under a von Karman swirling flow configuration between two disks (Groisman and Steinberg, 2000). Three main features, all of which are analogous to hydrodynamic turbulence, were found for this turbulent-like flow: pronounced growth of flow resistance, algebraic decay of angular velocity spectra over a wide range of time scale, and orders of magnitude higher mixing performance compared with Newtonian solvent, as shown in Figure 2.3.
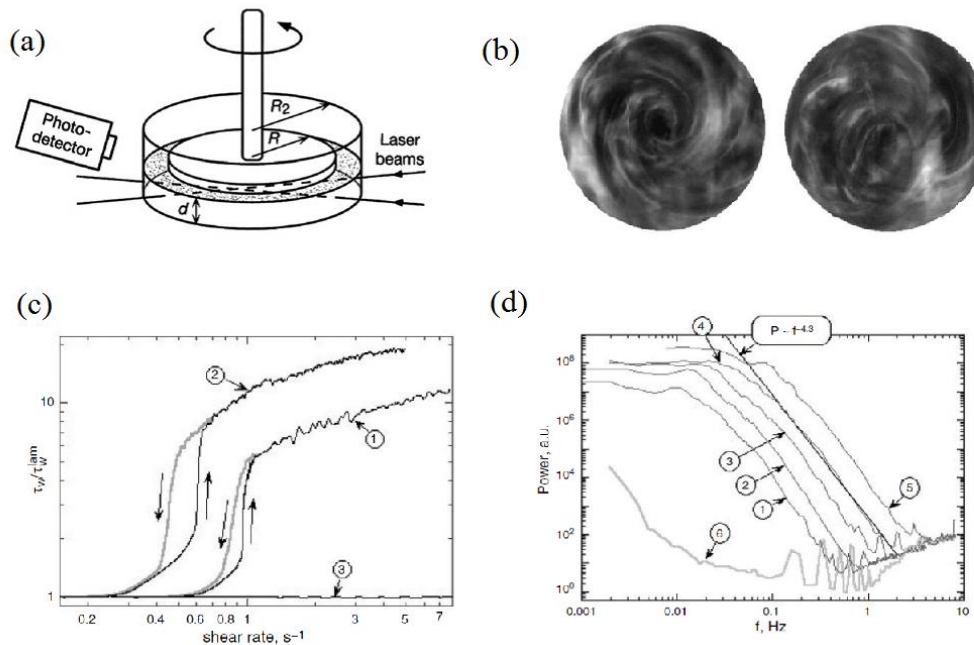
Figure 2.3 Classic properties of elastic turbulence. (a) Swirling flow set-up; (b) irregular flow patterns; (c) sharp increase of flow resistance; (d) power law decay spectra of velocity fluctuation.

Later, the elastic turbulence was also observed in Couette-Taylor geometry and curvilinear channels (Groisman and Steinberg, 2001; Groisman and Steinberg, 2004). The sequences of transition profiles from the onset of elastic instability to elastic turbulence regime were systematically investigated as followed (Schiamberg et al., 2006). A key quantitative feature of the elastic turbulence is the exponent value of the power-law spectra, which is significantly different from that of the inertial turbulence of -5/3 (Kolmogorov, 1941). A value in the regime of -3 ~ -4.3 can be regarded as a signal of the occurrence of the elastic turbulence (Fouxon and Lebedev, 2003; Groisman and Steinberg, 2004; Burghelea et al., 2006; Jun and Steinberg, 2009).

Owing to the low Reynolds number flow instability, elastic turbulence could have many potential applications such as efficient mixing performance as aforementioned above (Gan et al., 2006a; Gan et al., 2006b; Groisman and Steinberg, 2001). It has been shown that a viscoelastic fluid could achieve four orders of magnitude enhancement in mixing in a swirling flow region between two parallel plates (Groisman and Steinberg, 2004). Similar intensification has also been observed for micro/mini channels (Burghelea et al., 2004a; Burghelea et al., 2004b). This was attributed to an efficient mixing layer induced by polymer relaxation, leading to an efficient mass transfer process. Particularly, the elastic turbulence could contribute to the emulsification process between two immiscible liquids (Poole et al., 2012), that yield to enhanced oil recovery during the stage of polymer flooding. (Clarke et al., 2015; Howe et al., 2015; Mitchell et al., 2016).

In fact, the mixing performance is significantly relied on the critical onset of elastic instability, which is highly dependent on the rheological properties of polymer solutions and the geometric elements of flow channel. Even with same apparatus, such as swirling flow, the aspect ratio could affect the onset of elastic turbulence pronouncedly (Burghelea et al., 2007). A skewness of the probability density functions (PDFs) of the angular velocity was observed in elastic regime, which was mainly attributed to the mixing layer, where excessive elastic stresses were supposed to be injected into bulk (Burghelea et al., 2004a; Burghelea et al., 2004b; Burghelea et al., 2006; Belan et al., 2018). This skewness, however, showed independent relationship with polymer concentration when the concentration was lower than 900 ppm (Jun and Steinberg, 2009). When the scale goes down to micro level, especially in curvilinear channels, the elastic turbulence becomes more challenging to be characterized. The onset of elastic turbulence in such a geometry was normally characterized based on the mixing performance coupled with velocity

profiles captured by a micro-PIV (μ-PIV) system (Souliès et al., 2017). With more advanced Digital Holographic microscope, a three-dimensional velocity field was achieved (Li et al., 2016b; Li et al., 2016c). It was found that the elastic stresses were not saturated in elastic turbulence regime in serpentine channel, which was mainly due to the boundary layer in bounded flow channels (Souliès et al., 2017). In addition, unlike the swirling flow, a steady secondary flow was observed in such a geometry before the onset of elastic turbulence (Ducloue et al., 2018). Besides these standard geometries related to rheometer, elastic turbulence was also triggered in any other geometries, such as porous media (Scholz et al., 2014; Clarke et al., 2015; Howe et al., 2015; Mitchell et al., 2016; Kawale et al., 2017), cross-slot channels(Sousa et al., 2018; Wang et al., 2016) and viscous disk pump (Ligrani et al., 2016; Lund et al., 2016). From these curvilinear geometries, the curvature of the geometry was regarded as an essential condition to induce elastic turbulence and the concomitant effects were systematically investigated by Zilz et.al (Zilz et al., 2012). However, this assumption was controversial as the elastic turbulence was also triggered in a straight channel by inserting numbers of obstacles in the center (Pan et al., 2013; Qin and Arratia, 2016; Qin and Arratia, 2017; Norouzi et al., 2016; Shi and Christopher, 2016; Gryparis et al., 2019). A direct numerical simulation (DNS) of a three-dimensional flow in two parallel plates also proved this controversy (Zhang et al., 2016a). Until now, the roles of the curvature played during the elastic instability transition are still unclear and further studies are urgently required.

Besides the geometry, the rheological properties of polymer solution demonstrated significant impacts on the onset of elastic turbulence. The polymer type, concentration and solvent type are all related to the occurrence of elastic turbulence. Different polymers such as PAM, PEO (Latrache et al., 2012; Poole et al., 2012), DNA (Malm and Waigh, 2017) and hydrolyzed PAM (HPAM) (Scholz et al., 2014; Clarke et al., 2015; Howe et al., 2015; Mitchell et al., 2016; Bodiguel et al., 2015), due to the discrepancies of polymer relaxation time, chain length and molecular weight, induce elastic turbulence with various onset conditions. Not only for polymers, micelles were capable of induce similar elastic turbulence phenomena (Fardin et al., 2010; Li et al., 2010; Majumdar and Sood, 2011; Beaumont et al., 2013). Particularly, studies indicated that the rheological properties of polymer solutions, such as shear thinning behaviour (Poole et al., 2012; Bodiguel et al., 2015; Casanellas et al., 2016), also influenced the onset condition even with same polymer. However, these various rheological properties were only investigated based on the variations of solvent or polymer concentration. In many polymer applications,

such as HPAM flooding for enhanced oil recovery, the complicated water chemistry (such as pH, ionic strength and dissolved organic matter contents and properties) would affect the performance significantly. Because of the charged carboxylate along the backbone, the rheology of HPAM is sensitive to many factors, among which salinity is one of the most noteworthy (Schweins et al., 2003a). The effects of such sensitivity on the onset of elastic turbulence have not been investigated, which forms the another motivation of this work. In addition, the transition from laminar to elastic turbulence was accompanied by polymer coil-stretch transitions observed by Gerashchenko et al (Gerashchenko et al., 2005). HPAM could have different morphologies under different salt concentrations, as revealed recently by experiments and simulations.(Yao et al., 2018; Wu et al., 1995b; Pohlmeier et al., 2004) How such variations of initial configurations would affect the elastic turbulence is still unclear and require further investigations.

2.2.3 Heat transfer intensification by elastic turbulence

Theoretically, such vigorous mass transport and dramatic increase in the flow resistance contribute to the heat transfer as well. It is surprising that until now there are quite few studies focused on this subject. Traore et al (Traore et al., 2015) investigated the effective heat conduction within bulk fluid by a sucrose-based polymer solution in a swirling flow between parallel disks, where heat was transferred four time rapidly than that in a pure sucrose solution. Besides, a convective heat transfer performance up to 380 % between the fluid and the wall was achieved in a millimetre-sized curvilinear channels by Abed et al (Whalley et al., 2015; Abed et al., 2016). The effects of shear-thinning phenomena on the heat transfer intensification were discussed. This enhancement could enlarge to as high as two orders of magnitude by using polymer aqueous solution without sucrose when the size of the curvilinear channel is scaled down to micro meter size according to the investigation by Li et al (Li et al., 2016a; Li et al., 2017). A few other experiments (Copeland et al., 2017; Ligrani et al., 2017) were conducted in different geometries, and all showed the capability of elastic turbulence in improving the heat transfer performance with the presence of different levels of heat transfer intensification.

Even of these few studies, with the different degree of intensification being neglected, there are still some controversial results. For example, the heat transfer enhancement against *Wi* increases with increasing the polymer concentration in Ref (Abed et al., 2016), which appears disagree with the observation of Li et al (Li et al., 2017). The enhancement of heat transfer

begins after the occurrence of elastic instability, which is highly dependent on the polymer contribution to the viscosity and the Wi_c (Muller et al., 1989; Larson et al., 1990; Groisman and Steinberg, 1998). The variations of polymer concentration and solvent viscosity changing the polymer contribution and elastic property significantly influence the threshold, however, whose effects on the heat transfer side have not considered. In addition, the hydrolysed polyacrylamide used in EOR is sensitive with ions effects due to the charged carboxylate groups (Yao et al., 2018). These ions effects such as salinity effects are normal phenomena in oil reservoir, and have dramatic impacts on the polymer rheological properties (Schweins et al., 2003a), whose effects on the heat transfer have not been investigated as well.

2.3 Effects of sensitivities on the polymer rheology and conformation

As discussed above, the onset of elastic turbulence is significantly dependent on the polymer rheology. Most of investigations were focused on the neutral polyacrylamide (PAM) polymer with its high molecular weight, whose rheological properties are mainly relied on its own concentration and molecular weight. The ionic effects driven from the solvent show less effects in this condition. With some degree of hydrolysis, the hydrolysed PAM (HPAM) exhibits strong interaction with ions due to the charged carboxylate groups along the polymer backbone chain, which will cause either variations of rheological properties or the changes of polymer configuration, influencing concomitant onset conditions of elastic turbulence expectedly. Priority to the investigation in elastic turbulence section, effects of polymer sensitivities on the polymer rheology and conformation should be reviewed and studied first to give a guidance and provide reasonable mechanism for the further investigations. Here the HPAM is mainly discussed due to it is conducted through all over the subject.

2.3.1 Effect of hydrolysis

The degree of hydrolysis is an important variable that determines both salinity and pH sensitivity because it represents the percent of carboxyl groups that carry negative charges along the polymer chains. These negative charges on the hydrolysed carboxyl groups cause repulsion within the molecules and an uncoiling of the polymer chain (Choi, 2008). When dissolved in distilled water, an uncoiled molecule occupies a greater volume in a solvent, resulting in higher solution viscosity (Muller et al., 1980). The greater the degree of the hydrolysis, the greater the number of negatively charged carboxyl groups

within the polymer chain, and the more likely repulsion can occur with the negatively charged molecules. Besides that, the degree of hydrolysis affects the polymer relaxation time which is one of key parameters in determination of the onset of elastic turbulence. It is shown that as the degree of hydrolysis increased, the relaxation time increases first and then decreases when the degree of hydrolysis exceeds 25%. Chois et al (Choi, 2008) indicated this may be due to the tight arrangement of negative charges on the backbone chain in high hydrolysed polymer.

2.3.2 Effect of pH

The pH sensitivity of PAM is mainly related to the existence of ionic groups in the polymer molecules, which are determined by the degree of hydrolysis. The viscosity and the conformation of the unhydrolyzed PAM (hereafter PAM) in pure water is independent of the pH (Choi, 2008). For hydrolysed PAM (hereafter HPAM), the carboxyl groups along the HPAM back-bone chain mainly controlled the pH-sensitive rheological properties. At a high pH, the carboxyl groups fully dissociated and were negatively charged, thereby developing a strong electrostatic repulsion between them. This repulsion made the polymer chains stretch, resulting in the increase of solution viscosity. On the other hand, in low pH case, the carboxyl groups were protonated with hydrogen ions, thereby no repulsion within polymer chain. The polymer molecules were now in a tightly coiled state, which contributed to low viscosity of solution. Chois (Choi, 2008) pointed out that the pH dependence of HPAM solution was saturated when pH was lower than a critical value. All the carboxyl were pronated by hydrogen ions and excessive hydrogen ions only contributed to decreasing pH value rather than shrink the polymer. Similarly, the polymer chain reached their maximum extension at a higher value of pH, where the carboxyl groups were totally dissociated. These saturations are determined by degree of hydrolysis. With different degree of hydrolysis, different numbers of carboxyl groups are produced, resulting in different saturations of pH dependence.

2.3.3 Effect of salinity

The mechanism of salinity responding for polymer conformation is quite similar to the pH effect, where salt cations replace the role of protons. The presence of salt cations shields the carboxyl groups along the polymer chain, leading to polymer shrinkage with consequent viscosity reduction. The higher salts concentration, the more significant shrinkage occurred (Muller et al., 1979). But it was also observed a critical salinity, above which salinity no longer affected the polymer conformation, existed because the limitation of

numbers of carboxyl groups to be shielded by salt cations. In addition, Muller et al (Muller, 1981; Muller et al., 1980; Muller et al., 1979) indicated that the effect on polymer conformation of divalent salts was more marked than of monovalent salts at same salt concentrations. Recently, Chen et al (Chen et al., 2012) used molecular dynamics (MD) method theoretically described the transition of PAM and HPAM polymer conformation from low salinity to high salinity. The PAM showed insensitive dependence of salts while the results of HPAM made a great agreement with experiments been presented so far.

2.3.4 Effect of other parameters

Besides the effect parameters mentioned above, others factors can also influence the conformation of PAM or HPAM. Muller et al (Muller et al., 1979; Muller et al., 1980; Muller, 1981) demonstrated the temperature could control the extent of hydrolysis. Higher temperature resulted in increasing rate of hydrolysis and thereby more carboxyl groups were available for pH or salinity responding. Molloy et al (Molloy et al., 2000) found at same salt concentrations there was a small shrinkage for polymer chain as the temperature increased, though this phenomenon was not significant. In addition, the molecular weight could affect the hydrodynamic radius of PAM or HPAM chain. A polymer chain with higher molecular weight showed larger hydrodynamic radius, which meant larger extension of single polymer chain (Seright et al., 2010).

Most investigations were focused on the macroscopic properties such as viscosity of polymer solutions to indirectly predict the effect of pH, salinity and others on the conformation of single polymer molecule (Jung et al., 2013; Kamel and Shah, 2009; Meng and Hu, 2010; Ye et al., 2016). The mechanism of these ionic effects are attributed to the polymer structure, which is difficult to obtain the detailed morphologies by experimental approach.

2.3.5 Experimental measurement for polymer configuration

To obtain information about the conformation of polyelectrolytes in aqueous solution and consequently to reveal the mechanism of its physical properties, a series of studies have been performed by different experimental techniques. The shrinkage and swelling phenomenon of PAA chains were evaluated successfully by using quartz crystal microbalance with dissipation monitoring (QCM-D) (Delcroix et al., 2013). The fluorescence label method was employed to monitor PAA chains conformation at the alumina-water interface. An increase of polymer concentration was found to stretch polymer chains (Fan et al., 2000; Pan et al., 2001). The conformation transition of PAA chains

as a function of ionic strength was determined by adsorption isotherms and force measurements using atomic force microscopy (AFM). As ionic strength increases, the repulsive force between the negatively charged carboxylate groups along the PAA chain was reduced due to the counter-ion screening, leading to the change of PAA conformation from a stretched to a coiled configuration (Kim et al., 2008). The deuteron magnetic resonance (DMR) spectra titration was used to study the conformation in protein and weakly charged polyelectrolytes (Dong et al., 1977; Dianoux et al., 1985).

In addition, the dynamic light scattering (DLS) measurements, supplemented by static light scattering (SLS) and more advanced small-angle neutron scattering (SANS) methods, are widely adopted to study the chain conformation of polyelectrolytes, such as PAA, poly(styrenesulfonate) (PSS), and PMA (Hara and Nakajima, 1980; Noda et al., 1983; Schweins et al., 2003a; Schweins and Huber, 2001; Schweins et al., 2003b; Wu et al., 1995a; Pohlmeier and Haber-Pohlmeier, 2004). Based on the presented investigations, the changes of polymer conformation are mainly attributed to the following parameters: charge density of backbone, counter-ion screening effect, special counter-ion bonding effect, and solvate quality. It should be addressed that these four factors are interacted each other as well. The ionization of polymer always related to the solubility, which in return, makes the solvate is regarded as good solvate or poor solvate (Schweins and Huber, 2001; Schweins et al., 2003b). The poor solvent conditions give rise to a competition between the attractive interaction of the backbone and the electrostatic repulsion of polyelectrolytes charges. Adding organic solvents into dilute polyelectrolytes solutions, a counter-ion specific coil-globule transition occurs, which is not solely driven by the solvent quality, but also related to counter-ion binding and temperature as well(Satoh et al., 2013a; Takani and Satoh, 2016a). Besides, with addition of salts into solutions (Borochov and Eisenberg, 1994; Schweins et al., 2003a), the shielding effect strengthens as well as the solvate quality decrease. Therefore, the PAA molecules gradually collapse due to the counter-ion screening effect. For monovalent sodium chloride, continually dissolving salt into solutions, a so called theta solvent condition reached, where the PAA molecules stay an unperturbed conformation(Flory and Osterheld, 1954; Takahashi and Nagasawa, 1964). The chain expansion due to a decrease in the concentration of salt could be satisfactorily interpreted by a theory by Peterlin et al. (Peterlin, 1955) and a worm like chain model applied by Kratky et al. (Kratky and Porod, 1980). When the amount of salt concentration exceeds a specific value, the precipitation of polyelectrolytes with salt, usually called

"salting out" occurs (Ikegami and Imai, 1962). In contract, if the multivalent salt ions are adopted, the polyions are binding with cations and consequently forms a further globule coil (Huber, 1993; Schweins and Huber, 2001; Schweins et al., 2003b). This transition depends on the types, concentrations and even size of cations (Satoh et al., 2013a). These behaviours have been captured in the field-theoretical studies (Muthukumar, 2004; Wang et al., 2004), which succeed in achieving a qualitative understanding of strong polyelectrolyte behaviour. However, they don't have the capacity for chemical detailed description and they do not provide a molecular-level insight on the morphology of polymer chains. In addition, some physical interactions vary form polymer chemical structure. The effect of tactility and the characteristic of hydrogen-bonding effect is normally difficult to interpret or require prior knowledge, which are not easily accessible to be achieved experimentally in advance.

2.3.6 Molecular dynamics simulation for polymer chain

Molecular dynamics (MD) simulation, on the other hand, has proven to be a valuable tool to study the self-assembly of polymers at the microscopic level, which could reveal detailed three dimensional conformational and structural behaviour (Wang et al., 2012; Shang et al., 2008; Cao et al., 2011; Yuan et al., 2010). The physical structure and thermodynamics properties of NaCl in water have been abundantly investigated in prior investigations using both experimental and numerical methods(Zhang et al., 2016b; Zhang et al., 2015; Uchida and Matsuoka, 2004; Patra and Karttunen, 2004; Chowdhuri and Chandra, 2001; Driesner et al., 1998; Lyubartsev and Laaksonen, 1996; Zhu and Robinson, 1992). For long-chained PAA, Reith et al (Reith et al., 2002) adopted a coarse-grained model and the results were supported by DLS data. Several other coarse-graining strategies were also employed to study the size and pH effects (Laguecir et al., 2006; Pantano et al., 2011; Mantha and Yethiraj, 2015), the influences of salt cations (Carrillo and Dobrynin, 2014) and even the effect of solvent quality (Dimitrov et al., 2007; Limbach and Holm, 2003; Zhou and Daivis, 2009) on conformation behaviours of polymer chains. However, the coarse-grained model failed to capture the hydrogen bonding effects, interactions between charged ions (Ramachandran et al., 2013) and the effects of tacticity (Sitar et al., 2014). The solvent quality was studied just by changing the interaction parameters between the polymer and solvent, which cannot tell a real interaction for a specific solvent and cannot tell whether a solvent is in good or poor quality for a certain polymer. To reveal these effects, Sulatha et al adopted atomistic MD simulation method with

Gromos 53a6 force field and showed that the radius of gyration of a single PAA was dependent on the charge density along the chain. The corresponding hydrogen behaviours and counter-ions distribution can be well captured by MD simulations (Sulatha and Natarajan, 2011; Sulatha and Natarajan, 2012). Similar force field was used to study the conformation behaviours of PAA chains with different concentration or non-water-solvate conditions (Sappidi and Natarajan, 2016; Katiyar and Jha, 2017), as well as the effect of salt species (Gupta and Natarajan, 2017). It was found that there was a strong binding between divalent Ca^{2+}/Al^{3+} and polyion, which led to Na^+ far away from the PAA chain (Bulo et al., 2007; Molnar and Rieger, 2005; Patel et al., 2017). The atomistic molecular dynamics simulation was also achieved to characterise the effect of tactics on polymer conformations in salt free solutions both in single or multi-chain system (Katiyar and Jha, 2017; Gupta and Natarajan, 2016). Different associations attributed to tacticity and deprotonation are indeed influence the polymer behaviours in salt free solutions.

It shall be noted that there were a wide variation of the number of monomers of PAA chains (i.e., chain size) and solvent molecules used in different studies, which could lead to different results (Ramachandran et al., 2013; Hoda and Larson, 2009). A systemic study about this simulation size sensitivity, in the presence of different salts, to reveal the details of a single HPAM chain has not been studied, which still needs further investigation in this work.

2.4 Summary and work plans

From the literature review, elastic turbulence does show some potentials for the flow and heat transfer intensification in places where other conventional methods become insufficient. This enhancement is highly relied on the onset of elastic turbulence, which is dominated by the degree of polymer stretching by primary flow, polymer contribution to viscosity and geometric factors.

Most of investigations were focused on the geometric effects on the onset of elastic turbulence by applying various curvilinear geometries. However, few studies paid attention to the influences of polymer itself. Even within those few studies, the polymer concentration is always the only one attracting researchers' attention. Indeed, both the polymer stretching and the polymer contribution to the viscosity are highly dependent on the polymer rheology, which as discussed above, with the polymer hydrolysis, is sensitive not only to its own properties such as concentration or molecular weights, but also to

the solution chemistry like salinity or pH, etc. Such ionic effects, which may change the polymer structure directly, shall have different mechanism of influencing the polymer rheology. The concomitant effects on the onset condition of elastic turbulence are blank and deserved to be investigated as the onset of elastic turbulence is accompanying with the polymer coil-stretch transition, which is highly related to the polymer structure. Due to the limitation of experimental techniques, a microscopic understanding of polymer morphology variation by the ions effects is still lacking at the moment.

It also shows that the elastic turbulence discussed in the previous investigations were all passively induced by the geometric curvature. The flow irregularity is fully relied on the inlet velocity and the geometry. The onset of elastic turbulence occurs when the degree of stretching of the polymers by the primary flow exceeds a critical value.

Aiming to advance the basic understanding and application of polymer solutions, this projects proposes a fundamental study of flow and heat transfer intensification by elastic turbulence, and to explore the possibility of active control and induction of elastic turbulence, from both bulk and microscale.

At the bulk scale, Various polymer solution with different salinities and polymer concentrations will be used in three levels.

1. The rheology of polymer solutions with different salinities and polymer concentrations are to be measured first to reveal how the salinity or polymer concentration affects the polymer rheology. This works are introduced in the Chapter 3. The rheological properties such as viscosity and shear-thinning phenomenon are demonstrated.

2. The salinity and polymer concentration effects on the onset of elastic turbulence are investigated in Chapter 4 in two geometries, a swirling flow configuration and a curvilinear microchannel. The critical shear rate and Weissenberg number are determined by the sharp increase of shear stress curves. Statistical analyses such as probability distribution functions (PDFs) and power spectra density (PSD) are applied to reveal the effects of salinity on fully developed elastic turbulence regime. In addition, another micro curvilinear channel is used to validate the results.

3. The heat transfer performance based on such rheological properties is studied in Chapter 5. The enhancement in heat

transfer by elastic turbulence is validated by a sucrose Newtonian fluid in the swirling flow configuration. The effects of salinity and polymer concentration on heat transfer side are revealed, especially on the dependence of *Nu* on *Wi*. Particularly, the effects of solvent are discussed by varying the proportion of sucrose added into the polymer solution. The onset condition hasn't been measured due to the flow instability observed in such experiments, which is not only driven by elastic nonlinearity but also by the inertial effect.

At the microscale, molecular dynamics (MD) simulation are conducted to exam the HPAM morphology variation under the influence of salts and external electric field to investigate the possibility of active control /induction of elastic turbulence.

1. The detailed microscopic morphology with various salinity are appended in Chapter 3 to provide a molecular-level mechanism of the rheology measurement and also to visualize relationship between the morphology evolution of polymers and the rheology variation. All of those work would support the interpretation for the effects on the onset of elastic turbulence in the following sections and contribute to the possible approach for active control of polymer motions/properties.

2. With the involvement of ionic effects in the present work, controlling the motion of ions would weaken the shielding effects, which increases the polymer relaxation time and makes the elastic turbulence could be induced in a relative smaller velocity or Wi. The mechanism and feasibility of this method is modelled through the variations of polymer morphology by MD simulations in Chapter 6.

Chapter 3
Rheology dependence on polymer sensitivities: effects of polymer concentration and salinities.

From the literature review, it is clear that the onset of elastic turbulence is highly dependent on the rheological properties of polymer solutions. The polymer contribution to viscosity and the concomitant shear-thinning phenomenon determine directly the degree of elastic nonlinearity within the flow. Most of the polymers used in elastic turbulence investigation were non-ionic types such as polyacrylamide (PAM), polyethylene (PE), polyethylene oxide (PEO), DNA and so on, where the polymer concentration and the solvent proportion are the two vital parameters for determining the rheological properties. Unlike those neutral polymers, with hydrolysis or substitute, some polymers exhibit strong electronic interaction with water chemistry (salinity or pH) due to the existence of charged functional groups along the polymer chain. Such electronic interaction modifies the polymer initial configuration and varies the rheological properties, which would affect the onset of elastic turbulence accordingly. However, few studies are focused on this topic and how these polymer sensitivities influence the elastic turbulence has not been revealed, which requires further investigations.

In this chapter, the variations of rheology based on different salinities and polymer concentrations are investigated experimentally and the microscopic polymer variation are studied by the molecular dynamics (MD) simulation to reveal the mechanisms of how salinity affects the rheological properties.

3.1 Working fluid description

3.1.1 Materials

A high-molecular-weight partially hydrolysed polyacrylamide (HPAM), provided from Shandong Tongli Chemical Company, was chosen for all measurements in this section. The HPAM was selected based on following reasons: (a) the large molecular weight contributes to the polymer elasticity and can induce elastic turbulence much easier; (b) Compared with pure polyacrylamide, the negative charged carboxylate functional groups are included in the HPAM, see figure 3.1, which allows the polymer to interact with salt cations. The corresponding effects of salinity on rheology and further on elastic turbulence are accessible to be investigated; (c) the HPAM is widely used in many industrial engineering and its cost is quite cheap. Therefore, the

achievements based on HPAM are able to be applied in practical cases easily and economically.
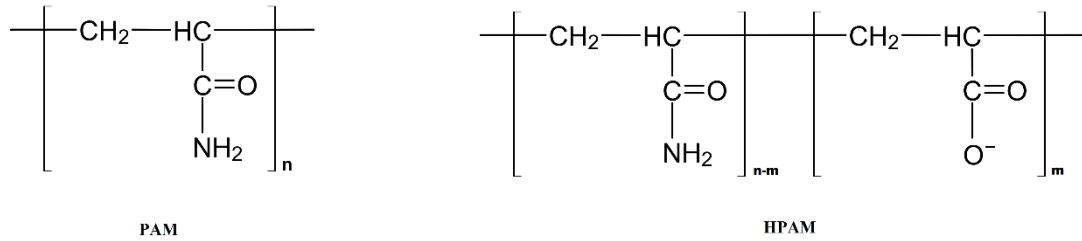
Figure 3.1 Structure of PAM and HPAM

Reagent grade sodium chloride (NaCl) was used as salts to prepare polymer solutions with different salinities. Table 3.1 summarizes all the chemicals conducted in experiments with their important physical properties.

Table 3.1 Details of chemicals

Chemical name	Properties
HPAM	M_W:5-22 M Degree of hydrolysis :25-30%
Sodium Chloride	concentration: 1M

3.1.2 Preparation of working fluids

3.1.2.1 Polymer solution preparation with different concentrations

A concentrated HPAM solution with 3000 ppm was first prepared by mass-balance and used as a stock solution for the entire course of the experiments. It was conducted by dissolving 0.6 g HPAM powder into 199.4 g deionized water by gentle shaking. Next the solution was stirred for over 12 h in a mechanical mixer with a propeller at a moderate speed. After that, the solution was allowed to stand overnight to ensure fully hydration. The well prepared HPAM solution could be easily diluted to 50 ppm, 100 ppm, 200 ppm, 300 ppm, and 500 ppm respectively. All diluted samples were mixed by a magnetic stirrer for at least one day but no more than two days at a medium speed.

3.1.2.2 Polymer solution preparation with different salinities

The polymer concentration was kept constant at 200 ppm after some trial-and-error experiments. According to the investigation in next chapter, the polymer solution of lower concentration exhibits similar properties with Newtonian liquids and the effects of polymer were hardly to identify, which made elastic turbulence occur at a higher shear rate. On the other hand, the polymer solution with higher concentration led the solution to be semi-dilute, while it was not suitable for polymer size measurements and molecular dynamics simulation in the future. Overall, 200 ppm concentration was reasonable.

In the interest of accurate measurements, a series of NaCl solutions with different concentrations (0.1%, 1%, 10%) were previously prepared. 8 g of 1000 ppm HPAM and desired quantities of NaCl solutions were added to each samples and water was added up to 40g. Finally, 200 ppm HPAM solutions with a wide range of salinities (0.01%, 0.03%, 0.05%, 0.1%, 0.3%, 0.5%, and 1%, respectively) were made.

All the samples were mixed by a magnetic stirrer for at least one day but no more than two days at a medium speed and after standing overnight the polymer solutions were able to be used for measurements. The idea behind the procedure is to cause mechanical degradation of HPAM molecules with highest weights, and to cut a high *Mw* tail of the broad molecular weight distribution of the HPAM sample. In a solution with a broad distribution of polymer molecular weights, the heaviest molecules, that are most vulnerable to mechanical degradation, may also make a major contribution to the solution's elasticity. A possible negative effect of that is a significant degradation of elasticity during experimental runs, and inconsistency in the results of the experiments. The procedure of pre-degradation in the mixer leads to substantial reduction of the degradation during the experiments and to substantial improvement of their consistency.

3.2 Rheology dependence measurement

3.2.1 Description of equipment and measurement protocol

For the rheology measurements, a stress-controlled Anton Paar MCR 301 was used as shown in Figure 3.2. This rheometer is suitable for low viscosity fluids as it has a high performance air bearing motor and a patented force rebalance transducer. In these measurements, the viscosity appealed to key attentions since its changes represent the main rheological properties and can imply the polymer contribution to the viscosity.

Figure 3.2 The Rheometer for the measurement of rheology

The cone-plate geometry was used due to its wide measuring range and its accurate temperature controlled ability. What's more, such geometry provides uniform shear rate during test, which is essential for shear-thinning fluids like polymer solutions. The diameter and angle of the cone were selected as 75 mm and 0.157π rad, respectively, since it was more appropriate for low shear rate and low viscosity measurements. The measuring position between the cone and the plates is 0.149 mm. The schematic diagram and the working principle of the measurement are discussed as followed:
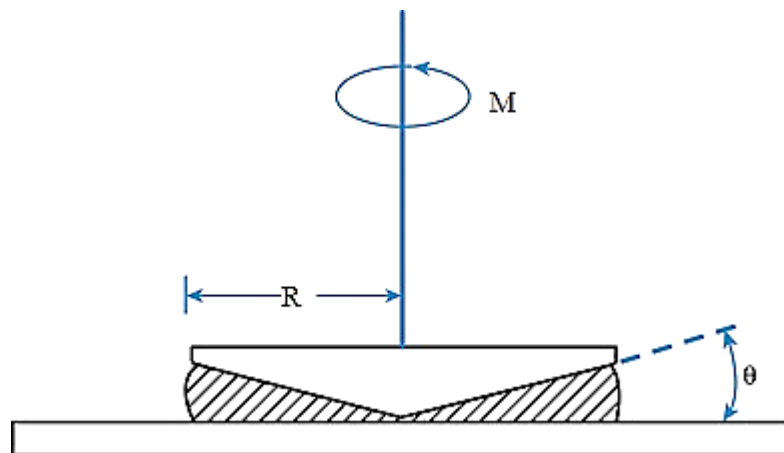
Figure 3.3 The schematic diagram of rheological measurement

For a laminar shear of fluid between two plates, friction between the fluid and the moving plates causes the fluid to shear. The force required for this action is a measure of the fluid's viscosity. This viscous forces were expressed as:

$$F = \eta \cdot A \cdot \frac{u}{h} \tag{3.1}$$

Where η, A, u, and h represent viscosity, the area of the upper surface, the radial velocity and axial length respectively. The shear stress τ is defined as F/A and the shear strain is described by the ratio between shear deformation Δu and the axial length h. The rate of change of strain is referred to as shear rate and is found as a function of time. The formulas for the shear stress and the shear rate are shown below:

$$\tau = \frac{F}{A} \tag{3.2}$$

$$\gamma = \frac{1}{h} \cdot \frac{\delta u}{\delta t} = \frac{u}{h} \tag{3.3}$$

Then the equation (3-1) can be simplified as:

$$\tau = \eta \cdot \gamma \tag{3.4}$$

In cone-plates geometry, the shear rate is same at a random position all over the whole upper plate and is proportional to the angular velocity. The shear stress is only dependent on the torque forced on the motor.

$$\gamma = \omega \cdot \frac{1}{\tan\theta} = n \cdot \frac{2\pi}{60} \cdot \frac{1}{\tan\theta} \tag{3.5}$$

$$\tau = \frac{3M}{2\pi R^3} \tag{3.6}$$

Where ω, n, M, R are defined as angular velocity of upper plate, speed and torque of the motor and radius of the cone, respectively.

It can be found from the equation (3.5) and (3.6) if either shear stress or shear rate is set as independent variable and the other dependent variable is measured by rheometer, the viscosity is obtained by the ration between these two variables. These two kinds of measuring modes are referred as strain-controlled and stress-controlled mode in Anton Paar Rheoplus Software respectively. Generally speaking, the viscosity measured by each mode is same. Here the stress-controlled mode was chosen since the polymer solution showed shear-thinning behaviours, thereby it was more convenient to probe the variation of the viscosity as shear rate increased gradually.

The elastic turbulence was induced at very low shear rate. Therefore, the rheology measurements were mainly conducted with shear rate ranging from 0.1 to 10 s^{-1} at room temperature (25 °C). Prior to any measurements, the rheometer was tested with a standard oil and pure water at room temperature to ensure the instrument was calibrated. In addition, the measurements for the Newtonian fluid (65% sucrose solution) were conducted first and the experimental results were validated by the previous studies, which indicates good reliability of the results and the experimental protocol.
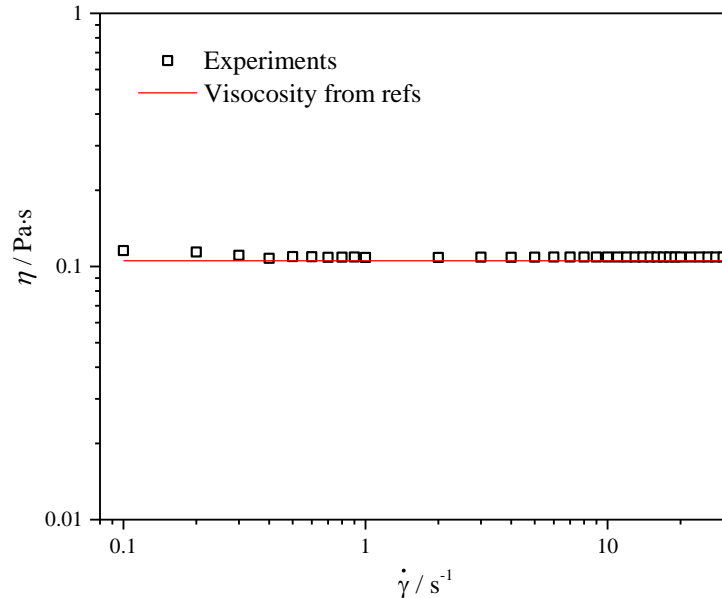
Figure 3.4 comparison between measured viscosity of 65% sucrose solution and results from ref (Swindells et al., 1958) **.**

3.2.2 Stress controlled transient test

The transient test accurately measures the steady-state properties at a constant shear rate during the selected time duration. The fluid behaviour at low shear rate takes more time to equilibrate. Therefore, two separate zones (where the user defines a low shear rate and its time duration) can be programmed to investigate the time required for polymer solution to reach the steady-state flow regime. The major purpose of our measurements is to obtain an accurate viscosity at a specific shear rate. The tests for two low shear rates (0.1 and 1 s^{-1}) were separately run for each sample as a function of time. The measurement profile for 200 ppm HPAM solution without salt addition is shown in Figure 3.5. The shear steady viscosity at a specific shear rate is obtained by taking an average of the values in plateau region. The interval time for 0.1 s^{-1} was determined as 200 s. At $\dot{\gamma} = 1$ s^{-1}, the viscosity becomes stable when time exceeds 50 s. Due to higher shear rate requires shorter time

to equilibrate, therefore, the interval time of the viscosity measurement for the maximum shear rate was set 50 s to allow the viscosity fully stable. Each measurement was repeated three times at one sample and the error bar was built based on these results.
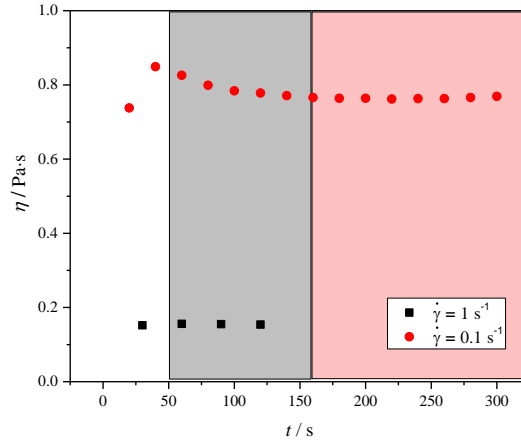
Figure 3.5 transient test for 200 HPAM solution with different shear rate

3.2.3 Effect of concentration on polymer viscosity

(a) Viscosity   (b) shear stress
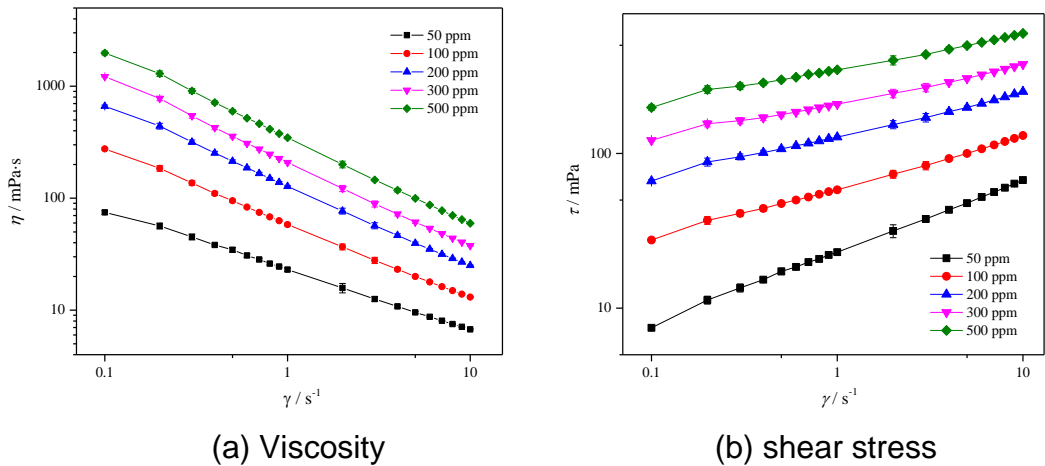
Figure 3.6 Variation of the rheology with shear rate at different polymer concentration

(a) Viscosity   (b) shear stress
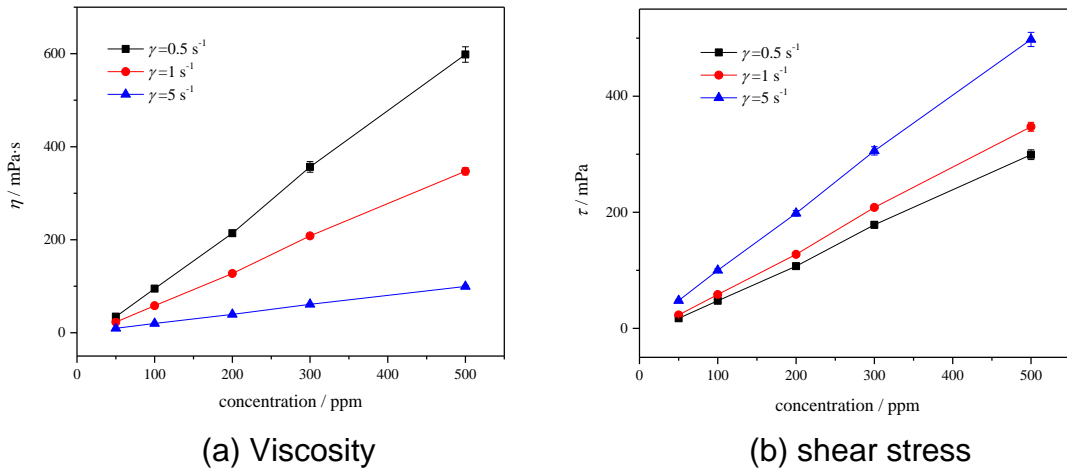
Figure 3.7 Variation of the rheology with polymer concentration at different shear rate

Figure 3.6(a) demonstrates the variations of the apparent viscosity with shear rate for various polymer concentrations at 25 °C. For all samples measured, a so-called shear thinning phenomenon was obtained that the viscosity decreased with increasing the shear rate. The relationship between viscosity and shear rate was fitted with the power-law model, which was similar with results in Nasr-El-Din's work (Nasr-El-Din et al., 1991). This viscosity drop was induced by the aligning of the polymer chains when exposed to the shear flow.

It also can be found that the viscosity increased linearly with the increasing polymer concentrations as shown in both Figure 3.6(a) and 3.7(a). This because the increased numbers of polymer molecules resulted in more interactions between polymer chains, which cause more frictional effects to the increase of viscosity. The variation became more significant at lower shear rate and the shear-thinning behaviour at higher concentration was more remarkable as well.

Figure 3.6(b) shows the shear stress curve as a function of shear rate. The shear stress (or torque) was proportional to the shear rate and no sharp changes occurred, which represented that there was no instability in the flow. Thereby the results were reasonable.

3.2.4 Effect of sodium chloride on polymer viscosity

(a) Viscosity   (b) shear stress
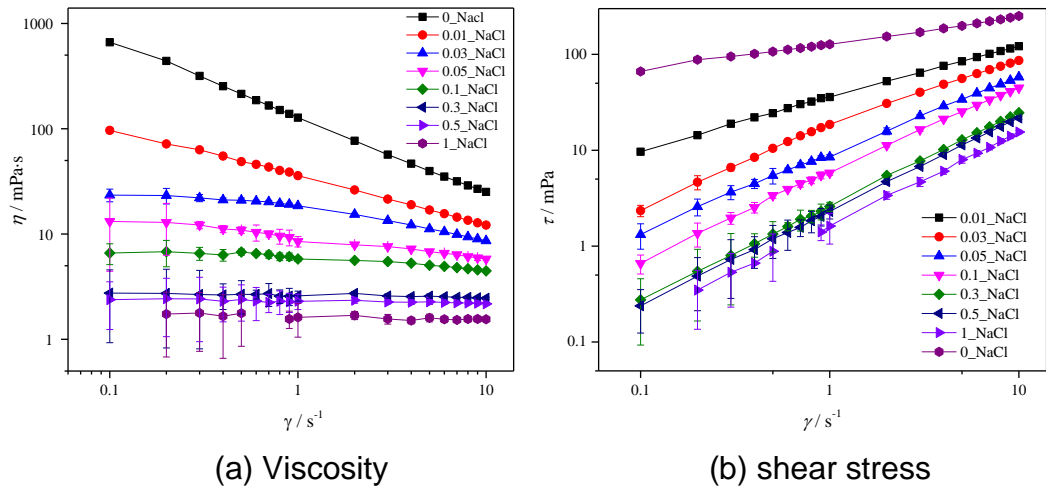
Figure 3.8   Variation of the rheology with shear rate at different salt concentration

Figure 3.8 shows the flow curves of a polymer solutions with 200 ppm and various NaCl concentrations at 25 °C. At a given shear rate, the viscosity of polymer solutions decreased significantly as the salt concentration increased, especially at low shear rate. A similar shear-thinning behaviour with pure polymer solutions was found when the salinity was low. However, unlike the low salinity, when the salt concentration was high, a Newtonian behaviour was observed before the shear-thinning behaviour as the shear rate increased gradually. The higher the salt concentrations were, the larger the value of this critical shear rate was. These trends were similar to those investigated by Ward and Martin (Ward and Martin, 1981). Due to the resolution of the equipment, when the viscosity or the shear rate is extremely smaller, the measured uncertainty becomes larger.

The HPAM has two functional groups (amide and carboxyl) along its back-bone chains. When dissolved into the water, the carboxyl groups are negatively charged, thereby developing a strong electrostatic repulsion between them. The repulsion makes the polymer chain stretch. This means the hydraulic radius of the polymer chain is large and the viscosity is high consequently. When adding sodium chloride into the water, the negatively charged carboxyl groups are shielded with sodium cations, resulting in the diminishment of the repulsion effect and the shrinkage of the polymer molecules. This reduction decreases the hydraulic radius of the polymer and the viscosity of the polymer solutions. Also, additional shear forces should be occupied to overcome the charge shielding effect to fulfil the aligning of the polymer molecules. Hence there is a critical shear rate above which the shear-

thinning appears, while, otherwise, Newtonian behaviour is obtained. As the salt concentration is increased, the shielding effect strengthens, thereby the critical shear rate increases.

However, with increasing the salt concentration continually, the salinity no longer affects the viscosity any more as shown in Figure 3.9(a). The viscosity tends to a constant value which is independent with salinity. It is because the numbers of carboxyl groups in polymer chain to be shielded by salt cations are limited. Therefore, the polymer molecules have already shrunk by a critical salinity and above that there is no more influence. After the carboxyl groups are saturated, based on the experiments done by Ward and Martin (Ward and Martin, 1981), the critical shear rate for the transition is no more changed as well.

(a) Viscosity   (b) shear stress
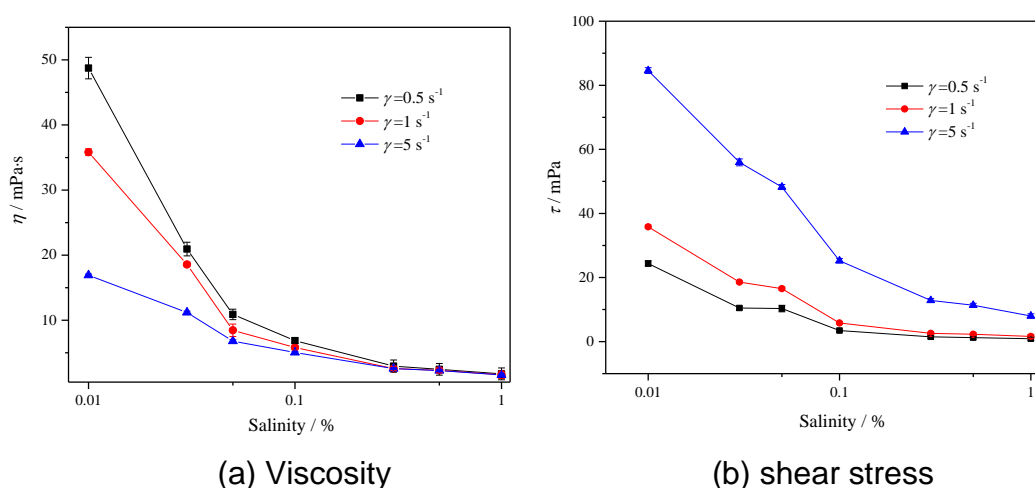
Figure 3.9 Variation of the rheology with salinity at different shear rate

3.3 Morphology measurement

The increase of viscosity by polymer concentration is mainly due to the enhancement of the interaction between polymers. When the polymer solution is still in dilute regime, the polymer concentration demonstrates slightly on polymer structure. However, due to the shielding effects by the cations, the salinity effects on the viscosity are ascribed to the variations of polymer configuration from stretch state to coil state. A morphological observation could give a solid support to this mechanism. In addition, the onset of elastic turbulence is related to the polymer coil-stretch transition. The salinity exhibits significant effects on the polymer structure, which correspondingly affects the onset of elastic turbulence. Therefore, to study the morphology under different salinity is important and will give further information or mechanism in

explanation of its effects on the onset of elastic turbulence, which will be described in the following chapters

3.3.1 Experimental measurement for polymer size

To measure the polymer size, the Malvern Zetasizer Nano ZS with Dynamic Light Scattering method was conducted. DLS is based on the extraction of spectral information derived from time-dependent fluctuations of the light scattered from a spatially limited volume within the sample. Then the diffusion coefficient is obtained by the intensity correlation function and thereby the hydrodynamic radius of the particles is calculated by the Stoke-Einstein equation.

The particles suspended within a liquid undergo the Brownian motion. The larger the particles, the slower the Brownian motion will be. Specially, when a suspension of particles is hit by a monochromatic coherent beam of light, generated scattered light waves spread out in all directions. Scattered waves interference in the far field region generates a net scattered light intensity $I_s(t)$. Due to the random motion of the suspended particles within the sample the interference can be stochastically either constructive or destructive, hence resulting in a stochastic light intensity signal.

The corresponding measured normalized intensity correlation function is written as:

$$G(\tau) = \frac{\langle I_s(t) \cdot I_s(t+\tau) \rangle}{\langle |I_s(t)|^2 \rangle} \tag{3-7}$$

Where t and τ means time and time lag. For monodisperse particles:

$$G(\tau) = A[1 + B exp(-2\Gamma\tau)] \tag{3-8}$$

Where A and B are correction factor that depends on the geometry and alignment of the laser beam in the light scattering setup, and Γ is decay rate. From the definition of Γ:

$$\Gamma = q^2 D \tag{3-9}$$

Where q is the wave vector, which is depended of the scattering angle θ.

$$q = \frac{4\pi n}{\lambda} sin\left(\frac{\theta}{2}\right) \tag{3-10}$$

Where n is the refractive index of the sample and λ is the incident laser wavelength.

The diffusion coefficient D is then related to the radius R of the particles by means of the Stoke-Einstein equation:

$$D = \frac{k_B T}{6\pi\eta R} \tag{3-11}$$

Where k_B is the Boltzmann constant, T is the temperature and η is the viscosity.

The speed at which the particles are diffusing due to Brownian motion is measured by recording the rate at which the intensity of scattered light fluctuates. In a word, DLS is based on the extraction of spectral information derived from time-dependent fluctuations of the light scattered from a spatially limited volume within the sample. Then the diffusion coefficient is obtained by the intensity correlation function and thereby the hydrodynamic radius of the particles is calculated by the Stoke-Einstein equation.

The relationship between the hydrodynamic radius of a HPAM chain and the salinity is represented in Figure 3.10. The hydrodynamic radius of polymer decreases quickly with increasing the salinity. This downtrend becomes slower when the salt concentration exceeds 0.1%, which is consistent with the results in viscosity measurements. Figure 3.10 also shows the existence of the critical salinity, after which the polymer size is independent on salt concentrations. As a result, the viscosity of the polymer was no longer affected by the salinity.
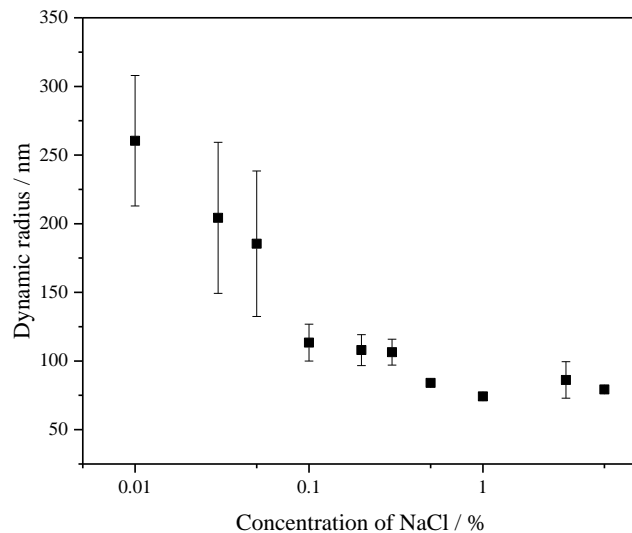
Figure 3.10 The influence of NaCl concentration on the dynamic radius of polymer

The size distribution curves of three samples with different salinities are shown in Figure 3.11. In terms of high salt concentrations, the size of polymer is uniformly distributed. While for the low salt concentrations, a sharp peak occurs, which means most of the polymer are at such a size, and this peak moves to the right to a larger size when the salinity decreases.
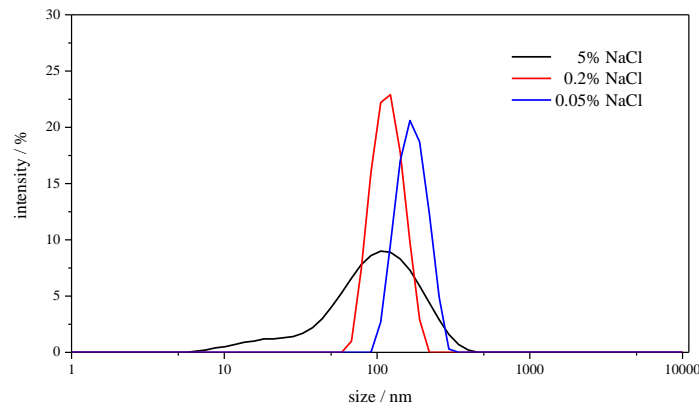
Figure 3. 11 The intensity of size distribution at different NaCl concentration

Although the results obtained by DLS are quite consistent with the rheological properties of polymer solutions, it should be noticed that the polymer size measured by DLS is hydrodynamic radius, which related to Brownian motion. This radius cannot directly reflect the conformation of polymer. In addition, the diameter of a single polymer is too thin to be measured practically. It is very challenging to obtain the morphology of a single polymer. However, the morphology of a single polymer contributes to the understanding of the elastic instability in shear flow. Therefore, an efficient approach is required to sort these problems.

Molecular dynamics (MD) simulation, on the other hand, has been proven to be a valuable tool to study the self-assembly of polymers at the microscopic level, which could reveal detailed three dimensional conformational and structural behaviour (Wang et al., 2012; Shang et al., 2008; Cao et al., 2011; Yuan et al., 2010). Although a high weight molecular HPAM chain is always long, the short chain was proved to be capable of capturing the properties of long chain polymers (Reith et al., 2002). What's more, the MD simulation can reveal the microscopic mechanism of the interaction between polymer and salts ions in atomic level, which gives more details for the salinity effect.

3.3.2 Simulation details by MD simulations

3.3.2.1 Governing equations

The traditional MD method uses classic Newton's second law for each particles i of the N-atoms system:

$$m_i \vec{r} = \vec{F}_i \tag{3.12}$$

Where m_i and $\vec{r}$ is the mass and acceleration of atom i. $\vec{F}_i$ is the force exerted on the atom i, also expressed as the gradient of the potential energy:

$$\vec{F}_i = -\nabla E(\vec{r}_i) \tag{3.13}$$

Where the potential E is a function of all the relative atom positions only. Combining these two equations yields:

$$-\frac{dE}{d\vec{r}_i} = m_i \frac{d^2\vec{r}_i}{dt^2} \tag{3.14}$$

Thereby if the potential energy E is given, the velocity and position of a single atom can be obtained. From the statistical mechanics, the thermodynamic state of a system is able to be represented. The total configuration field potential E of an N-atoms system could be written as:

$$E_{total} = E_{intromolecular} + E_{intermolecular} + E_{external} \tag{3.15}$$

$$E_{intramolecular} = \Sigma_i^N E_{bond} + \Sigma_i^N E_{angle} + \Sigma_i^N E_{dihedral} + \cdots \tag{3.16}$$

The function computes the system potential energy as a sum of terms that describe intramolecular interactions, intermolecular interactions and external field potential. The intramolecular potential consists of bond energy, angle energy, and dihedral energy and so on. The intermolecular potential energy also known as energy between non-bonded pairs of atoms arises form van der Waals interactions (regarded as short-ranged) and electrostatic interactions (coulombic, long-ranged). Normally, this pair wise potential field is approximated using the Lennard-Jones (LJ) potential (Rahman, 1964), which is most widely used and is actually a good interpretation for most complex fluids. The LJ potential can be described as follow:

$$E(\vec{r}_{ij}) = 4\varepsilon \left\{ \left(\frac{\sigma}{\vec{r}_{ij}}\right)^{12} - \left(\frac{\sigma}{\vec{r}_{ij}}\right)^6 \right\}, \quad |\vec{r}_{ij}| \le |\vec{r}_c| \tag{3.17}$$

$$E(\vec{r}_{ij}) = 0, \quad |\vec{r}_{ij}| > |\vec{r}_c| \tag{3.18}$$

Although the LJ potential describes the interaction of pairs of molecules, it also shows very good agreement to experimental data for real systems which have two and greater body interactions (Tildesley and Allen, 1987).

3.3.2.2 Potential and force field models

With development of computing science, many different force fields were used to characterize the molecular interaction in molecular levels. The function field form of a force field depends on the accuracy required for its purpose. For example, CHARMM, GAFF and Amber force field were well established for capturing the physical properties of proteins and polymers. The OPLS force field was designed mainly to describe the small liquid molecules, such as n-decane. The CVFF and PCFF force fields are widely applied for inorganic salt. There are many other designed force field parameters for some specific

conditions. Indeed, a suitable force field parameter should be conducted by using high-level quantum calculations and by fitting to presented experimental data. Only the required force field parameters are applied, the concomitant properties could be captured expectantly by MD simulations.

In this project, GAFF force field (Gromos 53a6) was used for the description of the polymer motion since this force field has suitable potential parameters for amide function group and carboxyl function group along the HPAM backbone. Many investigation of similar polymer solution has been done in such force field (Bhowmik et al., 2007; Lau et al., 1994). Therefore, it is suitable for the present simulations. Detailed force field parameters will be introduced in the later.

3.3.2.3 Integration algorithm

Once the potential is determined, the corresponding acceleration for each atom can be calculated and thereby the velocity and position could be estimated integration algorithms, e.g. leaf-frog Verlet algorithm (LFV), Velocity-Verlet algorithm (VV). Most integration algorithms predict the positions, velocities and accelerations can be approximated by a form of Taylor series expansion.

The work described in this study uses the LFV scheme due to its simplicity and speed, which can be easily applied to complex molecular systems and combined with constraint algorithms. The LFV scheme can be described as follow:

The forces of atoms at time t, $\vec{F}(t)$, in the system are firstly updated with by the force field parameters. Then the velocity at time $t+1/2\Delta t$ could be integrated by:

$$\vec{V}\left(t + \frac{1}{2}\Delta t\right) = \vec{V}\left(t - \frac{1}{2}\Delta t\right) + \frac{\Delta t}{m}\vec{F}(t) \qquad (3.19)$$

Where m is the mass of an atom and the Δt is the timestep. The coordinates of the atoms at time t+Δt are estimated using the updated half-step velocities:

$$\vec{r}(t + \Delta t) = \vec{r}(t) + \Delta t \cdot \vec{V}\left(t + \frac{1}{2}\Delta t\right) \qquad (3.20)$$

With the updated coordinates of atoms, the forces between atoms are changed and molecular dynamic motion is achieved by the repetition of the procedures mentioned above. When the system is equilibrated, e.g. the total energy or density is stable, the desired properties can be obtained by statistical analysis of atomic positions, velocities and energies, etc.

3.3.2.4 Statistical Mechanics

In molecular dynamics simulation, the connection between microscopic simulations and macroscopic properties is made via statistical mechanics, which provides mathematical expressions that relate macroscopic properties to the distribution and motion of the atoms. The thermodynamic state of a system is usually defined by basic parameters such as the temperature T, the pressure p, and the number of particles N.

The mechanical or microscopic state of a system is defined by the atomic position $r(t)$ and momenta $p(t)$ at a time t. For example:

Temperature:

$$T = \sum_{i=1}^{N} \frac{(V_i V_i) \cdot m_i}{N_f k_B}$$

$$(3.21)$$

Where m_i is the mass of an atom, $\vec{V}$ is the velocity of an atom, N_f is degree of freedom of a system, k_B is Boltzmann constant.

Pressure:

$$P = \frac{N k_B T}{\vec{V}} + \frac{\sum_{i=1}^{n}(\vec{r}_i \cdot \vec{F}_i)}{d\vec{V}}$$

$$(3.22)$$

Where V is the volume of the system, $\vec{r}_i$ is the position of an atom, $\vec{F}_i$ is the force added to an atom and d is the dimensionality of the system.

There are many different ensembles with different characteristics, such as micro canonical ensemble (*NVE*), canonical ensemble (*NVT*), isobaric-isothermal ensemble (*NPT*) and grand canonical ensemble (*μVT*). Which ensemble is suitable for simulation based on what properties are mainly focused on. Generally, the molecular dynamic is most easily performed in the constant *NVT* ensemble:

In this project, the gyration radius of HPAM is simulated, which follows the below formula:

$$R_g^2 = \frac{1}{M} \sum_{1}^{N_p} (m_i(\vec{r}_i - \vec{r}_{cm})^2)$$

$$(3.23)$$

Where M is the total mass of the polymer molecules, N_p is the total numbers of atoms in polymer molecules, r_{cm} is the centre-of-mass position of the molecules.

3.3.2.5 Modelling packages selection

Popular MD packages such as LAMMPS, GROMACS, AMBER and DL_POLY have similar features. However, the different force fields and parallel scalability built in the packages make them more suitable in their own specific

area. The GROMACS and AMBER are powerful in simulations of biomolecules, while the DL_POLY is famous for the characteristic of interface. And the LAMMPS is widely used in materials science.

In this project, the MD package Gromacs was chosen to undertake the simulation of polymer solutions due to its extremely fact calculating speed for the non-bonded interactions (which usually dominates simulations). What's more, the Gromacs is known to be primarily designed for biochemical molecules like proteins, lipids and nucleic acids, etc. The built-in Gromos force field is suitable and validated for polymer simulations. Although with some modifications, the Gromos force field can also be applied in any other packages such as LAMMPS, considering the time consumption and simulation convenience, the Gromacs was selected to go through the all simulations of this project.

3.3.2.6 Simulation details (progress, potential parameters)

All MD simulations were conducted by GROMACS simulation package (version of 2016.03) (Hess et al., 2008). The Gromos 53a6 force field parameters (Oostenbrink et al., 2004) were used to describe the properties of PAA chains, Na^+ and Cl^- ions, including the potential of bonds, angles, dihedrals and non-bond interactions. The aliphatic carbon atoms with its bonded hydrogen in PAA chain were regarded as united atoms to speed up the calculations, and the Rychaert-Bellemans (RB) potential was used for the descriptions of aliphatic torsion (CH2-CH1-CH2-CH1). The simple point charge (SPC) model was conducted to characterise water molecules. The non-bond interactions were represented by a short-range 12-6 Lennard-Jones (LJ) potential and a long range Coulombic potential, expressed in a form of pairwise interacting atomic charges. The LJ potential between two atoms can be written as follow:

$$V_{LJ}(r_{ij}) = 4\epsilon_{ij}\left[\left(\frac{\sigma_{ij}}{r_{ij}}\right)^{12} - \left(\frac{\sigma_{ij}}{r_{ij}}\right)^{6}\right] \qquad (3.24)$$

The parameters σ and ε represent energy constant and diameter of one of the atoms, which depend on atom types. The Lorentz-Berthelot combining rules were used to describe LJ potential between different atom types. The charges of atoms were adopted from previous studies (Biermann et al., 2001; Hoda and Larson, 2009; Oldiges and Tönsing, 2002; Sulatha and Natarajan, 2011). All parameters for PAA solutions are listed in Table S4 in the Supplement documents.

The leapfrog algorithm was used to integrate the motion of atoms with a time step of 2 fs. The Coulombic electrostatic interactions were calculated by using the particle Mesh Ewald (PME) method with a cut-off distance of 1.0 nm and Fourier spacing of 1.2 nm. The cut-off distance for short-range van der Waals interaction was 1.0 nm. To remove initial strain, the initial configuration was conducted by energy minimization using the Steepest Descent method. This was followed by 500 ps NVT and 500 ps NPT simulations with position restraints on PAA chains and not on water molecules to achieve a well equilibrated system. A Berendsen thermostat and a parrinello-rahman barostat were used to control the temperature and pressure at 300 K and 1 bar during the calculation with relaxation time of 0.1 ps and 0.5 ps, respectively. After full relaxation, a further 120 ns NVT simulation was performed with the water molecules fixed with SETTLE algorithm and all bonds constrained by using SHAKE procedure. The last 60 ns were conducted for the sampling and analysis.

3.3.3 Validation of force field parameters

The force field and MD code were first validated by conducting a simulation of a Polyacrylic acid chain and comparing the results with previous investigations.

3.3.3.1 Model construction

A atactic PAA chain was generated using Bernoullian statics by assigning random dihedral angle values. Six values of DoI (i.e., 0, 0.2, 0.4, 0.6, 0.8, and 1.0, respectively) for each polymer chain were achieved by random deprotonation of the carboxylic acid groups along the chain. The DoI, f, is defined as the ratio between the number of charged monomers, N_c, and the total number of monomers along the chain, N_m. 4000 water molecules were put into a cubic box with length of 5 nm, which leads to PAA concentration of approximately 1.96 wt%. The Na^+ counter-ions were added into simulation boxes for the neutrality of the system. Figure 3.12 shows the front view of the simulation box containing 20-monomers-PAA, water molecules and Na^+ ions. An extended conformation is allocated as an initial structure of the PAA chain.
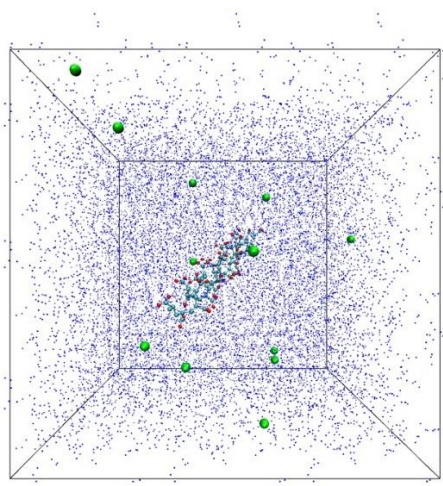
Figure 3.12 The initial configuration of the 20-monomers-PAA solution with f=0.4 (blue: water; red and white: oxygen and hydrogen atoms along the PAA chain, respectively; cyan: PAA backbone; green: Na+ ions)

After 120 ns simulation, the energy variations and water distributions from the sampling period are shown in Figure 3.13, which implies a well equilibrated system and the reasonability of production.
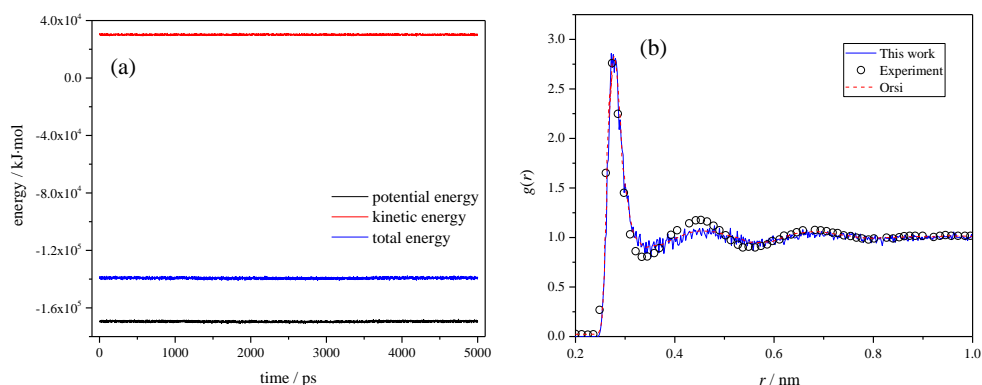
Figure 3.13 Energy variations and water distributions in equilibrated system. (a) Energy profiles; (2) Radial distribution functions of Water

3.3.3.2 Gyrate radius of PAA with different DoI

To reveal detailed three-dimensional information, a series of snapshots at different DoI are performed in Figure 3.13. It can be seen that the unionized PAA chain is in a coiled state. As expected, this collapsed PAA chain gradually extends with the increase of the charge density, and finally reaches a stretched state.
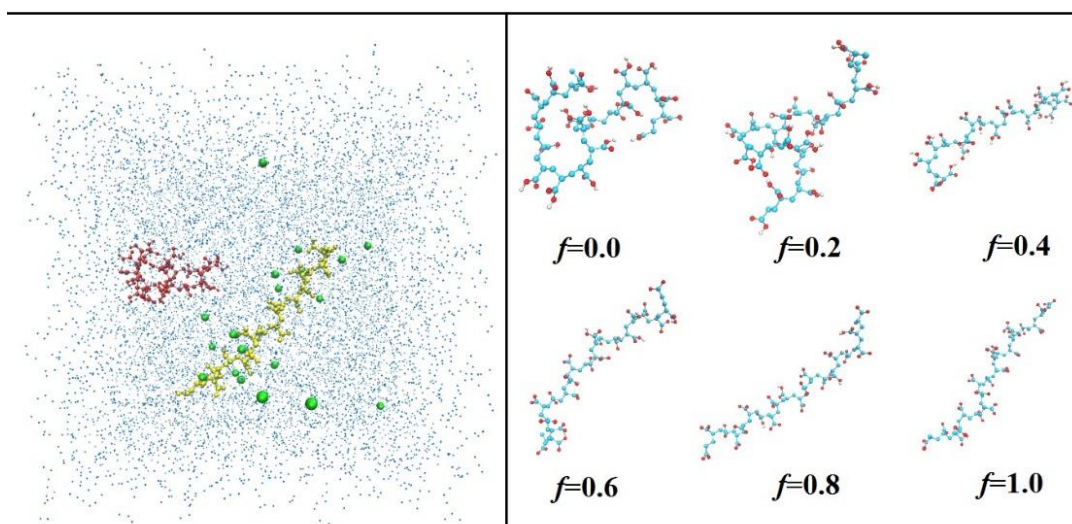
Figure 3.14 Snapshots of PAA chains with different ionization at an equilibrated state (The left shows structure comparison of PAA chains in solutions, where the chain with red colour represents f=0.0, with yellow represents f=1.0. The green atoms represent Na$^+$ ions)

The average radius of gyration of 20-monomers-PAAs as a function of DoI is shown in Figure 3.15(b). The gyrate radius of PAA continually increases from approximately 0.68 nm to 1.18 nm as the ionization increases from 0 to 1. Significant increase of the gyration radius is observed at DoI > 0.2, which levels off around 0.8 nm. It shows that the increased charge density cannot make the poly-ion to stretch itself to the fully length even it is totally ionized. This is because the interaction between poly-ion and courier-ions Na$^+$ would result in repression of the ionization effect, which will be discussed later. The transient variations of radius of gyration show that PAA macromolecules equilibrate thermodynamically due to the Brownian motion effect, Figure 3.15(a). For partially ionized PAAs, these fluctuations are found to be stronger than either fully ionized or unionized PAAs, which is due to the random allocation of the charged COO$^-$ groups.
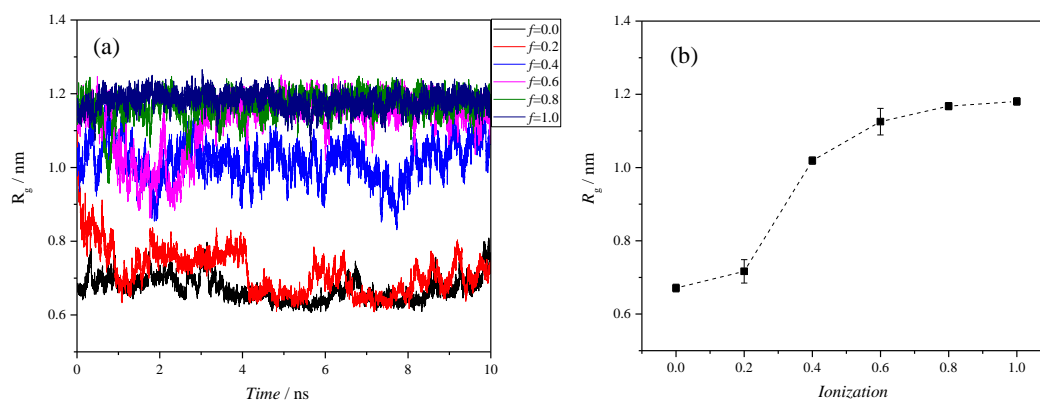
Figure 3.15 Variations of PAA conformation with different degrees of ionization: (a) Instantaneous radius of gyration against time; (b) average radius of gyration

In this work, the radius of gyration of a fully ionized 20-monomers-PAA was given a value of 1.18 nm from the last 10 ns MD simulation trajectory, which is agreed well with the previous results, as shown in Table 3.2, , indicating the validation of both force field parameters and simulation protocol.

Table 3.2 Radius of gyration of fully ionized PAA calculated in other works

	Brownian Dynamics	Monte Carlo	Molecular simulation			Our results
Force field	coarse-grained		CHARMM 27	GROMOS 96	GROMOS 53a6	GROMOS 53a6
Rg of PAA [nm]	1.15 (Reith et al., 2002)	1.11 (Reith et al., 2002)	1.05-1.30 (Katiyar and Jha, 2017)	1.14 (Biermann et al., 2001)	1.06 (Sulatha and Natarajan, 2011)	1.18

3.3.3.3 RDFs of PAA with different DoI

The radius distribution function (RDF) is used to investigate the interaction between PAA molecules and water as well as PAA molecules and courtier-ions Na$^+$, which provides further interpretation of the polymer chain formations from microscopic view. The deprotonation of the carboxylic acid function groups leads to the essential differences between ionized PAA and non-ionized PAA. Therefore, the RDFs corresponding to carboxylate (COO$^-$) or carboxyl groups (COOH) and water molecules can provide better understanding on the effect of ionization. Figure 3.16(a-b) shows the interaction for the PAA carboxylate oxygen atoms with respect to the water oxygens and hydrogens. Two peaks are founded in both RDFs profiles indicating that a double electronic layer (EDL) existed around PAA molecules. The first peaks at 0.18 nm for carboxylate oxygen atoms and water oxygen

atoms, and 0.28 nm for water hydrogen atoms are similar to the hydrogen bonding distance in bulk water. These mean a strong hydrogen bonding effect dominating the interaction between carboxylate groups and water molecules. An increase of the intensity of this interaction is also observed as increased the DoI, which demonstrates that more numbers of carboxylate groups are able to attract more water molecules.

The RDFs for the carbonyl oxygen atoms and water molecules is shown in Figure 3.16(c-d). Although the first peaks are observed at same locations with carboxylate oxygen atoms, the peak intensities are much lower. In addition, the second peaks vanish, indicating that the interaction between carbonyl oxygen atoms and water molecules are too weak to form the second water layer. In the case of RDFs corresponding to hydroxyl oxygen atoms and water oxygen atoms, as presented in Figure 3.16(e), the first peak is allocated at a slightly closer distance. However, as shown in Figure 3.16(f), the nearest bonding distance between hydroxyl oxygen atoms and water hydrogen atoms is approximately 0.35 nm, which shows a very weak hydrogen bonding effect between these atoms. It can be concluded that due to the reduction of peak intensities and hydrogen bonding effect, the carboxylate oxygen atoms interact more intensively with water in comparison with the carbonyl oxygen and hydroxyl oxygen. Although the number of carbonyl oxygen atoms and hydroxyl oxygen atoms reduces with increasing the charge density, the increase of interaction between carboxylate oxygen and water attracts more water around PAA chain, resulting in a stronger interaction between unionized carboxyl group and water. Therefore, the trends of the ionization effect on the carbonyl oxygen and hydroxyl oxygen are similar with those of carboxylate oxygen.

The RDF profile between centre of mass of the PAA chain and water oxygen atoms is plotted in Figure 3.16(g). There are two peaks dominated by hydrogen and oxygen atoms, respectively, when the distance is closer than 0.3 nm. As the DoI increases, the first peak vanishes gradually and in contrast, the second peak increases abruptly, which is attributed to the reduction of the number of hydroxyl hydrogen atoms and the increase of the number of oxygen atoms in carboxylate groups. As discussed above that the carboxylate groups attract more water than carboxyl groups, therefore, more hydrogen bonds should be formed in fully ionized PAA. From Table 3.3, it can be found that the number of hydrogen bond between PAA chains and water molecules increases as the increase of the charge density. As a result of ionization, the repulsion between intramolecular along PAA chains and the hydrogen

bonding effect stretch the atoms away from the each other and attach to the water molecules, which leads to the expanding of the PAA coils and reaches a stretch state at final.

Table 3.3 Variation of H-bonds as a function of degree of ionization

Ionization	f=0.0	f=0.2	f=0.4	f=0.6	f=0.8	f=1.0
H-bonds	46	59	77	97	116	134

The distribution of Na^+ counter ions in the vicinity of PAA chain is represented using RDF of carboxylate oxygen atoms with respect to Na^+ ions in Figure 3.16(h). There are two sharp peaks: a first peak locates at 0.25 nm and a second peak locates at 0.4 nm, respectively. Although the absolute values of peaks are very high, the number of sodium ions in the near proximity are very small as described by the coordination number curves (Ramachandran et al., 2013). This is agreed well with the experimental fact that Na^+ are not bonded to the carboxylate groups in PAA at higher charge densities (Koda et al., 1982). From the variations of the second peak, the Na^+ ions are preferentially closer to the chain backbone, which, in return, weakens the electrostatic repulsions along the PAA chain. Therefore, in case of sodium polyacrylate, increasing ionization cannot stretch the polymer chain to its full length even at fully degree of ionization.

Both the results from gyrate radius and RDFs show good agreement with previous studies, which, as a result, gives a solid validation for the feasibility of the force field, MD packages and even the simulation details. When replace the hydroxyl with amide groups, the HPAM chain is formed. The force field parameters to characterize the amide groups could be obtained from Ref (Ma et al., 2016), where the amide is well interpreted. Therefore, with these suitable potential parameters, the properties of HPAM is capable of investigating.
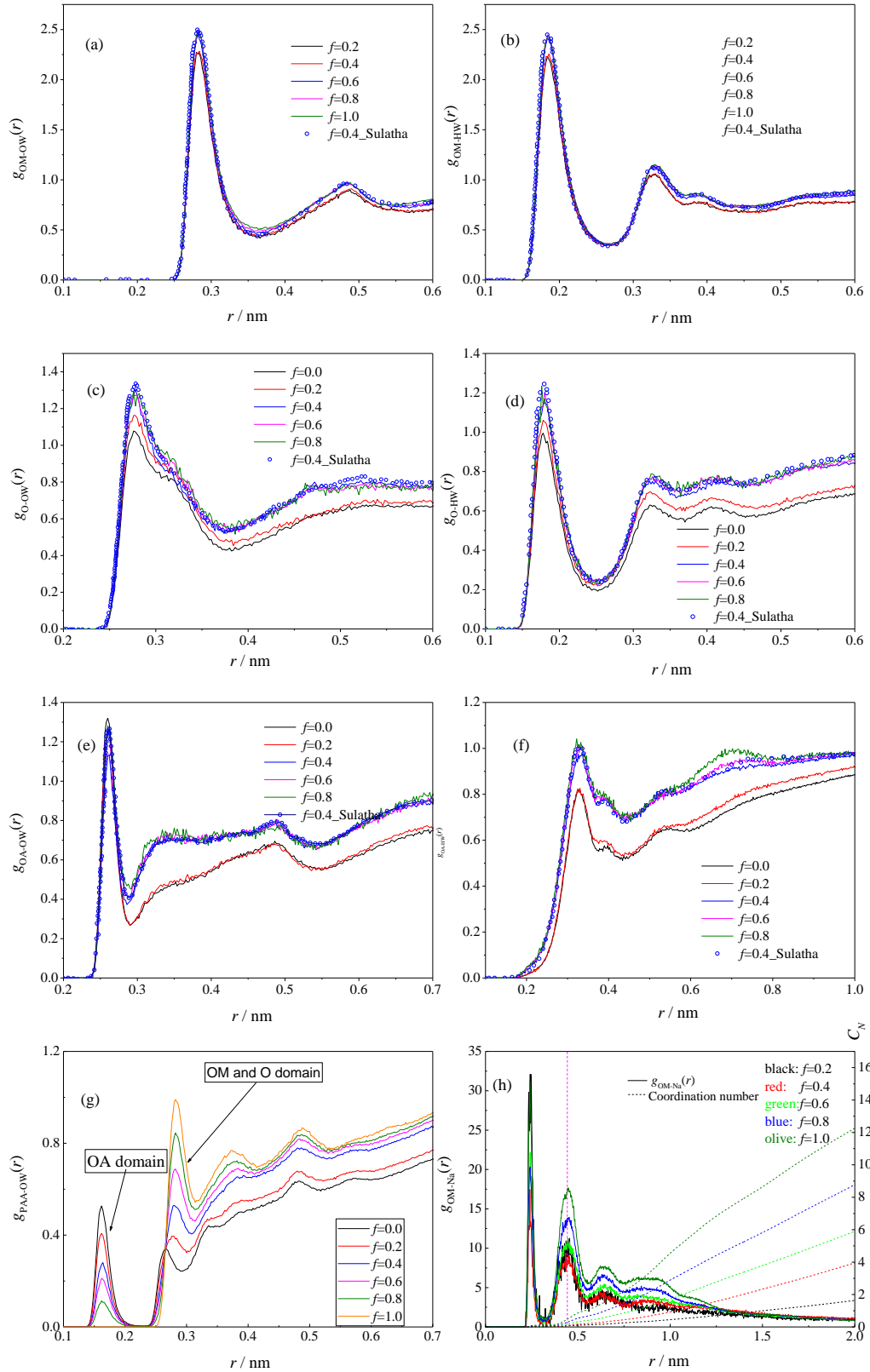
Figure 3.16 Radial distribution functions as a function of degree of ionization. (a) Carboxylate oxygen-water oxygen pairs; (b) Carboxylate oxygen-water hydrogen pairs; (c) Carbonyl oxygen-water oxygen pairs; (d) Carbonyl oxygen-water hydrogen pairs; (e) Hydroxyl oxygen-water oxygen pairs; (f) Hydroxyl oxygen-water hydrogen pairs

3.3.3.4 simulation size sensitivities

In this section, the effects of system size on the simulation results are discussed. With the same PAA concentration, six isotactic PAA chains with different numbers of monomers were first investigated, whose radii of gyration are shown in Figure 3.17. Similar trends are observed for all curves that as the charge density increases, the radius of gyration of the PAA chains becomes larger. The PAA chains expand rapidly with charged carboxylate groups increases ($f < 0.4$) and then slow down due to the weakening of the electrostatic repulsions caused by counter ions Na^+ ($f > 0.4$). Particularly, with the same DoI, the PAA chain with more numbers of monomers holds greater values of the radius of gyration. This is occurred even in non-ionized PAA chains, indicating that longer polymer chains tend to form larger coils in neutral state. If a shrinkage is defined as the ratio of gyrate radius of non-ionized PAA chain to fully ionized PAA chain, thereby with increasing the numbers of monomers, a reduction of the shrinkage rate is observed, indicating that the deformation of the PAA chain is more dramatic. In another word, it is much more obvious to study the conformation of a single PAA chain with more monomers.
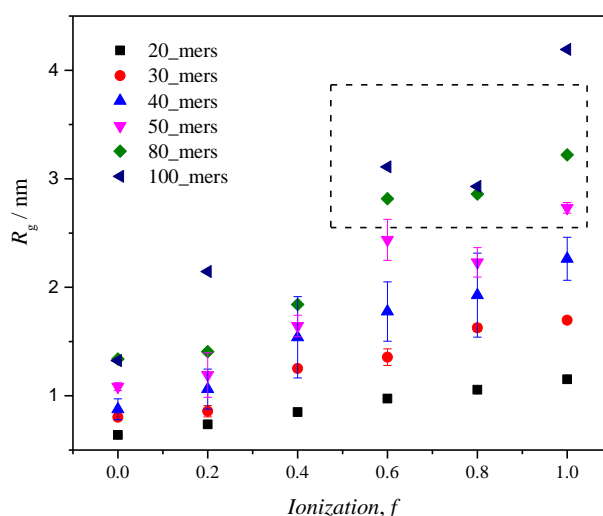
Figure 3.17 The averaged radius of gyration of PAA chains with different numbers of monomers

The results for PAA chains with more numbers of monomers show unexpected perturbations especially at higher DoI, which should be related to the periodicity artefacts. With a same polymer concentration, the initial and fully ionized polymer length exceed the length of the simulation box. This over-length polymer chain will be interacted with other polymer chains due to the periodic boundary conditions, which makes the polymer solutions in semi-dilute regime. Therefore, to correctly characterize behaviours of a larger

oligomer in dilute state a suitable solvate volume is required. A length ratio of a fully ionized PAA chain to the box is introduced and compared in Figure 3.18. It can be observed that the length ratio is continually increasing with the increase of the numbers of monomers. As a result, when the length ratio is large enough (e.g., L_{fully}/L_{box}=0.4), the boxed water becomes too small for the long chain PAA to provide efficient information. Based on prior studies(Patel et al., 2017; Katiyar and Jha, 2017; Gupta and Natarajan, 2017; Gupta and Natarajan, 2016; Sulatha and Natarajan, 2011) , a length ratio value below 0.3 was generally used and showed promising results. Further studies are conducted for 20-monomers both in large and low length ratio situations to interpret the effect of solvent volume. In addition, an enlarged simulation system with 13.4 nm for 50-monomers PAA chains also investigated as a validation.
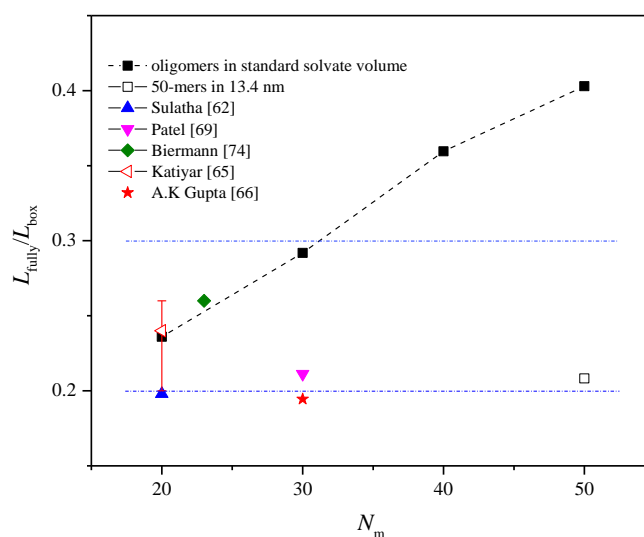
Figure 3.18 Variations of length ratio as a function of number of monomers

The variations of the radius of gyration in different solvent volume are plotted in Figure 3.19. When reducing the solvate volume to 3 nm with high length radio, the behaviour of 20-monomers PAA chain in low DoI fails to be captured correctly. The R_g keeps nearly constant with the increase of DoI, which is contrast with practical conditions. In comparison with standard simulations, the enlarged solvate indeed shows good descriptions for the conformation properties of 50-monomers PAA chains. However, the corresponding calculation of such a solvate volume is time consuming and expensive. Further decrease the length radio, same trends are obtained compared with a suitable solvent volume, which indirectly indicates that though the polymer concentration calculated in this study is as high as 1.9 wt%, it still can be

regarded as a dilute solution since there is no interaction between polymer chains.

(a) 20-monomers PAA   (b) 50-monomers PAA
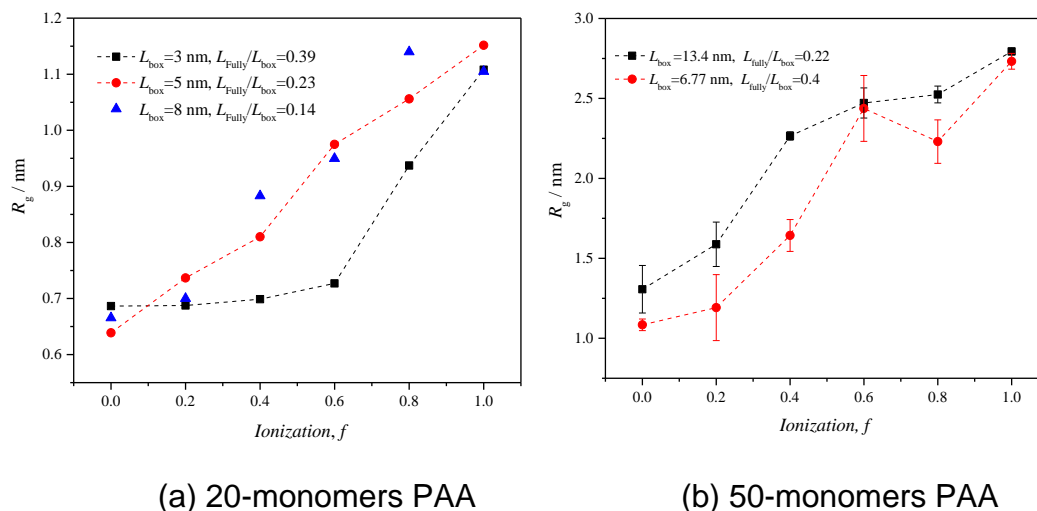
Figure 3.19 Effects of solvent volume on the radius of gyration of PAA chains

With a suitable solvent volume, the RDF profiles between PAA molecules and water as a function of the number of monomers are performed in Figure 3.20(a). The numbers of monomers exert slightly effect on the RDFs, which indicates that neither the chain size nor the solvate volume does not affect the interaction intensity between polymer chains and water molecules. Therefore, the variations of hydrogen-bonding effect are mainly attributed to the numbers of carboxylate functional groups, which can easily be estimated from a short oligomer. The numbers of PAA-water H-bonds against different numbers of monomers PAA are calculated in Table 3.4. With increasing the numbers of monomers along the PAA chains, more H-bonds numbers are formed for both unionized PAA chains and fully ionized PAA chains. It is observed that the ionized PAA chains form about three times the number of the H-bond as that of the neutral PAA. The number of H-bonds is proportional to the chain size as the equations shown in Figure 3.20(b). Therefore, based on the discussion mentioned above, although the longer chain exhibits much more obvious behaviours than a short chain in dilute solutions, the trends are similar, and the detailed molecular interactions are able to be inferred from a short chain polymer. This is indirectly in support of the theory that short chain polymers can represent some properties (e.g., gyrate radius) of long chain polymers in practical (Reith et al., 2002).
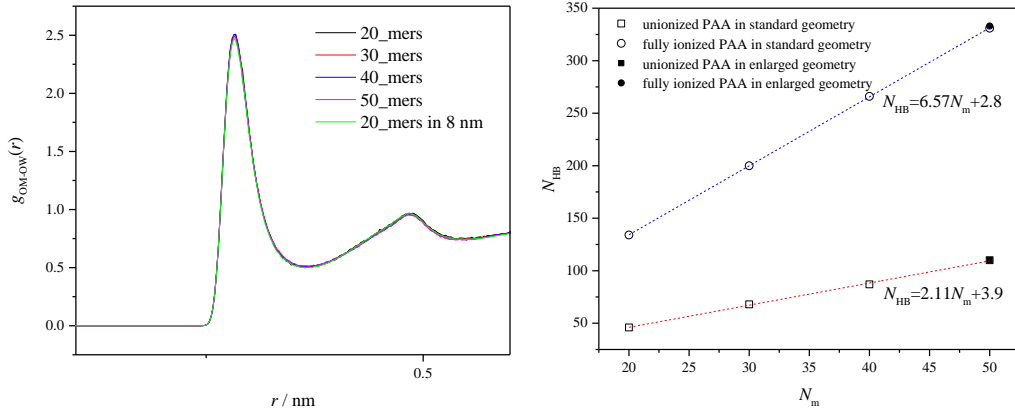
(a) RDF between carboxylate groups and water   (b) hydrogen bonds between PAAs and water

Figure 3.20 Effects of numbers of monomers on the hydration effect

Table 3. 4 Numbers of H-bonds at different numbers of monomers

N_m	Neutral PAA	Fully ionization
20	46	134
30	68	200
40	87	266
50	110	331
50_8nm	110	333

3.3.3.5 Effect of tacticity

In this section, the effects of tacticity of different DoI are discussed since the charge along the PAA chain contributes to intramolecular repulsion theoretically and could behave variously due to the monomer associations. The average values of R_g are plotted in Figure 3.21.
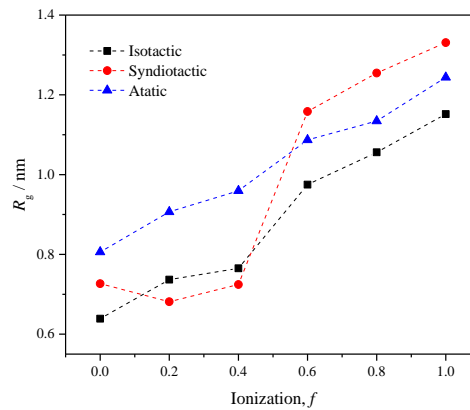
Figure 3.21 Variations of PAA conformation with different degrees of ionization

Whatever tacticity of the PAA chain is, the gyrate radius continually increases from approximately 0.64 nm to 1.15 nm as the ionization increases from 0 to 1. It shows that the increased charge density cannot make the polyion to stretch itself to the fully length (compared with initial configuration) even it is totally ionized. This is because the interaction between polyion and courier-ions Na$^+$ would result in repression of the ionization effect, which will be discussed later. With same deprotonation patterns for these three polymer chains, the only discrepancy of the results is caused by tacticitry. For the neutral case, the R_g varies with tacticity in the order atactic > syndiotactic > isotactic, which is consistent with results by A.K Gupta et al. (Gupta and Natarajan, 2016). Rather than attribute to this difference to PAA initial chain configurations that adjacent COOH groups are on the opposite side of syn-PAA chain thereby holding less hydrophobic attraction than iso-PAA (Katiyar and Jha, 2017), the interpretation is performed in the Figure 3.22 and described as followed. For iso-PAA, there is an interaction between monomers due to the addiction of carboxylate oxygen atoms with hydroxyl hydrogen atoms in adjacent function groups. However, for syn-PAA, there exists slightly repulsion between monomers since the end of adjacent function groups are in same polarity. It is noticed that the repulsion in syndiotactic PAA is suppressed by the neighbouring repulsion as well, which weaken the stretching along the whole polymer chain. In particular, because of the random arrangement of functional groups, atatic PAA behaves both repulsions and attractions along the backbone, where the attraction strengthen the repulsion, making the polymer chain more stretched compared with syn-PAA.
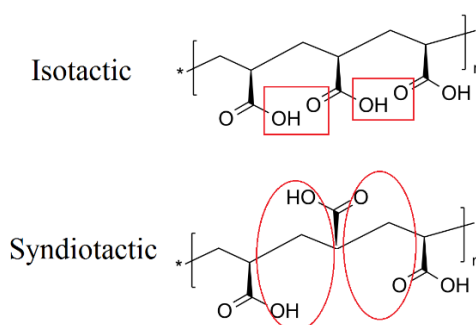
Figure 3.22 Tacticity effects on the polymer chain configuration, rectangular: attraction; ellipse: repulsion

For deprotonated cases, due to the existence of sodium counter-ions, the R_g is mainly influenced by the strong electrostatic repulsions between charged groups and the shielding effects by the cations instead of the weak interaction between the neutral monomers. The effects of tacticity are dependent on DoI. At lower DoI, the R_g varies with tacticity in the order atactic > isotactic >

syndiotactic while at higher DoI, an order of syndiotactic > atactic > isotactic is formed. This is because, from the RDFs shown in Figure 3.26, the syn-PAA is more attractive with Na$^+$ at lower DoI, which reduces the electrostatic repulsions and shrinks the polymer chain. This attraction even weakens the repulsion between the neutral monomers as well resulting in a further collapse compared with the non-ionized case. For higher DoI, however, the iso-PAA exhibits higher interaction with Na$^+$ than syn-PAA, which leads to a smaller R_g.

Figure 3.23 shows the interaction for the PAA carboxylate oxygen atoms with respect to the water oxygens and hydrogens. The atatic PAA shows stronger hydrophilic behaviours than the other two cases in the lower partially ionized conditions, which agreed well with the average gyrate radius trends. This discrepancy becomes insignificantly for the fully ionized PAA chains, indicating the numbers of charged groups dominates the hydration effect and the effect of tacticity of polymer can be neglected.

(a) Lower DoI   (b) higher DoI
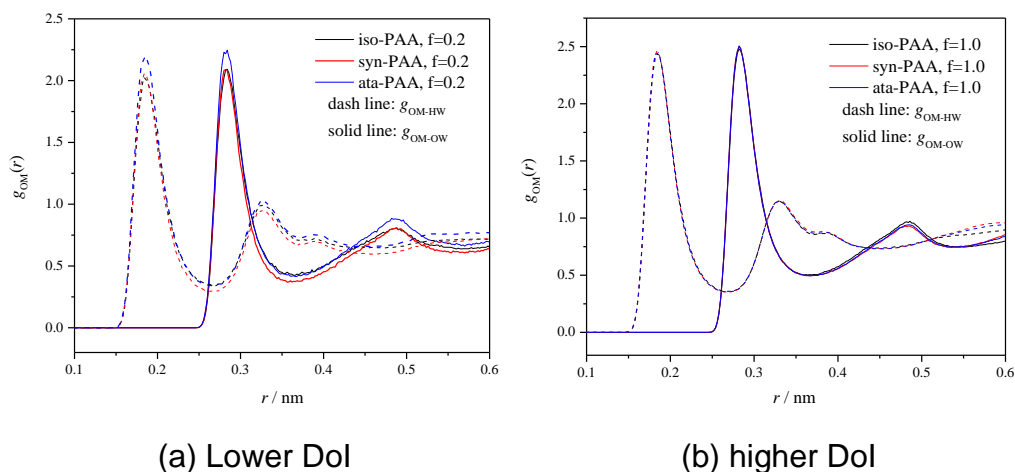
Figure 3.23 Radial distribution functions of carboxylate oxygen respects to water

The RDFs for the carbonyl oxygen atoms and water molecules is shown in Figure 3.24. It is interested that for neutral case, the shoulder behaviour discussed in the previous section is independent on tacticity but for the highly ionized case, the shoulder disappears gradually as the PAA chain transform from isotactic state to syndiotactic configurations. In the case of RDFs corresponding to hydroxyl oxygen atoms and water molecules, as presented in Figure 3.25, the first peak is allocated at a slightly closer distance. However, the nearest bonding distance between hydroxyl oxygen atoms and water hydrogen atoms is approximately 0.35 nm, which shows a very weak hydrogen bonding effect between these atoms. The tacticity shows significant relationship between hydroxyl oxygens. The first peak intensity has a sharp

reduction for the syndiotactic PAA compared with isotactic PAA at highly ionized conditions, indicating the hydration effect of hydroxyl oxygens in syn-PAA is the weakest.
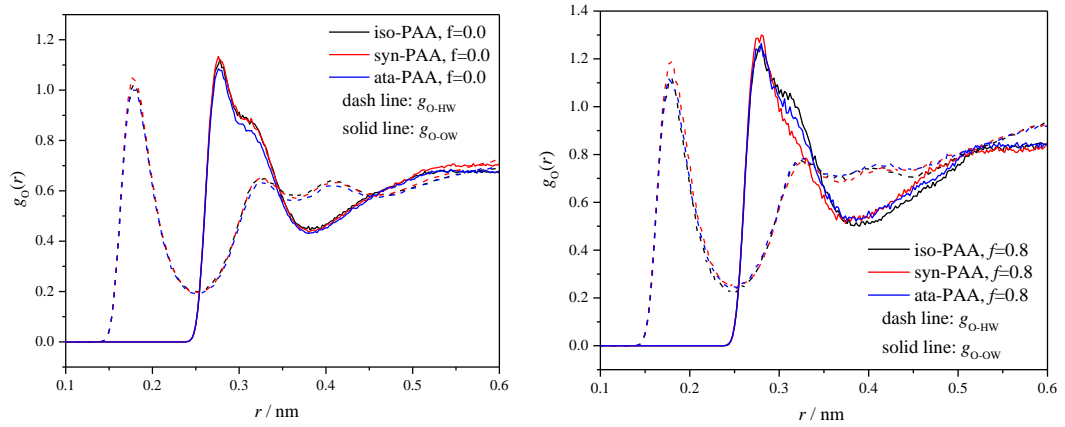
(a) Carbonyl oxygen-water at lower DoI   (b) Carbonyl oxygen-water at higher DoI

Figure 3.24 Radial distribution functions of carbonyl oxygen respects to water
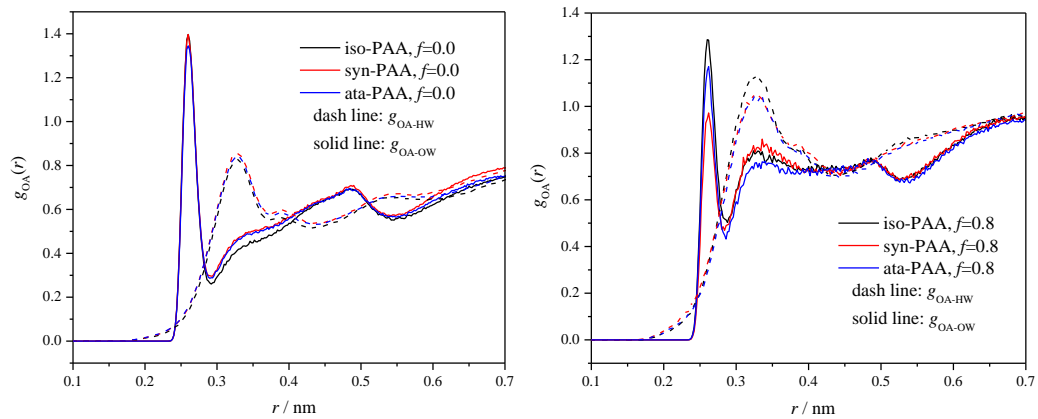
(a) Hydroxyl oxygen-water at lower DoI   (b) Hydroxyl oxygen-water at higher DoI

Figure 3.25 Radial distribution functions of hydroxyl oxygen respects to water

The variation of the number of PAA-water H-bonds across the tacticity is studied in Table 3.5. It can be found that the number of hydrogen bond between PAA chains and water molecules increases with the increase of the charge density since the carboxylate groups attract more water than carboxyl groups. With increasing the DoI, the repulsion between intramolecular along PAA chains and the hydrogen bonding effect stretch the atoms away from the each other and attach to the water molecules, which leads to the expanding of the PAA coils and reaches a stretch state at final. Although the effects of tacticity is not significant as the electrostatic repulsion, the atactic chain forms more H-bonds compared other stereoregular chains. However, such close

results demonstrate the tacticity cannot dramatically affect the hydrophilic characteristic at same ionizations, which is in contrast with the interpretation that it is the stereochemical configuration structure make the polymer chain more hydrophilic or hydrophobic to induce the discrepancy of R_g.

Table 3.5 Variation of H-bonds as a function of degree of ionization

tacticity	f=0.0	f=0.2	f=0.4	f=0.6	f=0.8	f=1.0
Isotactic	46.1	59.7	77.6	98.4	115.6	134.2
Syndiotactic	45.1	54.8	75.5	99.0	114.8	133.9
Atactic	**47.1**	**63.8**	73.9	95.6	**109.4**	**132.6**

The distribution of Na$^+$ counter ions in the vicinity of the PAA chain is represented using RDF of carboxylate oxygen atoms with respect to Na$^+$ ions in Figure 3.26. There are two sharp peaks: a first peak locates at 0.25 nm and a second peak locates at 0.4 nm, respectively. Although the absolute values of peaks are very high, the number of sodium ions in the near proximity are very small as described by the coordination number curves (Ramachandran et al., 2013) in the Figure 3.16(h). This is agreed well with the experimental fact that Na$^+$ are not bonded to the carboxylate groups in PAA at higher charge densities (Koda et al., 1982). From the variations of the second peak, the Na$^+$ ions are preferentially closer to the chain backbone, which, in return, weakens the electrostatic repulsions along the PAA chain. Therefore, in case of sodium polyacrylate, increasing ionization cannot stretch the polymer chain to its full length even at fully degree of ionization. This counter-ions interaction with polyions varies dramatically with tacticity. For isotactic PAA chain, the intensity of the second peak strengthens with increasing the ionizations. However, these trends are not available for the syndiotactic PAA chain as the peaks along the later are almost independent on the DoI. Therefore, the interaction between polyions and counter-ions in syndiotactic case is higher than those in isotactic case at lower DoI and a revere situation occurs at higher DoI, which as discussed above leads to different chain conformations.

(a) *f*=0.2   (b) *f*=1.0
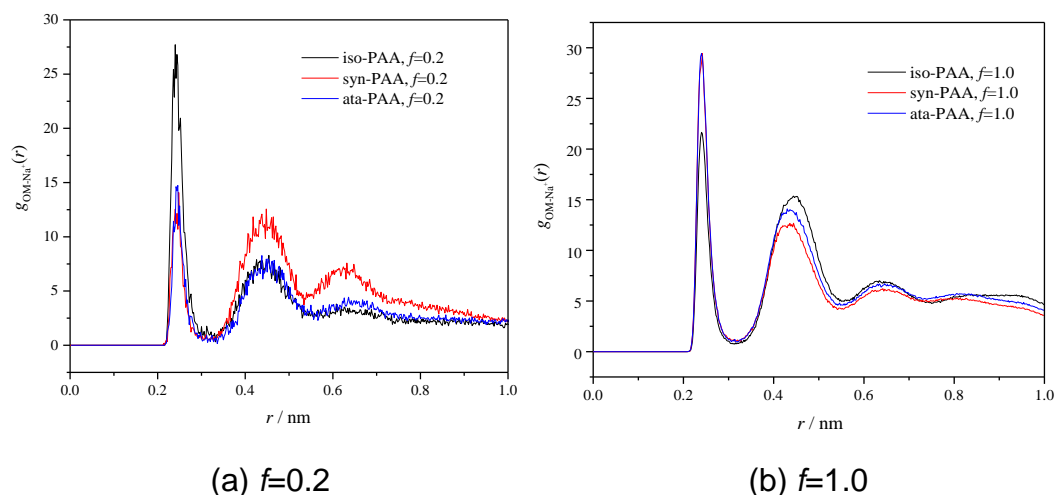
Figure 3.26 Radial distribution functions of PAA to counter-ions, Na⁺

3.3.4 MD on HPAM structure

3.3.4.1 Effects of hydrolysis

The simulation box was constructed in similar method described before, where the PAA chain was replaced by a HPAM chain. The simulation box is shown in Figure 3.27. The degree of hydrolysis, DoH, defined as the ratio between the numbers of monomers with carboxylate groups and the total number of monomers along the whole chain, varies from 0 to 1. The HPAM chain gradually expands from coiled state to stretch state with the increase of the degree of hydrolysis, which is similar with the effects of DoI in PAA cases. In fact, the mechanism is same, which is mainly ascribed to the electronic repulsion between charged carboxylate groups. The quantitative gyrate radii of HPAM with different DoH are demonstrated in Figure 3.28.
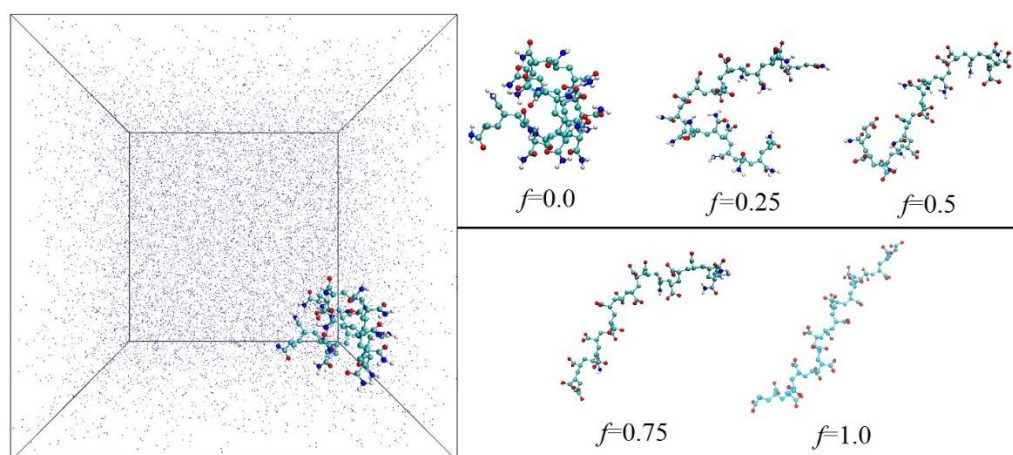
Figure 3.27 Snapshots of HAPM chains with different ionization at an equilibrated state (The left shows structure of HPAM chain with DoH of 0 in solutions, where the blue atom represents Nitrogen atom)
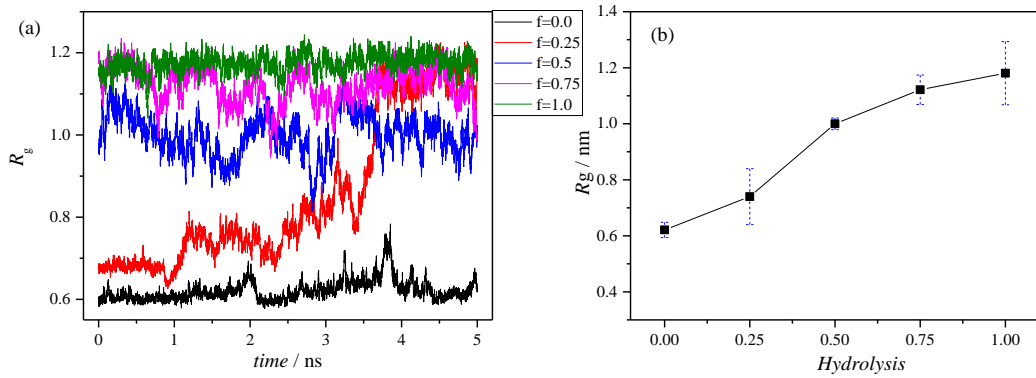
Figure 3.28 Quantitative variations of HPAM conformation with different DoH: (a) Instantaneous radius of gyration against time; (b) average radius of gyration

As shown in the figure 3.29, the hydration effects of nitrogen atom are not as strong as those of hydroxyl oxygen in the PAA chains, which results in the reduction of the hydration effects of carboxyl groups as well. Such decrease dose not significantly affect the whole interaction between water and HPAM since the carboxylate oxygen atoms still show strong interaction and dominate the whole hydrogen effects. With charge density increasing, the interaction between carboxylate oxygen atom and water oxygen atoms strengthens, which increases the hydration effects of HPAM and makes the polymer easier to dissolve into the water.
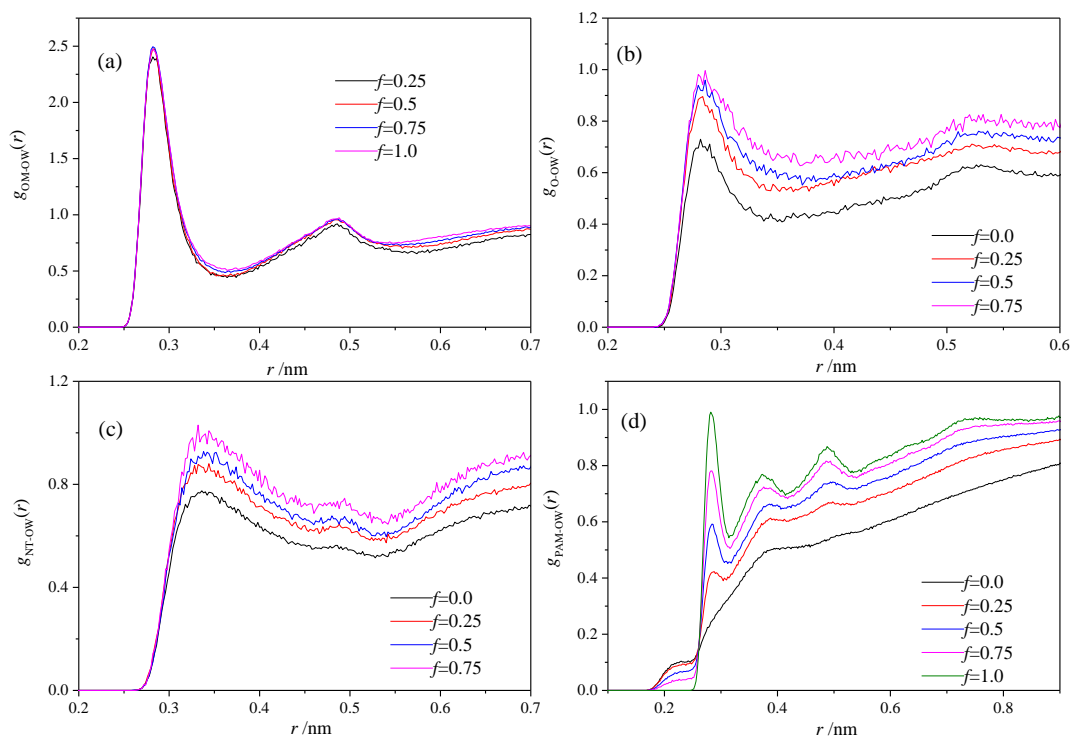
Figure 3.29 Radial distribution functions as a function of degree of ionization. (a) Carboxylate oxygen-water oxygen pairs; (b) Carbonyl oxygen-water oxygen pairs; (c) Amide nitrogen-water hydrogen pairs; (d) whole HPAM chain-water oxygen pairs

3.3.4.2 Effects of salinity

The effects of salt on the conformation of HPAM chains are discussed in this section. The salt ionic strength was adjusted by adding additional Na^+ cations and Cl^- anions into the solvated box. Six salt concentrations were applied, which are 0 M, 0.06M, 0.13 M, 0.33 M, 0.66 M and 1.33 M, respectively. An example of a 20-monomers-HPAM solution with 0.33 M NaCl was shown in Figure 3.29. The DoH for all polymer chains studied in this section was kept constant at value of 0.5.

The final configuration snapshots of each PAA chains after 80 ns simulation period are presented in Figure 3.30. At salt free conditions, the HPAM chains behave a stretching-like conformation. With increasing the salt concentration, the HPAM chains collapse gradually. In particular, a coil-like conformation is formed by shielding effect when salt concentration reaches the critical value.
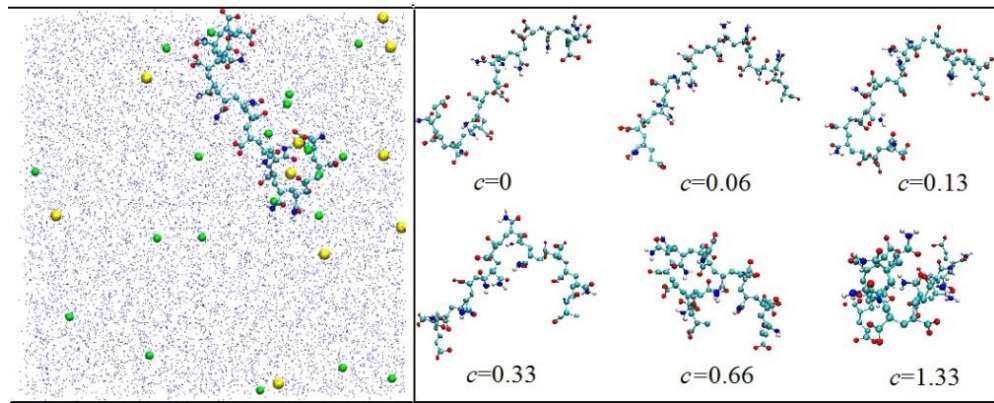
Figure 3.30 Series of snapshots of PAA structure against different salinities. The left view demonstrates the simulation box, where the green atom indicates the Na+ ions and the yellow atom indicates the Cl- ions

The variations of radius of gyration along with salinity are shown in Figure 3.31. It can be observed that the radius of gyration is continually reducing with the increase of salt concentrations. There is a critical value (around 0.4 mol·L^{-1}) of salinity for, above which the salinity no longer affects the HPAM conformation significantly. This is because the numbers of charged carboxylate groups to be shielded by salt cations are limited.
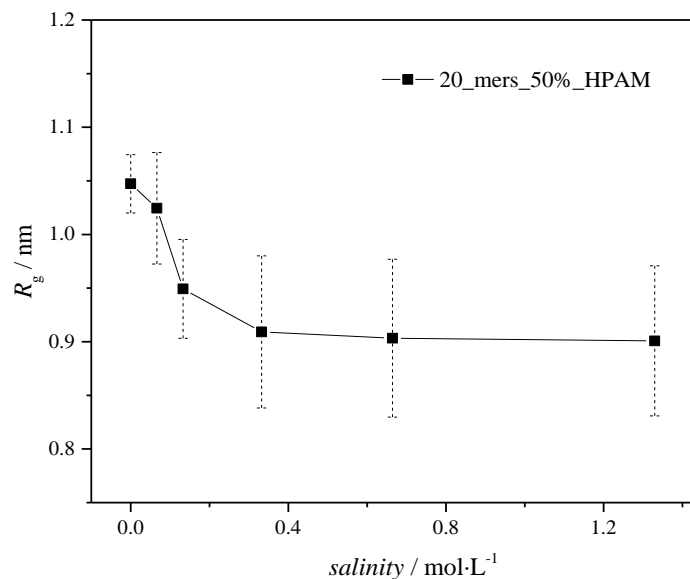
Figure 3.31 The variations of radius of gyration against salinity

The RDF profiles between HPAM molecules and water under different salinities are shown in Figure 3.32 to reveal the further effects of salinity. It can be found that the increase of salinity can indeed weaken the interaction between amide nitrogen atoms and water oxygen atoms in Figure 3.32, which consequently diminish the hydrogen bonding effect. These indicate that the water prefers to diffuse into the bulk and less water is attached to HPAM macro molecules. However, the salinity effect on hydrogen interaction is not

dramatic as the number of H-bonds between the water and the HPAM chain changes not significantly due to that the interaction between carboxylate oxygen atoms and water oxygen, which mainly contributes to the hydration effect, shows independent on the salinity. The values of H-bonds slightly 78 to 74. Therefore, it can be inferred that the salinity changes the HPAM chain conformation mainly by purely electrostatic interactions between HPAM chains and salt ions rather than the hydrogen bonding effects of HPAM chains respected to water molecules. The electrostatic interactions also called shielding effect or electrostatic screening effect increases with the increase of salt concentrations, which in return, causes a reduction in the attractive interactions between the HPAM chain and salt ions, represented by a decrease of peak intensity in Figure 3.32(d).
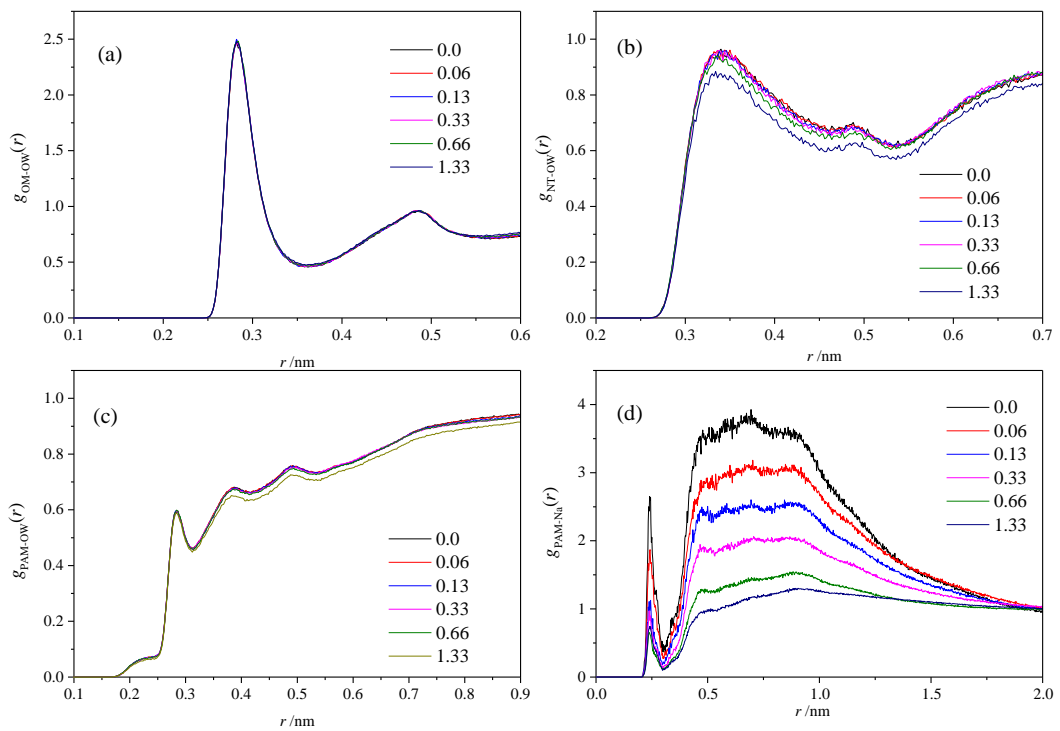
Figure 3.32 RDFs s between HPAM and water as a function of salinity. (a) Carboxylate oxygen-water oxygen pairs; (b) Carbonyl oxygen-water oxygen pairs; (c) HPAM molecular with water oxygen pairs; (d) HPAM molecular with sodium ions paris

3.4 Conclusions

The viscosity of polymer solutions with various concentration and salinities were conducted first. The increase of polymer concentration and the reduction of the salinity leads to the increase of the viscosity. In terms of salinity case, there exists a critical salinity after which the viscosity is independent with salts. The DLS method was used to verify the results. The hydrodynamic radius

measured by DLS shows agreements with the rheological properties. The reduction of the viscosity was attributed to the decrease of hydrodynamic radius of polymer molecules.

The conformational and hydration behaviour of a single polyacrylamide (HPAM) chain in dilute solutions as a function of degree of hydrolysis, and salt concentrations were investigated by atomistic molecular dynamics simulations. The non-hydrolysed HPAM performs a coil-like conformation. With increasing the degree of hydrolysis, the HPAM chain expands and reaches a stretching-like conformation at fully hydrolysed form. The charged carboxylate function groups are more attractive with water, which leads to the increase of hydrogen bonding effects between HPAM chains and water molecules.

Adding salt into polymer solutions induces the collapse of polymer chains. There exists a critical value of salt concentration, above which the salinity is no longer affect the radius of gyration of a single HPAM chain. It should also be noted that the salt effects on the conformation of HPAM are mainly attributed to the electrostatic screening effects rather than the hydrogen bonding effect.

Chapter 4
The onset of elastic turbulence based on various rheological properties: effects of concentration and salinity

From the literature review, recent studies showed the importance of rheological properties of polymer solutions on the onset of elastic turbulence. However, the variations of rheological properties based on polymer sensitivities such as salinity and its corresponding effects on the elastic turbulence have not been revealed. The salinity, as discussed in the former chapter, has significant influences on the polymer rheology and polymer contracture. In this chapter, the concomitant effects of salinity on the onset of elastic turbulence are introduced, Two geometries, a swirling flow geometry and a curvilinear microchannel, were conducted to characterise the salinity effects. The variations of statistical properties, such as probability distribution functions (PDFs) and power spectra density (PSD) of injected power, with different salinity were analysed. The chapter are introduced as followed. The experimental set-up and material properties are firstly demonstrated, followed by the introduction of the data analysis. Then the measurements of the onset of elastic turbulence with different polymer concentration are discussed as a validation of the existence of the purely elastic instability. The salinity effects are systematically analysed in the following section. At last, similar working fluids were applied in a curvilinear microchannel to study the mixing performance with different salinities and the discrepancies between these two geometries are discussed.

4.1 Experimental Measurements

4.1.1 Experimental setup

The schematic diagram and experimental system are shown in Figure 4.1. The polymer solution was held in a stationary transparent cup with a flat bottom. A co-axial rotating upper plate was just touching the surface of the fluid. The transparent bottom of the cup as the lower plate was attached concentrically above the rheometer base. The upper plate was connected to the shaft of the rheometer, which allows precise control of its rotation velocity, Ω, and measurements of the torque, T.
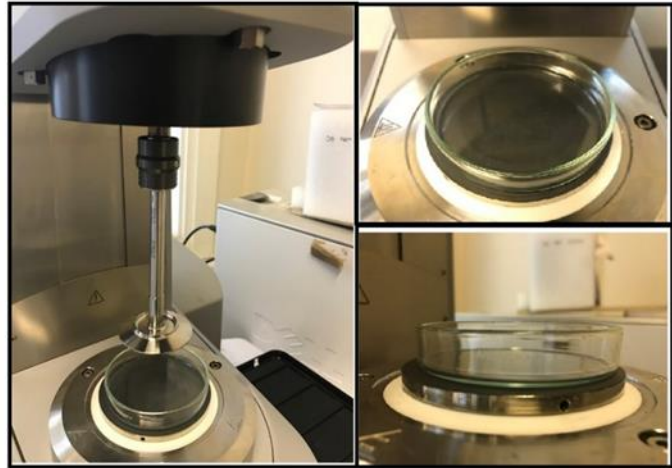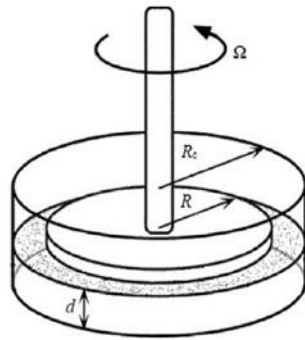
Figure 4.1 The experimental swirling flow set-up

Based on previous studies(Burghelea et al., 2007; Zilz et al., 2012), the onset of elastic turbulence was sensitive to geometrical aspect ratio. When the radius of the cup, R_c, is kept constant, the onset values of the relevant physical quantities such as shear rate or Weissenberg numbers increases as the gap between the two plates, d, decreases. Similarly, if the distance between two plates is set as a fixed value, these threshold values become higher with increasing the radius of the cup. Therefore, a small radius of the cup associated with a large gap is able to induce elastic turbulence more easily. In this study, the radii of the upper plate and the cup were chosen as R=25 mm and R_c=35 mm, respectively, and the gap between the plates was d=10 mm.

The examination of the salinity effects on the mixing performance were conducted in a curvilinear channel. Such a geometry is selected not only because of its popularity in microfluidic systems, but also allowing extended continuous experiments with well controlled initial conditions. The experimental system and the structure of the channel are shown in Figure 4.2. It consists of a sequence of smoothly connected half-rings with square cross-section. The total length of the channel is 121 mm and the width (depth) is 640 μm. The mixing experiments were tested by injecting two liquids simultaneously by a syringe pump at a specific flow rate. Chemical composition of these two liquids are same but one of those was dyed by fluorescein rhodamine B. The mixing performance was observed by a CCD camera from the top of the channel. The mixing performance was captured with different flow rates ranging from 5~200 μl/min. Each flow rate was measured separately and was last 20 minutes to equilibrate.
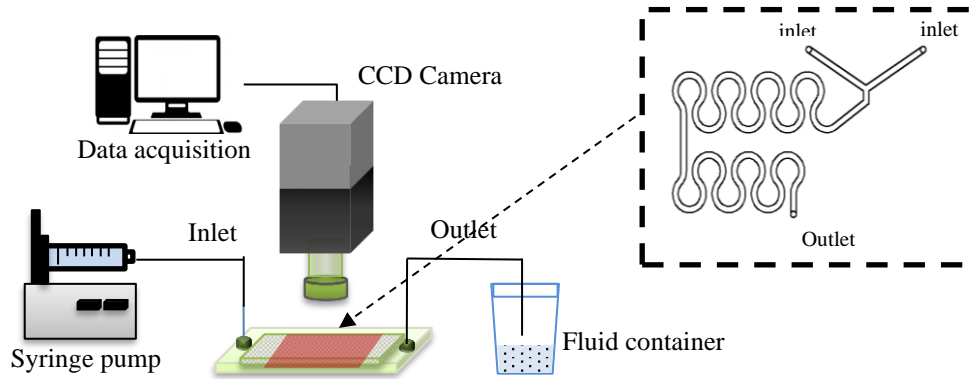
Figure 4.2 The microchannel system for flow visualization

4.1.2 Working fluids preparation

Two types of test fluids were used in this study, Newtonian fluid and viscous elastic fluid. The Newtonian fluids, regarded as base fluids, were 65% sucrose aqueous solutions with two different concentrations of sodium chloride (NaCl), 0% and 1 %, respectively (referred to "sucrose solution" hereafter). The addition of NaCl was conducted to exclude the effects of salinity on the base fluid. The viscous elastic fluids were prepared based on 65% sucrose solutions with different concentrations of HPAM (*MW*: 22 M g/mole) and NaCl (referred to "HPAM solution" hereafter). Three dilute polymer concentrations from 100 to 300 ppm were prepared to reveal the effects of polymer concentration on the onset of elastic turbulence as well as determine an optimal concentration for the following study on the effects of salinity. A wide range of NaCl concentrations, from 0.01% to 1% were investigated. Hereinto, 65% sucrose was used as both the base fluid and the solvent of the HPAM solutions since it could maximise the relaxation time of the solution and minimise the Reynolds numbers, thereby the flow instabilities were due to the elastic effect rather than the inertial effect.

4.1.3 Rheological properties

The viscosities of working fluids were measured by cone and plate geometry of a stress-controlled rheometer (Anton Paar MCR 301, Austria) at 25 ºC, as shown in Figure 4.3(a). The sucrose solutions show shear constant phenomenon while a shear thinning property is observed for polymer solutions. For a given shear rate, the viscosity increases approximate 1.5 times higher as the polymer concentration increases from 100 ppm to 300 ppm. The increased numbers of polymer molecules result in more interactions between polymer chains, which causes more frictional effects and thereby increases the viscosity. However, the polymer concentration shows slightly

effect on the shear-thinning behaviour. This is because all working fluids are dilute polymer solution. The shear thinning is ascribed to the single polymer alignment, which is similar in dilute regime.
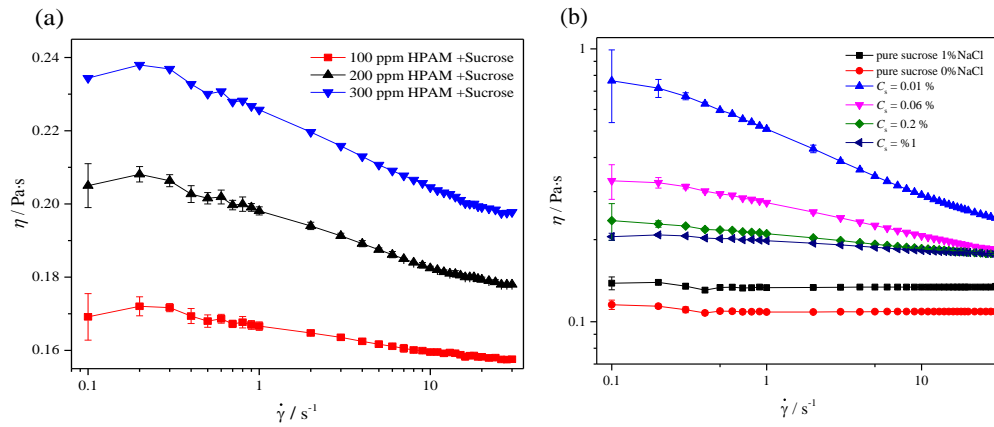
Figure 4. 3 Viscosity profiles of test fluids applied during experiments: (a) effects of polymer concentration; (b) effects of salinity

Figure 4.3(b) highlights the salinity effects on the viscosity. With increasing the salinity from 0.01% to 1%, the viscosity decreases sharply at first then becomes gentle after the salinity exceeds 0.2 %. A clear shear-thinning trend is observed for polymer solutions with lower salinity (less than 0.2%). However, such behaviour gradually disappears as continual increase of the salinity. The polymer solution with salinity above 0.2% behaves like Newtonian fluid and is regarded as a Boger fluid.

The salinity dependence on HPAM solution is ascribed to the ion effects (shielding effects) due to the presence of cations. As mentioned above, the HPAM has two functional groups, amino and carboxyl, along its back-bone chain, between which the carboxyl groups mainly contribute the sensitivities of rheology. The charged carboxyl groups dissociate and develop a strong negative electrostatic repulsion between them, which makes the polymer chain stretch and leads to the increase of solution viscosity. With the presence of the cations, the polymer chain is shielded, resulting in molecular shrinkage with the concomitant viscosity reduction. Particularly, such coiled polymer molecules contribute slightly to the polymer alignment when the polymer concentration in dilute regime, which, as a result, gives rise to the disappearance of the shear-thinning behaviour.
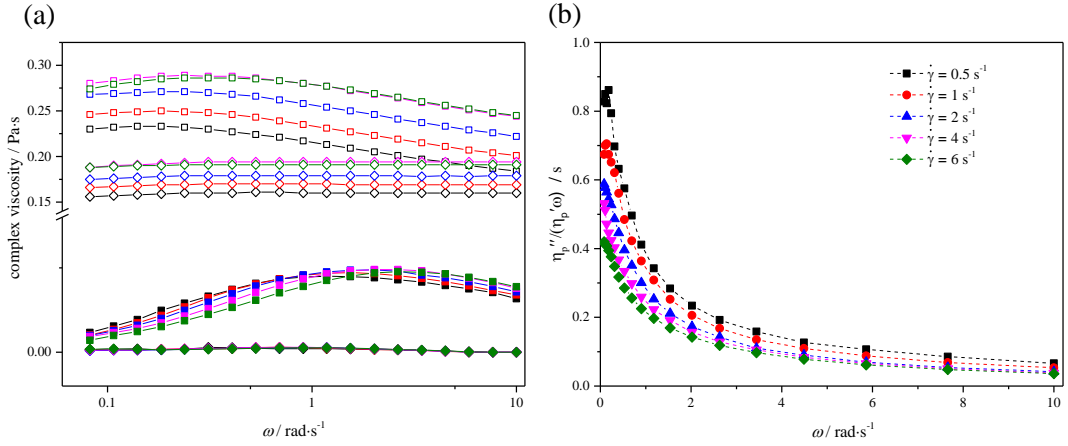
Figure 4.4 The complex viscosity profiles of 200 HPAM solution and sucrose solution at angular frequencies ranging from 0.06 to 10 rad·s^{-1} with different shear rates. The symbol square and diamond refer to 200 ppm HPAM solution and sucrose solution, respectively. The symbol with open Interior and solid interior represent in-phase viscosity profiles and out-of-phase viscosity profiles, respectively; The shear rate, $\dot{\gamma}$, varies by different colours, where black, red, blue, pink, green indicates 0.5 s^{-1}, 1 s^{-1}, 2 s^{-1}, 4 s^{-1}, 6 s^{-1} respectively. (b) Angular frequency dependence of $\eta_p''/(\eta_p'\omega)$.

The polymer relaxation time, λ, was measured in the oscillatory mode. The in-phase and out-of-phase viscosity of polymer solution, η' and η'', respectively, were measured in long series at different angular frequencies ranging from 0.06 to 10 rad·s^{-1}. Same procedures were applied to the pure sucrose solutions and the η_s' and η_s'' were measure as well. The measured complex viscosity of 200 ppm HPAM solution with 1% NaCl and sucrose solution with 1% NaCl are demonstrated in Figure 4.4(a) as an example. The values for the polymer in-phase and out-of-phase viscosity were calculated as $\eta_p'=\eta'-\eta_s'$ and $\eta_p''=\eta''-\eta_s''$. The polymer relaxation time at a fixed shear rate was then obtained as:

$$\lambda = \lim_{\omega \to 0} \left\{ \frac{1}{\omega} \left[\frac{\eta_p''(\omega)}{\eta_p'(\omega)} \right] \right\} \tag{4.1}$$

The polymer relaxation time with different shear rate for 200 ppm HPAM solution with 1% NaCl was predicted by fitting the experimental results at the angular frequency close to zero as performed in Figure 4.4(b).

The dependence of the polymer relaxation time on the shear rate with different concentration and salinity are demonstrated in Figure 4.5. All solutions show a clear shear thinning behaviour as a function of shear rate, with the scaling $\lambda \propto \dot{\gamma}^{-\alpha}$, which is consistent quite well with the results found earlier.(Burghelea et al., 2007) It is noted that increasing the polymer concentration results in the

increase of polymer relaxation time. In contrast, an increase of the degree of salinity causes a reduction of the polymer relaxation time.
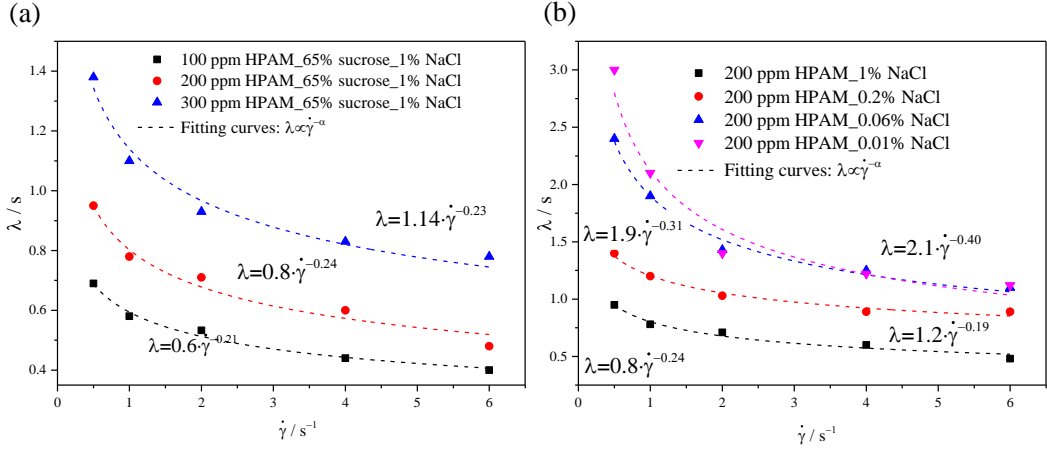
Figure 4.5 Polymer relaxation time profiles for different working fluids. (a) Effects of polymer concentration; (b) Effects of salinity

4.1.4 Data analysis details

For the swirling flow between two plates, the bulk shear rate is significant inhomogeneous. When a narrow gap applied, $d/R << 1$, the shear rate along the axial direction can be regarded as constant and the radial shear rate varies from zero at $r = 0$ to maximal value of $\Omega R/d$ at $r = R$. The average shear rate over the surface of upper plate is then calculated as $2\Omega R/3d$. However, for the case with large gap, the shear rate becomes strong non-homogeneous along the axial direction. In this case, the average shear rate is no longer equal to $2\Omega R/3d$ and should be several times larger. To estimate the real shear rate of the experimental setup, 65% pure sucrose solution was tested in both narrow gap (1 mm) and wide gap geometry (14 mm). It shows that the average shear rate $\dot{\gamma}_{av}$ is proportional to Ω, being $\dot{\gamma}_{av} = 3\Omega R/d$ in this experimental setup.

The sharp growth of flow resistance is a key feature of the elastic turbulence. The ratio of the average stress, τ_w, at the upper plate to the imaginary stress in the laminar flow, τ_w^{lam}, at the same angular velocity is a suitable parameter to characterize this growth. The average stress of the upper plate was measured by rheometer automatically while the imaginary laminar stress would depend on an average shear rate and viscosity of the polymer solution, defined as $\tau_w^{lam} = \eta(\dot{\gamma}_{av})\ \dot{\gamma}_{av}$. To characterize the Weissenberg number and Reynolds number, a simple expression $\Omega R/d$ was used as a characteristic shear rate. Therefore, the Weissenberg number (*Wi*) and Reynolds number (*Re*) can be calculated as:

$$Wi = \lambda \frac{\Omega R}{d} \tag{4.2}$$

$$Re = \frac{\Omega R d \rho}{\eta} \qquad (4.3)$$

4.2 Effects of polymer concentration on the onset of elastic turbulence

Figure 4.6 shows the dependence of normalized flow resistance on the shear rate for three polymer solutions with different concentrations. The shear rate was increased gradually in time (1000 points per decade) from 0.1 to 20 s^{-1} with each shear rate being held by 10 s. A sharp growth of stress ratio has been observed in higher polymer concentration, which indicates a strong non-linearity in the swirling flow and confirms that the HPAM is indeed capable of inducing the elastic instability at low Reynolds numbers. Under the same applied shear rate, the pure Newtonian fluid is remaining in laminar regime without any sharp variations during the experimental test, which indicates that the inertial effect in this situation can be omitted and the sharp growth of flow resistance is solely driven by the elastic instability, similar to previous studies.(Groisman and Steinberg, 2004)
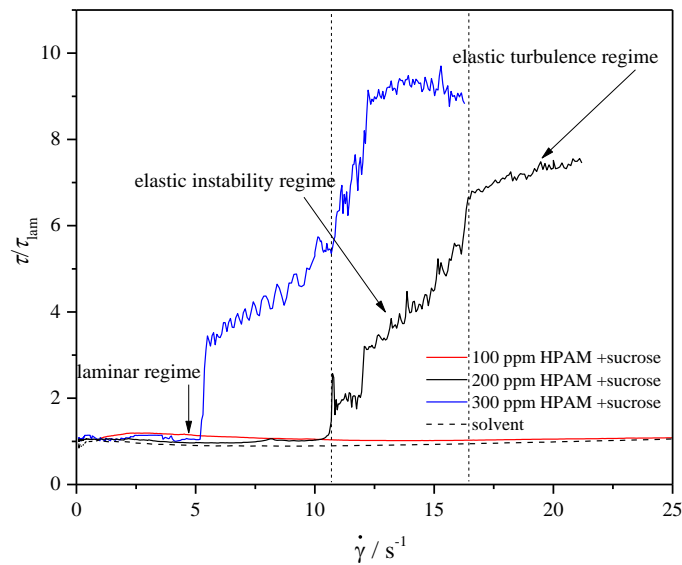
Figure 4.6 The ratio of the average stress at the upper plate, τ, to the stress, τ_w^{lam}, in imaginary laminar shear flow as a function of the shear rate, $\dot{\gamma}$, with different polymer concentration

Growth of the flow resistance is affected significantly by polymer concentration. At low concentration such as 100 ppm in this study, the polymer elasticity is too weak to induce the flow instabilities at such applied shear rates, showing similar phenomenon as the sucrose solution. With increased polymer concentration, three flow stages are evolved as laminar state, elastic instability regime and elastic turbulence regime, respectively. The onset values of elastic

instability are dependent on polymer concentrations. With a higher concentration, the polymer solution tends to be unstable easily and the stress ratio saturates at higher values. The reasons are attributed to the large amount of polymer molecules in solutions, which limits the degree of the perturbations induced by polymer conformation feedback. Therefore, to get a same perturbation, for less polymer concentration, a single polymer chain should contribute more instabilities. Similarly, the total shear stress growth is smaller when the elastic stress provided by a single polymer chain saturates.

The quantitative results are listed in Table 4.1. The increase of the critical shear rate coupled with the decrease of the polymer relaxation time makes the critical Weissenberg number, Wi_c, of the onset of elastic instability slightly increases, which are 4.1 and 4.7, respectively. This agrees well with the investigations conducted by Jun et al.(Jun and Steinberg, 2009; Jun and Steinberg, 2017) Indeed, a suggested criterion of the elastic instability for a dilute polymer solution in a shear flow follows the form:

$$K \equiv \frac{d}{R_c} \cdot \frac{\eta_p}{\eta} \cdot Wi_c^2 \tag{4.4}$$

The elastic instability should take place when the parameter K exceeds a specific value, which depends on the gap radio, d/R_c, polymer contribution to the viscosity, η_p/η, and the degree of stretching of the polymers by the primary flow, Wi. The polymer contributes more viscosity with higher concentration, which results in the reduction of the Wi_c. For a given gap ratio, the critical Wi_c for the elastic instability depends on the polymer concentration to the viscosity as $Wi_c \sim (\eta_p/\eta)^{0.5}$. In this study, the dependence can be fitted well with the prediction with exponent of 0.51, as shown in Figure 4.7, which is very close to the expected value of 0.5.

Table 4.1 Properties of polymer solutions and flow characteristics: $\dot{\gamma}_c$ is the threshold shear rate of the elastic instability; λ is the relaxation time of the polymer solutions at critical shear rate; Wi_c is the threshold Weissenberg number of the elastic instability

c (ppm)	sucrose	100	200	300
$\dot{\gamma}_c$ (s^{-1})	--	--	10.8	5
λ (s)	--	--	0.44	0.81
Wi_c	--	--	4.7	4.05
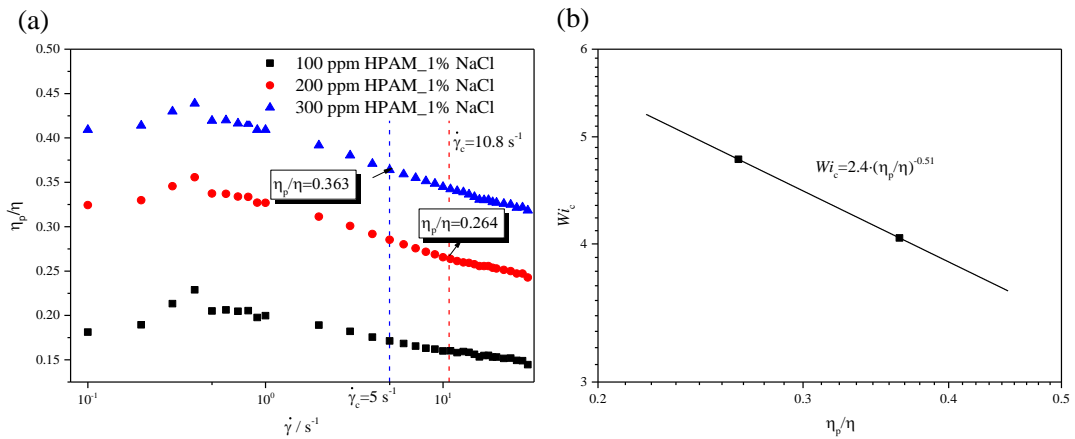
Figure 4.7 (a) the polymer distribution to viscosity with different polymer concentration; (b) the critical Weissenberg number as a function of η_p/η at experiments for effects of polymer concentration

4.3 Effects of salinity on the onset of elastic turbulence

4.3.1 Observations of elastic turbulence

The onset of elastic instability is associated with the coil-stretch transition of polymer molecules, which is likely be affected by the polymer's initial conformation. Compared with pure polyacrylamide (PAM), HPAM is different since part of acrylamide monomers are substituted by acrylate, along which the carboxyl function group is sensitive with cations. With various amounts of salts being added into polymer solutions, the onset values of elastic instabilities should be different. In this section, the effects of salinity on the onset of elastic turbulence are discussed in details.
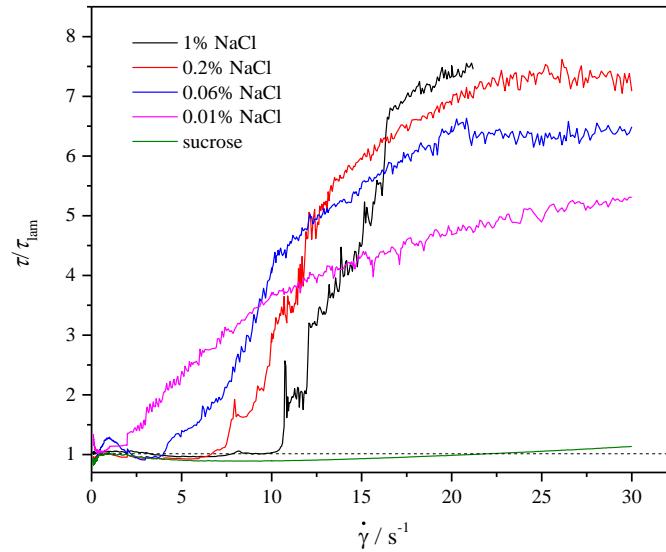
Figure 4.8 The ratio of the average stress at the upper plate, τ, to the stress, $\tau_w{}^{lam}$, in imaginary laminar shear flow as a function of the shear rate, $\dot{\gamma}$, with different salt concentration

The variations of stress ratio with different salinity are shown in the Figure 4.8. Both curves of polymer solutions follow the rules mentioned above: increasing rapidly over a value of shear rate and saturating at a higher value. With the same controlled parameters, however, the Newtonian solvent stays in the laminar state, indicating the inertial effect can be negligible. It is much more difficult to induce elastic instability at higher salt concentrations, which mainly attributed to the reduction of polymer relaxation time due to the shielding effect on the negative charged polymer backbone. As shown in Figure 4.9(b), increasing salinity reduces the polymer relaxation time correspondingly. Based on the definition of the Weissenberg number, if a small relaxation time is provided, a high shear rate should be applied to trigger the flow instability.
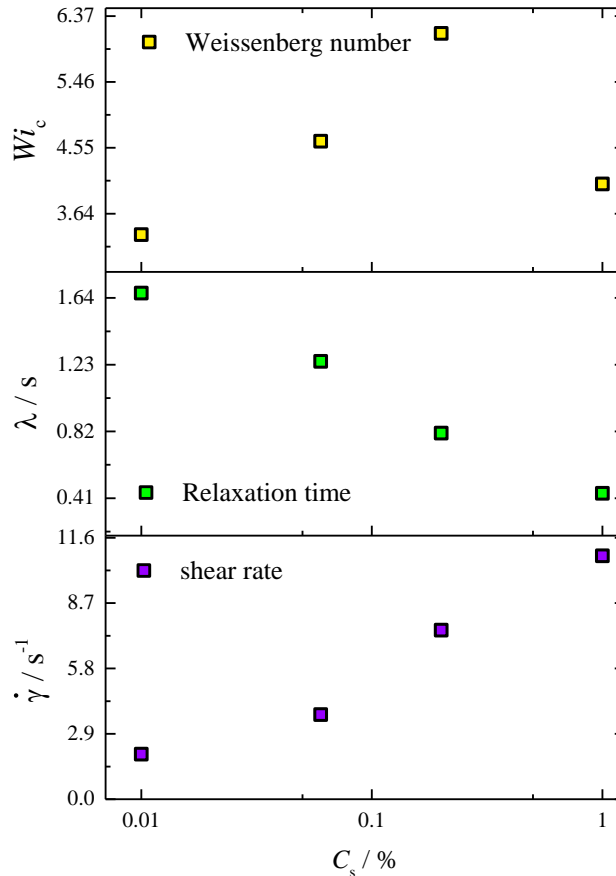
Figure 4.9 Salinity effects on the threshold properties of polymer solutions at the onset of elastic instability

From Figure 4.9(c), it can be demonstrated that the critical Weissenberg number (Wi_c) increases first with increasing the degree of salinity of polymer solutions and continual increase of salinity induces a slight reduction of the Wi_c. As discussed above, the shear-thinning behaviour gradually disappears with increase of the salinity, which weakens the polymer contribution to the viscosity. Therefore, according to the equation (4.4), to trigger elastic instability the corresponding Wi_c should be higher when the salinity increases. The reduction with further increasing the salinity is mainly ascribed to the solvent quality. When the negative carboxylate groups along the polymer chain have already been fully shielded, continually increasing the salinity makes the polymer collapse in a denser coil state.(Satoh et al., 2013b; Takani and Satoh, 2016b) Although the viscosity shows independent or slightly increasing trend with salinity, the polymer conformation significantly changes. Due to the limitation of results in this work, it cannot be quantitatively concluded the influences of such polymer configuration on the onset of elastic instability. However, it does play some roles for the occurrence of flow perturbation since the dependence of Wi_c on η_p/η for 1 % NaCl polymer solution is not consistent well with others as shown in Figure 4.10(b). Indeed,

the suggested criterion even cannot satisfy polymer solutions with lower salinity because the instability criterion presented in equation (4.4) is derived for a Boger fluid and in the approximation of the Oldroyd-B model when $\eta_s \gg \eta_p$, so it cannot be used for a quantitative comparison with experimental results taken in dramatic shear-thinning polymer solutions. However, it still can serve as a guide for a scaling relation in this work. The fit to the data at $C_s <$ 0.2% gives $Wi_c = 2.52 \, (\eta_p/\eta)^{-0.95}$ with the exponent approximate 1 instead of the expected value of 0.5. This discrepancy can be explained by the different mechanism exerting on the rheology. The salinity affects the rheological properties by changing the polymer configuration accompanied with significant shear-thinning behaviours, which makes single polymer physical properties play more important roles for the onset of elastic instability. In contrast, for the polymer concentration experiments, increasing polymer concentration within the dilute regime, the polymer stays in coiled form and contributes slightly to the onset condition, where the degree of the stretching of the polymer should be more dramatic to generate the secondary flow. It is interesting that a similar exponent 1 was observed for the semi-diluted polymer solution,(Jun and Steinberg, 2017) which may be owing to the increase of the shear-thinning due to the polymer network.
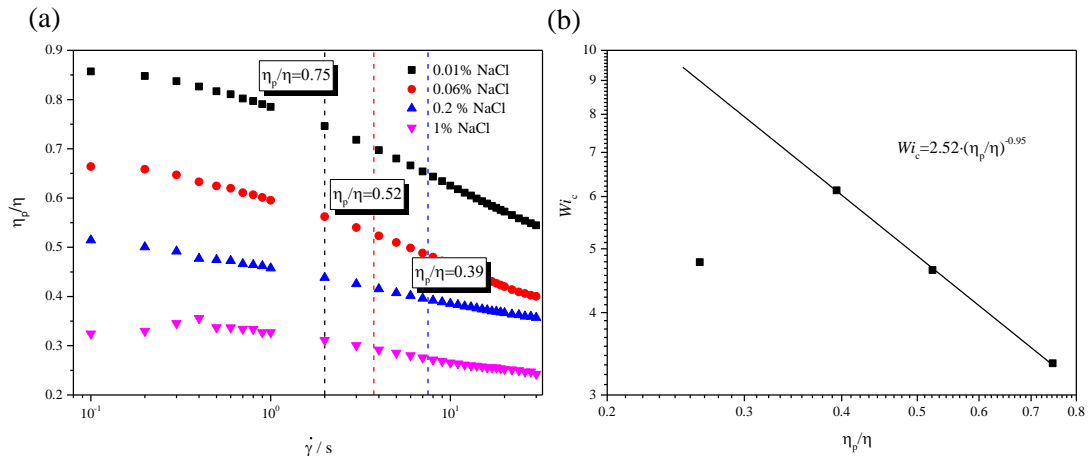
Figure 4.10 (a) the polymer distribution to viscosity with different polymer concentration; (b) the critical Weissenberg number as a function of η_p/η at experiments for effects of polymer concentration.

In addition, the transition from laminar state to elastic turbulence regime becomes rapidly with the increase of the salinity. Due to the reduction of the polymer relaxation time and viscosity, polymer molecules are required less time to equilibrate and are more disperse with high salinity, which accelerates the transition. Besides, it is also indicated that polymer solution with concentrated salinity has a better performance of flow intensification in the regime of elastic turbulence. Indeed, similar averaged shear stresses over the

upper plates were obtained for all polymer solutions as shown in Figure 4.11, which implies that the shielding effects are no longer effective when the flow is fully developed into elastic turbulence regime. This also could be validated from the independent spectra profiles on salinity at highest shear rate as discussed following. However, the addition of salts diminish the viscosity of polymer solutions, which results in lower imaginary laminar shear stress and thereby performing higher stress ratio. In other words, the shear stress in elastic turbulence regime is constituted of initial viscous force and flow friction based on flow instabilities. With the same total shear stress, the polymer solution with lower viscosity holds better performance of flow intensification.
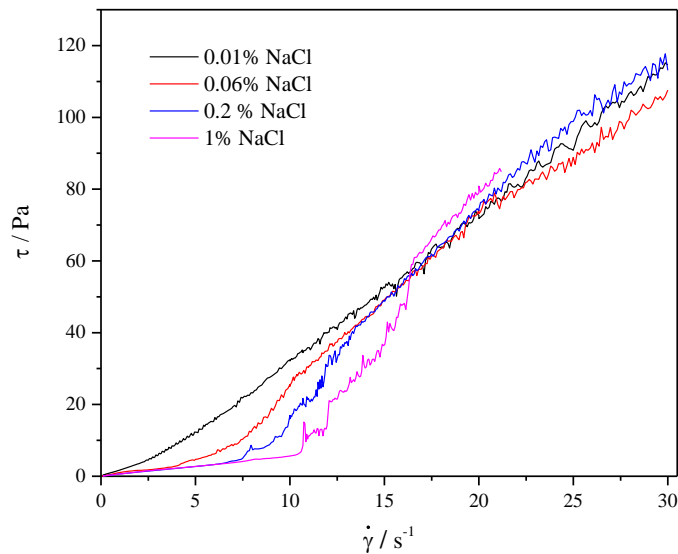
Figure 4.11 Variations of shear stress as a function of shear rate with different salinity

4.3.2 Salinity effects on the statistical properties of elastic turbulence

The fluctuation of the injected power, defined at any case as $P=T \cdot \Omega$, is another main feature to characterize elastic turbulence. The time series of the injected power at different Wi under Ω controlled mode for HPAM solution with 1% NaCl is presented in Figure 4.12. The average values of the injected power do not change significantly during the total data acquisition times, indicating that no major polymer degradation occurred. For low control parameters in laminar regime, $\dot{\gamma} < \dot{\gamma}_c$, the power fluctuations are only attributed to instrument noise. However, in elastic turbulence regime, the fluctuation becomes intensive and irregular. These fluctuations of injected power reflect fluctuations of the elastic stress averaged over the upper plate, which estimates that motion of the polymer is spatially random.

For each run with specific values of C_s and Wi, the probability distribution functions (PDFs) are based on 2×10^4 measured data points evenly sampled in time (Δt=50 ms). Here, the PDFs of HPAM solution with C_s = 1% as a function of shear rate is displayed in the Figure 4.13(a). In the elastic turbulence regime, the PDFs of the inject power fluctuations strongly deviate from the Gaussian distribution and show a left skewness, which is mainly attributed to intermittently injection of excessive elastic stresses from boundary to bulk flow.(Burghelea et al., 2006) This skewness becomes more dramatic as the shear rate or Weissenberg number increases. The PDFs of inject power fluctuations collapse into a single curve when normalized by their maximum value as plotted in Figure 4.13(b), where P^{rms} is the root-mean-square values.
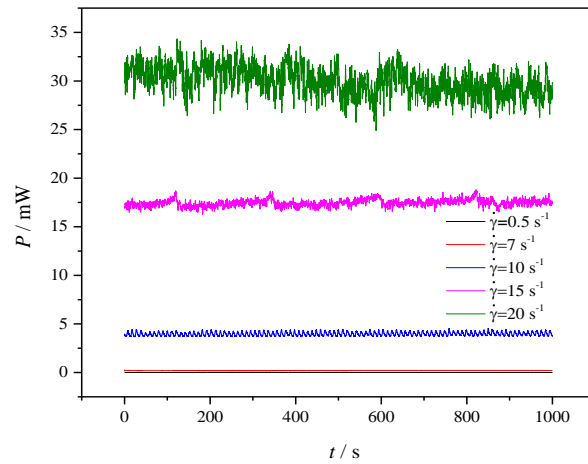
Figure 4.12 The time averaged fluctuations of inject power for different shear rate
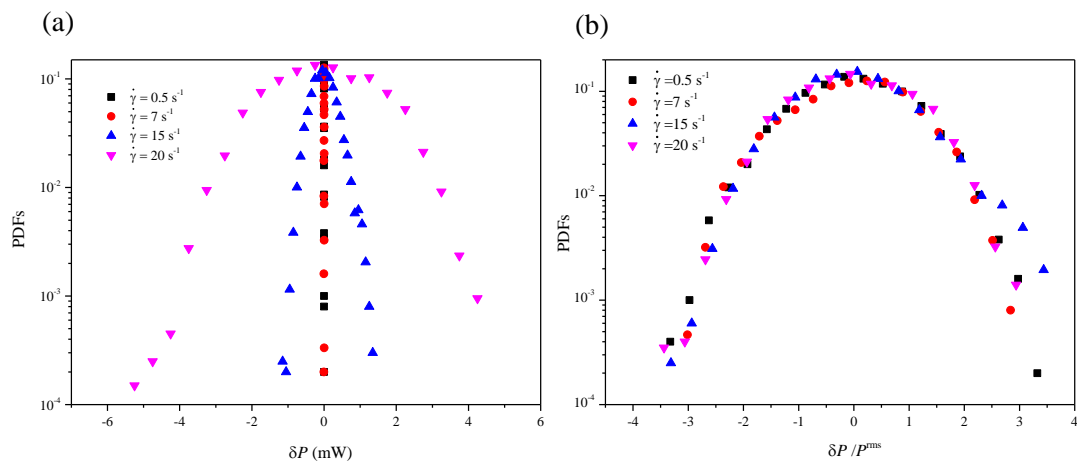
Figure 4.13 PDFs of δP and $\delta P/P^{rms}$ for different shear rate of HPAM solution with 1% NaCl: (a) spectra profiles of δP; (b) spectra profiles of $\delta P/P^{rms}$

The normalized PDFs for salinity from 0.01% to 1% at the highest shear rate (20 s^{-1}) are presented in the Figure 4.14(a). Both curves are skewed toward the

negative values. It can be noticed that this skewed trend becomes more obvious with higher salinity, which also quantitatively characterized in the Figure 4.14(b). Both the skewness, S, and flatness, F, of the fluctuation of inject power increase as the salinity increases. These PDFs properties implies that the polymer solution with higher salinity drives more intensive flow perturbations.
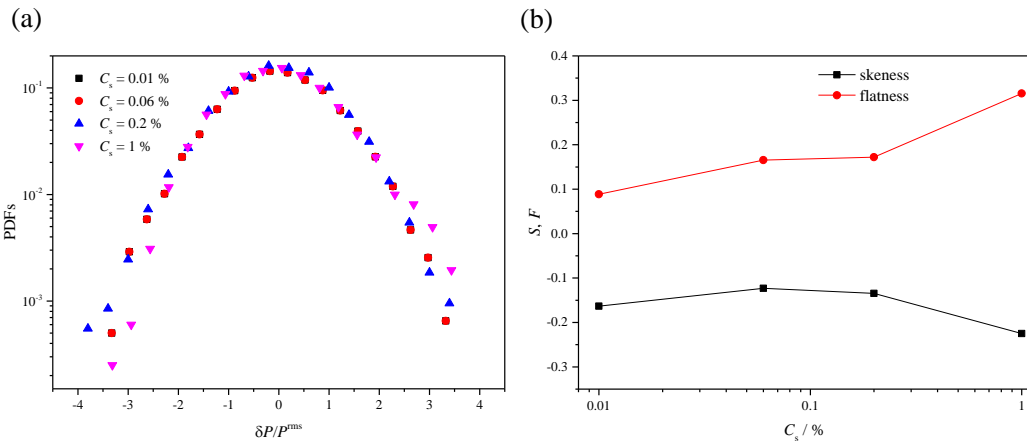
Figure 4.14 The statistic properties for fluctuations of inject power of HPAM solutions with different salinity: (a) PDFs of $\delta P/P^{\mathrm{rms}}$; (b) Skewness and Flatness of PDFs as a function of salinity

The frequency power spectra of injected power of the upper plate at different averaged shear rates were measured to reveal more detailed features of the flow dynamics. The spectra transition profiles for HPAM solution with 1% NaCl are shown in Figure 4.15. The curve evolves to a power-law decay, $P \propto f^{-\alpha}$, as the shear rate gradually increases into elastic turbulence regime and this law becomes more established at higher shear rate. The steep decay is resulted from the transfer of energy from the low-frequency mode down to high frequency by stretching and folding of elastic stress field by a random flow. All spectrum in the elastic turbulence regime behaves similar appearance: a broad region at $f < f_{\mathrm{vor}}$, and a steep power-law decay over decades at $f > f_{\mathrm{vor}}$, where f_{vor} is main vortex frequency with a peak visible on the plot at $f = f_{\mathrm{vor}}$. The f_{vor} tends to higher frequency domain region with the increase of shear rate as shown in Figure 4.16, which agrees well with the previous study.(Jun and Steinberg, 2017) Before the flow dully developed into elastic turbulence regime, the power exponent slight increases and keeps constant at the value around -4.3, which is consistent with the exponent obtained from Groisman et al(Groisman and Steinberg, 2004) and Jun et al(Jun and Steinberg, 2009) of -4.3 and -4, respectively, and much larger than the one in inertial turbulence. The spectrum of HPAM solutions with other degree of salinity are presented in Figure 4.17(a)-(c).
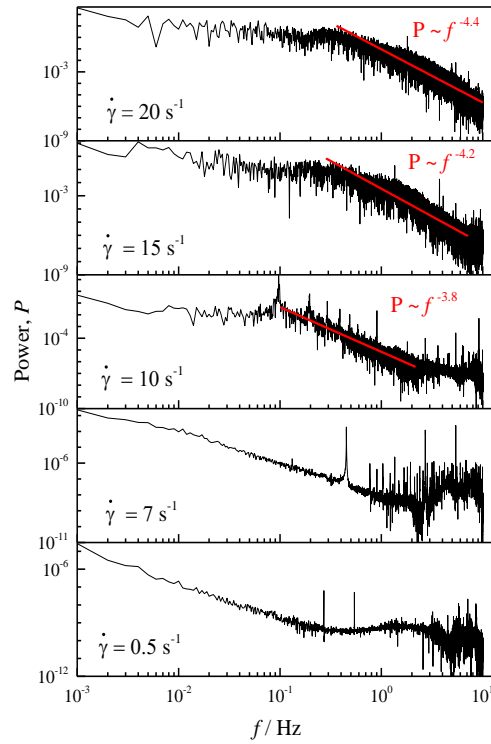
Figure 4.15 The frequency power spectra of injected power of the upper plate with different shear rate for HPAM solution with 1% NaCl
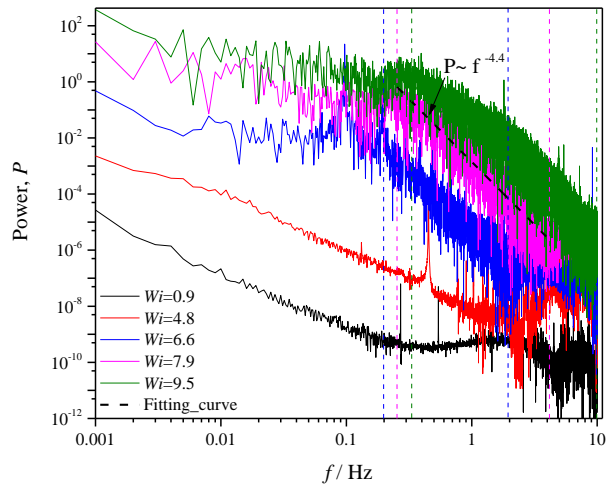
Figure 4.16 Power spectra of fluctuations of injected power of the upper plate at different *Wi*
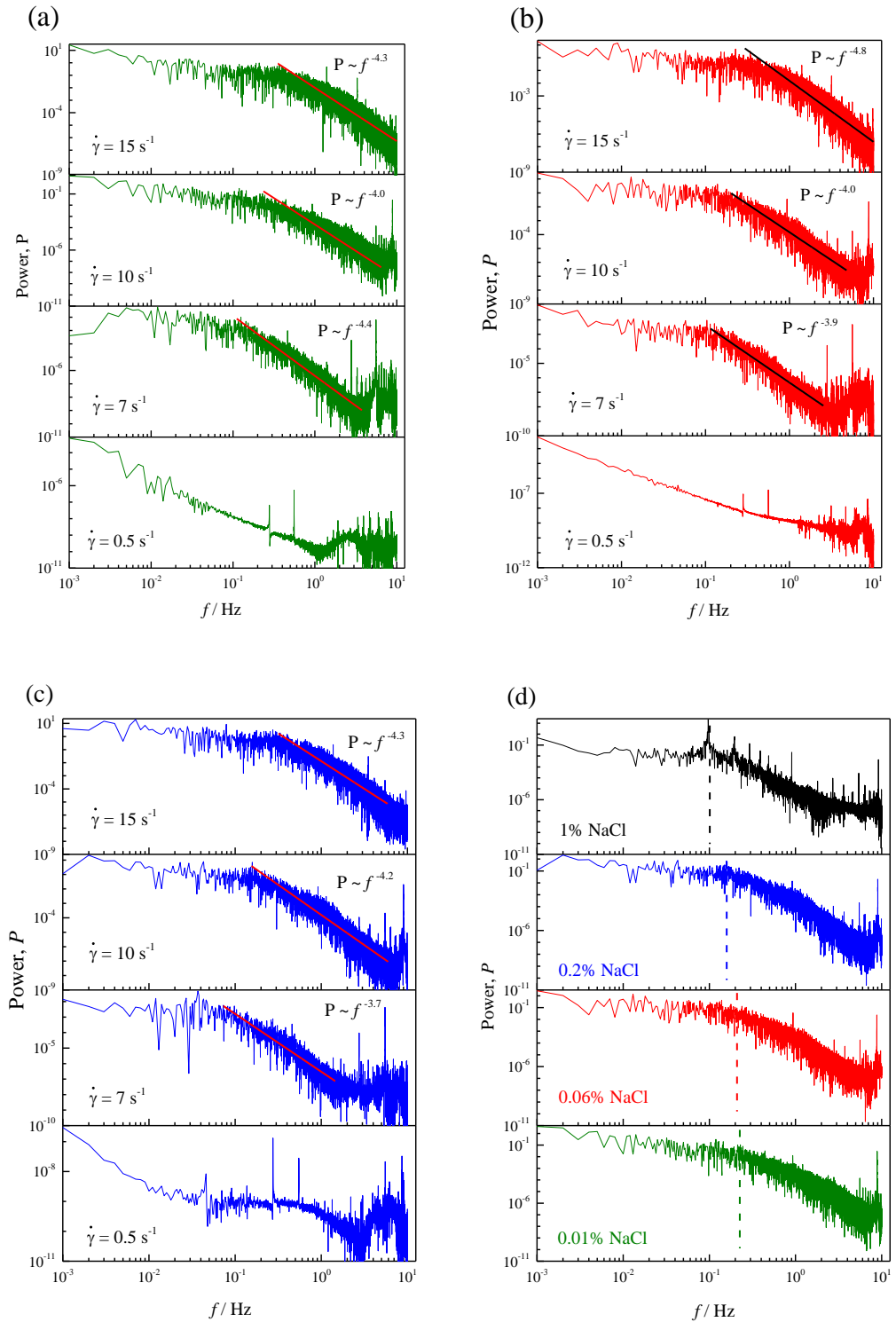
Figure 4. 17 Power spectra of fluctuations of injected power of the upper plate. (a) HPAM solution with 0.01% NaCl at different shear rate; (b) HPAM solution with 0.06% NaCl at different shear rate; (c) HPAM solution with 0.2% NaCl at different shear rate (d) with different salinity at a fixed shear rate 10 s^{-1}

The spectrum of inject power with different salinity at three shear rates are presented in Figure 4.18 (the spectrum at $\dot{\gamma}$=10 s^{-1} are listed in Figure 4.17(d)).

Through the spectrum profiles, one can see that with lower salinity, the power-law-decay is more easily observed, which shows great consistency with the results of stress ratio discussed above. At lower shear rate, as shown in Figure 4.18(a), the power exponent increases with the reduction of the salinity and the f_{vor} moves to large frequency domain since the HPAM solutions with high salinity are not fully develop in elastic turbulence regime. However, at high shear rate, as displayed in Figure 4.18(b) and Figure 4.19, the power exponent is independent on salinity and keeps constant value around -4.3. The normalized peak frequency, f_{vor}/f_{rot}, as a function of Wi/Wi_c is plotted in Figure 4.20. As the flow evolves into elastic turbulence regime, this normalized peak frequency equilibrate toward a constant value at 0.22, which is totally same with results analysed by Jun (Jun and Steinberg, 2017). It shall be noticed that even at the highest shear rate, the spectrum of sucrose solution does not show any turbulent-like phenomenon, which again proves the existence of elastic turbulence and supports the results of salinity effects.
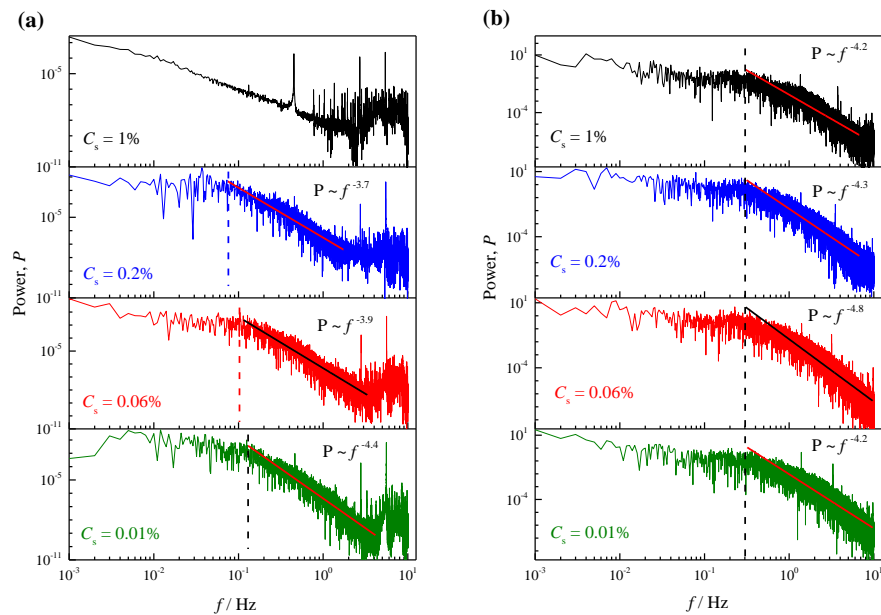
Figure 4.18 Power spectra of fluctuations of injected power of the upper plate at different salinity: (a) $\dot{\gamma} = 7$ s^{-1}; (b) $\dot{\gamma} = 15$ s^{-1}
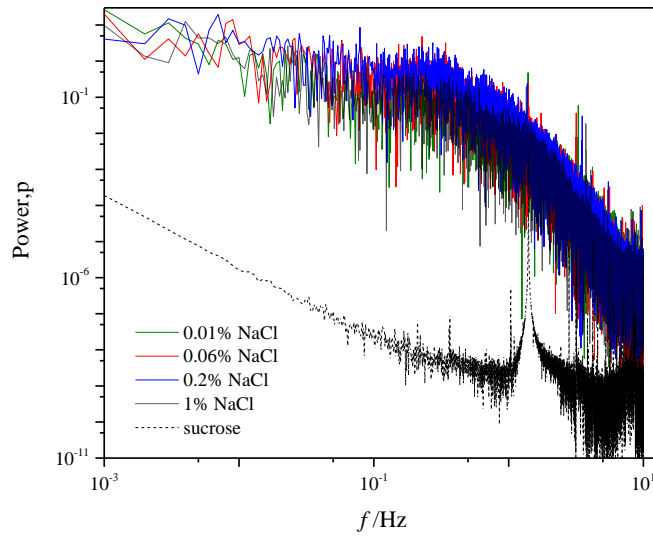
Figure 4.19 Power spectra of fluctuations of injected power for HPAM solution with different salinity at maximum *Wi*
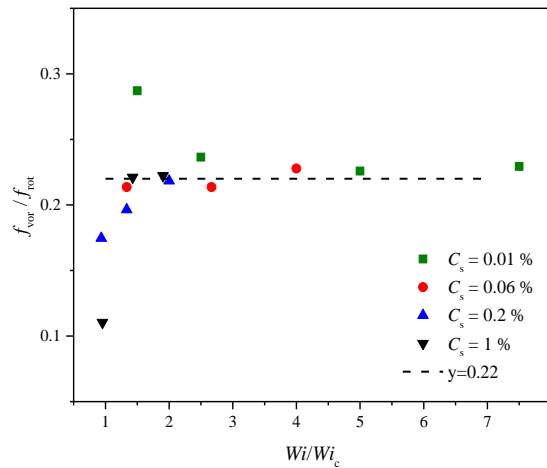
Figure 4.20 The normalized frequency of the main vortex f_{vor}/f_{rot} as functions of Wi/Wi_c at different salinity

4.4 Salinity effects on mixing performance in a microchannel

The experiments of mixing performance are presented in this section. The working fluids used were same with precious section. There are two inlets of the microchannel, both of which were injected by similar working fluids but one of those was dyed by fluorescein rhodamine B. The snapshots of 65% pure sucrose solution are shown in Figure 4.21. At the maximum applied flow rate, $Q = 200$ μl/min, there still exists a clear interface between two types of fluids, which indicates the flow rate and the curvature of the geometry do not affect the mixing results at given working conditions. The Re number of the sucrose

solution is ranging from 0.001 to 0.09 when the flow rate increases from 5 to 300 μl/min.

$Q = 5$ ul/min $\qquad$ $Q = 10$ ul/min $\qquad$ $Q = 30$ ul/min

$Q = 50$ ul/min $\qquad$ $Q = 100$ ul/min $\qquad$ $Q = 200$ ul/min
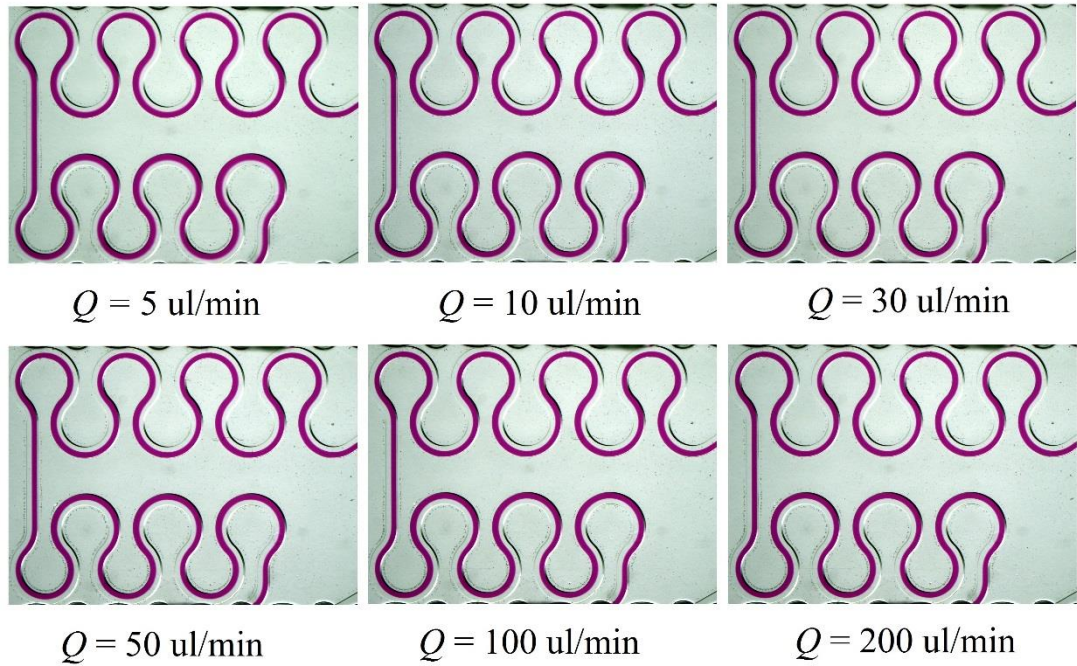
Figure 4. 21 Snapshots of mixing performance with different flow rate of pure sucrose solution with 1% NaCl

The snapshots for mixing performance of HPAM solution with 1% NaCl are partially displayed in Figure 4.22. A clear interface is found between two injected liquids at the position close to the inlet at low flow rates. This interface turns to be less dramatic downstream due to the diffusion of the fluorescein caused by the slight flow instability, which induced by the curvature of the microchannel. Such instability is too weak to trigger elastic turbulence as there is still no chaotic streamline observed. It is consistent well with the recent point view that there exists a steady secondary flow before the onset of elastic instability.(Ducloue et al., 2018; Sousa et al., 2018) The hysteretic transition from laminar to elastic turbulence is possible due to this steady instability. The dimensionless mixing length, defined here as the ratio of the numbers of rings with clear interface to the total rings of the microchannel, increases as the flow rate is enlarged. This is mainly due to that the high flow rate forces the flow passing through the channel rapidly, which suppresses the dispersion of dye to the direction of cross section. The flow becomes chaotic when the flow rate reaches a specific level, making the clear interface disappear suddenly even close to the inlet of the channel. This behaviour is accompanied by a significant streamline cross, indicating the occurrence of the elastic turbulence. Indeed, based on the previous studies,(Groisman and Steinberg, 2004; Pan et al., 2013; Qin and Arratia, 2016) the amounts of curvilinear rings

or inserted obstacles do affect the flow dynamics. The more numbers of those the fluid flowing through, the more intensive of the flow perturbations due to the acceleration of the flow instability. It is challenging to characterize such onset of elastic instability around outlet of the channel even with detailed velocity profile. Therefore, a simple condition at which the whole channel is fully mixed is regarded as the signal of the onset of elastic turbulence.
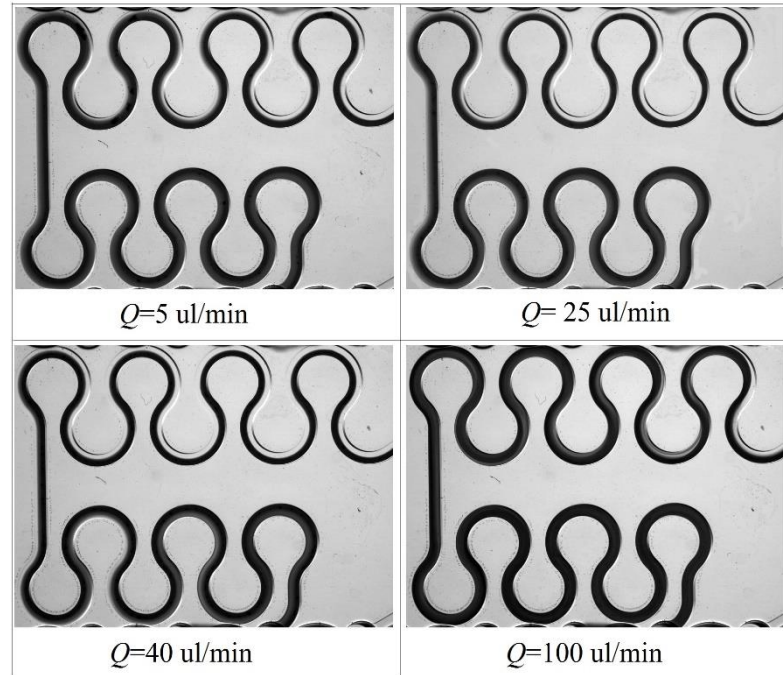
Figure 4.22 Snapshots of mixing performance with different flow rate of HPAM solution with 1% NaCl

Same series of salt concentration were conducted to investigate the mixing performance in the curvilinear microchannel. The variations of mixing length for HPAM solutions with different salinities are quantitatively plotted in Figure 4.23, and some representative snapshots at flow rate of 20 μl/min are shown in Figure 4.24 as well. The mixing length increases first and then decrease sharply with gradually increasing the flow rate for both curves. This sudden reduction is corresponding to the onset of elastic turbulence, which has been discussed above.

The HPAM solution with higher salt concentrations induces the elastic turbulence at larger average shear rate (flow rate). As shown in the Figure 4.24, for a given shear rate of 20 μl/min, the HPAM solutions with low salinity such as 0.01% and 0.06% are already fully mixed within whole channel while for the HPAM solutions with higher salinity, the clear interface is still existing. The numbers of ring with clear interface are also displayed in the Figure 4.24. An uptrend is found with the increase of salinity.

Ahead of the occurrence of elastic turbulence, the mixing length increases as the salinity increases, which means less channel rings are dyed at a low flow rate. This is related to effects of the curvature of the geometry as discussed above. The addition of the salt leads to the reduction of relaxation time of the polymer solution and its elasticity, making the HPAM hard to induce flow instability at the position close to the inlet of channel. More contributions from the curvilinear channel are required to perturb the stable flow. As a result, the mixing occurs far from the inlet and the mixing length becomes larger.
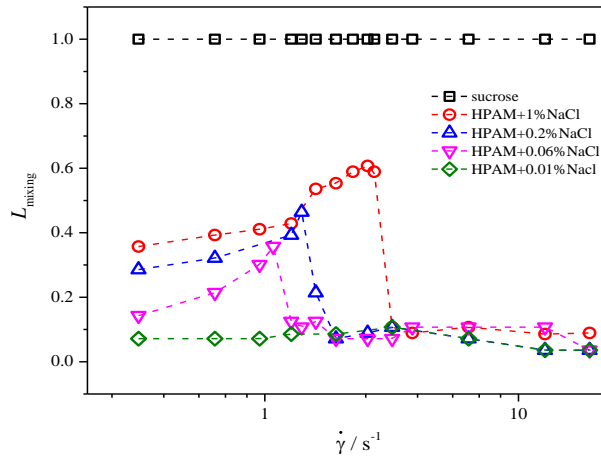
Figure 4.23 Quantitative comparison of mixing performance with different salinity
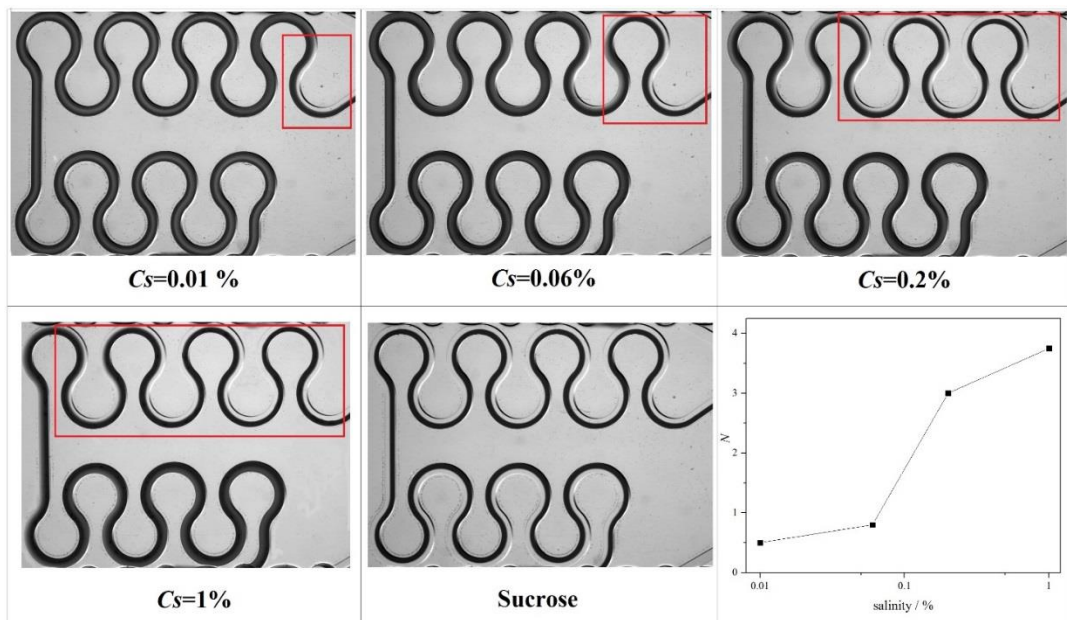
Figure 4.24 Snapshots of mixing performance with different salinities at value of flow rate 20 μl/min

The onset values of shear rate and Weissenberg number at different salt concentrations are performed in the Figure 4.25. Similar trends are obtained with the results concluded in swirling flow. The threshold shear rate and

Weissenberg number go up to a higher value when the salinity increases, followed by a slight reduction at the maximum salinity. Here, the shear rate of the HPAM solution with 0.01% NaCl is calculated from the minimum applied flow rate (5 μl/min) as no clear interface condition was observed during the experiments. Both the values of shear rate and Weissenberg number are smaller than those in swirling flow due to the discrepancy of the geometry. It is interesting to present the dependence of critical shear rate on polymer relaxation time. Figure 4.25(b) highlights the similarity of such dependence in two geometries. Both curves follow a logarithmic relationship between $\dot{\gamma}_c$ and λ, which indicates the mechanism of salinity effects is independent on geometry.
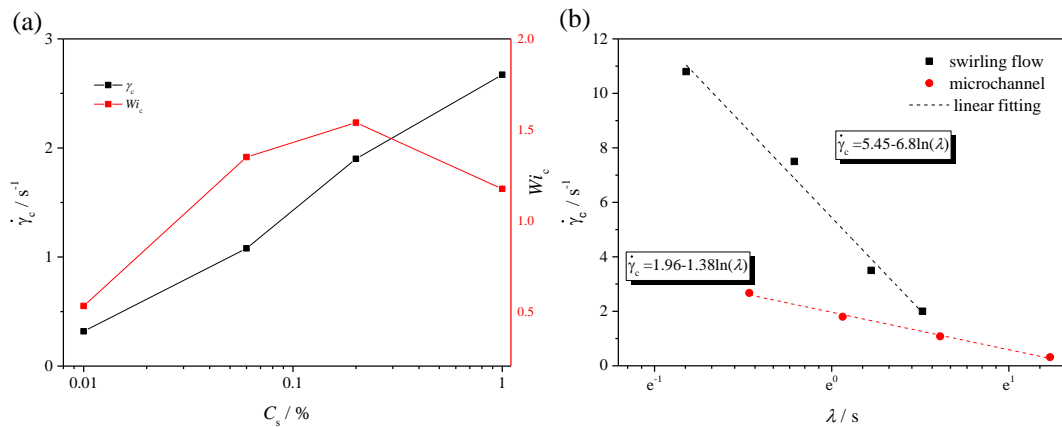
Figure 4.25 (a) Salinity effects on the threshold properties of polymer solutions in curvilinear microchannel; (b) dependences of critical shear rate versus relaxation time in two geometries.

4.5 Conclusions

The effects of salinity on the onset of elastic turbulence have been investigated experimentally in swirling flow and micro serpentine channels. With increasing salinity, the polymer contribution to the viscosity decreases, resulting in a higher threshold Wi_c for the onset of elastic instability. Owing to the dramatic shear-thinning behavior caused by the polymer configuration, the dependence of Wi_c on η_p/η can be fitted well by $Wi_c \sim (\eta_p/\eta)^{-\alpha}$ with exponent of 1. With continual increase in the salinity, the poor quality of solvent makes the Wi_c disobey the rules.

The shielding effects seems to be ineffective when the flow is fully developed into elastic turbulence regime. These trends are consistent with the variations of spectra profiles of injected power. A power-law pattern is gradually observed as the flow transfers from laminar to elastic turbulence, where the

exponent increases first and then keeps constant around a value of -4.3. In fully developed elastic regime, both the exponent and the normalized peak frequency become independent of salinity. Although high salinity delays the occurrence of elastic turbulence, the growth of flow intensification is more dramatic due to the reduction of the viscosity, accompanied with more intensive skewness of the PDFs of injected power. Similar trends are applied well on the mixing performance and threshold properties in a curvilinear microchannel. The discrepancy of the values is ascribed to the geometry effects. The diffusion of the fluorescein at low flow rate indicates the possible existence of steady secondary flow instability.

Chapter 5
Flow and heat transfer intensification based on elastic turbulence

The elastic turbulence, as discussed above, is capable of perturbing laminar flow into turbulent-like flow. Such low Reynold number chaotic flow motion would reduce the thermal boundary layer, strengthening the heat and mass transfer. What's more, the onset condition and the degree of flow irregularity at the fully developed regime are highly dependent on the rheology of the polymer solution, but its concomitant effects on the heat transfer side have not been investigated. This Chapter investigates the heat transfer performance induced by elastic turbulence to reveal the effects of polymer rheological properties varied by polymer concentration and salinity. The outline of the chapter is organized as followed. The experimental details are firstly demonstrated, where the descriptions of the experimental set-up, measurement protocol and analysis method are introduced. The heat transfer performance by pure sucrose solution (Newtonian fluid) is discussed next as a validation of the reliability of experimental system and acts as the base condition. Finally, the heat transfer performance based on elastic turbulence (elastic instability) is introduced and the effects of polymer concentration and salinity are discussed.

5.1 Experimental details

5.1.1 Experimental set-up
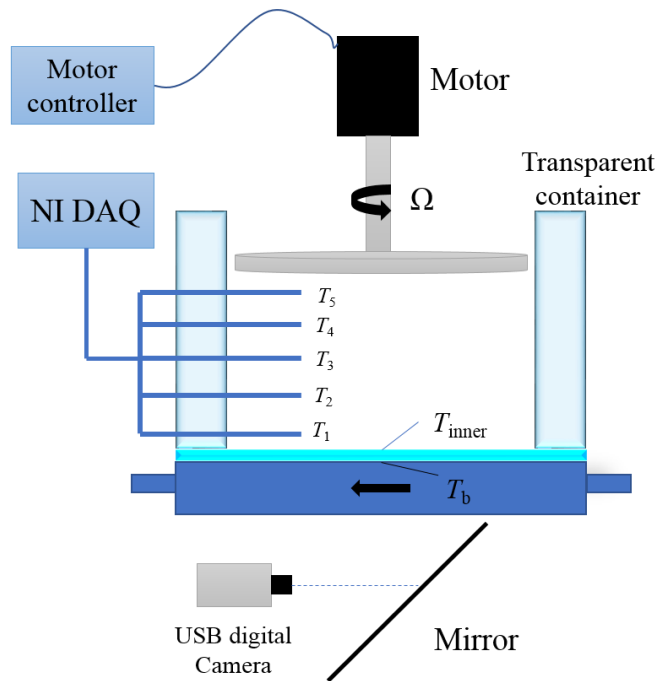
Figure 5.1 Schematic view of the experimental setup

The experimental rig that was used to investigate the behaviour of the flow and convectional heat transfer performance of viscoelastic fluids in swirling flow is shown in Figure 5.1. It consists of an acrylic fluid container with inner diameter $D_{in} = 56$ mm and optically transparent walls. The thicknesses of side wall and bottom wall are 10 mm and 5 mm, respectively. The flow is driven by a aluminium rotating round disk with a radius $R_d = 25$ mm mounted on an electric motor whose controlling precision is up to 0.1 rpm. An insulating cover is placed on the top of the container to reduce convection loss. The distance between the top disk and the bottom of the fluid container is set at a constant value, $H = 40$ mm, for all experiments. A circulating fluid bath is attached to the bottom of the fluid container and the temperature within which was set to below the room temperature at a value of 5 °C to avoid thermal convection inside the bulk flow. To ensure a good repeatability and reproducibility of the experiments, the room temperature was maintained around 23 °C by an air conditioning system.

The temperature distribution into the flow was monitored by an array of five thermocouples (i.e., T_1 to T_5) disposed equidistantly (5 mm each point) along the vertical direction z and positioned at the radial position at the half radius of the fluid container. To measure the temperature of the inner wall, a thermocouple was carefully mounted on the bottom and the wire was fixed

along the side wall to avoid additional secondary flow. The temperature of the outer wall of the fluid container was averaged based on four thermal couples mounted uniformly along the circular direction in the cooling plate. All thermocouples used in this work were K-type with wire diameter of 0.125 mm, which were calibrated against a mercury thermometer of certified accuracy (± 0.5 °C). The signals of the thermocouples were collected by a National Instrument data acquisition system (NI 9185) and were post-analysed by LabVIEW software

Besides the temperature measurements, a digital camera and a mirror were coupled together to visualize the flow patterns during the experiments. The mirror tilted by 45° was placed under the fluid container and was used to illuminate the fluid and to relay images of the flow to the camera. It should be noticed that the flow visualization was conducted without circulating fluid bath since the existence of that blocks the light going through. However, the captured images still show significant difference and indicates the occurrence of elastic instability, which contributes much to the descriptions of the heat transfer performance analysis.

The protocol of the measurement is described as followed:

1) Fill the fluid container with specific working fluid and let the upper disk just attach to the top surface of the liquid.

2) Turn on the temperature measurement module.

3) Turn on the refrigerator but keep the circulating system close to let the refrigerant reach to 5 °C.

4) Set the rotating speed of the upper disk with specific value. After 15 minutes or so of steady operation, turn on the circulating value.

5) When all the temperature measurements equilibrate, turn off the equipment and wait until the temperature of fluid container back to initial conditions.

6) Fill the fluid container with fresh working fluid and repeat the protocol from 2) to 5).

It should be noted that for the experiments related to the effects of concentration and salinity, the process curve is not necessary. Therefore, when the temperature profiles of the current rotating speed has equilibrated, one can change the rotating speed directly and run the next experiment.

5.1.2 Working fluids

The working fluids applied in this study were comprised of different amount of hydrolysed polyacrylamide (HPAM), sucrose and sodium chloride (NaCl). Sucrose and sodium chloride with laboratory reagent grade were supplied by Fisher Scientific Ltd. The hydrolysed polyacrylamide with molecular weight 22M g/mole were purchased from Shandong Tongli Chemical Co., Ltd. (China). A concentrated HPAM solution with 2000 ppm was prepared first. By adding specific amounts of concentrated HPAM solution, sucrose and NaCl into deionized water, the working fluids were then well prepared after 3h moderate mixing under a mechanical stirrer. With each variable was set different, the effects of polymer concentration, solvent viscosity and degree of salinity were investigated, respectively. The overview of working fluids are listed in the Table 5.1.

Table 5.1 Working fluids applied in this study

Controlled parameters	Index	HPAM (ppm)	Sucrose (%)	NaCl (%)	Thermal conductivity $(W \cdot m^{-1} \cdot K^{-1})$
Polymer concentration	1	100	65	1	
	2	200	65	1	0.365 ± 0.01
	3	300	65	1	
Degree of salinity	1	200	65	0	
	2	200	65	0.1	0.365 ± 0.01
	3	200	65	0.5	
Proportion of solvent	1	200	0	0	0.563 ± 0.01
	2	200	20	0	0.510 ± 0.01
	3	200	40	0	0.453 ± 0.01
	4	200	65	0	0.362 ± 0.01

5.1.3 Analysis description
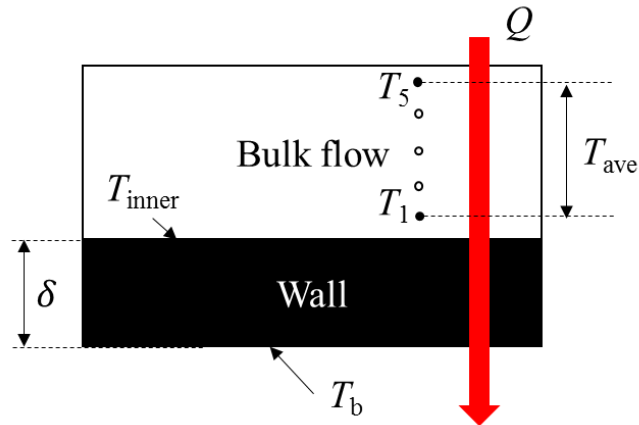
Figure 5.2 Schematic diagram of the heat transfer process during experiments

The heat transfer process during experiments is introduced below. The out wall of the fluid container is set as a constant temperature boundary condition by the cooling circulating system. The side wall can be regarded as a thermal insulation boundary. The amount of heat flux removed by cooling wall can be quantitatively calculated by equation (5.1).

$$Q = k_{acrylic} \cdot \frac{T_{inner} - T_b}{\delta}$$

(5.1)

Where δ is the thickness of the acrylic wall, T_{inner} and T_b are the temperatures of the top and the bottom surface of the wall, respectively; $k_{acrylic} = 0.18$ W·m^{-1}·K^{-1} is the standard thermal conductivity of acrylic materials. To evaluate the heat transfer performance, the effective thermal conductivity, k^*, defined by the ratio of the total measured heat flux and the temperature gradient between the top and the bottom of the fluid container, and the global heat transfer coefficient, h^*, calculated based on the average temperature of the bulk fluid and the inner surface of the wall, are adopted here to characterize the heat transfer enhancement inside the bulk fluid and between the fluid and the wall, which are represented by equations (5.2) and (5.3), respectively:

$$k^* = \frac{Q}{\frac{T_5 - T_1}{x_5 - x_1}} \cdot$$

(5.2)

$$h^* = \frac{Q}{(T_{ave} - T_{inner})}$$

(5.3)

Where T_1 and T_5 are the equilibrated temperature of thermocouples mounted near the bottom and top plates, respectively; T_{ave} is the average temperature

of working fluids, see equation (5.4), and T_{inner} is the temperature of the bottom of the fluid container. x_1 and x_5 represent the height of the thermocouple T_1 and T_5 from the inner bottom of the fluid container. The corresponding Nusselt number can be obtained by equation (5.5), where the H represents the gap between the upper plate and the inner bottom of the fluid container; the k represent the thermal conductivity of the applied working fluid.

$$T_{ave} = \frac{T_1 + T_2 + T_3 + T_4 + T_5}{5}$$

(5.4)

$$Nu^* = \frac{h^* H}{k}$$

(5.5)

In the present work, the temperature and the depth of the fluids are measured directly by thermocouples and ruler meter. The errors of indirect parameters, for example heat flux, Nusselt number and so on are calculated from the errors of direct measurement parameters using root-sum-square approach as shown in equation (5.6). The maximum errors of experimental parameters are listed in Table 5.2.

If

$$\chi = S_1^a S_2^b \dots S_N^n$$

(5.6)

Then

$$\frac{\delta \chi}{\chi} = \sqrt{\left\{ \left(a \frac{\delta S_1}{S_1} \right)^2 + \left(b \frac{\delta S_2}{S_2} \right)^2 + \cdots + \left(n \frac{\delta S_N}{S_N} \right)^2 \right\}}$$

(5.7)

Table 5.2 Error estimation of direct and indirect parameters

Parameter	Error (%)	Indirect parameter	Error (%)
T_1 to T_5	2.67	Q	5.67
H	0.25	h	6.26
k	5	Nu	8.01
T_{inner}, T_{wall}		k^*	6.27

5.1.4 Rheological properties measurement of working fluids

The rheological properties of working fluids were measured by cone and plate geometry of a stress-controlled rheometer (Anton Paar MCR 301) at a temperature of 15 °C, which is similar with the average temperature of bulk fluid. The effects of polymer concentration on the rheology are shown in Figure 5.3. The viscosity increases with increasing the polymer concentration for a given shear rate. All curves exhibit a shear-thinning behaviour whereas higher polymer concentration induces more dramatic reduction. This increment is ascribed to the more interactions between polymer chains, which causes more frictional effects to increase the viscosity. Figure 5.3(b) shows the response

of complex viscosity profiles as a function of angular velocity for different polymer concentration. The results show both the out-of-phase viscosity and in-phase viscosity increases as the polymer concentration increases. The values for polymer-driven in-phase and out-of-phase viscosity were obtained by excluding the solvent contribution at same working conditions, $\eta_p'=\eta'-\eta_s'$ and $\eta_p''=\eta''-\eta_s''$, respectively. Then the polymer relaxation time was calculated according to equation (5.8) as shown in Figure 5.3(c) for the 200 ppm HPAM solution with 65% sucrose and 1% NaCl at different shear rate for instance. The dependence of the polymer relaxation time on the shear rate with different polymer concentration is performed in Figure 5.3(d). Both curves shows a clear shear thinning behaviour as a function of the shear rate, with scaling $\lambda\sim\gamma^{-\alpha}$, similar to previous investigation in Ref (Liu et al., 2007a), which also implies why the increase of *Wi* is normally slower than the increase of shear rate. In addition, with higher polymer concentration, the polymer relaxation time becomes longer, which means the increase of HPAM solution elasticity. As a result, that may contribute to the onset of elastic turbulence or instability.

$$\lambda = \lim_{\omega \to 0}\left\{\frac{1}{\omega}\left[\frac{\eta_P''(\omega)}{\eta_P'(\omega)}\right]\right\} \tag{5.8}$$
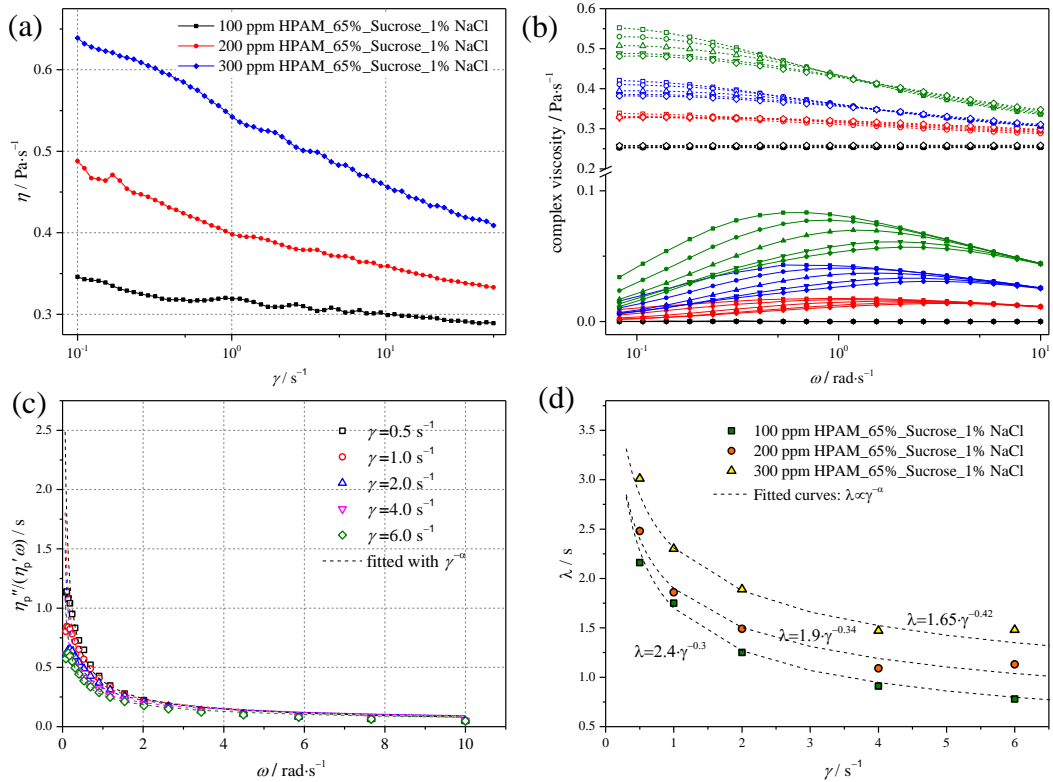
Figure 5.3 Effects of polymer concentration on the rheology of polymer solution. (a) The viscosity dependent on polymer concentration; (b) The measured complex viscosity with different shear rate; (c) Angular frequency dependence of $\eta_p''/(\eta_p'\omega)$ (d) The shear rate dependence of polymer relaxation time with different polymer concentration

Figure 5.4 highlights the salinity effects on the rheology of polymer solution. The presence of salts has a buffering effect, shielding the charges along the polymer chain with salt cations, resulting in polymer molecules shrinkage and consequent viscosity reduction. This shrinkage also contributes to alignment of polymer molecules, which significantly reduces the shear-thinning phenomenon. Indeed, the shielding effect is limited by the numbers of charge groups along the polymer chain. Thereby a critical salinity exists above which the salinity shows slightly effects. Continually increase the salinity, a so-called poor solvent is obtained, increasing the polymer interactions, resulting the increase of viscosity. In such condition, the salinity is not the only influence parameters any more. In this study, the salinity of 1% was excluded to eliminate the effects of poor solvent. The corresponding relaxation times with different salinity are concluded in Figure 5.4(d).
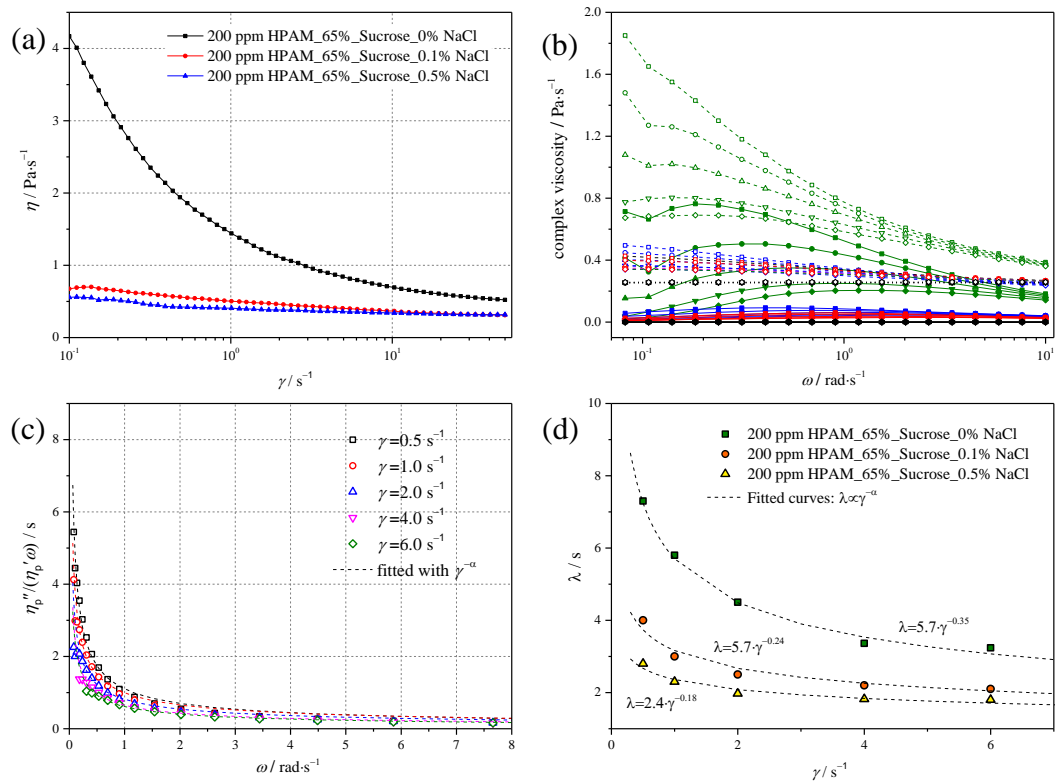
Figure 5.4 Effects of salinity on the rheology of polymer solution. (a) The viscosity dependent on polymer concentration; (b) The measured complex viscosity with different shear rate; (c) Angular frequency dependence of $\eta_p''/(\eta_p'\omega)$ (d) The shear rate dependence of polymer relaxation time with different polymer concentration

Figure 5.5 demonstrates the effects of solvent on the rheological properties of polymer solutions by varying the proportion of sucrose. Adding sucrose into the polymer solution, as expected, both the viscosity and relaxation time increase, which is consistent well with previous theory that the polymer

relaxation time is proportional to the viscosity of solvent (Groisman and Steinberg, 1998). One can see the difference between polymer solution with 20% sucrose and 40% sucrose is slight. This small contribution interprets why at high applied swirling velocity the heat transfer enhancement of polymer solution with 20% sucrose is better than that of 40% sucrose, which will be discussed in details in the later section.
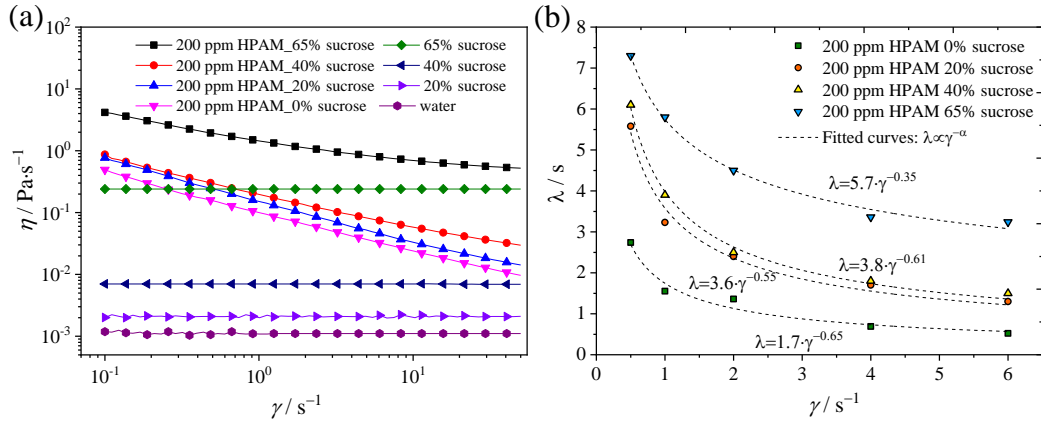
Figure 5.5   Effects of sucrose proportion on the rheology of polymer solution.(a) Viscosity variations with different sucrose concentration; (b) Shear rate dependence on polymer relaxation time with different amount of sucrose addition

5.1.5 Thermal properties of working fluids

Differential scanning calorimetry (DSC) was used to measure the specific heat capacity of working fluids at temperature ranging from 30 to 70 °C as shown in Figure 5.6. The characteristic values of specific heat capacity at 15 °C were then estimated by fitting the experimental data. The addition of polymers to Newtonian solvent does not significantly change the specific heat capacity and the estimated values for both working fluids were agreed well with previous studies (Abed et al., 2016). Measurement of thermal conductivity was conducted through probe method (KD2pro thermal properties analyser) at room temperature since an independent relationship between thermal conductivity of sucrose solutions and temperature was performed (Li et al., 2016a). The measured thermal conductivity was consistent well with the results of Lee et al. (Lee et al., 1981), who demonstrated that the addition of polymer up to 10000 ppm to Newtonian solvents does not affect the values of thermal conductivity for these solutions. Therefore, the influence of conduction performance of working fluids on the heat transfer could be eliminated. The representative thermal properties applied in this study are listed in Table 5.3. The heat specific capacity and thermal conductivity are used for the validation

case. Therefore, the corresponding thermal properties for other working fluids such as polymer solution with different concentration or salinity are not shown.
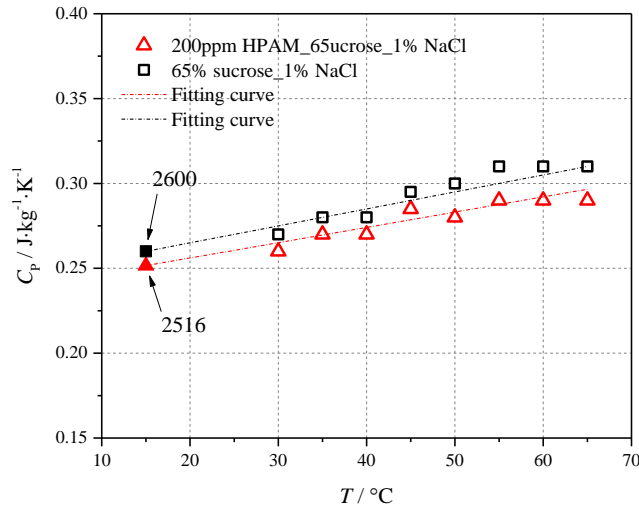
Figure 5.6 Measurement of specific heat capacity with various temperature

Table 5.3 Thermal properties of working fluids

Working solutions	Density (Kg·m^{-3})	heat specific (J·K^{-1}·kg^{-1})		thermal conductivity (W.m^{-1}.K^{-1})	
		Measured	Ref.	Measured	Ref.
sucrose	1280	2600	2606 (Abed et al., 2016)	0.37	0.368 (Abed et al., 2016)
HPAM	1301	2600	-	0.376	

5.2 Heat transfer performance for pure sucrose solution

The experiments for both sucrose solution and HPAM solution were conducted with applied rotating angular speed ranging from 0 to 10 rpm. Within the entire range of angular speeds, the Reynolds number of sucrose solution, $Re = \rho\Omega R_d^2/\eta$, was evaluated in the range between 0 and 3.5, which is significantly larger than the largest Re investigated during the experiments with the HPAM solution. Therefore, the comparison between these two working fluids is reasonable to eliminate the influence of inertial effect and the flow instability is solely driven by elastic stresses. Prior to investigating the heat transfer process in a regime of elastic instability, the heat transfer

performance based on sucrose Newtonian solution with various angular speed was introduced first as a validation.

The time against temperature distribution profiles of the sucrose solution along the vertical direction at various rotating angular speed are shown in Figure 5.7(a) (where only temperature profiles at the maximum rotating speed is shown due to the similarity). The initial temperature of working fluid is homogeneous around 21 °C across the whole bulk fluid, followed by a sharp reduction due to the refrigeration system. The temperature near the bottom of the fluid container decreases first and equilibrates at the lowest temperature since the heat is conducted from bottom to top gradually. The measurements for all thermocouples are stable after almost the same time. Even for the maximum applied rotating speed, an obvious separation of temperature layer, which is strongly dependent on the z coordinate, is still observed, indicating a significant inhomogeneous temperature distribution and a conduction like heat transportation. Such behaviours are consistent well with the features of laminar flow. Further analysis was conducted by introducing the reduced temperature θ as defined by equation (5.9).

$$\theta = \frac{T_0 - T}{T_0 - T_b} \tag{5.9}$$

Transient measurements of the reduced temperature at maximum applied rotating angular speed are performed in Figure 5.7(b). The reduced temperature increases as time accumulates with a logarithmic scaling part before reaching a steady plateau state and each transient data is fitted by

$$\theta = A \cdot erfc\left(\frac{B}{\sqrt{t}}\right)^C \tag{5.10}$$

$$B = \frac{z}{(4a)^{\frac{1}{2}}} \tag{5.11}$$

where *erfc* is the complementary error function, the parameter A describes the equilibrium temperature and B describes the local intensity of the heat transfer process. This function gives exact description for the one-dimensional transient heat transfer in the case of a semi-infinite planar domain with a constant temperature boundary condition when the parameter $C = 1$. By letting C vary as an extra fit parameter, it is reasonable to be applied on finite size conditions. The relationship between fitted coefficients B and the position coordinates z of the thermocouples is shown in Figure 5.7(c). The thermal diffusivity of the sucrose solution, a, is obtained by linearly fitting the equation (5.11). The fitted values, as shown in Figure 5.7(d), show independent on angular speed and are consistent well with measured values, $a_{meas} = k/(\rho c_p)$, where k is the measured thermal conductivity, ρ is density of the working fluid

and c_p is the specific heat capacity of the working fluid, respectively. This reveals a conductive like heat transfer behaviour occurring within the sucrose solution. This finding corroborates well with a laminar flow behaviour and indicates no inertial instability contributing to the heat transfer intensification. Indeed, CFD simulations by FLUENT 18.1 were conducted to benchmark the experimental results as well. The simulation details are illustrated in the Appendix B. The temperature distribution along the vertical direction is demonstrated in Figure B.4, where a clearly layered temperature profiles is obtained, which is consistent well with the experimental results. What's more, the concomitant Nu and k^* calculated based on the simulation results also show a good agreement with experiments as shown in Figure 5.12 and 5.13 in the next section.
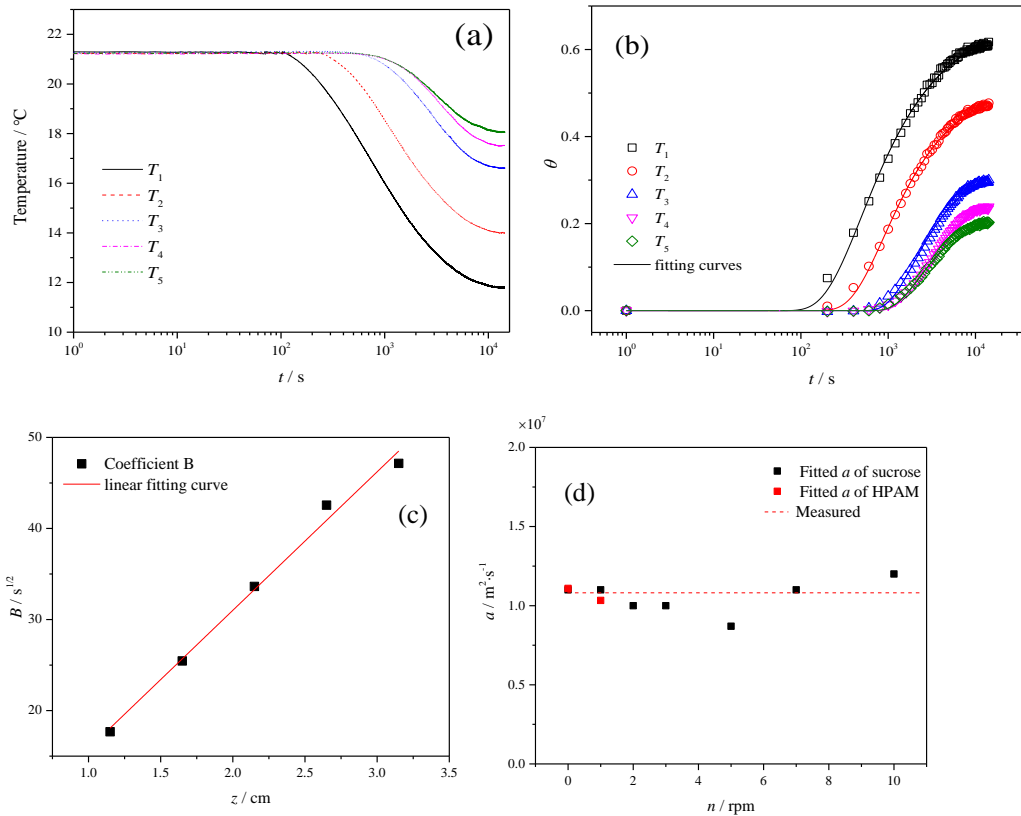
Figure 5.7   Temperature distribution profiles for sucrose solution. (a) measured temperature from thermocouples directly at n=10 rpm; (b) reduced temperature distribution at n=10 rpm; (c) thermal diffusivity fitting curve at n=10 rpm (d) variations of thermal diffusivity against different applied rotating speed. The thermal diffusivity for HPAM solution at the two lowest rotating speed are also included

With seeding 1% lighting reflecting flakes into working fluids, the flow visualization was achieved. This particle-filled liquid, so called as Kalliroscope or Rheoscopic liquid, is effective in capturing the flow patterns by reflecting differing intensities of light, making the movement of the streamline visible.

Two representative snapshots of the sucrose solution at different rotating speed viewed from below are shown in Figure 5.8. No obvious irregular flow pattern or vortex is observed even at the largest applied rotating speed. The flow looks quite uniform and is completely laminar, which consistent perfectly with the temperature distribution profiles measured by thermocouples mentioned above. Therefore, it can be concluded that, for pure sucrose solution, the flow stays in laminar regime and the inertial effects could be neglected within the range of rotating angular speed applied during the experiments.
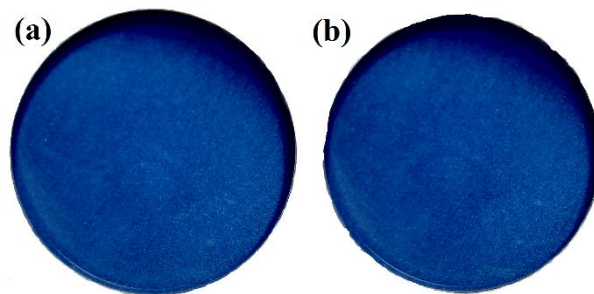
Figure 5.8 Flow patterns observed from below at 1 rpm (a) and 10 rpm (b), respectively

5.3 Heat transfer performance by elastic turbulence

5.3.1 Variations of process curves

Measurements of the time series of the reduced temperature θ for polymer solutions performed within different flow regime are presented in Figure 5.9. Different from the pure sucrose solution, due to the presence of flow instabilities, the complementary error function is no longer suitable for fitting the experimental data of polymer solutions, especially at higher applied rotating angular speed. For cases with lower applied angular speed, as shown in Figure 5.9(a) and (b), the process curves show similar trends with pure sucrose as discussed above that a separated temperature layer is observed, which indicates that the flow is still in laminar flow. Before the logarithmic scaling regime, the reduced temperature pass through a local minimum with $\theta_{min} < 0$. The magnitude of this minimum decreases and disappears gradually as the position moves from the top to the bottom of the fluid container. This phenomenon is attributed to the local viscous heating of the polymer solution (Traore et al., 2015).
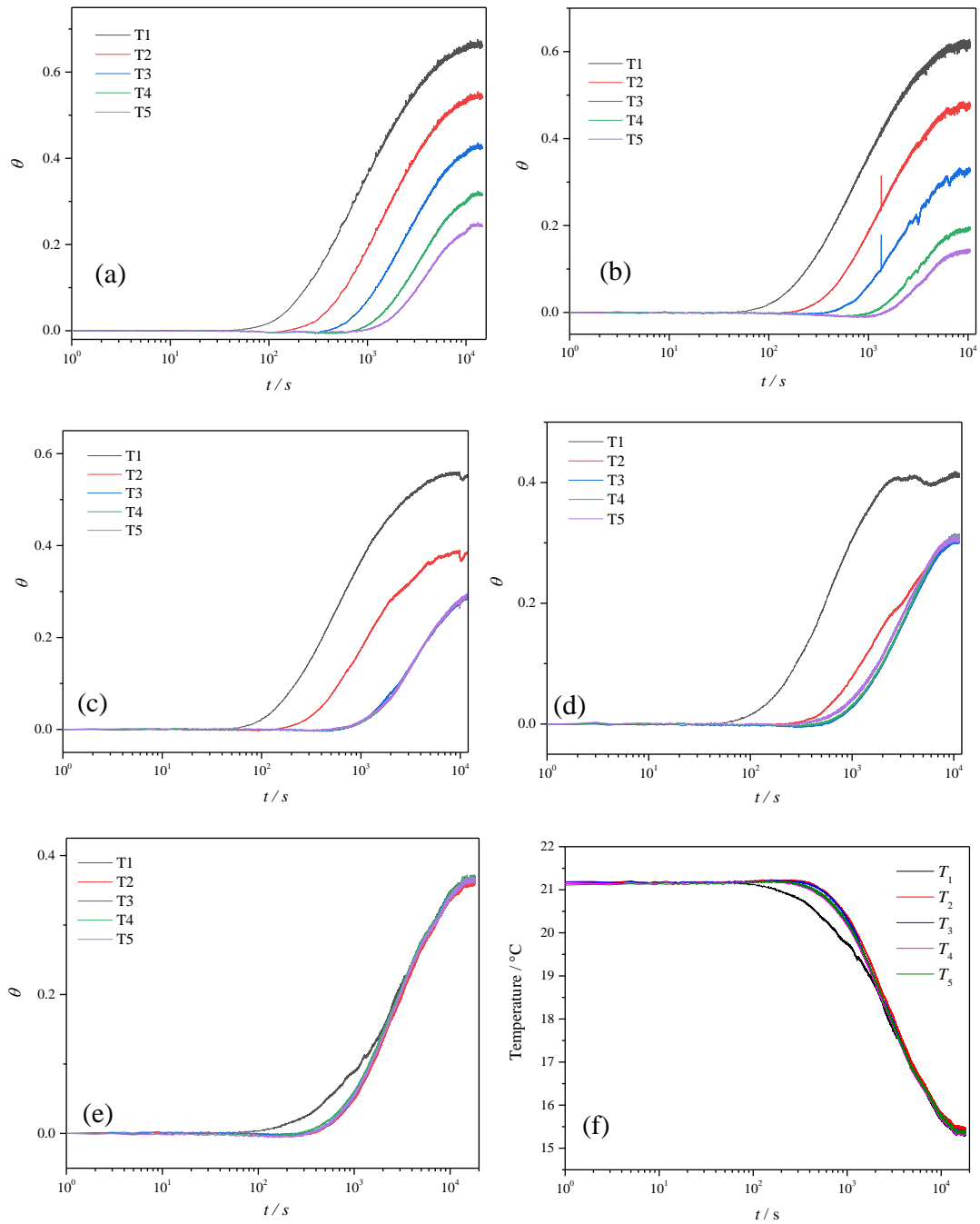
Figure 5.9 Temperature distribution of HPAM solution at different rotating speeds, where (a) to (e) was conducted at 0 rpm, 1 rpm, 3 rpm, 5 rpm, and 10 rpm, respectively.

As the applied rotating speed increases, the temperature profiles exhibit different trends, as plotted in Figure 5.9(c) and (d). The separation between each curve is no longer exist especially in the location near the top rotating plate, where the reduced temperature profiles collapse into a single curve. The collapsed value becomes even larger with increasing the angular speed. This is an indication that the flow in the region near the bottom of the fluid container still behaves conductive-like properties while an unsteady flow pattern is induced in the vicinity of the top surface homogenising the vertical

distribution of the reduced temperature more efficiently than steady laminar flow. This flow instability becomes more intensively and leads to the irregular flow spreads all over the bulk at a higher applied rotating speed. It also should be noticed that for undisturbed region, the equilibrated reduced temperature turns lower and the difference between each value becomes even larger than those in lower rotating speed. This is mainly because of the incremental of the heat flux transferred due to the chaotic flow vortex, which is also discussed later. The previous study was mainly focused on the effective heat transfer performance inside the flow, for example the distribution of the reduced temperature (Traore et al., 2015). However, the quantities of heat removal based on the flow elastic instability also shows promising improvement. In addition, one can see that the upward trends of the reduced temperature are induced at earlier time due to the rapid heat transferred caused by unsteady vortexes or flow streamlines.

A fully homogenous distribution of the reduced temperature and measured temperature profiles are obtained at largest rotating speed as shown in Figure 5.9(e) and (f). The temperature distribution along the vertical direction of the whole bulk entirely collapses into a single curve. This significant discrepancy compared with the pure sucrose solution indicates the elastic instability excites the whole bulk flow.

$n = 1$ rot·min^{-1} $n = 3$ rot·min^{-1} $n = 5$ rot·min^{-1}

$n = 7$ rot·min^{-1} $n = 10$ rot·min^{-1}
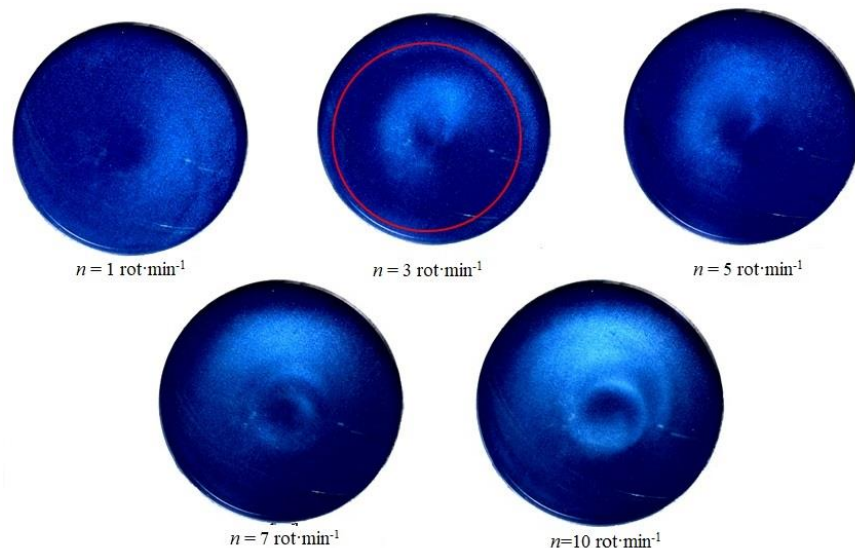
Figure 5.10 Snapshots of flow patterns captured from bottom for HPAM solution at different rotating speed

The corresponding flow behaviours of the HPAM solution captured from the bottom of the fluid container are shown in Figure 5.10. The patterns of the polymer solution at higher rotating speed look quite irregular and exhibit structures of different sizes. The evolution of these secondary flow patterns

could be interpreted by the transition pathway to elastic turbulence in parallel-plate flow observed by Schiamberg et al (Schiamberg et al., 2006). The flow sequentially develops as so-called Base state, Stationary ring mode, Competing spirals mode and Multi-spiral chaotic mode, respectively, with increasing the driven shear forces. Compared with the final elastic turbulence mode, the spiral-like flow pattern at maximum applied rotating speed is less intensive, which consistent well with statistical properties discussed in the later section, indicating the flow in still in the transition to elastic turbulence regime. These spiral-like forms are probably imposed by the average of azimuthal flow and circular symmetry of the set-up. Furthermore, a peak point is observed in the middle at stationary ring mode, which corresponds to the centre of a big persistent toroidal vortex and evolves to a spiral vortex latter. Direction of the bursting spiral motion is downwards near the centre and outwards near the bottom, which is attributed to the Weissenberg effect and is opposite to the motion in Newtonian fluids. The visual impression is consistent well with the previous temperature distribution and the existence of the vortexes recommend the elastic turbulence as a potential candidate to enhance heat transfer at least within swirling flow.

5.3.2 Convective heat transfer performance

The equilibrated reduced temperatures are shown in Fig. 5.11. For the sucrose solution, the equilibrated reduced temperatures for all thermocouples are independent on rotation speed. For the HPAM solution, on the other hand, each reduced temperature decreases slightly at beginning, increases rapidly at a certain value of rotating speed, and collapses into a similar value. This gentle decrease at the beginning is mainly because more heat is transferred into the bulk from the atmosphere due to the instable flow, which makes the temperature near the top region higher. As a result, the temperature even near the bottom increases because of the conductive-like heat transportation. However, such perturbation has slightly effects on the heat transfer performance, which indicates that the temperature distribution profiles cannot represent the heat transfer process sufficiently. The increase after the critical rotating speed is due to that the perturbation moves further in depth which results in lower average temperature. The critical rotating speed varies with the vertical coordinates due to the evolution of the irregular flow. The reduced temperature at the top region is first influenced, followed by the remaining area sequentially from top to bottom.
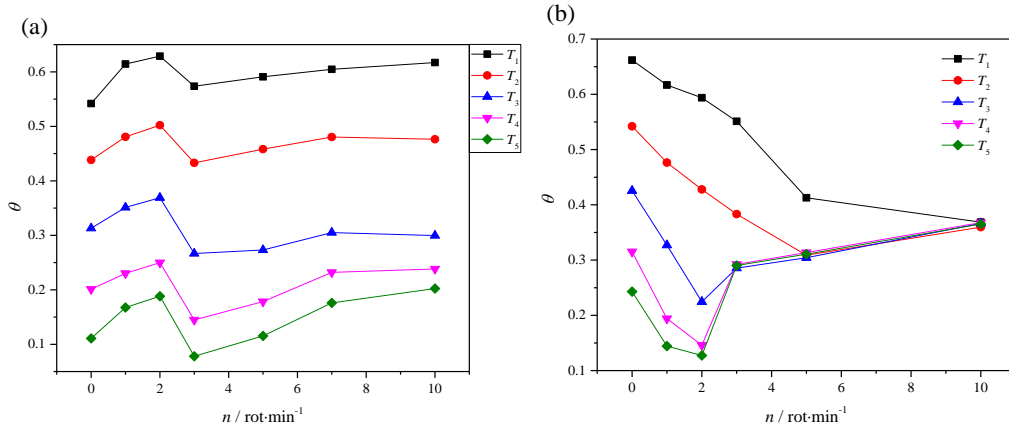
Figure 5.11 The equilibrated reduced temperatures for the sucrose solution and the HPAM solution against with rotating speed, (a) the profiles for sucrose solution; (b) the profiles for polymer solution

Based on the equilibrated temperature gradient, the effective thermal conductivities for sucrose and HPAM solutions as a function of n and Wi are demonstrated in Figure 5.12. Due to the sufficiently small temperature difference at larger rotating speed, the estimated effective thermal conductivity is too large to reasonably compare with that for sucrose solution in laminar state. Therefore, only results at the rotating speed lower than 7 rpm are demonstrated. The Weissenberg number was calculated as $Wi = \lambda \gamma^*$, where λ is the characteristic polymer relaxation time, $\lambda = 1.9(\gamma^*)^{-0.34}$, and the γ^* is the modified average shear rate of the bulk fluid. With a viscosity measurement in the rheometer, the shear stress and viscosity are followed equation:

$$\tau = \eta(\gamma_{av}) \cdot \gamma_{av} \qquad (5.12)$$

In the simplest case of a narrow gap (standard geometry), $d/R \ll 1$, the shear rate along the z direction is almost constant. So the shear rate grows along the radius, from zero at $r = 0$ to the maximal value of $\Omega R/d$ at $r = R$ and the averaged shear rate over the top surface is $2\Omega R/3d$, where the d and R indicates the gap between two parallel disks and the radius of rotating disk, respectively. When the gap is quite wide, for example in our geometry, the shear rate becomes strongly non-homogeneous along z direction and the averaged shear rate is no longer $2\Omega R/3d$ but a several times larger, which is the ratio of measured viscosity in large gap geometry and the standard viscosity in narrow gap geometry at same applied shear rate, as shown in Figure 5.13. It shows that the average shear rate γ^* was proportional to Ω, being $\gamma^* = 7.4\Omega R/d$ in this experimental setup. In this study, the representative shear rate γ^* are modified to give a more accurate definition of Weissenberg number Wi.

Both the experimental and modelling effective thermal conductivity of sucrose solution show independent relationship with rotation speed, indicating that there is no chaotic flow behaviour and the flow remains in laminar regime. The only way for heat being transferred from one layer to another is through conduction at the shear layer, which requires more time. The measured effective thermal conductivity agrees well with the simulation results but a bit larger (0.6 and 0.4 $W \cdot m^{-1} \cdot K^{-1}$, respectively), which is mainly ascribed to the position of probe of thermal couples. Due to the soft thermocouple wire, the distance between each probe might be shorter, which results in a larger effective thermal conductivity. This doesn't influence the comparison of Nu since the average temperature was conducted for the calculation of Nu.

Unlike sucrose solution, the HPAM solution exhibits a steady period at low rotating speed and a rapid rise starting near $n =2$ rpm. This tuning point is a reflection of the onset of elastic instability, where the corresponding critical Weissenberg number $Wi_c = 1.8$. The enhancement of the effective thermal conductivity after the occurrence of elastic instability follows an exponential relationship as a function of Wi. Compared with the sucrose solution, even the rotating speed is quite low at value of 7 rpm, where the $Wi = 4.3$ and $Re = 0.8$, respectively, the enhancement of the thermal conductivity of HPAM solution is 22 times higher. It is also interesting to compare the intensification of the heat transport by elastic turbulence with similar experiments performed with Newtonian fluids at large Re in the regime of inertial turbulence. Indeed, at the largest applied rotating speed, the effective thermal conductivity is reached to as high as 155 $W \cdot K^{-1} \cdot m^{-1}$. The effective thermal diffusivity $D^* = K^*/\rho c$, is obtained as an approximately value of 0.5 $cm^2 \cdot s^{-1}$, which corresponds to the increase observed in Ref (Gollub et al., 1991) at $Re \approx 1500$.
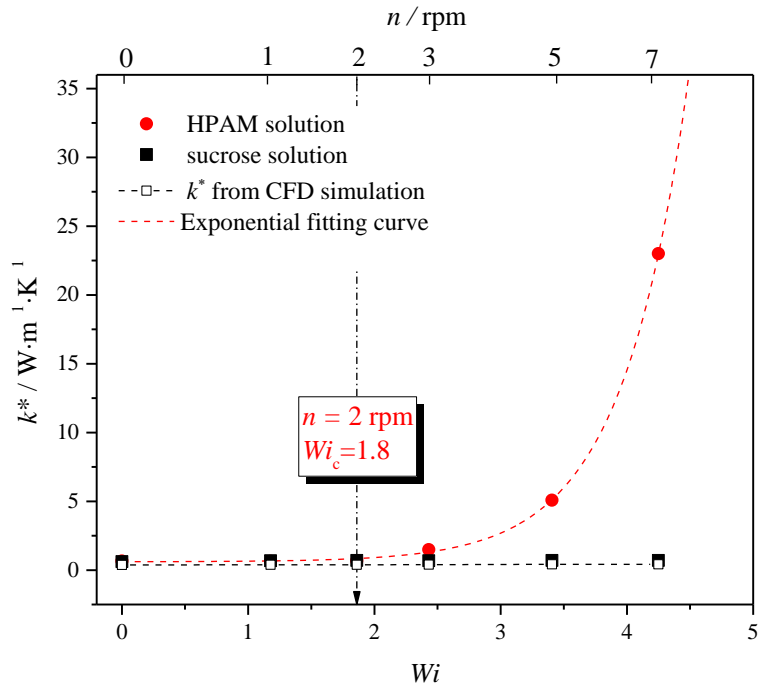
Figure 5.12 Dependence of effective thermal conductivity within bulk fluids on degree of rotation for sucrose solution and HPAM solution
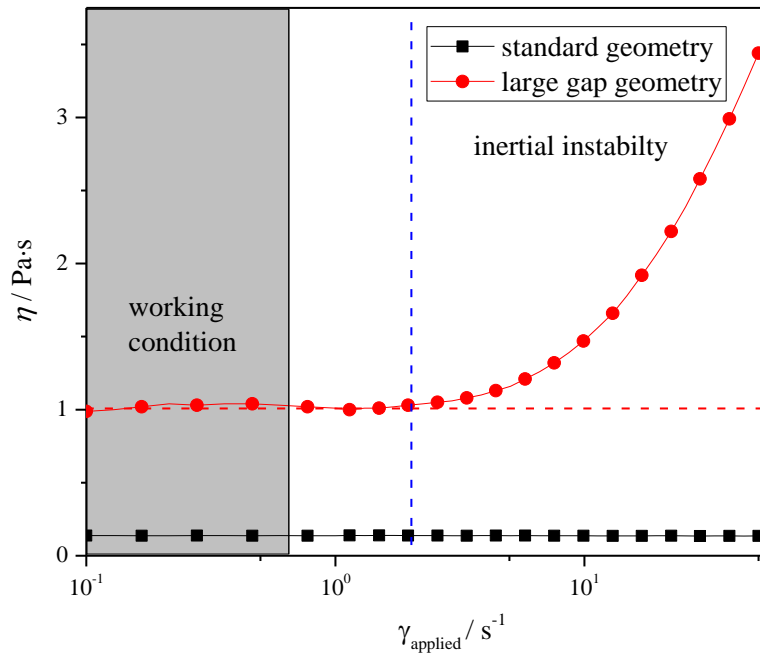
Figure 5.13 The ratio of averaged viscosity in the wide working gaps to the viscosity in a standard geometry

The effective thermal conductivity is sensitive with the temperature gradient within the bulk, which is good for capturing the onset condition of the flow instability but fail to characterize the heat transfer performance when the temperature is fully homogeneous. The convective heat transfer Nu between the bottom wall and the bulk was conducted as shown in Figure 5.14. As

expected, before the elastic instability occurrence, these two fluids exhibit equal heat transfer performance. However, the *Nu* of HPAM solution increases steeply when the rotating speed exceeds the critical value. The flow irregularity moves from one region to another (see from Figure 5.10), carrying energy between regions, improving the heat transfer performance. After the occurrence of the elastic instability, the *Nu* increases linearly with *Wi*, which is consistent with the results from the investigation of Abed et al (Abed et al., 2016), where the surface heat transfer for a 100 ppm polymer solution by as much as 240% and by 380% for a 500 pm polymer solution. Indeed, surface convective heat transfer was enhanced dependently by the nonlinear interaction between elastic normal stresses created within the flowing polymer solution and the streamline curvature of the geometry. In the present study, the intensification of the surface heat transfer could reach to 6 times higher, which is in similar degree of heat transfer enhancement with the results from Abed et al and Copeland et al (Copeland et al., 2017) but still seems to be much lower than the enhancement obtained by Li et al (Li et al., 2017). Indeed, the experiments discussed here were conducted in different working conditions. The experimental rig, polymer rheology and even the analysis method were different. It is hard to draw a standard conclusion that how much degree can the elastic turbulence contribute to the heat transfer intensification theoretically since the effects of polymer rheology on the heat transfer are required. However, one can see that elastic turbulence indeed benefits the convective heat transfer performance.
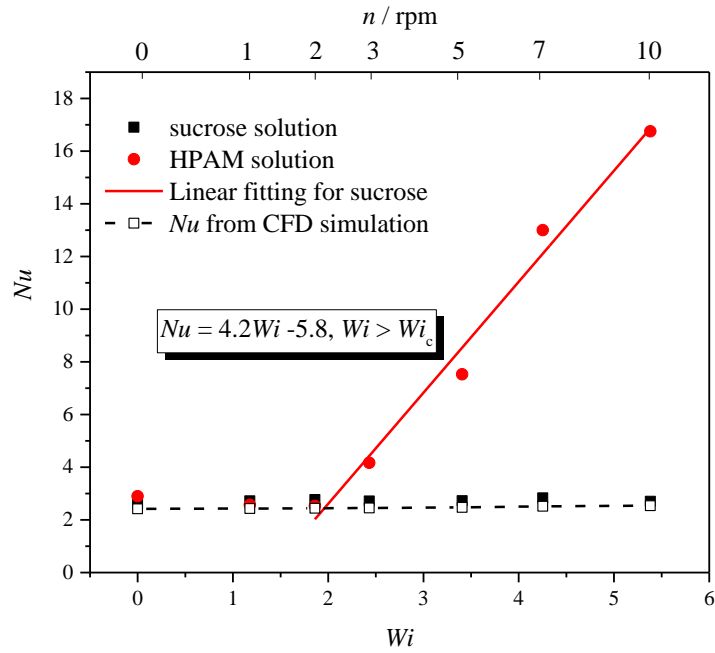
Figure 5.14 Dependence of Nusselt number on degree of rotation for sucrose solution and HPAM solution

5.3.3 Statistical analysis
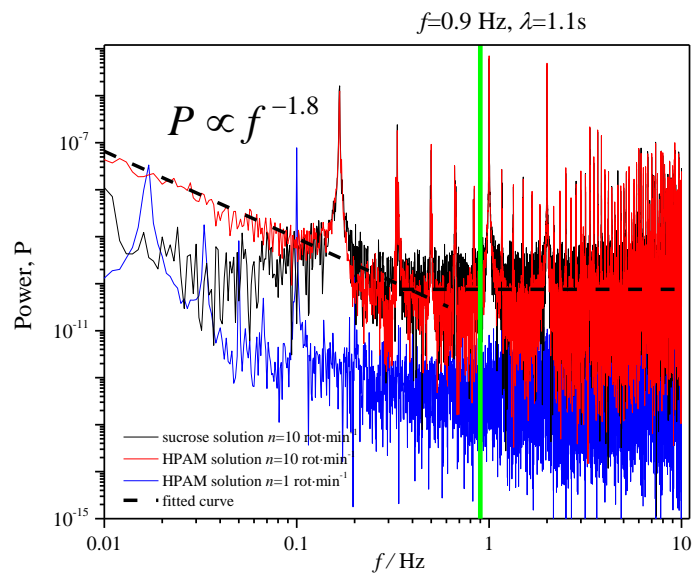
Figure 5.15 Power spectra of angular velocity as a function of frequency with various rotating speed

The sharp heat transfer intensification indicates the existence of elastic instability. However, whether this chaotic flow develops into elastic turbulence regime cannot be concluded yet. From the flow patterns captured from below view, the flow seems on its way to elastic turbulence. A main characteristic feature of the elastic turbulence is the power law spectrum of the angular velocity with the exponent value of -3 to -4.3 (Groisman and Steinberg, 2004;

Jun and Steinberg, 2009). In this work, the statistic properties for angular velocity both for sucrose and HPAM solution are shown in Figure 5.15. There are some instrumental peaks at f for both curves, which are multiples of the average frequencies of the rotating plate, $\Omega/(2\pi)$. In an elastic turbulence regime, the sharp decay of power spectra of angular velocity occurs when $f > f_{vor}$, where f_{vor} is the main vortex frequency and the frequency $1/\lambda$ corresponds to a low-frequency range (flat dependence rather than power law decay was observed). It can be seen from Figure 5.15, there is no clear power-law phenomenon observed after $f=1/\lambda$, which indicates the flow is still not in fully elastic turbulence regime. Such spectra profiles with some distinct peaks and a power-law decay with exponent 1.8 in low frequency domain are quite similar with our previous studies as shown in Figure 4.15. It is possibly a representative spectra for flow in laminar regime or the beginning of the transition to elastic turbulence, which is indeed directly related to the large-scale vertical flow. In fact, the big toroidal vortex driven by the hoop stress is quite well known to appear in swirling flow of viscoelastic fluids (Stokes et al., 2001b) and is the first flow motion above the elastic instability threshold level (Groisman and Steinberg, 2004). What's more it was regarded as the transition to elastic turbulence in the swirling flow between two plates. This is because the toroidal vortex where the liquid and stress tensor imbedded in is chaotically advected and this type of advection can generate variations of stress in a range of smaller scales, which causes small scale fluid motion as a result. As the accumulation of the small-scale motion, the flow transits to the turbulence regime and shows power-law behaviours in high frequency domain, which as described in both our previous works and other's investigations.
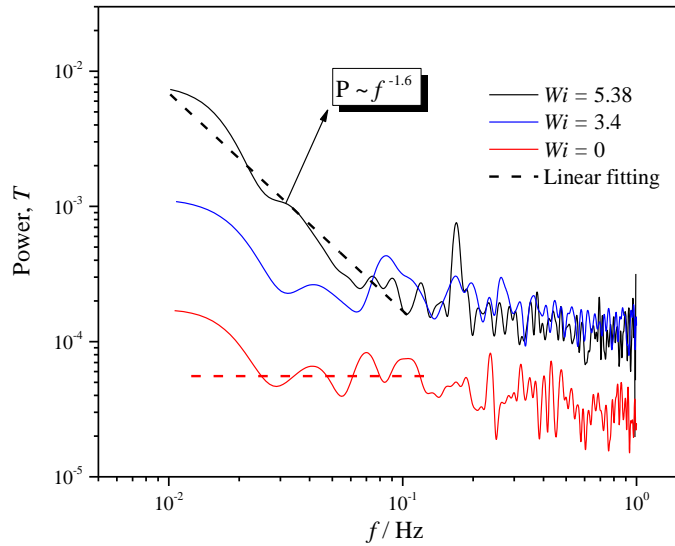
Figure 5.16 Power spectra of reduced temperature as a function of frequency with various rotating speeds

The power spectra of the fluctuations of the reduced temperature are shown in Figure 5.16. A similar power law dependence of the spectra of temperatures is obtained with exponent of 1.6, which is well consistent with the value of 1.1 observed by Traore et al (Traore et al., 2015) and Li et al (Li et al., 2017). It should be noticed that such a power law exponent hasn't been identified as a symbol of elastic turbulence since the geometry, materials used in their experiments were different. As we discussed above, the flow in the maximum applied rotating speed is still in the transition region to elastic turbulence. Therefore, such power law dependence only can indicate the existence of elastic instability. Indeed, one of well-known features of temperature in turbulence regime is the near-exponential probability behaviour. Figure 5.17(a) shows the probability distribution functions of the fluctuations of reduced temperature at T_4 with various rotating speeds. Both curves are fitted well to the Gaussian equation. However, compared to low rotating speed, with increasing the degree of rotation the PDFs appear to be not far from an exponential function since the tails of the curve seems to be linear and more widely, which is consistent well with the discussion mentioned above that the flow stays in the transition regime rather than elastic turbulence regime. The normalised PDFs for all positions of thermocouples performs similar trends at same applied rotating speed are shown in the Figure 5.17(b) and (c). At lower degree of rotation, the flow is quite stable, and the PDF curves collapsed into a single Gaussian curve without any derivations. For higher rotating speed, there are some discrepancies found between each curves, which implies the asymmetric intensity of the flow irregularity. The tails of PDF curves near the

position of T_1 thermocouple are not fitted with Gaussian equation and seems to be more irregular.
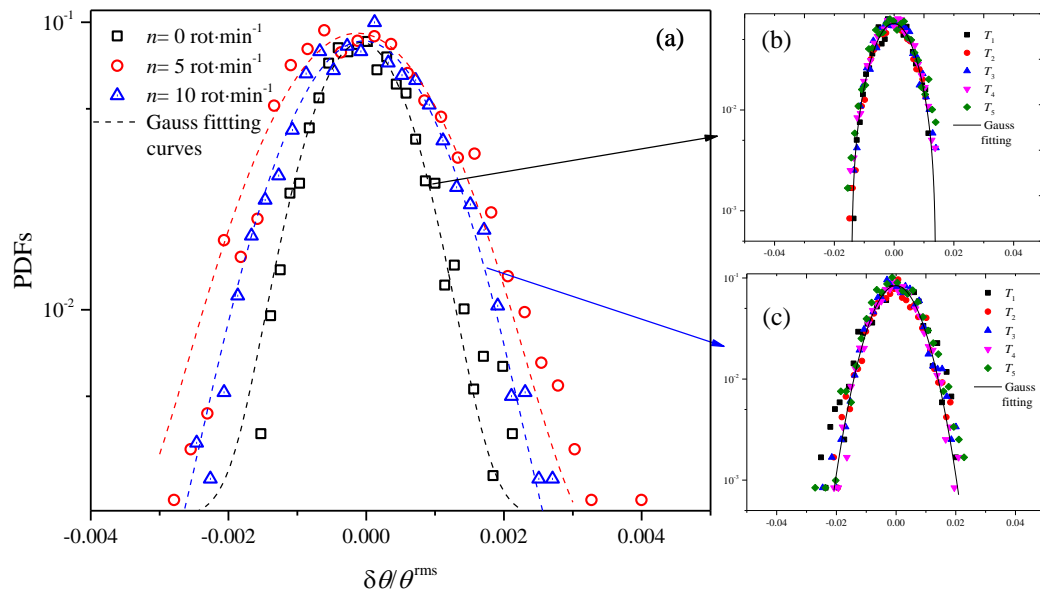
Figure 5.17 (a) PDFs of temperature of HPAM solution at T_4 with various rotating speed. (b) and (c) shows the PDFs of temperature at all thermocouples with $n = 0$ rpm and $n = 10$ rpm, respectively

5.4 mixing performance difference

Besides the heat transfer performance, the presence of elastic instability has shown great potential for the intensification of mass transfer. A droplet of dye inserted into the working fluid before stating the rotation of the upper plate was used to investigate both the mixing performance and flow streamline to provide more detailed interpretation for heat transfer performance. The droplet was made by dissolving dye powders into small amount of the applied working fluid to match the density of the working fluids and was initially placed near the centre at about a half of the fluid depth. The amount of the droplet was about 200 μl. The fluids were viewed from both below and side to catch the flow pattern of the normal and radial direction.

Consecutive snapshots of mixing for both sucrose and HPAM solution at rotating speed of 5 rpm are shown in Fig.18. For sucrose solution, the dye droplet moves upwards first and starts to spread over the surface of the upper plate after around 4 min. It continually diffuses down to the bottom along with the vortical flow motion. Even in the later moments of 20 min, the distribution of the dye remains in homogeneous and a separate layer is observed in the axial direction, indicating an ordered and stationary vortex motion within the

flow. This can be also revealed from the bottom view, where no chaotic streamline presents during the spreading process. Indeed, in a confined cylindrical swirling of Newtonian liquids, the rotation of the lid produces a non-uniform centrifugal force along the base and a secondary flow in the cylinder normal to the primary flow is generated. A so-called Ekman layer acts as a centrifugal pump, driving the fluid outwards along the rotating plate, down the sidewalls and inwards along the stationary bottom surface and finally up the central axis in a spiral motion where it is then sucked back into pump layer again (Stokes et al., 2001a). This Newtonian-like flow phenomenon is consistent well with the motion of the dye droplet and this is why the droplet rises up first at the beginning of the rotation.

In the case of HPAM solution, however, the droplet goes down along the axis as well as spread over the radial direction. Even at the early stage of the rotation, one can see many scale structures, which is due to the significant stretching of fluid elements along their Lagrangian trajectories by large scale eddies as mentioned above. Due to the presence of normal stresses, the polymer solution experiences a force directly radially inwards along the disk, opposing centrifugal effects, producing an inverse secondary flow pattern compared to the sucrose solution (Stokes et al., 2001b). Unlike the regular flow motion within the sucrose solution, the dye moves quite randomly because of the large spiral instability. In addition, in the snapshots taken at later moments in time 20 min, strong chaotic streamline curves are observed from the bottom view and the colour intensity becomes lighter as shown in the side view, which both indicate the HPAM solution behaves better mixing performance.

There is a clear layer near the position of thermocouple T_4 as marked in the snapshot at 14 min, in the vicinity of which the density of dye is more intensively and below which an ordered flow pattern is observed. This is consistent well with the temperature distribution discussed above. At the rotating speed 5 rpm, the temperature distribution between T_2 and T_5 is uniform while a temperature gap still exists between T_1 and T_2.
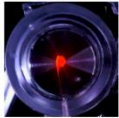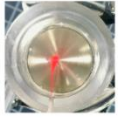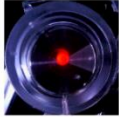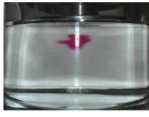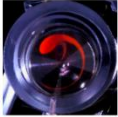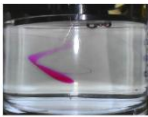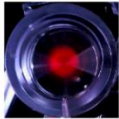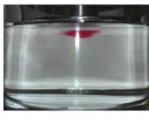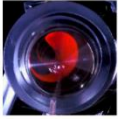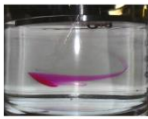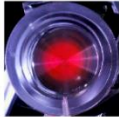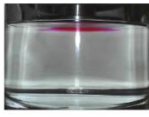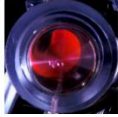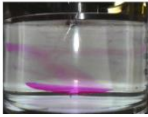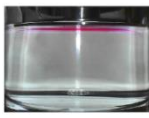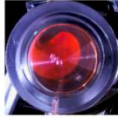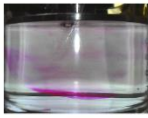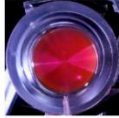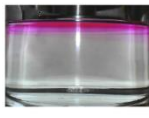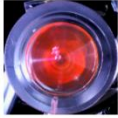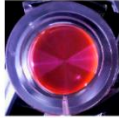
Figure 5.18 Consecutive snapshots of mixing for both sucrose and HPAM solution at rotating speed of 5 rpm

The snapshots of mixing for both sucrose and HPAM solution at equilibrated state with different degree of rotation are listed in Fig. 19. The equilibrated state is defined according to the time when the flow patterns observed is no longer changing. With increasing the rotating speed, the mixing performance of both working fluids are improved. In terms of sucrose solution, an obvious vortex is formed in the centre as the degree of rotation increases. This stationary vortex was mainly attributed to the surrounding laminar flow and no mixing process is observed in the core of the vortex. Indeed, the motion of the vortex is extremely slow. There is no significant transportation behaviour of dye can be visualised after the flow patterns are equilibrated. In addition, it is still easy to identity the laminar streamlines in the mixing area. Therefore, even at highest applied rotating speed, the sucrose solution is still flowing in layers and there is no interlayer motion. The only way for heat to transfer from one layer to another is through conduction at the shear layer, which requires more

time. These layered phenomena are also validated by the numerical simulation results as shown in Figure B.4.

On the other hand, for HPAM solution, a similar vortex as performed in snapshot of the sucrose solution has been formed in low rotating speed 3 rpm. However, the motion of this vortex accompanied by a dramatic dye transportation is highly intensive, and breaks the flow layers in the axial direction, moving fluids from one region to another, carrying energy between regions and distributing packets of it among neighbouring particles. Such process intensifies the heat and mass transfer in this work and results in a uniform temperature distribution as discussed in previous section. It is should be noticed that the positions of the boundary of the mixing area are consistent well with the temperature distribution results in all cases. Continually increasing the degree of rotation, the vortex evolves from large scale to small scale and the vortical instability strengthens, which leads to the enhancement of the mixing performance and the degree of the irregularity for flow streamline. This transition also indicates that the flow has not fully developed into elastic turbulence regime but just stays in the transition stage as concluded above.
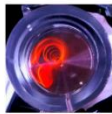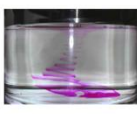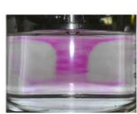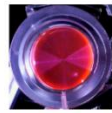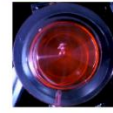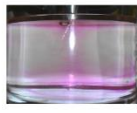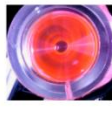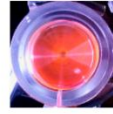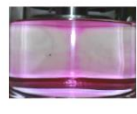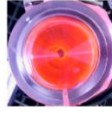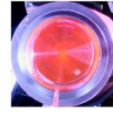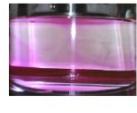
Figure 5.19 The snapshots of mixing for both sucrose and HPAM solution at equilibrated state with different degree of rotation

5.5 Effects of polymer rheology on the heat transfer enhancement

5.5.1 Effects of polymer concentration

The equilibrated reduced temperatures along the vertical direction as a function of rotating speed with different polymer concentration are shown in Figure 5.18. Without rotation, the temperature distribution along the vertical direction of all solutions are in layers and the temperature difference between neighbouring thermocouples are almost similar. With the degree of rotation of the top disk increasing, for polymer solutions, the temperature distribution gradually tends to be homogeneous, which indicates the existence of the flow instability. This flow instability is mainly attributed to the elastic stress rather than viscous stress due to there is no collapsing phenomenon observed in sucrose solution. Especially, when the polymer concentration is higher, the elastic flow instability becomes more intensively. With same applied rotating speed, more bulk regions are perturbed and at lower swirling velocity, the more concentrated polymer solution is fully chaotic.
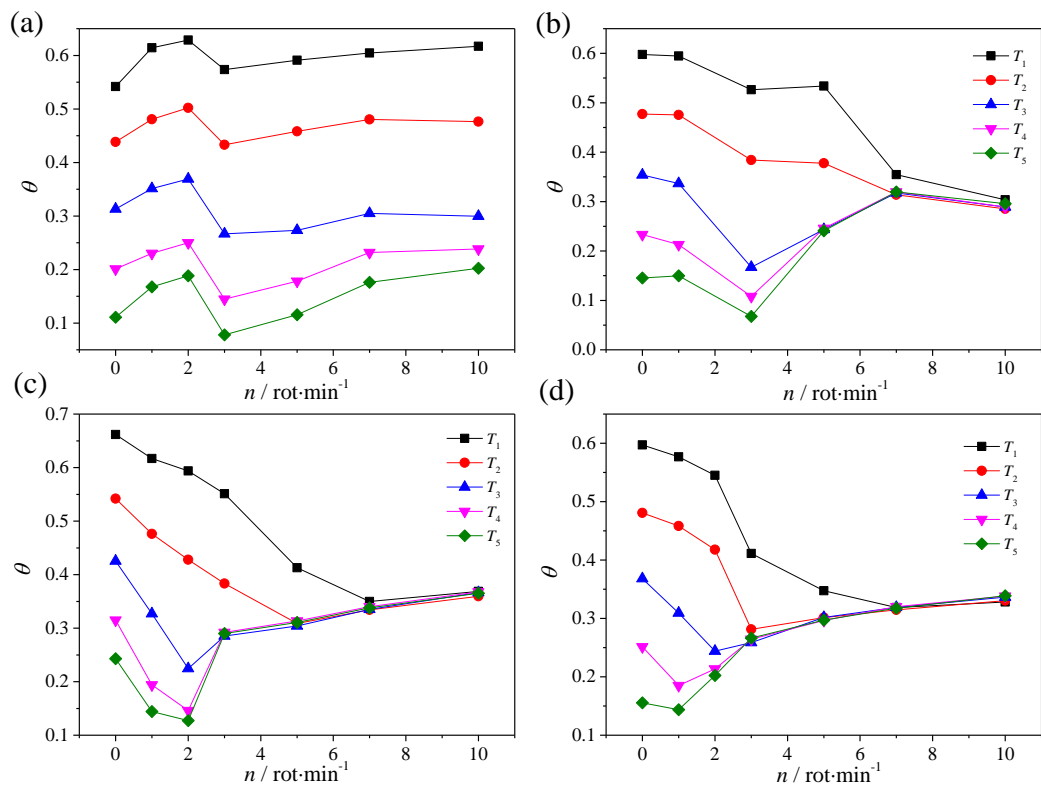
Figure 5.20 Equilibrated reduced temperature profiles for different polymer concentration: (a) pure sucrose solution, (b) 100 ppm HPAM sucrose solution, (c) 200 ppm HPAM sucrose solution, (d) 300 ppm HPAM sucrose solution

Figure 5.19(a) shows the effective thermal conductivity as a function of rotating speed with different polymer concentration. The variations of the effective thermal conductivity applied here are also regarded as a signal to characterize the onset of elastic instability. It is clear found that polymer solution with higher concentration is much easily to induce elastic instability. The critical rotating speed to induce elastic instability is estimated varying from 4.2 rpm to 1 rpm when the polymer concentration increases from 100 ppm to 300 ppm, respectively. The corresponding critical Wi_c numbers is also reduced, which is consistent well the previous results in Ref . Indeed, the elastic instability is highly dependent on geometry gap ratio, d/R, polymer contribution to viscosity, η_p/η, and degree of stretching of the polymers by the base flow, Wi. With the shear thinning phenomenon is probably considered, the elastic instability threshold could be determined by a parameter K, defined as:

$$K \sim \frac{\eta_p}{\eta} \frac{d}{R} Wi^2 \qquad (5.13)$$

The elastic instability then occurs when K exceeds a certain threshold. The polymer contribution to the viscosity is more significant with the increase of polymer concentration. Therefore, when the gap ratio is fixed, the Wi at the instability threshold should depend on it as $Wi_c \sim (\eta_p/\eta)^{-0.5}$, which results in the reduction of Wi_c. In the present work, the relationship between estimated Wi_c from the Figure 5.19(b) and η_p/η from Figure 5.3(a) is demonstrated in Figure 5.20, where the dependence can be well fitted by the power law $Wi \sim (\eta_p/\eta)^{-\alpha}$, with the exponent α=0.6, which is quite close to the expected value of 0.5.
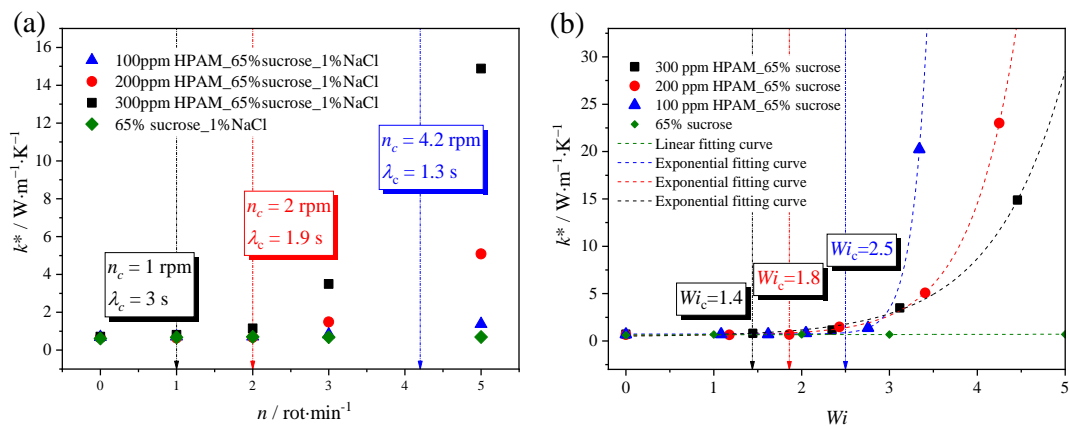
Figure 5.21 Effects of polymer concentration on the effective thermal conductivity (a) as a function of rotating speed and (b) as a function of Wi
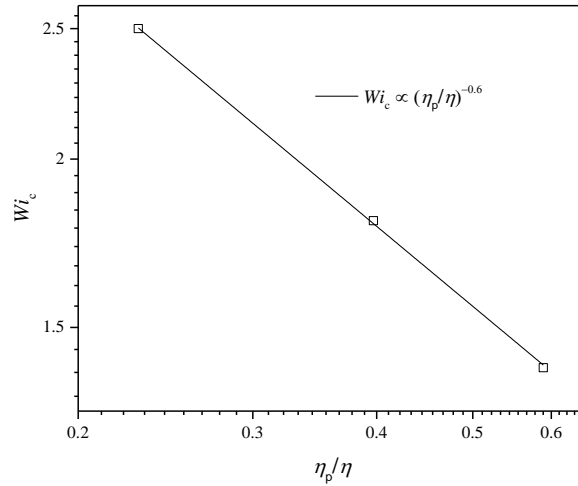
Figure 5.22 The generalized Wi_c number as a function of η_p/η at the onset of elastic instability from concentration series of experiments

For all polymer solutions after the occurrence of elastic instability, a remarkable rise of k^* appears. For a given swirling flow, the polymer solution with higher concentration exhibits better heat transfer performance within the bulk, indicates that the degree of flow irregularity intensifies as the polymer concentration increases, which results in more heat is transferred between flow layers. The enhancement of effective thermal conductivity for the 300 ppm polymer solution could reach to 23 times larger than that of sucrose solution, which is even higher than the enhancement of inertial turbulence of a Newtonian fluid in swirling flow at Re=2500 (Gollub et al., 1991), where 10 times incremental was obtained.
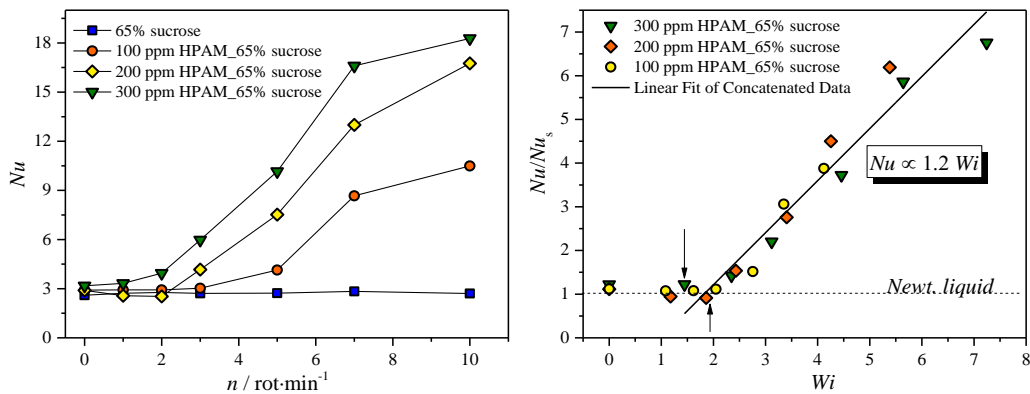
Figure 5.23 Effects of polymer concentration on the convective heat transfer performance (a) as a function of rotating speed and (b) as a function of Wi

Figure 5.21 demonstrates the Nu between wall and fluid against degree of rotation with different polymer solutions. For a given rotating speed, as shown in Figure 5.21(a), similar trends are observed with effective thermal

conductivity. The *Nu* increases with increasing the polymer concentration. When n=10 rpm, the convective heat transfer of 300 ppm HPAM solution can reach to 6 times more efficiency than that of sucrose solutions, which is in same orders with previous studies (Traore et al., 2015; Abed et al., 2016; Copeland et al., 2017). The small discrepancy is ascribed to the polymer properties and streamline curvature of the geometry. The reason for the dependence of polymer concentration on the convective heat transfer is that when the swirling velocity is fixed, the *Wi* of the higher concentration HPAM solution is larger than that of polymer solution with lower concentration due to its longer relaxation time. Therefore, more elastic nonlinearity is generated, which leads to stronger instability in the flow and enhances the heat transfer more significantly.

This dependence becomes different when the *k** and *Nu* are demonstrated as a function of *Wi*, where the polymer relaxation discrepancy is included. The polymer solution with higher concentration still shows slight heat transfer enhancement before the elastic instability is induced in lower concentration polymer solution. Continually increase *Wi*, when all solutions are instable, a steep enhancement in heat transfer is observed for all polymer solutions with the *Nu* collapsing into a single curves by $Nu \propto 1.2 Wi$, which is consistent well with the observations form Ref.(Abed et al., 2016). Indeed, the elastic turbulence is highly related to rheology of the base fluid. In dilute polymer solutions, due to the presence of the high salt concentrations, the shear thinning phenomenon is not such dramatic. Therefore, when the stretching degree of polymer solution (characterised by *Wi*) is in same level, the intensity of elastic turbulence should be similar, and the concomitant heat transfer enhancement shows similar behaviours. However, it should be mentioned that the saturation of fully developed elastic turbulence is limited by the polymer concentration. The more numbers of polymer contributes to the stronger flow intensifications, which also implies that the experiments conducted here, the flow is still in transition regime and on its way to fully developed elastic turbulence.

5.5.2 Effects of salinity

In this section, the effects of salinity on the heat transfer performance are investigated. Figure 5.22 demonstrates the equilibrated reduced temperature distribution varies rotating speed with different salinity. Increasing the degree of salinity makes the temperature distribution curves more difficult to converge. Especially, when the salinity is 0.5 %, even at the maximum applied rotating velocity, the temperature distribution is still in layers, which indicates

the increase of salinity weakens and postpones the onset of elastic instability. The salinity effect on the onset of elastic instability is estimated for the Figure 5.25. The polymer solution with lower salinity is capable of inducing elastic instability at relatively smaller rotating velocity, thereby perturbing the flow and intensifying the heat transfer within the bulk. While increasing the salinity, more driven forces and higher rotating velocity are required to trigger the flow instability. The critical Wi_c on the onset of elastic instability shows similar trends with the rotating velocity though the concomitant relaxation time is reduced. As discussed above, the onset of elastic instability is highly dependent on the polymer contribution to the viscosity and the critical Wi_c. In the presence of salt cations, due to the shielding effects, the conformation of polymer tends to coil state rather than elongated form, which results in the reduction of the polymer contribution to the viscosity. As a result, the critical Wi_c on the onset of elastic instability increases. The dependence of estimated Wic from the Figure 5.25 on the η_p/η is shown in the Figure 5.26. The results can still be fitted with power law $Wi \sim (\eta_p/\eta)^{-\alpha}$. However, rather than expected value of 0.5, the exponent α goes higher to 0.95, which is consistent with our previous investigations. Such discrepancies are possibly ascribed to the various configuration of polymer due to the shielding effects. In terms of the polymer solution with high salinity, the polymer molecules are in coils and additional force is required to stretch the polymer to elongation state.
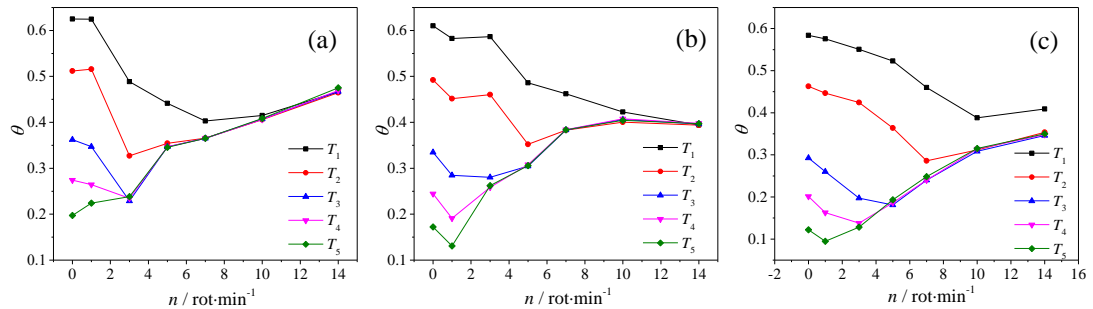
Figure 5.24 Equilibrated reduced temperature profiles for different salt concentration: (a) 200 ppm HPAM solution without salt; (b) 200 ppm HPAM solution with 0.1% NaCl; (c) 200 ppm HPAM solution with 0.5% NaCl

The effects of salinity on the effective thermal conductivity and convective Nusselt number are displayed in Figure 5.25 and Figure 5.27, respectively, both of which are improved after the occurrence of elastic instability. With same rotating velocity, the polymer solution with lower salinity exhibits better heat transfer performance which is mainly because the polymer relaxation time reduction by shielding effect decrease the elastic nonlinearity. However, this trend is different when the degree of the rotation exceeds a certain value,

here n=10 rpm in this study, similar Nu values which are approximately 6 time higher than sucrose solution are obtained for all working fluids and such heat transfer performance seems to be independent on salinity. A possible reason can be ascribed to the similar polymer concentration for all the working fluids after all. Although the presence of the salt changes the onset conditions of the elastic instability of the polymer solution, it exerts slight effects on the irregularity of the primary flow at high swirling velocity. The shielding effect at such conditions is too weak to be efficient. This also can be implied from the viscosity profiles in Figure 5.4(a), where the variations of viscosity due to the presence of salt become undramatic at high shear rate. Particularly, the Nu of the polymer solution with 0.5 % NaCl is smaller than that of other solutions with lower salinity, which is mainly because the elastic instability has not fully evaluated across the whole bulk fluid.
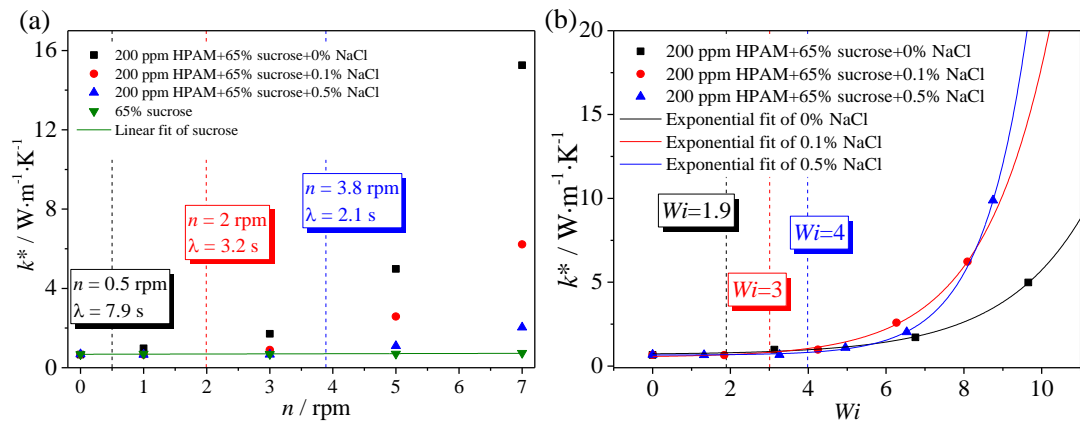
Figure 5.25 Effects of degree of salinity on the effective thermal conductivity (a) as a function of rotating speed and (b) as a function of Wi
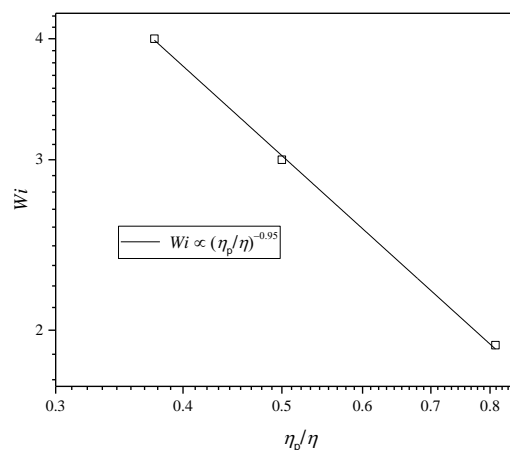
Figure 5.26 The generalized Wi_c number as a function of η_p/η at the onset of elastic instability from salinity effects series of experiments

It also should be noticed that the heat transfer enhancement after the occurrence of elastic instability for lower salinity seems to be more rapid,

which also can imply the inefficient effects of shielding effect at high swirling velocity. Indeed, the onset of elastic instability is suppressed by the shielding effect of cations. The more amounts of cations are, before the critical value based on the limitation of carboxylate groups are reached, the stronger the shielding forces are, and the more difficult for polymer solution to be perturbed. However, if the shielding effect is overcome by the additional driven force (increasing rotation speed), the elastic instability is induced, and the concomitant heat transfer performance is enhanced. Due to the weak shielding effect, such enhancement is rapid and gradually gets close to the solution even without salt addition.
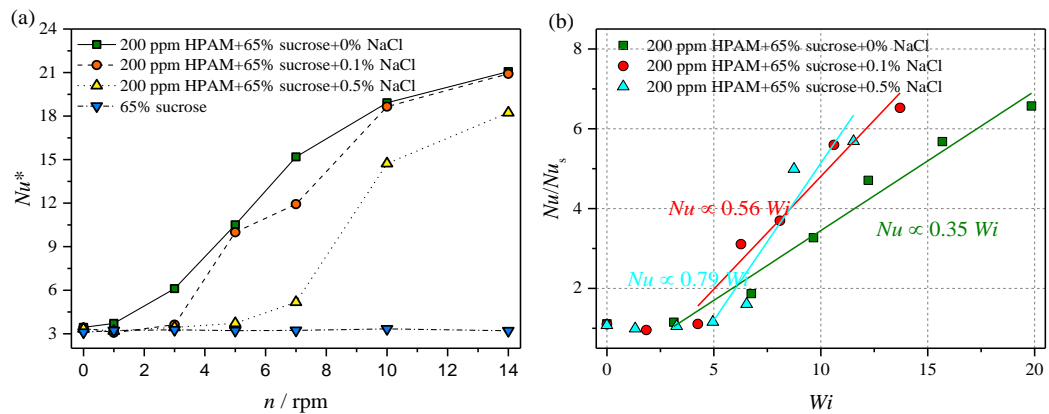
Figure 5.27 Effects of degree of salinity on the convective heat transfer performance (a) as a function of rotating speed and (b) as a function of *Wi*

The variations of k^* and Nu^* as a function of Wi are presented in Figure 5.25(b) and Figure 5.27(b), respectively. The results are indicating that the Nu is a function of both Wi and the degree of shear-thinning of the fluids. Unlike the discussion for the effects of polymer concentration, the increase of Nu as a function of Wi is no longer concreated into a single curve but is highly dependent on the shear-thinning degree. The significant shear-thinning phenomenon suppresses the evolution of Nu as the polymer solution without salt presence indicates. In fact, recent studies have demonstrated a stabilizing effects by shear thinning, where the high shear thinning will leads to an increase of the critical Weissenberg number. Such trend cannot captured by the scaling argument for the instability criterion and thereby the exact mechanism of the elastic flow instability is still unclear. One of the proposed explanation for this is that the shear rate inside the flow is significant non-uniform and this gradient of shear force could balance with stretch of polymer to somehow, which, as a result, the flow becomes stable and exhibits less

heat transfer enhancement. The effects of shear thinning is quite complicated and further investigations are required to reveal the mechanism.

5.5.3 Effects of solvent concentration
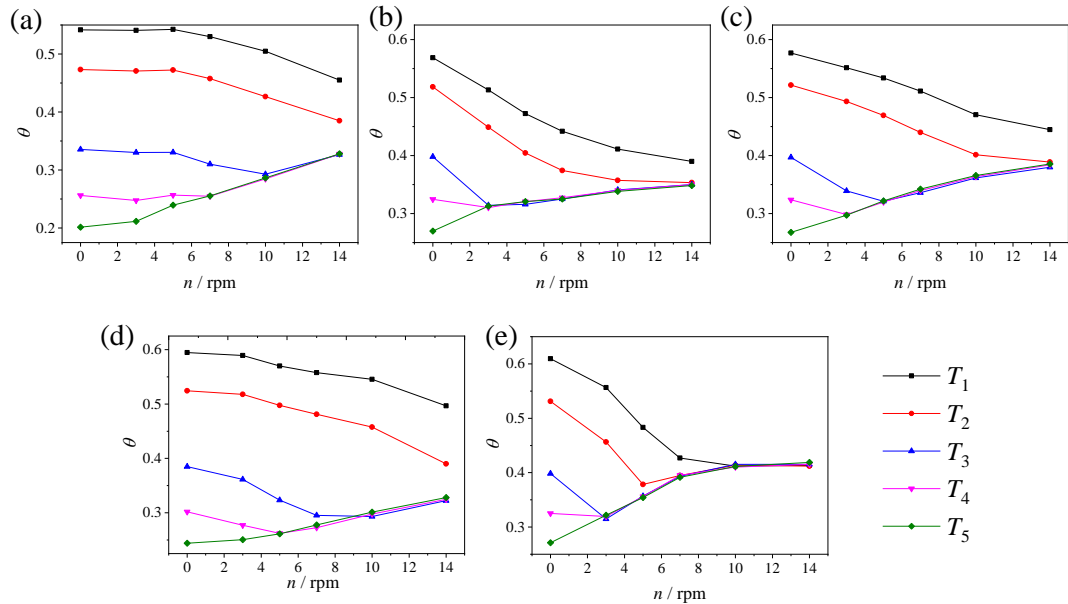
Figure 5.28 Equilibrated reduced temperature profiles for different amounts of sucrose addition: (a) pure water (b) 200 ppm HPAM solution without sucrose; (c) 200 ppm HPAM solution with 20% sucrose; (d) 200 ppm HPAM solution with 40% sucrose; (e) 200 ppm HPAM solution with 65% sucrose

The solvent effects were conducted in this section by varying the proportion of the sucrose to the polymer solution. The reduction of sucrose is expected to decrease the viscosity of the polymer solution and to weaken the polymer relaxation capacity, which leads to a higher *Re* and a lower *Wi* when the shear rate is fixed. On one hand, the increase of *Re* intensifies the inertial effect and makes the flow more instable. On the other hand, the highly reduction of the polymer relaxation time is less capable to induce the elastic instability. The temperature distribution and the heat transfer performance under same working conditions for pure water were presented in Figure 5.28 and Figure 5.30, respectively. Compared with those of 65% sucrose solution, a clear enhancement of *Nu* is observed, which indicates the inertial instability has already occurs. Therefore, by changing the proportion of sucrose, the flow instability is not solely driven by the elastic stress. A so called inertial-elastic instability should be considered in such conditions. Based on the variations of Nu for water solution, the inertial effects could be neglected below *n*=7 rpm.

Figure 5.28 also demonstrates the reduced temperature distribution of polymer solutions with different sucrose concentrations. The temperature

curves of polymer solutions without sucrose and with 65% sucrose additive are first collapsing, sequentially followed by polymer solutions with 20% sucrose and 40% sucrose, respectively, which indicates that the onset of flow instability is first postponed by increase the suction concentration and continually increasing will make the flow instability more easily induced. This could also be implied from the heat transfer performance in Figure 5.30(b). As discussed above, the inertial instability at n < 7pm can be neglected. Therefore, such flow instability is mainly ascribed to elastic instability. The effects of addition of sucrose on the rheological properties of polymer solution is complicated. In the first place, the polymer contribution to the viscosity decreases with increasing the sucrose concentration as shown in Figure 5.29, which indicates a relatively smaller critical Wi_c is required to trigger the elastic instability. When the shear rate is fixed, the polymer solution with short polymer relaxation time is capable of triggering the elastic instability. For another, the addition of sucrose enhances the polymer elasticity and concomitant polymer relaxation time becomes larger. Whether the elastic instability is induced is dependent on the combination of these two effects. Obviously, in this study, when the sucrose concentration has not reach as high as 65 %, the polymer contribution to the viscosity is dominant, which makes the polymer solution with lower sucrose concentration is more easily to induce the elastic instability. However, when the sucrose concentration saturates at 65 %, the significant increase of the polymer relaxation time makes the polymer solution even at low shear rate become instable.
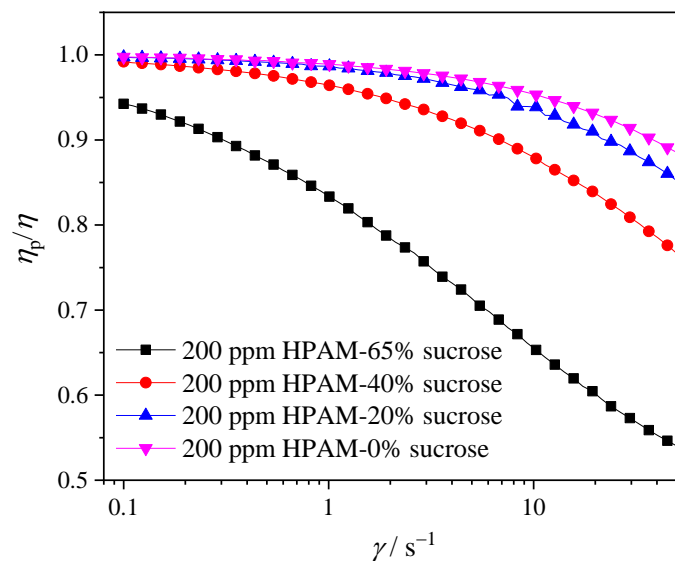
Figure 5.29 The variations of polymer contribution to the viscosity with different sucrose addition

The effective thermal conductivity and convective Nu as a function of rotating speed is demonstrated in Figure 5.30. The polymer solutions which are first perturbed exhibit better heat transfer performance before others are instable. It is interesting that after the occurrence of flow instability, the heat transfer enhancement of the polymer solutions with 65 % sucrose is most significant, followed by 20%, 0% and 40%, respectively. Theoretically, with the increase of the sucrose concentration, the intensity of the flow irregularity increases. However, it can be seen from the heat transfer performance from pure water solution, an inertial instability exists. Therefore, the heat transfer enhancement is not sole driven by the elastic instability and it should be influenced by the coupling effects between inertial and elastic nonlinearity. Compared with the pure HPAM solution, the HPAM solution with 20% sucrose can generate more intensively elastic irregularity due to the improvement of the polymer relaxation time, and the corresponding heat transfer performance increases. Continually increasing the sucrose concentration to 40%, the polymer elasticity does not change significantly, while the Re, as shown in Figure 5.31(a), decreases rapidly which weakens the inertial instability and makes the heat transfer performance of the polymer solution with 40% sucrose even worse than pure HPAM solution without sucrose addition. Indeed, the elasticity numbers, El, of the polymer solutions with 20% and 40% sucrose are similar as shown in Figure 5.31(c). The elasticity number represents the relative importance of elastic stress to inertial effect, $El=Wi/Re$. With same El, the flow tends to small-scale vortex at high Re but large-scale at low Re. This small-scale vortex is much closer to the turbulent-like behaviours and results in a more significant enhancement of heat transfer (Varshney and Steinberg, 2018). When the sucrose concentration reaches to 65%, though the inertial nonlinearity does not exist anymore, the strong elastic nonlinearity perturbs the flow and enhance the heat transfer consequently. It also reveals that the heat transfer enhancement based on elastic instability at low flow rate is more dramatical than that based on inertial instability. Due to the low flow velocity, the inertial instability is far from the turbulence region thereby the degree of flow irregularity is not strong enough. In other words, the elastic instability or elastic turbulence does a promising method for heat transfer intensification at low Re conditions.
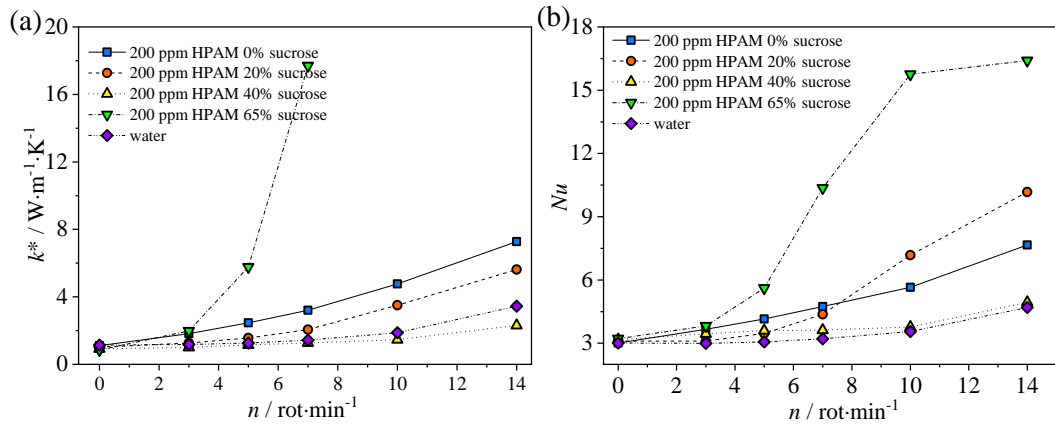
Figure 5.30 Effects of sucrose concentration on (a) effective thermal conductivity and (b) convective Nusselt number as a function of rotating speed.
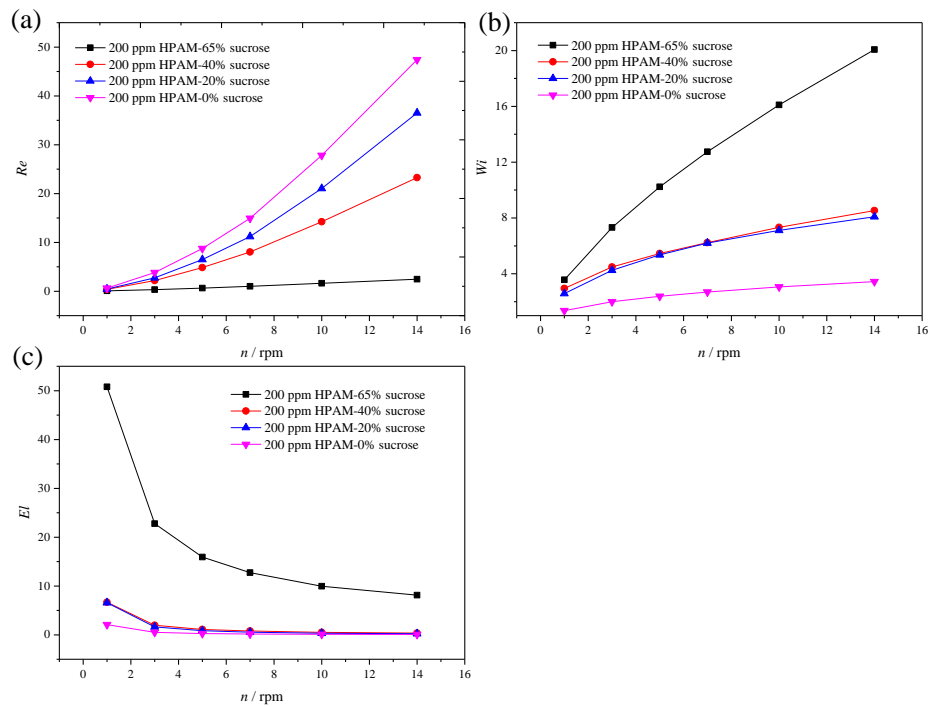
Figure 5.31 Variations of (a) Reynold number, (b) Weissenberg number, and (c) Elasticity number as a function of rotating speed with different sucrose concentration

It is also should be noticed that the profiles of the effective thermal conductivity and convective Nu show different trends especially for polymer solutions with 20% and 40% sucrose. The effective thermal conductivity is dependent on the temperature distribution, which is highly sensitive with the onset of flow instability. It cannot reveal the amounts of heat removal from the wall, which is ascribed to the intensity of flow irregularity. Therefore, both the effective thermal conductivity and convective surface Nu are required to investigate the heat transfer performance within the bulk and between wall and liquid. In

addition, the thermal conductivity of working fluids is different. The thermal conductivity decreases with increasing the sucrose concentration and such reduction declines the effective thermal conductivity as well. However, this discrepancy is delimited when calculates the *Nu* due to its definition.

5.6 Conclusion

The convective heat transfer performance of viscoelastic fluids in a swirling flow between two parallel plates with excitation of pure elastic flow instability was conducted. The effects of polymer rheology on the degree of enhancement of heat transfer were also revealed. Based on the experimental results discussed above, the following conclusion can be drawn.

1. Before the occurrence of elastic instability, the HPAM solution exhibits similar heat transfer performance with that of sucrose. The temperature distribution inside the bulk shows clear layered profile. The *Nu* and *k* are almost independent on the rotation speed. Even at the maximum applied rotating speed, the heat transfer process of sucrose solution is still conduction-like. However, with continually increasing the rotation speed, the elastic instability is induced for the HPAM solution, and irregular flow intensifies the heat transfer coefficient both within bulk fluid and between the wall and the fluid, which makes the temperature distribution become homogenous.

2. The corresponding flow behaviours show similar results. No chaotic irregular flow patterns are observed for the pure sucrose solution whereas a vortical-like flow motion is revealed in the polymer solution. Such spiral-like flow behaviour, consistent with statistical analysis of temperature and angular velocity, indicates that the flow is still in the transition stage to elastic turbulence. The power-law exponent 1.8 at low frequency domain is possible due to the large scale vortex induced by the onset of elastic instability.

3. With increase of polymer concentration and reduction of the salinity, the onset of elastic instability shifts to an earlier critical swirling velocity and Weissenberg number. The heat transfer enhancement begins after the occurrence of elastic instability.

4. For a given swirling velocity, the enhancement increases with increasing polymer concentration. The maximum enhancement is dependent on polymer concentration. For polymer solution with 300 ppm the convective Nusselt number could reach more than 6 time higher than that of pure sucrose solution at the maximum rotating

speed. After the occurrence of the elastic instability, the heat transfer enhancement exhibits linear relationship on Wi, i.e., $Nu/Nu_s \propto 1.2Wi$, which is independent on polymer concentration. This independence is attributed to the small discrepancies of shear-thinning in the dilute regime.

5. At low rotating speeds, the heat transfer enhancement increases with the reduction of the salinity for a giving swirling velocity. However the enhancement becomes independent on the salinity when the swirling velocity exceeds a critical value, which is possibly due to the reduction of the shielding effect. It becomes clear that the salinity influences the onset of elastic instability, but the maximum enhancement is limited by the polymer concentration. In addition, due to the significant discrepancies of shear-thinning, the Nu dependence on Wi varies with different salinities. The polymer solution with low salinity shows more dramatic shear-thinning phenomenon, suppressing the increase of the heat transfer enhancement.

6. The effects of variations of solvent concentration on the enhancement is complicated due to the coupling effects between the inertial and elastic nonlinearity. However, it is clear that the enhancement based on pure elastic instability is dramatic and promising at low Reynolds numbers.

Chapter 6
Molecular dynamics simulation for polymer conformation under external electric force field

6.1 Introduction

It is clear from the previous chapter that the ions interaction shows significant effects on the onset condition of elastic turbulence. The polymer solution with low salinity, for a given polymer concentration, induces the elastic instability at a lower flow velocity, which ensures that the flow can exhibit the elastic chaotic flow in a smaller Reynolds number comparing to the polymer solution with high salinity. It will be an advantage if the ions effect could be controlled to remove the shielding effects on polymer conformation. Aiming to such motivation, this chapter investigate the possibility of using electric field to achieve the shielding effects. MD simulation is performed to as a feasibility study to achieve the control of ions motion by electric forcefield. The concomitant radius of gyration of polymer and relative radius distribution functions (RDFs) are demonstrated and discussed, which indicates the potential of using external electric forcefield to control the polymer conformation and thereby change the viscosity of polymer solution, modifying the onset condition of elastic instability.

6.2 Models and simulation details

6.2.1 Models construction

The initial configuration is shown in Figure 6.1. It consists of a $5\times5\times5$ nm^3 water box solvated with 0.66 M NaCl and a single atactic HPAM chain. The HPAM chain is similar with the one used in the Chapter two. Two Pt walls are placed just attached to the top and the bottom of the water box. The Material studio software was conducted to build the 20 monomers HPAM chain and the Packmol packaged was used to combine the salt, polymer, water, and Pt wall together. The effects of external electric force field were investigated by applying negative charge on both walls. Three different charge density were considered, which are -0.25 C/m^2, -0.5 C/m^2 and -0.75 C/m^2, respectively. The system was first relax by 80 ns without ant charge adopted on the wall and then with different charge density applied, the effects of external electric force field and the charge density can be studied. The concomitant potential of active control of elastic turbulence could be estimated based on the simulation results.
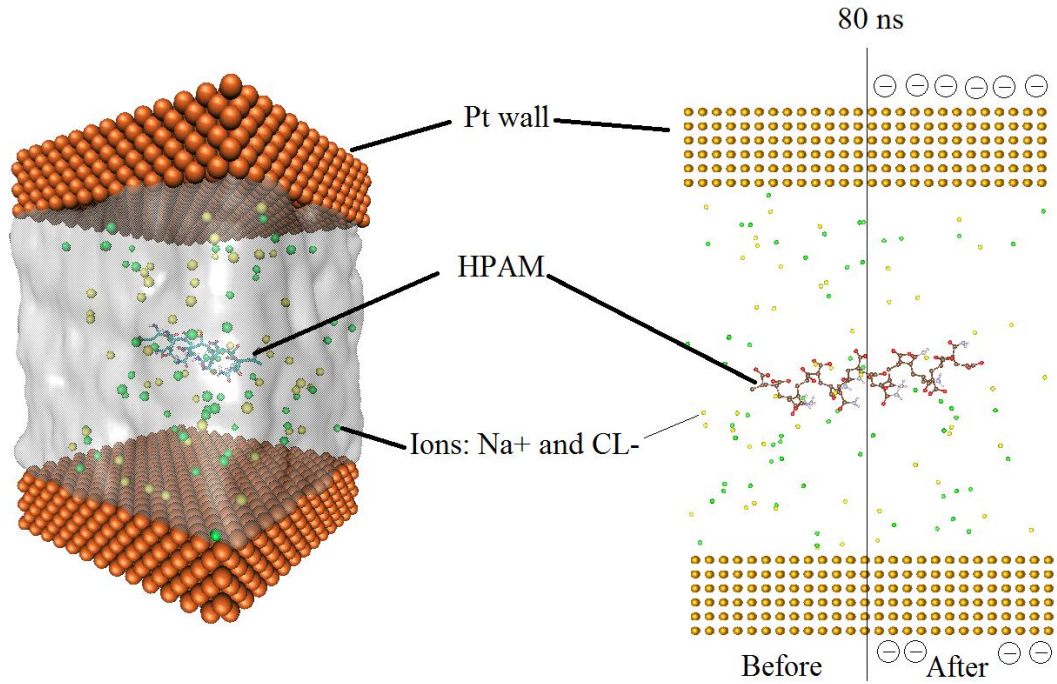
Figure 6.1 Initial structure of the system and the way for external electric force field applied

6.2.2 Simulation details

All MD simulations were conducted by GROMACS simulation package (version of 2019.03) (Hess et al., 2008). The Gromos 53a6 force field parameters (Oostenbrink et al., 2004) were used to describe the properties of PAA chains, Na$^+$ and Cl$^-$ ions, including the potential of bonds, angles, dihedrals and non-bond interactions, which successfully describes this kind of system based on the simulations work in Chapter 3. The aliphatic carbon atoms with its bonded hydrogen in PAA chain were regarded as united atoms to speed up the calculations, and the Rychaert-Bellemans (RB) potential was used for the descriptions of aliphatic torsion (CH$_2$-CH$_1$-CH$_2$-CH$_1$). The simple point charge (SPC) model was conducted to characterise water molecules. The force field parameters for Pt electrode were obtained from Ref (Zhang et al.), where the interaction between Pt and HPAM was set to zero to avoid the attraction of electrode. The non-bond interactions were represented by a short-range 12-6 Lennard-Jones (LJ) potential and a long range Coulombic potential, expressed in a form of pairwise interacting atomic charges. The LJ potential between two atoms can be written as follow:

$$V_{LJ}(r_{ij}) = 4\epsilon_{ij} \left[\left(\frac{\sigma_{ij}}{r_{ij}} \right)^{12} - \left(\frac{\sigma_{ij}}{r_{ij}} \right)^{6} \right] \qquad (6.1)$$

The parameters σ and ε represent energy constant and diameter of one of the atoms, which depend on atom types. The Lorentz-Berthelot combining rules

were used to describe LJ potential between different atom types. The charges of atoms were adopted from previous studies (Biermann et al., 2001; Hoda and Larson, 2009; Oldiges and Tönsing, 2002; Sulatha and Natarajan, 2011).

The leapfrog algorithm was used to integrate the motion of atoms with a time step of 1 fs. The Coulombic electrostatic interactions were calculated by using the particle Mesh Ewald (PME) method with a cut-off distance of 1.0 nm and Fourier spacing of 1.2 nm. The cut-off distance for short-range van der Waals interaction was 1.0 nm. To remove initial strain, the initial configuration was conducted by energy minimization using the Steepest Descent method. This was followed by 500 ps NVT and 500 ps NPT simulations with position restraints on PAA chains and not on water molecules to achieve a well equilibrated system. A Verlet thermostat and a Berendsen barostat were used to control the temperature and pressure at 300 K and 1 bar during the calculation with relaxation time of 0.1 ps and 0.5 ps, respectively. The water was fixed with SETTLE algorithm and all bonds constrained by using SHAKE procedure. The production process was conducted without the charge on Pt electrodes at the beginning of 80 ns. After that, the well equilibrated geometry was set as initial structure for the next long-term simulations with Pt electrodes charging with -0.25 C/m^2, -0.5 C/m^2 and -0.75 C/m^2, respectively. The effects of charged electrodes on the polymer conformation were analysed based on the statistic results captured from at least 150 ns simulations.

6.3 Results and discussions

6.3.1 Effects of charged wall on the system

The system was run for 80 ns to make the polymer fully relax and the final dynamic equilibrium-configuration was set as the initial configuration for the simulation with charged electrode. A representative snapshot of the equilibrated structure of polymer solution within two neutral electrodes is displayed in the Figure 6.2. As expected, with salt ions surrounded, the HPAM chain stays in coiled state. According to the number density profiles along the normal direction of the Pt walls, the distribution of water and salt ions are almost uniform in the system except that there is a small attraction between the wall surface and water molecules. Specially, no much addiction between salt ions and neutral Pt walls.
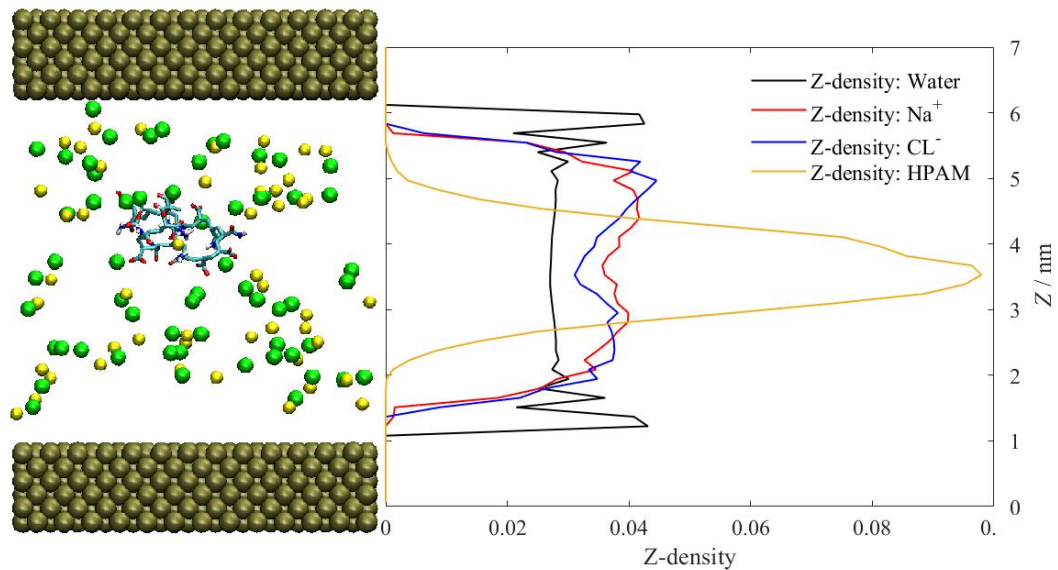
Figure 6.2 Snapshot and z-density of system with no charge on Pt wall. The snapshot is captured based on the most popularity structure from the PDF profiles shown later

The effects of the charged walls were captured from the results based on at least 150 ns simulation. The representative snapshots for the three different charge density are shown in Figure 6.3, 6.4 and 6.5, respectively. Those snapshots were selected at the radius of gyration of the HPAM around the peak values based on the probability density functions profiles.

When the Pt wall are negatively charged, the sodium cations are attracted by the electronic interaction. Such interaction becomes stronger when the charge density increases, which is consistent well with the number density profiles. At the negative charge density of the wall, Q, is 0.25 C/m^2, the interaction between Na^+ and Cl^- is still strong enough compared with the repulsion from the negative charged wall. Therefore, there is a Cl^- layer close to the Na^+ layers, which results in the less density in the bulk. This vacuum distribution may contributes to the expanding of the HPAM coils. With the increase of the charge density of the wall, the repulsion strongly affects the interaction between ions pairs, which separates the cations and anions. The distance between the Na^+ cluster and Cl^- cluster is highly dependent on the charged density.

The molecular distribution can be interpreted by the radius distribution functions (RDFs) profiles, as shown in Figure 6.6. The RDFs of water do not change significantly. However, for the RDFs between water and ions, due to the involvement of electric force field, the Cl^- hydration and interaction between Na^+ and Cl^- weaken and even no Na^+ and Cl^- pairs are observed for

the cases of Q=-0.75 C/m^2. The reason why the hydration effect of Na$^+$ increases first and then decreases is because with weak charge density applied, the Na$^+$ is gathering closer and forms a dense cluster appealing to the water molecules. Such dense cluster disappears gradually as the charge density increases. The Na$^+$ ions in the later are more preferred to attach to the Pt walls.
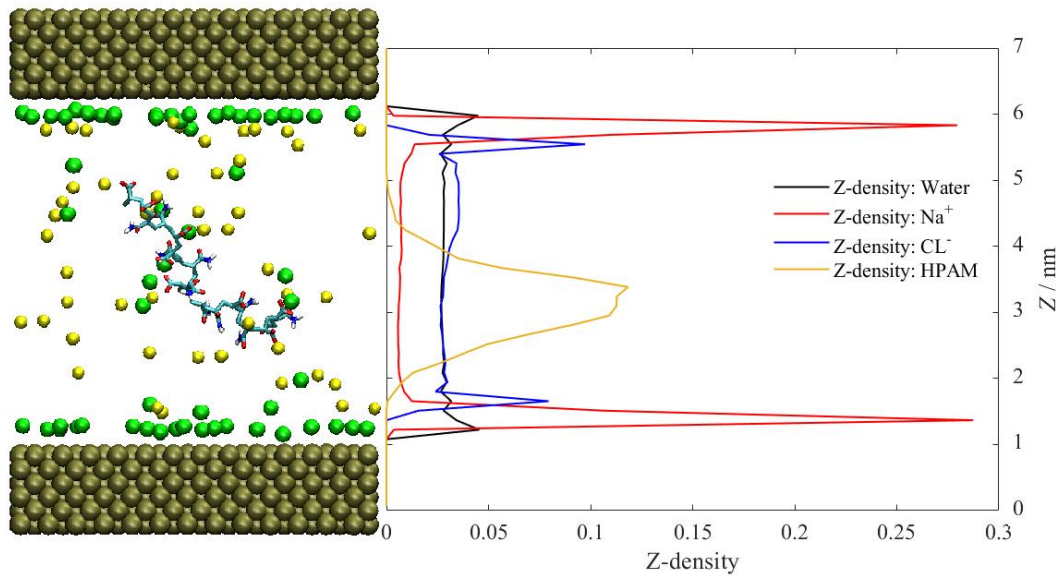
Figure 6.3 Snapshot and z-density of system with the Pt walls charged of -0.25 C/m^2
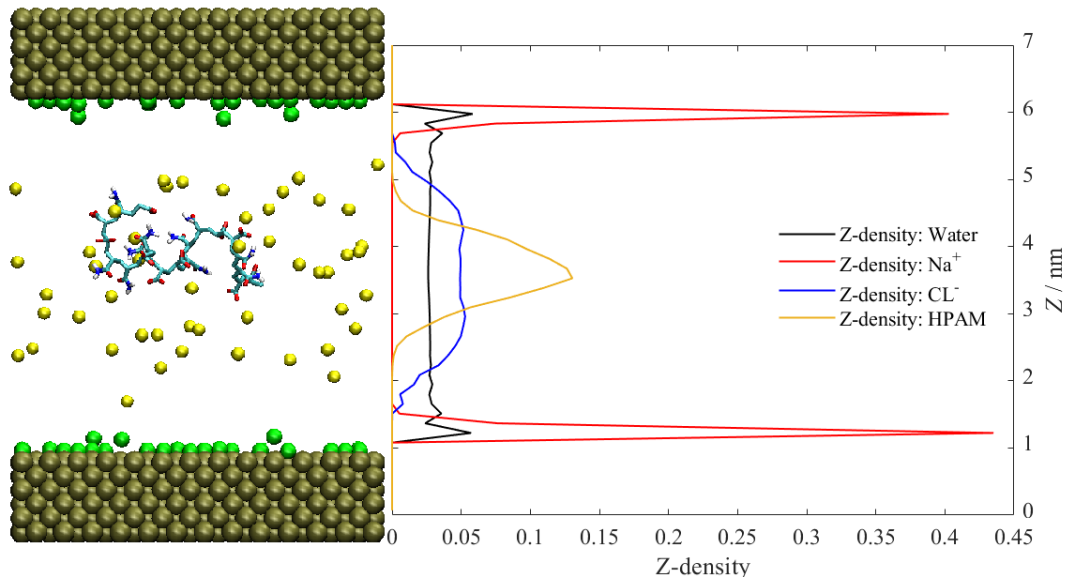
Figure 6.4 Snapshot and z-density of system with the Pt walls charged of -0.5 C/m^2
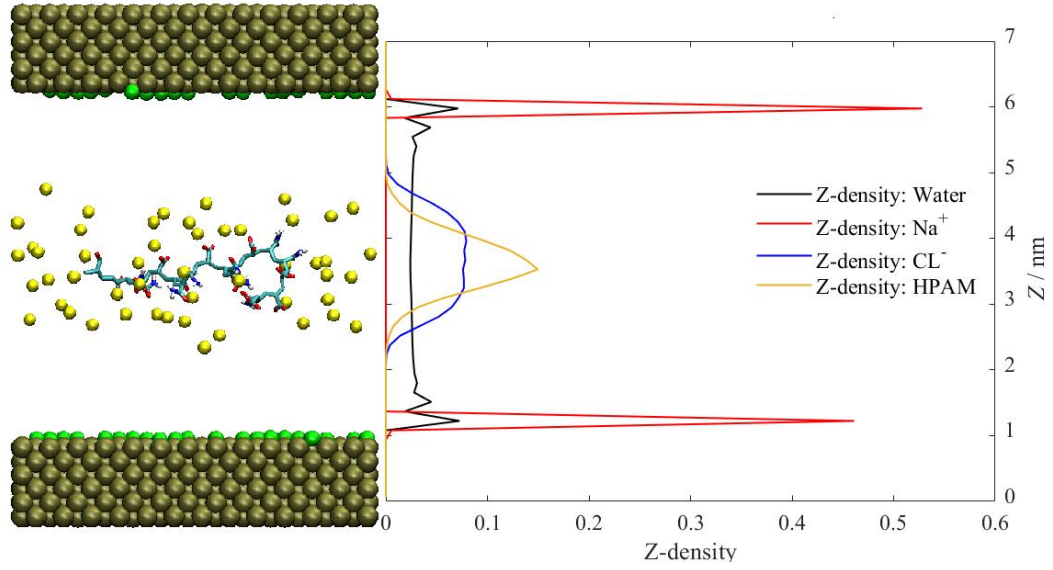
Figure 6.5 Snapshot and z-density of system with the Pt walls charged of -0.75 C/m²
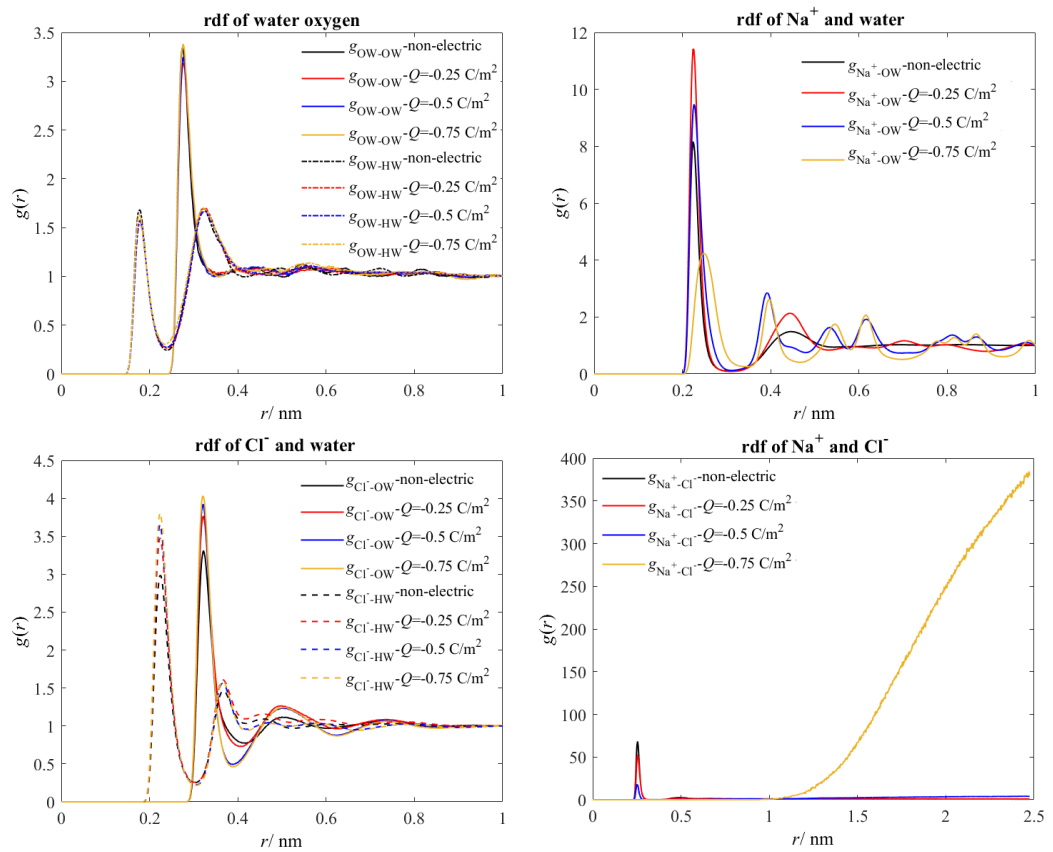
Figure 6.6 RDFs of water and ions with different charge density

6.3.1 HPAM chain dynamics

From the snapshots, the variations of HPAM structures are clearly observed. Compared with the neutral Pt wall, the radius of gyration of HPAM shows increasing behaviours when the Pt wall becomes charged. The radius of

gyration and the end-to-end distance are the two main parameters to characterize the polymer conformation. The time evolution of the radius of gyration and end-to-end distance with different charge densities are demonstrated in Figure 6.7 and 6.8, respectively.
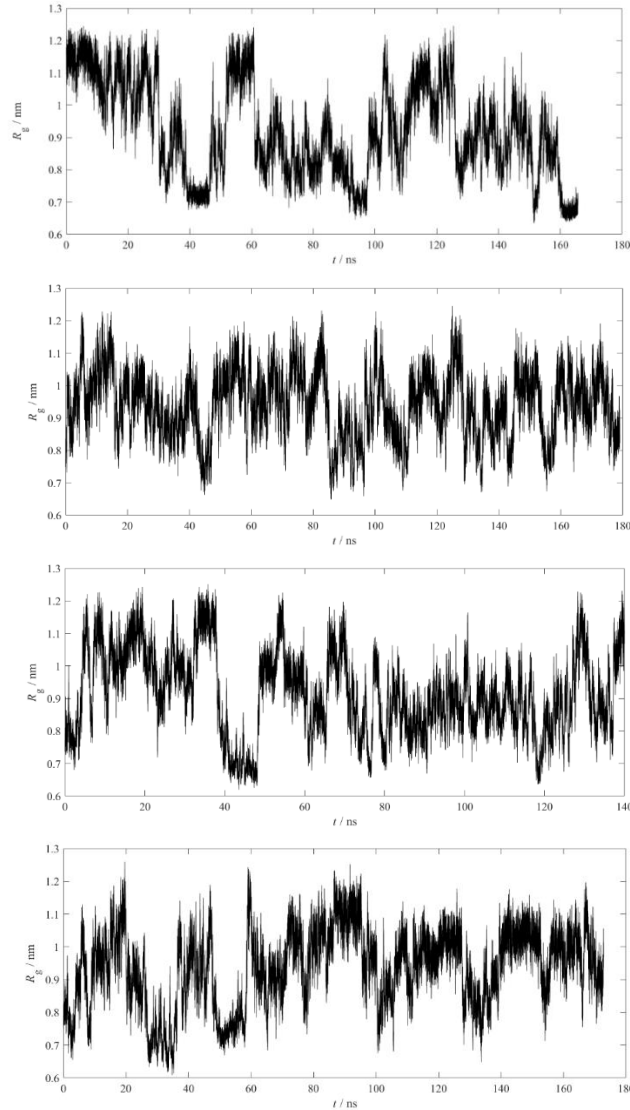
Figure 6.7 Time evolution of radius of gyration of HPAM under different charge density. From top to the bottom is recognized as Neutral, Q=-0.25 C/m^2, Q=-0. 5 C/m^2 and Q=-0.75 C/m^2,respectively

Dramatic fluctuations are observed both in the evolution of radius of gyration and End-to-End distance. The radius of gyration of HPAM for all charge density varies from 0.7 nm to 1.1 nm, while the End-to-End distance is ranging from 0.4 nm to 4 nm. The average values of the radius of gyration and End-to-End distance are listed in Table 6.1. It can be seen that both the average radius of gyration and End-to-End distance become higher when applied an external electric force field on the Pt walls. However, such enhancement in not obvious as the average value is calculated based on the time evolution

profiles, which undergoes a fast transition from a fully stretched conformation to the compact coiled conformation randomly.
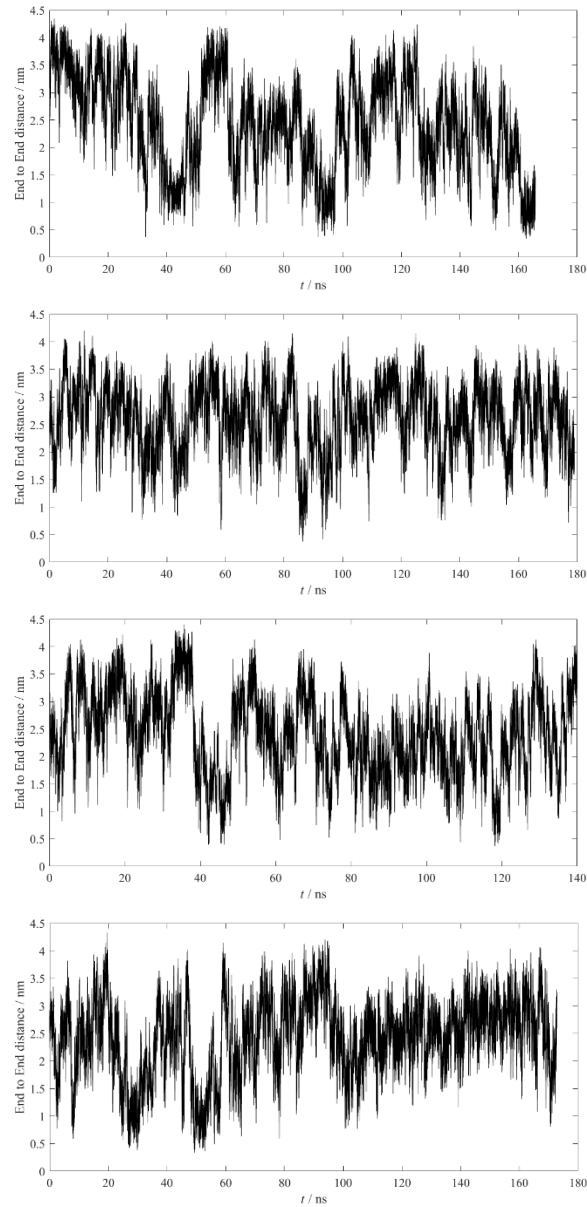
Figure 6.8 Time evolution of End-to-End distance of HPAM under different charge densities. From top to the bottom is recognized as Neutral, Q=-0.25 C/m², Q=-0. 5 C/m² and Q=-0.75 C/m²,respectively

Table 6.1 The average radius of gyration and End-to-End distance captured from time evolution profiles

	Neutral	Q=-0.25 C/m²	Q=-0.5 C/m²	Q=-0.75 C/m²
Radius of gyration (nm)	0.87	0.94	0.91	0.93

End-to-End distance (nm)	2.23	2.6	2.42	2.42

Indeed, it's a common phenomenon for a polymer chain exhibits such flexible properties as the free energy distribution shown in Figure 6.9. The free energy landscape is constructed on the basis of Boltzmann probability, $G(r)$, which can be calculated as

$$G(r) = -k_B T[lnP(r) - lnP_{max}(r)] \tag{6.2}$$

Where $P(r)$ is the probability distribution of the molecular system along an order parameter or a collective variable r, P_{max} is the maximum probability, k_B is the Boltzmann constant, and T is the simulation temperature. Figure 6.9 shows the free energy contours of HPAM with Pt walls under different charge density. It shows high polymer dynamics and a very flexible backbone for both cases, and even for the lowest free energy region, the radius of gyration of HPAM varies across almost 0.2 nm. However, one can still identify that for neutral charged Pt walls, the lowest free energy is mainly located in the region of R_g between 0.8 to 1 nm. For the other three charge densities, the radius of gyration is mainly allocated in the region of R_g between 0.9 to 1.1 nm, which indicates that the HPAM chain with external electric force field shows more expanding structure.
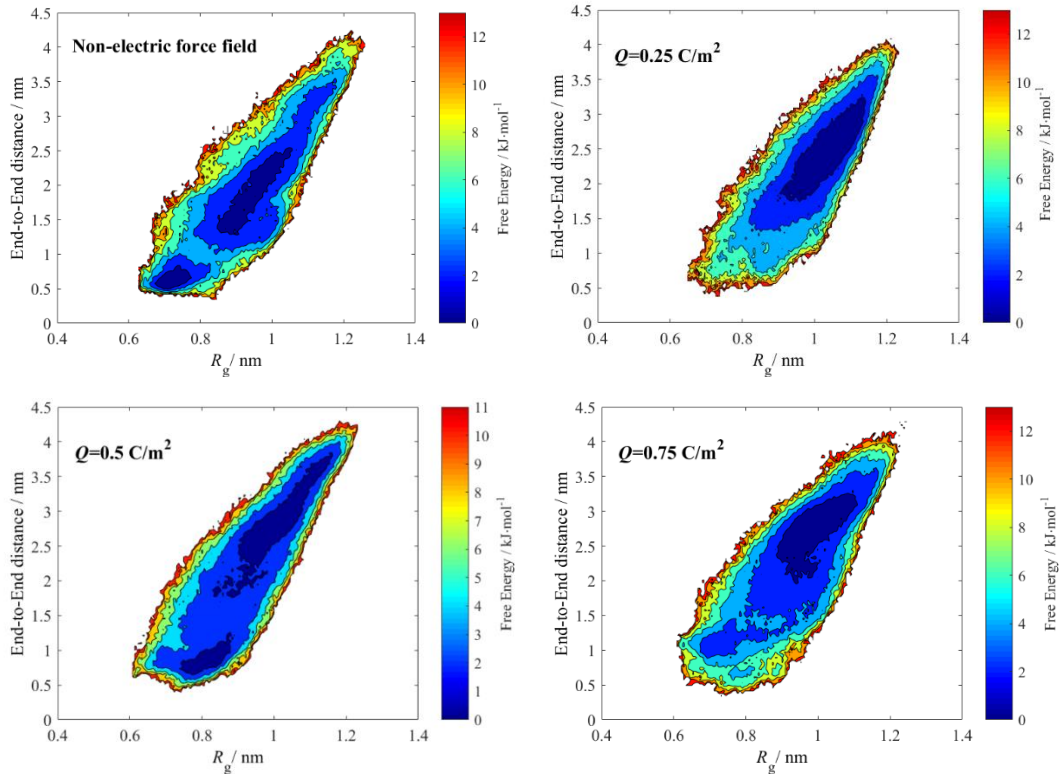
Figure 6.9 Free energy contours for different charge density

Therefore, to characterize the HPAM structure more accurately, the probability distribution functions (PDFs) of the radius of gyration and End-to-End distance are depicted in the Figure 6.10 and 6.11. For End-to-End distance, there is no significant trend observed, which is mainly because the End-to-End distance is solely driven by the distance between head atom and the tail atom. This is hard to capture the detailed structure of the backbone. For partially hydrolysed HPAM, the molecular itself cannot extend to the fully stretched structure and since the existence of the negative charged carboxylate groups along the polymer chain, the polymer is hard to collapsed into a dense coiled as well. Therefore, the End-to-End distance does not show obvious discrepancies. Unlike the End-to-End distance, the PDFs of radius of gyration varies with different charge density. For neutral Pt Walls, the HPAM populates the coiled conformation more frequently with the radius of gyration around the value of 0.82 nm and 0.68 nm. However, when the Pt walls are charged, such as Q=-0.25 C/m^2 and -0.75 C/m^2, the HPAM populates the stretched state with radius of gyration are 0.98 nm and 1.02 nm, respectively, which implies that the addition of external electric force field indeed affect the polymer conformation, making polymer from coiled state to stretched form. The radius of gyration of HPAM with Pt walls charged with -0.5 C/nm^2 is smaller than that of the other two. The peak of the PDFs is about 0.88 nm. The reason can be attributed to the distribution of Cl^- ions. For the Pt walls with charge density of -0.25 C/m^2,

the Cl⁻ is still attracted by Na⁺ ions and thereby most of ions including Na⁺ and Cl⁻, are allocated near the Pt walls. In such conditions, the HPAM chain is a polymer chain in pure water, where the HPAM is always show stretched state. When the charge density increases to 0.75 C/m², due to the repulsion form the wall, the Cl⁻ has already closely surrounded the HPAM chain. The ions contributes to the repulsion between the charged backbone and make it more attractive than the one in pure water case (Q=-0.25 C/m²). However, at a medium charge density, some ions stay in the middle area between wall and HPAM, which forms a anion shielding and encloses the HPAM. Therefore, the expansion of HPAM due to the repulsion of intramolecular is persisted by this anion layer.
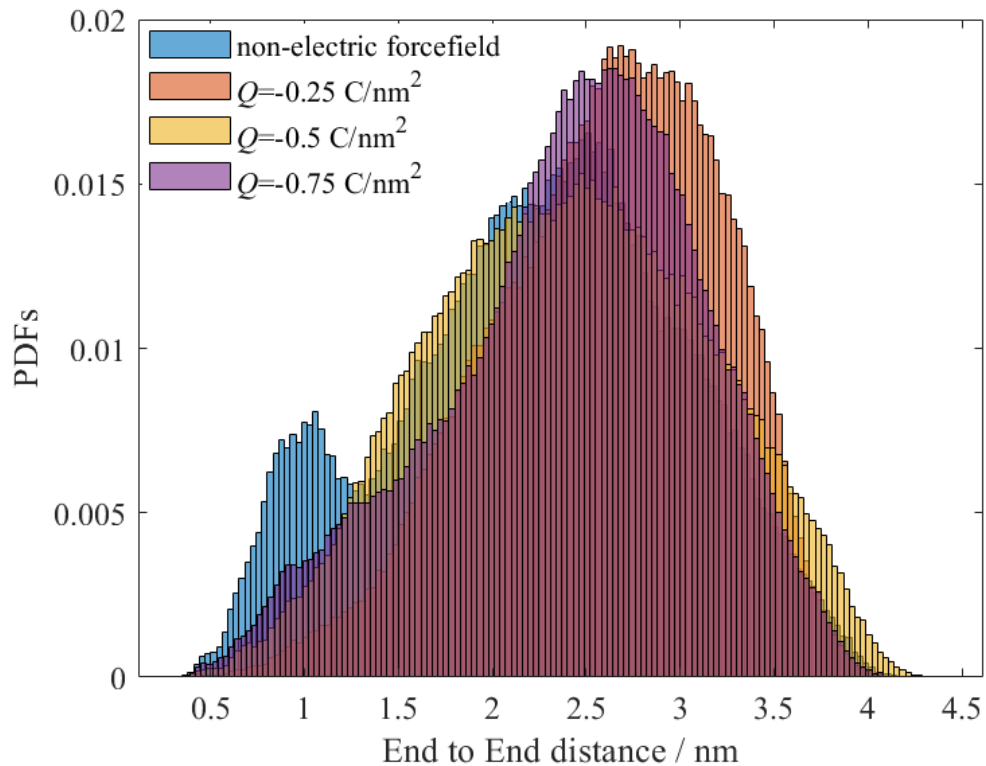
Figure 6.10 PDFs of End-to-End distance with different charge density
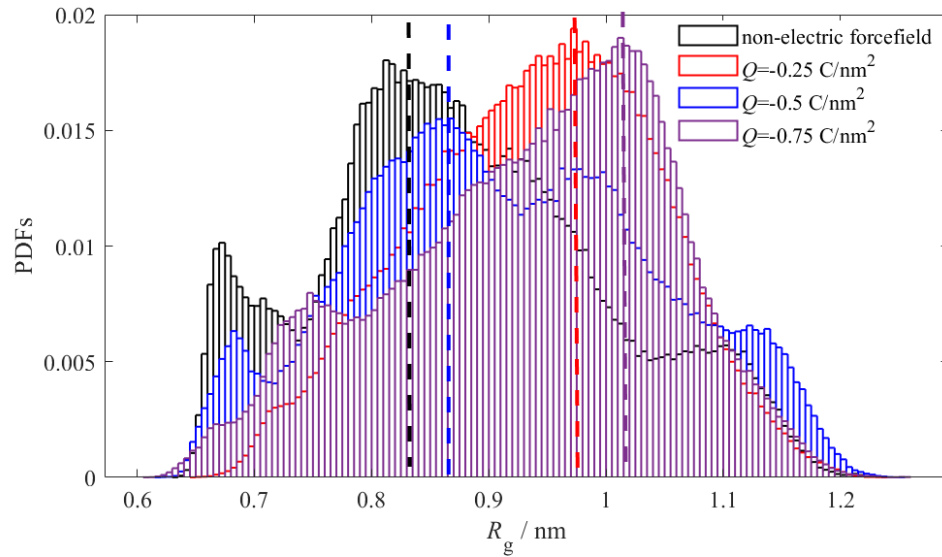
Figure 6.11 PDFs of radius of gyration with different charge density

The RDFs of HPAM with water and ions are shown in Figure 6.12 and 6.13, respectively. The charged Pt walls does not have a significant effect on the hydration of HPAM. Although the peak of carboxyl oxygen and water decreases as the charge density increases due to the weak interaction, it affects little on the whole HPAM molecules. The PDFs between HPAM and ions indirectly validate the possible interpretation for the statistic results. The interaction between HPAM and Cl⁻ decrease first and gradually increase as the charge density increases, which indicates the distribution of Cl⁻ ions are closer to the HPAM with enlarging the charge density.
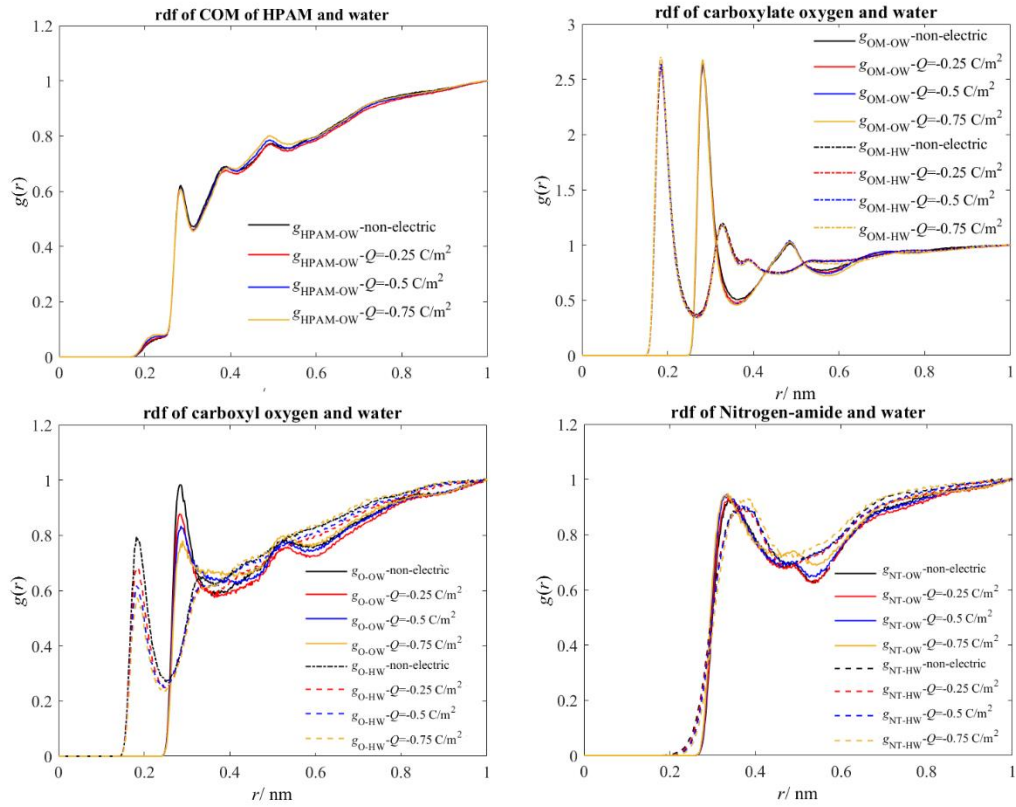
Figure 6.12 PDFs of HPAM and water
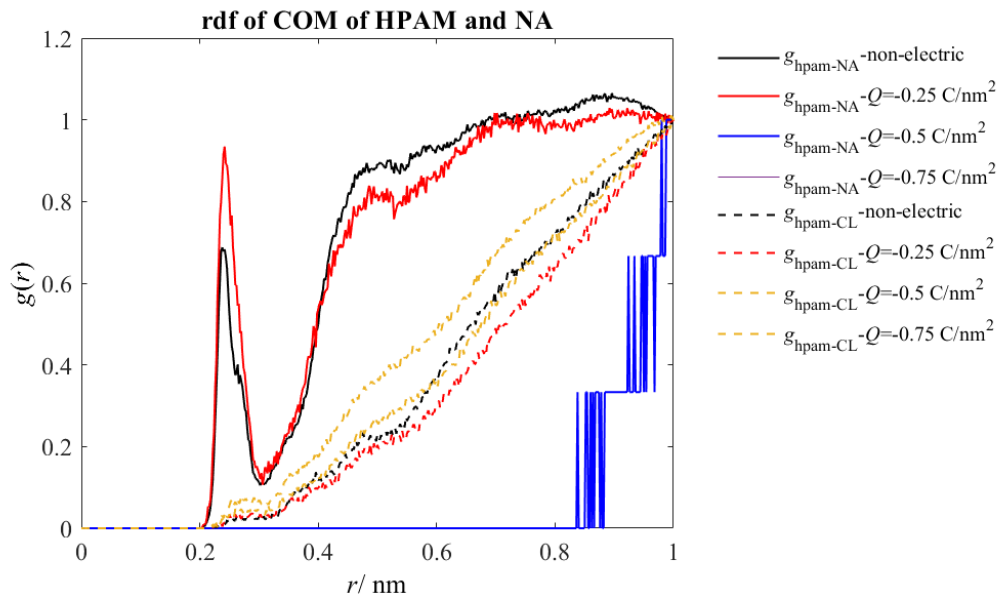
Figure 6.13 PDFs of HPAM and ions

6.4 Conclusions

MD simulation of HPAM chain morphology variation in a salt solution within two Pt walls was conducted under four different charge density to exam the possibility of active control /induce of elastic turbulence via external electrical

field. It shows that with external electric force field applied on the wall, the radius of gyration of the HPAM becomes larger and the HPAM prefers to behave stretched state rather than coiled form.

With continually increasing the charge density, the radius of gyration of HPAM decreases first and then increases to an even large value. This is because of the distribution of the Cl$^-$ ions, which forms anion layers outside the HPAM at a medium degree of charge density and suppresses the expansion of the HPAM due to the intramolecular repulsion.

The variations of HPAM conformation, as discussed in the previous chapters, have significant effects on the onset of elastic instability. Therefore, with external electric force field applied, it seems to be possible to control the motion of ions to change the polymer conformation, thereby inducing the elastic instability at even lower *Re* and *Wi*.

Chapter 7 Conclusions and Future work

7.1 Conclusion

This work conducted HPAM solution with different water chemistry such as polymer concentration, salinity and solvent proportion to study the effects of polymer sensitivities on the onset of elastic turbulence. The rheology dependence on polymer concentration and salinity was first investigated by both experimental measurement and modelling skills. Both results show significant effects of these polymer sensitivities on the rheological properties of polymer solution, as shown in Chapter 3. With the understanding of the condition of onset of elastic turbulence from the literature review, such effects on rheology could affect the onset value apparently and thereby the concomitant influence of the polymer concentration and salinity were conducted in a swirling flow geometry and a curvilinear channel in Chapter 4, followed by their effects on the heat transfer side in Chapter 5. Indeed, most of experiments presented previously adopted passive techniques (either by curvilinear geometry or inserted obstacles) to induce elastic turbulence for flow and heat transfer intensification. With the achievement of ions effects on the onset of elastic turbulence discussed in Chapter 5, it is possible by controlling the motion of salt ions to change the polymer rheology and then induce the elastic turbulence/instability at an even lower *Re* and *Wi*, through which could enlarge the application of the elastic turbulence in flow and heat transfer side. The results following the clues mentioned above are introduced below.

7.1.1 Rheology and polymer morphology dependence on polymer concentration and salinity

> ➢ From the standard rheology measurement, the increase of polymer concentration and the reduction of the salinity result in the increase of the viscosity. In terms of salinity effects, there exists a critical salinity after which the viscosity is independent with salts.

> ➢ The viscosity profiles are consistent well with the variations of hydrodynamic radius of polymer molecules, and the detailed morphology of a single HPAM chain as a function of hydrolysis, and salinity are demonstrated by atomics molecular dynamics simulations. The non-hydrolysed HPAM performs a coil-like conformation, while for the hydrolysed HPAM, the polymer chain expands and behaves a stretch-like structure. With the increase

of the hydrolysis, due to the increase of the number of charged carboxylate groups, the repulsion along the backbone strengthens, leading to a more stretching HPAM structure.

➢ The molecular dynamics simulation interpret the molecular level mechanism for the effects of salinity on the polymer rheology. Adding salt into polymer solutions induces the collapse of polymer chains, which is mainly attributed to the electrostatic screening effects by ions rather than the hydrogen bonding effect.

➢ It should be noted that the shear-thinning phenomenon is highly dependent on the degree of salt and polymer concentration. With low salinity or high polymer concentration, a dramatic shear-thinning phenomenon is observed, which would disappear gradually as the increase of salinity or the reduction of polymer concentration. This shear-thinning dependence, as a result, is also affect the onset of elastic instability significantly as previous study presented.

7.1.2 Effects of polymer concentration and salinity on the onset of elastic instability

As discussed above, the polymer concentration and salinity of polymer solution can affect the rheology significantly either by increasing the volume of polymer or by changing the polymer conformation. The concomitant effects on the onset of elastic instability or turbulence are introduced in a swirling flow geometry and a micro curvilinear channel, which are shown below.

➢ The polymer solution with higher polymer concentration could induce the elastic instability at a smaller critical shear rate and critical Wi_c. For a given gap ratio, the critical Wi_c for the elastic instability depends on the polymer concentration to the viscosity as $Wi_c \sim (\eta_p/\eta)^{-\alpha}$, with α is 0.51, which is very close to the expected value of 0.5.

➢ With increasing salinity, the polymer contribution to the viscosity decreases, resulting in a higher threshold Wi_c for the onset of elastic instability. Owing to the dramatic shear-thinning behavior caused by the polymer configuration, the dependence of Wi_c on η_p/η can be fitted well by $Wi_c \sim (\eta_p/\eta)^{-\alpha}$ with exponent of 1. With continual increase in the salinity, the poor quality of solvent makes the Wi_c disobey the rules.

➤ The shielding effects seems to be ineffective when the flow is fully developed into elastic turbulence regime. These trends are consistent with the variations of spectra profiles of injected power. A power-law pattern is gradually observed as the flow transfers from laminar to elastic turbulence, where the exponent increases first and then keeps constant around a value of -4.3. In fully developed elastic regime, both the exponent and the normalized peak frequency become independent of salinity. Although high salinity delays the occurrence of elastic turbulence, the growth of flow intensification is more dramatic due to the reduction of the viscosity, accompanied with more intensive skewness of the PDFs of injected power. This growth of flow intensification, however, is mainly due to the variations of initial viscosity since similar maximum shear stress is obtained for all polymer solutions at maximum *Wi*.

➤ Similar trends are applied well on the mixing performance and threshold properties in a curvilinear microchannel. The discrepancy of the values is ascribed to the geometry effects. The diffusion of the fluorescein at low flow rate indicates the possible existence of steady secondary flow instability.

7.1.3 Effects of polymer sensitivities on heat transfer side

The polymer sensitivities such as polymer concentration and salinity of polymer solution achieve in modifying the onset condition of elastic instability, and the flow intensification of elastic turbulence is affected. The convective heat transfer performance of such effects are probed in a flow between two parallel plates with large gap. The following conclusion can be drawn on related the heat transfer performance.

➤ Before the occurrence of elastic instability, the HPAM solution exhibits similar heat transfer performance with sucrose. The temperature distribution inside the bulk is in layers. The *Nu* and *k* are almost independent on the rotation speed. Even at the maximum applied rotating speed, the heat transfer process of sucrose solution is still conduction-like, while in contrast, continually increasing the rotation speed, the elastic instability is induced and irregular flow intensifies the heat transfer coefficient both within bulk fluid and between the wall and the fluid, which makes the temperature distribution become homogenous.

➢ The corresponding flow behaviours captured from the below also conduct similar results. No chaotic irregular flow patterns are observed for sucrose solution. A vortical-like flow motion is found in the polymer solution. The spiral-like flow behaviour corresponding with the statistical analysis of temperature and angular velocity indicate that the flow is still in the transition stage to elastic turbulence over the range of rotating speed applied. The power-law exponent 1.8 at low frequency domain is possible due to the large scale vortex due to the onset of elastic instability.

➢ With increase of the polymer concentration and reduction of the salinity, the onset of elastic instability shifts to an earlier critical swirling velocity and Weissenberg number. The heat transfer enhancement begins after the occurrence of elastic instability.

➢ For a given swirling velocity, the enhancement increases with increasing the polymer concentration. The maximum enhancement is dependent on polymer concentration. For polymer solution with 300 ppm at maximum rotating speed, the convective Nusselt number could reach more than 6 time higher than that of pure sucrose solution. However, the heat transfer enhancement exhibits linear relationship on Wi after the occurrence of the elastic instability, as $Nu/Nu_s \propto 1.2\,Wi$, which is independent on polymer concentration. This independence is attributed to the small discrepancies of shear-thinning in dilute regime.

➢ For a given swirling velocity at lower velocity region, with the reduction of the salinity, the heat transfer enhancement increases. But the enhancement seems to be independent on salinity when the swirling velocity exceeds an relative higher speed. A proposed mechanism of this could be the reduction of the shielding effect. Therefore, the salinity influences the onset of elastic instability, but the maximum enhancement is limited by the polymer concentration. In addition, due to the significant discrepancies of shear-thinning, the Nu dependence on Wi varies with different salinity. The polymer solution with low salinity, shows more dramatic shear-thinning phenomenon, suppressing the increase of the heat transfer enhancement.

➢ The effects of variations of solvent concentration on the enhancement is complicated due to the coupling effects

between inertial and elastic nonlinearity. However, it is clear that the enhancement based on pure elastic instability is most dramatic and promising at a low Reynold number.

7.1.4 Potential method for active control of elastic instability

The salinity effects on the flow and heat transfer enhancement are mainly based on its change on the polymer conformation, which differs the polymer rheological properties. The viscosity and shear-thinning phenomenon are both changed. With achievement of controlling the ions effects on the polymer molecules, an active method is proposed to induced elastic instability manually. The proposed method is investigated by MD simulations by capturing the variations of polymer conformation with the external electric force field applied on the flow passages or channels.

When applied the external electric force field on the system, the sodium ions are attracted by the wall, leaving the chloride ions in the bulk, which results in the increase of the radius of gyration of the HPAM chain and makes the polymer chain expands itself from the coiled form to stretch state. With continually increasing the charged density of the electric force field, the radius of gyration of HPAM decreases first and then increases to an even large value. This is because of the distribution of the Cl⁻ ions, which forms a anion layers outside the HPAM at a medium degree of charge density and suppresses the expansion of the HPAM due to the intramolecular repulsion.

The variations of HPAM conformation, related to the rheology of polymer solution as discussed in the previous chapters, have significant effects on the onset of elastic instability. Therefore, with external electric force field applied, it seems to be possible by controlling the motion of ions to change the polymer conformation, thereby inducing the elastic instability at even lower *Re* and *Wi*.

7.2 Future works

The elastic turbulence or elastic instability, as performed in this work, has been identified to be capable of intensifying the flow and heat transfer in a different level with various polymer concentration, salinity of polymer solution and even the proportion of solvent ingredients. What's more, in terms of the condition of salinity effects, with suitable controlling of the ions motion, the polymer rheology could be modified by applying an external force field. The results presented in the previous section do make contribution for the understanding of the elastic turbulence, especially how the polymer sensitivities influences the onset of elastic instability and the concomitant

effects on the flow and heat transfer enhancement. However, the mechanism of elastic turbulence is quite complicated, which even the rheology dependence on the occurrence of elastic instability is not clear and more works related to this area are still required. What's more, there are still many works related to this projects have not been investigated.

To make the heat transfer by elastic turbulence further understood, some future works are suggested to be focus on.

1. The heat transfer enhancement was conducted still in the transition regime, the dependence of *Nu* and *Wi* in fully developed elastic turbulence area has not been revealed. A much mode wide range of shear rate should be adopted to fulfil such shortage.

2. The experiments of active control of elastic turbulence should be scheduled followed by the simulation method. The effects of external force field, especially with the existence of salt, are deserved to be investigated.

3. With sucrose dissolving into the polymer solution, though the polymer relaxation is enlarged, the application of sucrose is limited due to the sticky properties and high sensitivity with temperature. By introducing nanoparticles into polymer solutions, either by bond interaction or non-bond interaction between polymer and nanoparticles, the polymer relaxation and rheology could be much improved, which could leads to same enhancement level in polymer relaxation with sucrose but the increase of pressure drop is smaller than the later. In addition, by adding nanoparticles, another active control method is accessible by stimulate the motion of nanoparticles thereby controlling the motion of polymer. Another advantages of the addition of nanoparticles could be attributed to the high thermal conductivity property, which could lead to more efficient heat transfer performance.

4. The MD simulation now is an efficient method to reveal mechanism of macro phenomenon. The effects of salinity or polymer concentration, such as disappearance of shielding effect when the fluid is flowing could be statistic analysed by applying Non-equilibrium MD simulations with some velocities or forces.

List of References

Abed, W.M., Whalley, R.D., Dennis, D.J.C. and Poole, R.J. 2016. Experimental investigation of the impact of elastic turbulence on heat transfer in a serpentine channel. *Journal of Non-Newtonian Fluid Mechanics.* **231**, pp.68-78.

Allen, P. and Karayiannis, T. 1995. Electrohydrodynamic enhancement of heat transfer and fluid flow. *Heat Recovery Systems and CHP.* **15**(5), pp.389-423.

Batchelor, G.K. 2000. *An introduction to fluid dynamics.* Cambridge university press.

Beaumont, J., Louvet, N., Divoux, T., Fardin, M.-A., Bodiguel, H., Lerouge, S., Manneville, S. and Colin, A. 2013. Turbulent flows in highly elastic wormlike micelles. *Soft Matter.* **9**(3), pp.735-749.

Belan, S., Chernykh, A. and Lebedev, V.J.J.o.F.M. 2018. Boundary layer of elastic turbulence. **855**, pp.910-921.

Berenson, P. 1962. Experiments on pool-boiling heat transfer. *International Journal of Heat and Mass Transfer.* **5**(10), pp.985-999.

Bergles, A. 1969. *Progress in heat and mass transfer, Vol. 1.* Pergamon Press, Oxford.

Bhowmik, R., Katti, K.S. and Katti, D. 2007. Molecular dynamics simulation of hydroxyapatite–polyacrylic acid interfaces. *Polymer.* **48**(2), pp.664-674.

Biermann, O., Hädicke, E., Koltzenburg, S., Seufert, M. and Müller-Plathe, F. 2001. Hydration of polyelectrolytes studied by molecular dynamics simulation. *arXiv preprint cond-mat/0101115.*

Bird, R.B., Armstrong, R.C., Hassager, O. and Curtiss, C.F. 1977. *Dynamics of polymeric liquids.* Wiley New York.

Bodiguel, H., Beaumont, J., Machado, A., Martinie, L., Kellay, H. and Colin, A. 2015. Flow enhancement due to elastic turbulence in channel flows of shear thinning fluids. *Phys Rev Lett.* **114**(2), p028302.

Bontemps, A., Garrigue, A., Goubier, C., Huetz, J., Marvillet, C., Mercier, P. and Vidil, R. 1994. Échangeurs de chaleur-Intensification des échanges thermiques. *Techniques de l'ingénieur.*

Borochov, N. and Eisenberg, H. 1994. Stiff (DNA) and flexible (NaPSS) polyelectrolyte chain expansion at very low salt concentration. *Macromolecules.* **27**(6), pp.1440-1445.

Bulo, R.E., Donadio, D., Laio, A., Molnar, F., Rieger, J. and Parrinello, M. 2007. "Site Binding" of Ca2+ Ions to Polyacrylates in Water: A Molecular Dynamics Study of Coiling and Aggregation. *Macromolecules.* **40**(9), pp.3437-3442.

Buongiorno, J. 2006. Convective transport in nanofluids. *Journal of heat transfer.* **128**(3), pp.240-250.

Burghelea, T., Segre, E., Bar-Joseph, I., Groisman, A. and Steinberg, V. 2004a. Chaotic flow and efficient mixing in a microchannel with a polymer solution. *Phys Rev E Stat Nonlin Soft Matter Phys.* **69**(6 Pt 2), p066305.

Burghelea, T., Segre, E. and Steinberg, V. 2004b. Mixing by polymers: experimental test of decay regime of mixing. *Phys Rev Lett.* **92**(16), p164501.

Burghelea, T., Segre, E. and Steinberg, V. 2006. Role of elastic stress in statistical and scaling properties of elastic turbulence. *Phys Rev Lett.* **96**(21), p214502.

Burghelea, T., Segre, E. and Steinberg, V. 2007. Elastic turbulence in von Karman swirling flow between two disks. *Physics of Fluids.* **19**(5), p053104.

Burghelea, T.I. 2005. *Elastic turbulence and mixing in a dilute polymer solution.* publisher not identified.

Cao, Q., Zuo, C., Li, L. and He, H. 2011. Self-assembled nanostructures of bottle-brush polyelectrolytes with oppositely charged surfactants: a computational simulation study. *Soft Matter.* **7**(14), pp.6522-6528.

Carrica, P., Di Marco, P. and Grassi, W. 1996. Electric field effects on film boiling on a wire. *Experimental Heat Transfer.* **9**(1), pp.11-27.

Carrillo, J.-M.Y. and Dobrynin, A.V. 2014. Salt effect on osmotic pressure of polyelectrolyte solutions: simulation study. *Polymers.* **6**(7), pp.1897-1913.

Casanellas, L., Alves, M.A., Poole, R.J., Lerouge, S. and Lindner, A. 2016. The stabilizing effect of shear thinning on the onset of purely elastic instabilities in serpentine microflows. *Soft Matter.* **12**(29), pp.6167-6175.

Cavallini, A., Del Col, D., Doretti, L., Longo, G.A. and Rossetto, L. 1999. A new computational procedure for heat transfer and pressure drop during refrigerant condensation inside enhanced tubes. *Journal of Enhanced Heat Transfer.* **6**(6).

Chen, P., Yao, L., Liu, Y., Luo, J., Zhou, G. and Jiang, B. 2012. Experimental and theoretical study of dilute polyacrylamide solutions: effect of salt concentration. *Journal of molecular modeling.* **18**(7), pp.3153-3160.

Choi, S.K. 2008. *pH sensitive polymers for novel conformance control and polymer flooding applications.* ProQuest.

Choi, S.U. and Eastman, J.A. 1995. *Enhancing thermal conductivity of fluids with nanoparticles.* Argonne National Lab., IL (United States).

Chowdhuri, S. and Chandra, A. 2001. Molecular dynamics simulations of aqueous NaCl and KCl solutions: Effects of ion concentration on the single-particle, pair, and collective dynamical properties of ions and water molecules. *The Journal of Chemical Physics.* **115**(8), pp.3732-3741.

Chu, K.-H., Enright, R. and Wang, E.N. 2012. Structured surfaces for enhanced pool boiling heat transfer. *Applied Physics Letters.* **100**(24), p241603.

Cipriani, M., MARCO, P.D. and Grassi, W. 2004. Effect of an externally applied electric field on pool film boiling of FC-72. *Heat transfer engineering.* **25**(6), pp.3-13.

Clarke, A., Howe, A.M., Mitchell, J., Staniland, J., Hawkes, L. and Leeper, K. 2015. Mechanism of anomalously increased oil displacement with aqueous viscoelastic polymer solutions. *Soft Matter.* **11**(18), pp.3536-3541.

Copeland, D., Ren, C., Su, M. and Ligrani, P. 2017. Elastic turbulence influences and convective heat transfer within a miniature viscous disk pump. *International Journal of Heat and Mass Transfer.* **108**, pp.1764-1774.

Delcroix, M., Demoustier-Champagne, S. and Dupont-Gillain, C.C. 2013. Quartz crystal microbalance study of ionic strength and pH-dependent polymer conformation and protein adsorption/desorption on PAA, PEO, and mixed PEO/PAA brushes. *Langmuir.* **30**(1), pp.268-277.

Dewan, A., Mahanta, P., Raju, K.S. and Kumar, P.S. 2004. Review of passive heat transfer augmentation techniques. *Proceedings of the Institution of Mechanical Engineers, Part A: Journal of Power and Energy.* **218**(7), pp.509-527.

Dianoux, A., Ferreira, J., Martins, A., Giroud, A. and Volino, F. 1985. Molecular Structure, Conformation and Orientational Order of Para-Azoxy-Anisole (PAA) in the Nematic Phase, and Their Temperature Dependence: Results from a Deuterium and Proton Magnetic Resonance Study. *Molecular Crystals and Liquid Crystals.* **116**(3-4), pp.319-352.

Dimitrov, D., Milchev, A. and Binder, K. 2007. Polymer brushes in solvents of variable quality: Molecular dynamics simulations using explicit solvent. *The Journal of chemical physics.* **127**(8), p084905.

Dong, R.Y., Tomchuk, E., Wade, C.G., Visintainer, J. and Bock, E. 1977. Deuteron line shape study of molecular order and conformation in the nematogens PAA and MBBA. *The Journal of Chemical Physics.* **66**(9), pp.4121-4125.

Driesner, T., Seward, T. and Tironi, I. 1998. Molecular dynamics simulation study of ionic hydration and ion association in dilute and 1 molal aqueous sodium chloride solutions from ambient to supercritical conditions. *Geochimica et Cosmochimica Acta.* **62**(18), pp.3095-3107.

Ducloue, L., Casanellas, L., Haward, S.J., Poole, R.J., Alves, M.A., Lerouge, S., Shen, A.Q. and Lindner, A.J.a.p.a. 2018. Secondary flows of viscoelastic fluids in serpentine microchannels.

Eapen, J., Li, J. and Yip, S. 2007. Mechanism of thermal transport in dilute nanocolloids. *Physical review letters.* **98**(2), p028302.

Fan, A., Turro, N.J. and Somasundaran, P. 2000. A study of dual polymer flocculation. *Colloids and surfaces a: physicochemical and engineering aspects.* **162**(1-3), pp.141-148.

Fand, R. 1965. The influence of acoustic vibrations on heat transfer by natural convection from a horizontal cylinder to water. *Journal of heat transfer.* **87**(2), pp.309-310.

Fardin, M.A., Lopez, D., Croso, J., Gregoire, G., Cardoso, O., McKinley, G.H. and Lerouge, S. 2010. Elastic turbulence in shear banding wormlike micelles. *Phys Rev Lett.* **104**(17), p178303.

Fernández, J. and Poulter, R. 1987. Radial mass flow in electrohydrodynamically-enhanced forced heat transfer in tubes. *International journal of heat and mass transfer.* **30**(10), pp.2125-2136.

Flory, P.J. and Osterheld, J.E. 1954. Intrinsic viscosities of polyelectrolytes. poly-(acrylic acid). *The Journal of Physical Chemistry.* **58**(8), pp.653-661.

Fouxon, A. and Lebedev, V. 2003. Spectra of turbulence in dilute polymer solutions. *Physics of Fluids.* **15**(7), pp.2060-2072.

Gan, H.Y., Lam, Y.C. and Nguyen, N.-T. 2006a. Polymer-based device for efficient mixing of viscoelastic fluids. *Applied Physics Letters.* **88**(22), p224103.

Gan, H.Y., Lam, Y.C., Nguyen, N.T., Tam, K.C. and Yang, C. 2006b. Efficient mixing of viscoelastic fluids in a microchannel at low Reynolds number. *Microfluidics and Nanofluidics.* **3**(1), pp.101-108.

Gerashchenko, S., Chevallard, C. and Steinberg, V. 2005. Single-polymer dynamics: Coil-stretch transition in a random flow. *Europhysics Letters (EPL).* **71**(2), pp.221-227.

Gollub, J.P., Clarke, J., Gharib, M., Lane, B. and Mesquita, O. 1991. Fluctuations and transport in a stirred fluid with a mean gradient. *Physical Review Letters.* **67**(25), p3507.

Groisman, A. and Steinberg, V. 2000. Elastic turbulence in a polymer solution flow. *Nature.* **405**(6782), pp.53-55.

Groisman, A. and Steinberg, V. 2001. Efficient mixing at low Reynolds numbers using polymer additives. *Nature.* **410**(6831), p905.

Groisman, A. and Steinberg, V. 2004. Elastic turbulence in curvilinear flows of polymer solutions. *New Journal of Physics.* **6**(1), p29.

Groisman, A. and Steinberg, V.J.P.o.F. 1998. Mechanism of elastic instability in Couette flow of polymer solutions: experiment. *Physics of Fluids.* **10**(10), pp.2451-2463.

Gryparis, E.A., Gkormpatsis, S.D., Housiadas, K.D. and Tanner, R.I. 2019. Viscoelastic planar elongational flow past an infinitely long cylinder. *Physics of Fluids.* **31**(3), p033104.

Gupta, A.K. and Natarajan, U. 2016. Tacticity effects on conformational structure and hydration of poly-(methacrylic acid) in aqueous solutions-a molecular dynamics simulation study. *Molecular Simulation.* **42**(9), pp.725-736.

Gupta, A.K. and Natarajan, U. 2017. Anionic polyelectrolyte poly (acrylic acid)(PAA) chain shrinkage in water–ethanol solution in presence of Li+ and Cs+ metal ions studied by molecular dynamics simulations. *Molecular Simulation.* **43**(8), pp.625-637.

Hara, M. and Nakajima, A. 1980. Characteristic behaviors of light scattering from polyelectrolyte in dilute solution region. *Polymer Journal.* **12**(10), p701.

Hess, B., Kutzner, C., Van Der Spoel, D. and Lindahl, E. 2008. GROMACS 4: algorithms for highly efficient, load-balanced, and scalable molecular simulation. *Journal of chemical theory and computation.* **4**(3), pp.435-447.

Hoda, N. and Larson, R.G. 2009. Explicit-and implicit-solvent molecular dynamics simulations of complex formation between polycations and polyanions. *Macromolecules.* **42**(22), pp.8851-8863.

Howe, A.M., Clarke, A. and Giernalczyk, D. 2015. Flow of concentrated viscoelastic polymer solutions in porous media: effect of M(W) and concentration on elastic turbulence onset in various geometries. *Soft Matter.* **11**(32), pp.6419-6431.

Huber, K. 1993. Calcium-induced shrinking of polyacrylate chains in aqueous solution. *The Journal of Physical Chemistry.* **97**(38), pp.9825-9830.

Hyun, S., Lee, D.-R. and Loh, B.-G. 2005. Investigation of convective heat transfer augmentation using acoustic streaming generated by ultrasonic vibrations. *International Journal of Heat and Mass Transfer.* **48**(3-4), pp.703-718.

Ikegami, A. and Imai, N. 1962. Precipitation of polyelectrolytes by salts. *Journal of Polymer Science.* **56**(163), pp.133-152.

Jun, Y. and Steinberg, V. 2009. Power and pressure fluctuations in elastic turbulence over a wide range of polymer concentrations. *Phys Rev Lett.* **102**(12), p124503.

Jun, Y. and Steinberg, V. 2017. Polymer concentration and properties of elastic turbulence in a von Karman swirling flow. *Physical Review Fluids.* **2**(10).

Jung, J.C., Zhang, K., Chon, B.H. and Choi, H.J. 2013. Rheology and polymer flooding characteristics of partially hydrolyzed polyacrylamide for enhanced heavy oil recovery. *Journal of Applied Polymer Science.* **127**(6), pp.4833-4839.

Kalinin, E. and Dreitser, G. 1998. in Heat Exchangers. *Advances in Heat Transfer.* **31**, p159.

Kamel, A. and Shah, S.N. 2009. Effects of salinity and temperature on drag reduction characteristics of polymers in straight circular pipes. *Journal of petroleum Science and Engineering.* **67**(1), pp.23-33.

Katiyar, R.S. and Jha, P.K. 2017. Phase behavior of aqueous polyacrylic acid solutions using atomistic molecular dynamics simulations of model oligomers. *Polymer.* **114**, pp.266-276.

Kawale, D., Marques, E., Zitha, P.L., Kreutzer, M.T., Rossen, W.R. and Boukany, P.E. 2017. Elastic instabilities during the flow of hydrolyzed polyacrylamide solution in porous media: effect of pore-shape and salt. *Soft Matter.* **13**(4), pp.765-775.

Keblinski, P., Phillpot, S., Choi, S. and Eastman, J. 2002. Mechanisms of heat flow in suspensions of nano-sized particles (nanofluids). *International journal of heat and mass transfer.* **45**(4), pp.855-863.

Khan, N., Pinjala, D. and Toh, K. 2004. Pool boiling heat transfer enhancement by surface modification/micro-structures for electronics cooling: a review. In: *Proceedings of 6th Electronics Packaging Technology Conference (EPTC 2004)(IEEE Cat. No. 04EX971)*: IEEE, pp.273-280.

Kim, J. 2009. Review of nucleate pool boiling bubble heat transfer mechanisms. *International Journal of Multiphase Flow.* **35**(12), pp.1067-1076.

Kim, Y.-H., Lee, S.-M., Lee, K.-J., Paik, U. and Park, J.-G. 2008. Constraints on removal of Si 3 N 4 film with conformation-controlled poly (acrylic acid) in shallow-trench isolation chemical–mechanical planarization (STI CMP). *Journal of Materials Research.* **23**(1), pp.49-54.

Koda, S., Nomura, H. and Nagasawa, M. 1982. Raman spectroscopic studies on the interaction between counterion and polyion. *Biophysical chemistry.* **15**(1), pp.65-72.

Kolmogorov, A.N. 1941. The local structure of turbulence in incompressible viscous fluid for very large Reynolds numbers. In: *Dokl. Akad. Nauk SSSR*, pp.299-303.

Kratky, O. and Porod, G. 1980. Rec. trav. chim.(1949) 68, 1106. *CrossRef Google Scholar.*

Laguecir, A., Ulrich, S., Labille, J., Fatin-Rouge, N., Stoll, S. and Buffle, J. 2006. Size and pH effect on electrical and conformational behavior of poly (acrylic acid): simulation and experiment. *European Polymer Journal.* **42**(5), pp.1135-1144.

Lajvardi, M., Moghimi-Rad, J., Hadi, I., Gavili, A., Isfahani, T.D., Zabihi, F. and Sabbaghzadeh, J. 2010. Experimental investigation for enhanced ferrofluid heat transfer under magnetic field effect. *Journal of Magnetism and Magnetic Materials.* **322**(21), pp.3508-3513.

Landau, L. and Lifshitz, E. 1987. Fluid mechanics. 1987. *Course of Theoretical Physics.*

Laohalertdecha, S., Naphon, P. and Wongwises, S. 2007. A review of electrohydrodynamic enhancement of heat transfer. *Renewable and Sustainable Energy Reviews.* **11**(5), pp.858-876.

Larson. 2000a. Fluid dynamics: turbulence without inertia. *Nature.* **405**(6782), p27.

Larson, R.G. 2000b. Fluid dynamics: Turbulence without inertia. *Nature.* **405**(6782), pp.27-28.

Larson, R.G., Shaqfeh, E.S. and Muller, S.J.J.J.o.F.M. 1990. A purely elastic instability in Taylor–Couette flow. *Journal of Fluid Mechanics.* **218**, pp.573-600.

Latrache, N., Crumeyrolle, O. and Mutabazi, I. 2012. Transition to turbulence in a flow of a shear-thinning viscoelastic solution in a Taylor-Couette cell. *Phys Rev E Stat Nonlin Soft Matter Phys.* **86**(5 Pt 2), p056305.

Lau, K.F., Alper, H.E., Thacher, T.S. and Stouch, T.R. 1994. Effects of switching functions on the behavior of liquid water in molecular dynamics simulations. *The Journal of Physical Chemistry.* **98**(35), pp.8785-8792.

Léal, L., Miscevic, M., Lavieille, P., Amokrane, M., Pigache, F., Topin, F., Nogarède, B. and Tadrist, L. 2013. An overview of heat transfer enhancement methods and new perspectives: Focus on active methods using electroactive materials. *International Journal of Heat and Mass Transfer.* **61**, pp.505-524.

Lee, W., Cho, Y., Hartnett, J.J.L.i.H. and Transfer, M. 1981. Thermal conductivity measurements of non-Newtonian fluids. **8**(4), pp.255-259.

Li, D.-Y., Li, X.-B., Zhang, H.-N., Li, F.-C., Qian, S.-Z. and Joo, S.W. 2016a. Measuring heat transfer performance of viscoelastic fluid flow in curved microchannel using Ti–Pt film temperature sensor. *Experimental Thermal and Fluid Science.* **77**, pp.226-233.

Li, D.-Y., Li, X.-B., Zhang, H.-N., Li, F.-C., Qian, S. and Joo, S.W. 2017. Efficient heat transfer enhancement by elastic turbulence with polymer solution in a curved microchannel. *Microfluidics and Nanofluidics.* **21**(1).

Li, F.-C., Kinoshita, H., Li, X.-B., Oishi, M., Fujii, T. and Oshima, M. 2010. Creation of very-low-Reynolds-number chaotic fluid motions in microchannels using viscoelastic surfactant solution. *Experimental Thermal and Fluid Science.* **34**(1), pp.20-27.

Li, K. and Parker, J. 1967. Acoustical effects on free convective heat transfer from a horizontal wire. *J. Heat Transfer.* **89**(3), pp.277-278.

Li, X.-B., Oishi, M., Matsuo, T., Oshima, M. and Li, F.-C. 2016b. Measurement of Viscoelastic Fluid Flow in the Curved Microchannel Using Digital Holographic Microscope and Polarized Camera. *Journal of Fluids Engineering.* **138**(9), p091401.

Li, X.-B., Oishi, M., Oshima, M., Li, F.-C. and Li, S.-J. 2016c. Measuring elasticity-induced unstable flow structures in a curved microchannel

using confocal micro particle image velocimetry. *Experimental Thermal and Fluid Science.* **75**, pp.118-128.

Ligrani, P., Copeland, D., Ren, C., Su, M. and Suzuki, M. 2017. Heat Transfer Enhancements from Elastic Turbulence Using Sucrose-Based Polymer Solutions. *Journal of Thermophysics and Heat Transfer.* **32**(1), pp.51-60.

Ligrani, P., Lund, B. and Fatemi, A. 2016. Miniature Viscous Disk Pump: Performance Variations From Non-Newtonian Elastic Turbulence. *Journal of Fluids Engineering.* **139**(2), p021104.

Limbach, H.J. and Holm, C. 2003. Single-chain properties of polyelectrolytes in poor solvent. *The Journal of Physical Chemistry B.* **107**(32), pp.8041-8055.

Liu, Y., Jun, Y. and Steinberg, V. 2007a. Longest relaxation times of double-stranded and single-stranded DNA. *Macromolecules.* **40**(6), pp.2172-2176.

Liu, Z.-h., Xiong, J.-g. and Bao, R. 2007b. Boiling heat transfer characteristics of nanofluids in a flat heat pipe evaporator with micro-grooved heating surface. *International Journal of Multiphase Flow.* **33**(12), pp.1284-1295.

Loh, B.-G., Hyun, S., Ro, P.I. and Kleinstreuer, C. 2002. Acoustic streaming induced by ultrasonic flexural vibrations and associated enhancement of convective heat transfer. *The Journal of the Acoustical Society of America.* **111**(2), pp.875-883.

Lund, B., Ligrani, P. and Brown, M. 2016. DEVELOPMENT AND CONTROL OF ELASTIC TURBULENCE WITHIN A MICRO-SCALE VISCOUS DISC PUMP. *Advances and Applications in Fluid Mechanics.* **19**(3), p517.

Lyubartsev, A.P. and Laaksonen, A. 1996. Concentration effects in aqueous NaCl solutions. A molecular dynamics simulation. *The Journal of Physical Chemistry.* **100**(40), pp.16410-16418.

Ma, Y., Zhang, H., Hao, Q., Liu, G., Wang, H. and Yuan, S. 2016. Molecular Dynamics Study on Mechanism of Preformed Particle Gel Transporting Through Nanopores: Deformation and Dehydration. *The Journal of Physical Chemistry C.* **120**(34), pp.19389-19395.

Majumdar, S. and Sood, A.K. 2011. Universality and scaling behavior of injected power in elastic turbulence in wormlike micellar gel. *Phys Rev E Stat Nonlin Soft Matter Phys.* **84**(1 Pt 2), p015302.

Malm, A.V. and Waigh, T.A. 2017. Elastic turbulence in entangled semi-dilute DNA solutions measured with optical coherence tomography velocimetry. *Sci Rep.* **7**(1), p1186.

Manglik, R.M. and Bergles, A.E. 1993. Heat transfer and pressure drop correlations for twisted-tape inserts in isothermal tubes: part I—laminar flows.

Manglik, R.M. and Bergles, A.E. 2003. Swirl flow heat transfer and pressure drop with twisted-tape inserts. *Advances in heat transfer.*   Elsevier, pp.183-266.

Mantha, S. and Yethiraj, A. 2015. Conformational properties of sodium polystyrenesulfonate in water: Insights from a coarse-grained model with explicit solvent. *The Journal of Physical Chemistry B.* **119**(34), pp.11010-11018.

Matsubara, M. and Alfredsson, P.H. 2001. Disturbance growth in boundary layers subjected to free-stream turbulence. *Journal of fluid mechanics.* **430**, pp.149-168.

Meng, H. and Hu, J. 2010. A brief review of stimulus-active polymers responsive to thermal, light, magnetic, electric, and water/solvent stimuli. *Journal of Intelligent Material Systems and Structures.* **21**(9), pp.859-885.

Miscevic, M., Rahli, O., Tadrist, L. and Topin, F. 2006. Experiments on flows, boiling and heat transfer in porous media: Emphasis on bottom injection. *Nuclear Engineering and Design.* **236**(19-21), pp.2084-2103.

Mitchell, J., Lyons, K., Howe, A.M. and Clarke, A. 2016. Viscoelastic polymer flows and elastic turbulence in three-dimensional porous structures. *Soft Matter.* **12**(2), pp.460-468.

Molloy, P., Smith, M. and Cowling, M. 2000. The effects of salinity and temperature on the behaviour of polyacrylamide gels. *Materials & Design.* **21**(3), pp.169-174.

Molnar, F. and Rieger, J. 2005. "Like-charge attraction" between anionic polyelectrolytes: molecular dynamics simulations. *Langmuir.* **21**(2), pp.786-789.

Muller, G. 1981. Thermal stability of high-molecular-weight polyacrylamide aqueous solutions. *Polymer Bulletin.* **5**(1), pp.31-37.

Muller, G., Fenyo, J. and Selegny, E. 1980. High molecular weight hydrolyzed polyacrylamides. III. Effect of temperature on chemical stability. *Journal of Applied Polymer Science.* **25**(4), pp.627-633.

Muller, G., Laine, J. and Fenyo, J. 1979. High‑molecular‑weight hydrolyzed polyacrylamides. I. Characterization. Effect of salts on the conformational properties. *Journal of Polymer Science: Polymer Chemistry Edition.* **17**(3), pp.659-672.

Muller, S.J., Larson, R.G. and Shaqfeh, E.S.J.R.A. 1989. A purely elastic transition in Taylor-Couette flow. *Rheologica Acta.* **28**(6), pp.499-503.

Muthukumar, M. 2004. Theory of counter-ion condensation on flexible polyelectrolytes: adsorption mechanism. *The Journal of chemical physics.* **120**(19), pp.9343-9350.

Nasr-El-Din, H., Hawkins, B. and Green, K. 1991. Viscosity behavior of alkaline, surfactant, polyacrylamide solutions used for enhanced oil recovery. In: *SPE International Symposium on Oilfield Chemistry*: Society of Petroleum Engineers.

Noda, I., Imai, M., Kitano, T. and Nagasawa, M. 1983. Particle scattering factor of polymer chains with excluded volumes. *Macromolecules.* **16**(3), pp.425-428.

Norouzi, M., Varedi, S.R. and Zamani, M. 2016. Wake instability of viscoelastic flows past an unconfined inclined square cylinder. *Physics of Fluids.* **28**(2), p023101.

Oldiges, C. and Tönsing, T. 2002. Molecular dynamic simulation of structural, mobility effects between dilute aqueous CH 3 CN solution and crosslinked PAA Part 1. Structure. *Physical Chemistry Chemical Physics.* **4**(9), pp.1628-1636.

Omidvarborna, H., Mehrabani-Zeinabad, A. and Esfahany, M.N. 2009. Effect of electrohydrodynamic (EHD) on condensation of R-134a in

presence of non-condensable gas. *International Communications in Heat and Mass Transfer.* **36**(3), pp.286-291.

Oostenbrink, C., Villa, A., Mark, A.E. and Van Gunsteren, W.F. 2004. A biomolecular force field based on the free enthalpy of hydration and solvation: the GROMOS force‐field parameter sets 53A5 and 53A6. *Journal of computational chemistry.* **25**(13), pp.1656-1676.

Pak, B.C. and Cho, Y.I. 1998. Hydrodynamic and heat transfer study of dispersed fluids with submicron metallic oxide particles. *Experimental Heat Transfer an International Journal.* **11**(2), pp.151-170.

Pan, L., Morozov, A., Wagner, C. and Arratia, P.E. 2013. Nonlinear elastic instability in channel flows at low Reynolds numbers. *Phys Rev Lett.* **110**(17), p174502.

Pan, Z., Campbell, A. and Somasundaran, P. 2001. Polyacrylic acid adsorption and conformation in concentrated alumina suspensions. *Colloids and Surfaces A: Physicochemical and Engineering Aspects.* **191**(1-2), pp.71-78.

Pantano, D.A., Klein, M.L., Discher, D.E. and Moore, P.B. 2011. Morphologies of charged diblock copolymers simulated with a neutral coarse-grained model. *The Journal of Physical Chemistry B.* **115**(16), pp.4689-4695.

Park, K.-J. and Jung, D. 2007a. Boiling heat transfer enhancement with carbon nanotubes for refrigerants used in building air-conditioning. *Energy and Buildings.* **39**(9), pp.1061-1064.

Park, K.-J. and Jung, D. 2007b. Enhancement of nucleate boiling heat transfer using carbon nanotubes. *International Journal of Heat and Mass Transfer.* **50**(21-22), pp.4499-4502.

Patel, K.H., Chockalingam, R. and Natarajan, U. 2017. Molecular dynamic simulations study of the effect of salt valency on structure and thermodynamic solvation behaviour of anionic polyacrylate PAA in aqueous solutions. *Molecular Simulation.* **43**(9), pp.691-705.

Patra, M. and Karttunen, M. 2004. Systematic comparison of force fields for microscopic simulations of NaCl in aqueous solutions: diffusion, free energy of hydration, and structural properties. *Journal of computational chemistry.* **25**(5), pp.678-689.

Peterlin, A. 1955. Excluded volume effect on light scattering of the coiled linear macromolecule. *The Journal of Chemical Physics.* **23**(12), pp.2464-2465.

Phan, H.T. 2010. *Effects of nano-and micro-surface treatments on boiling heat transfer.* thesis.

Phan, H.T., Caney, N., Marty, P., Colasson, S. and Gavillet, J. 2010. A model to predict the effect of contact angle on the bubble departure diameter during heterogeneous boiling. *International Communications in Heat and Mass Transfer.* **37**(8), pp.964-969.

Philip, J., Shima, P. and Raj, B. 2008. Evidence for enhanced thermal conduction through percolating structures in nanofluids. *Nanotechnology.* **19**(30), p305706.

Pirmohammadi, M. and Ghassemi, M. 2009. Effect of magnetic field on convection heat transfer inside a tilted square enclosure. *International Communications in Heat and Mass Transfer.* **36**(7), pp.776-780.

Pohlmeier, A. and Haber-Pohlmeier, S. 2004. Ionization of short polymethacrylic acid: titration, DLS, and model calculations. *Journal of colloid and interface science.* **273**(2), pp.369-380.

Pohlmeier, A., Haber-Pohlmeier, S.J.J.o.c. and science, i. 2004. Ionization of short polymethacrylic acid: titration, DLS, and model calculations. **273**(2), pp.369-380.

Poniewski, M. and Thome, J. 2008. *Nucleate boiling on micro-structured surfaces.* Heat Transfer Research, Inc.(HTRI).

Poole, R.J., Budhiraja, B., Cain, A.R. and Scott, P.A. 2012. Emulsification using elastic turbulence. *Journal of Non-Newtonian Fluid Mechanics.* **177-178**, pp.15-18.

Promvonge, P. 2008. Thermal augmentation in circular tube with twisted tape and wire coil turbulators. *Energy Conversion and Management.* **49**(11), pp.2949-2955.

Promvonge, P. and Eiamsa-Ard, S. 2007a. Heat transfer augmentation in a circular tube using V-nozzle turbulator inserts and snail entry. *Experimental Thermal and Fluid Science.* **32**(1), pp.332-340.

Promvonge, P. and Eiamsa-ard, S. 2007b. Heat transfer behaviors in a tube with combined conical-ring and twisted-tape insert. *International Communications in Heat and Mass Transfer.* **34**(7), pp.849-859.

Qin, B. and Arratia, P.E. 2016. Elastic Turbulence in Channel Flows at Low Reynolds number. *arXiv preprint arXiv:1609.08532.*

Qin, B. and Arratia, P.E. 2017. Characterizing elastic turbulence in channel flows at low Reynolds number. *Physical Review Fluids.* **2**(8).

Rahman, A. 1964. Correlations in the motion of atoms in liquid argon. *Physical Review.* **136**(2A), pA405.

Ramachandran, S., Katha, A.R., Kolake, S.M., Jung, B. and Han, S. 2013. Dynamics of dilute solutions of poly (aspartic acid) and its sodium salt elucidated from atomistic molecular dynamics simulations with explicit water. *The Journal of Physical Chemistry B.* **117**(44), pp.13906-13913.

Ravigururajan, T. and Bergles, A. 1996. Development and verification of general correlations for pressure drop and heat transfer in single-phase turbulent flow in enhanced tubes. *Experimental Thermal and Fluid Science.* **13**(1), pp.55-70.

Reith, D., Müller, B., Müller-Plathe, F. and Wiegand, S. 2002. How does the chain extension of poly (acrylic acid) scale in aqueous solution? A combined study with light scattering and computer simulation. *The Journal of chemical physics.* **116**(20), pp.9100-9106.

Sappidi, P. and Natarajan, U. 2016. Polyelectrolyte conformational transition in aqueous solvent mixture influenced by hydrophobic interactions and hydrogen bonding effects: PAA–water–ethanol. *Journal of Molecular Graphics and Modelling.* **64**, pp.60-74.

Satoh, K., Kuroki, S. and Satoh, M. 2013a. Charge density-dependent coil–globule transition of alkali metal polycarboxylates in aqueous organic solvent mixtures. *Colloid and Polymer Science.* **291**(6), pp.1453-1462.

Satoh, K., Kuroki, S., Satoh, M.J.C. and Science, P. 2013b. Charge density-dependent coil–globule transition of alkali metal polycarboxylates in aqueous organic solvent mixtures. **291**(6), pp.1453-1462.

Schiamberg, B.A., Shereda, L.T., Hu, H.U.A. and Larson, R.G. 2006. Transitional pathway to elastic turbulence in torsional, parallel-plate flow of a polymer solution. *Journal of Fluid Mechanics.* **554**(-1), p191.

Scholz, C., Wirner, F., Gomez-Solano, J.R. and Bechinger, C. 2014. Enhanced dispersion by elastic turbulence in porous media. *EPL (Europhysics Letters).* **107**(5), p54003.

Schweins, R., Hollmann, J. and Huber, K. 2003a. Dilute solution behaviour of sodium polyacrylate chains in aqueous NaCl solutions. *Polymer.* **44**(23), pp.7131-7141.

Schweins, R. and Huber, K. 2001. Collapse of sodium polyacrylate chains in calcium salt solutions. *The European Physical Journal E.* **5**(1), pp.117-126.

Schweins, R., Lindner, P. and Huber, K. 2003b. Calcium induced shrinking of NaPA chains: A SANS investigation of single chain behavior. *Macromolecules.* **36**(25), pp.9564-9573.

Seright, R.S., Campbell, A., Mozley, P. and Han, P. 2010. Stability of partially hydrolyzed polyacrylamides at elevated temperatures in the absence of divalent cations. *Spe Journal.* **15**(02), pp.341-348.

Shang, B.Z., Wang, Z. and Larson, R.G. 2008. Molecular dynamics simulation of interactions between a sodium dodecyl sulfate micelle and a poly (ethylene oxide) polymer. *The Journal of Physical Chemistry B.* **112**(10), pp.2888-2900.

Sheikholeslami, M., Hatami, M. and Ganji, D. 2014. Nanofluid flow and heat transfer in a rotating system in the presence of a magnetic field. *Journal of Molecular liquids.* **190**, pp.112-120.

Sheikholeslami, M., Rashidi, M. and Ganji, D. 2015. Effect of non-uniform magnetic field on forced convection heat transfer of Fe3O4–water nanofluid. *Computer Methods in Applied Mechanics and Engineering.* **294**, pp.299-312.

Sheikholeslami, M., Vajravelu, K. and Rashidi, M.M. 2016. Forced convection heat transfer in a semi annulus under the influence of a variable magnetic field. *International journal of heat and mass transfer.* **92**, pp.339-348.

Shi, X. and Christopher, G.F. 2016. Growth of viscoelastic instabilities around linear cylinder arrays. *Physics of Fluids.* **28**(12), p124102.

Sitar, S., Aseyev, V. and Kogej, K. 2014. Differences in association behavior of isotactic and atactic poly (methacrylic acid). *Polymer.* **55**(3), pp.848-854.

Smalley, R.E. 2005. Future global energy prosperity: the terawatt challenge. *Mrs Bulletin.* **30**(6), pp.412-417.

Souliès, A., Aubril, J., Castelain, C. and Burghelea, T. 2017. Characterisation of elastic turbulence in a serpentine micro-channel. *Physics of Fluids.* **29**(8).

Sousa, P.C., Pinho, F.T. and Alves, M.A. 2018. Purely-elastic flow instabilities and elastic turbulence in microfluidic cross-slot devices. *Soft Matter.* **14**(8), pp.1344-1354.

Sparrow, E.M. and Cess, R. 1961. The effect of a magnetic field on free convection heat transfer. *International Journal of Heat and Mass Transfer.* **3**(4), pp.267-274.

Stokes, J.R., Graham, L.J., Lawson, N.J. and Boger, D.V. 2001a. Swirling flow of viscoelastic fluids. Part 1. Interaction between inertia and elasticity. *Journal of Fluid Mechanics.* **429**, pp.67-115.

Stokes, J.R., Graham, L.J., Lawson, N.J. and Boger, D.V. 2001b. Swirling flow of viscoelastic fluids. Part 2. Elastic effects. *Journal of Fluid Mechanics.* **429**, pp.117-153.

Sulatha, M.S. and Natarajan, U. 2011. Origin of the difference in structural behavior of poly (acrylic acid) and poly (methacrylic acid) in aqueous solution discerned by explicit-solvent explicit-ion MD simulations. *Industrial & Engineering Chemistry Research.* **50**(21), pp.11785-11796.

Sulatha, M.S. and Natarajan, U. 2012. Molecular dynamics simulations of PAA–PMA polyelectrolyte copolymers in dilute aqueous solution: chain conformations and hydration properties. *Industrial & Engineering Chemistry Research.* **51**(33), pp.10833-10839.

Swindells, J.F., Snyder, C., Hardy, R.C. and Golden, P. 1958. *Viscosities of sucrose solutions at various temperatures: Tables of recalculated values.* US Department of Commerce, National Bureau of Standards.

Takahashi, A. and Nagasawa, M. 1964. Excluded volume of polyelectrolyte in salt solutions. *Journal of the American Chemical Society.* **86**(4), pp.543-548.

Takani, S. and Satoh, M. 2016a. Temperature-induced coil-globule transition of alkali metal polyacrylates in aqueous organic solvent mixtures. *Journal of Macromolecular Science, Part B.* **55**(9), pp.955-967.

Takani, S. and Satoh, M.J.J.o.M.S., Part B. 2016b. Temperature-induced coil-globule transition of alkali metal polyacrylates in aqueous organic solvent mixtures. **55**(9), pp.955-967.

Tennekes, H. and Lumley, J.L. 1972. *A first course in turbulence.* MIT press.

Tildesley, D. and Allen, M. 1987. Computer simulation of liquids. *Clarendon, Oxford.*

Toms, B.A. 1948. Some observations on the flow of linear polymer solutions through straight tubes at large Reynolds numbers. In: *Proceedings of the 1st International Congress on Rheology*: North-Holland Amsterdam, pp.135-141.

Traore, B., Castelain, C. and Burghelea, T. 2015. Efficient heat transfer in a regime of elastic turbulence. *Journal of Non-Newtonian Fluid Mechanics.* **223**, pp.62-76.

Tritton, D. 1988. *Physical fluid dynamics, Clarendon.* Oxford.

Uchida, H. and Matsuoka, M. 2004. Molecular dynamics simulation of solution structure and dynamics of aqueous sodium chloride solutions from dilute to supersaturated concentration. *Fluid Phase Equilibria.* **219**(1), pp.49-54.

Uttarwar, S. and Raja Rao, M. 1985. Augmentation of laminar flow heat transfer in tubes by means of wire coil inserts.

Varshney, A. and Steinberg, V. 2018. Drag enhancement and drag reduction in viscoelastic flow. *Physical Review Fluids.* **3**(10), p103302.

Vinogradov, G. and Manin, V.J.K.-Z.u.Z.f.P. 1965. An experimental study of elastic turbulence. *Kolloid Zeitschrift & Zeitschrift fiir Polymere.* **201**(2), pp.93-98.

Viskanta, R. 2018. Phase-change heat transfer. *Solar Heat Storage.* CRC Press, pp.153-222.

Wang, H., Zhang, H., Liu, C. and Yuan, S. 2012. Coarse-grained molecular dynamics simulation of self-assembly of polyacrylamide and sodium dodecylsulfate in aqueous solution. *Journal of colloid and interface science.* **386**(1), pp.205-211.

Wang, L. and Sunden, B. 2002. Performance comparison of some tube inserts. *International Communications in Heat and Mass Transfer.* **29**(1), pp.45-56.

Wang, Q., Taniguchi, T. and Fredrickson, G.H. 2004. Self-consistent field theory of polyelectrolyte systems. *The Journal of Physical Chemistry B.* **108**(21), pp.6733-6744.

Wang, Y., Do-Quang, M. and Amberg, G. 2016. Viscoelastic droplet dynamics in a Y-shaped capillary channel. *Physics of fluids.* **28**(3), p033103.

Ward, J. and Martin, F.D. 1981. Prediction of viscosity for partially hydrolyzed polyacrylamide solutions in the presence of calcium and magnesium ions. *Society of Petroleum Engineers Journal.* **21**(05), pp.623-631.

Wayner, P.C. 1999. Intermolecular forces in phase‐change heat transfer: 1998 Kern award review. *AIChE journal.* **45**(10), pp.2055-2068.

Weissenberg, K. 1947. A continuum theory of rheological phenomena. *Nature.* **159**(4035), pp.310-311.

Wen, D. and Ding, Y. 2005. Experimental investigation into the pool boiling heat transfer of aqueous based γ-alumina nanofluids. *Journal of Nanoparticle Research.* **7**(2-3), pp.265-274.

Wen, D., Ding, Y. and Williams, R.A. 2005. Pool boiling heat transfer of aqueous based Ti02ánanofluids. *Journal of Enhanced Heat Transfer.* **13**(3), pp.245-260.

Whalley, R., Abed, W., Dennis, D. and Poole, R. 2015. Enhancing heat transfer at the micro-scale using elastic turbulence. *Theoretical and Applied Mechanics Letters.* **5**(3), pp.103-106.

Witharana, S. 2003. *Boiling of refrigerants on enhanced surfaces and boiling of nanofluids.* thesis, Energiteknik.

Wu, C., Chan, K.K. and Xia, K.-Q. 1995a. Experimental study of the spectral distribution of the light scattered from flexible macromolecules in very dilute solution. *Macromolecules.* **28**(4), pp.1032-1037.

Wu, C., Chan, K.K. and Xia, K.-Q.J.M. 1995b. Experimental study of the spectral distribution of the light scattered from flexible macromolecules in very dilute solution. **28**(4), pp.1032-1037.

Yao, G., Zhao, J., Ramisetti, S.B. and Wen, D. 2018. Atomistic Molecular Dynamic Simulation of Dilute Poly(acrylic acid) Solution: Effects of Simulation Size Sensitivity and Ionic Strength. *Industrial & Engineering Chemistry Research.* **57**(50), pp.17129-17141.

Ye, T., Song, Y. and Zheng, Q. 2016. Salt response and rheological behavior of acrylamide-sulfobetaine copolymer. *Colloid and Polymer Science.* **294**(2), pp.389-397.

Yuan, S.-M., Yan, H., Lv, K., Liu, C.-B. and Yuan, S.-L. 2010. Surface behavior of a model surfactant: A theoretical simulation study. *Journal of colloid and interface science.* **348**(1), pp.159-166.

Zalba, B., Marın, J.M., Cabeza, L.F. and Mehling, H. 2003. Review on thermal energy storage with phase change: materials, heat transfer analysis and applications. *Applied thermal engineering.* **23**(3), pp.251-283.

Zhang, H.-N., Li, F.-C., Li, X.-B., Li, D.-Y., Cai, W.-H. and Yu, B. 2016a. Characteristics and generation of elastic turbulence in a three-dimensional parallel plate channel using direct numerical simulation. *Chinese Physics B.* **25**(9), p094701.

Zhang, J., Borg, M.K., Ritos, K. and Reese, J.M. 2016b. Electrowetting controls the deposit patterns of evaporated salt water nanodroplets. *Langmuir.* **32**(6), pp.1542-1549.

Zhang, J., Borg, M.K., Sefiane, K. and Reese, J.M. 2015. Wetting and evaporation of salt-water nanodroplets: A molecular dynamics investigation. *Physical Review E.* **92**(5), p052403.

Zhang, J., Borg, M.K., Sefiane, K., Reese, J.M.J.P.R.E.S.N. and Physics, S.M. Wetting and evaporation of salt-water nanodroplets: A molecular dynamics investigation. **92**(5), p052403.

Zhou, Z. and Daivis, P.J. 2009. Molecular dynamics study of polymer conformation as a function of concentration and solvent quality. *The Journal of chemical physics.* **130**(22), p224904.

Zhu, S.B. and Robinson, G.W. 1992. Molecular‐dynamics computer simulation of an aqueous NaCl solution: Structure. *The Journal of chemical physics.* **97**(6), pp.4336-4348.

Zilz, J., Poole, R.J., Alves, M.A., Bartolo, D., Levaché, B. and Lindner, A. 2012. Geometric scaling of a purely elastic flow instability in serpentine channels. *Journal of Fluid Mechanics.* **712**, pp.203-218.

Appendix A
MD simulation details for polymer morphology study

Table A.1 GROMOS Force Field Parameters Used in MD simulation

Non-bonded parameters

Atom type	q(e)	C_6 [kJ·mol^{-1}·nm^6]	C_{12} [kJ·mol^{-1}·nm^{12}]	M(amu)
CH_3	0	0.0096138	2.664624×10^{-5}	15.0350
CH_2	0	0.00746841	3.396558×10^{-5}	14.0270
CH	0	0.00606841	9.70225×10^{-5}	13.0190
C	0	0.00239708	2.053489×10^{-4}	12.0100
$C(COO^-)$	0.27	0.00234062	4.937284×10^{-6}	12.0100
$O(COO^-)$	-0.635	0.00226195	7.4149321×10^{-7}	15.9994
C(COOH)	0.33	0.00234062	4.937284×10^{-6}	12.0100
=O(COOH)	-0.45	0.00226195	1×10^{-6}	15.9994
O(COOH)	-0.288	0.00226195	1.505529×10^{-6}	15.9994
H(COOH)	0.408	0	0	1.0080
Na^+	+1	7.206312×10^{-5}	2.1025×10^{-8}	22.9898
Cl^-	-1	0.01380625	0.0001069156	35.4530
$C(CONH_2)$	0.38	0.00234062	4.937284×10^{-6}	12.0100
$O(CONH_2)$	-0.38	0.00226195	1×10^{-6}	15.9994
$N(CONH_2)$	-0.48	0.00243640	5.0625e-06	14.0067
$H(CONH_2)$	0.24	0	0	1.008

Bonded Parameters

bond type	length [Å]	force constant
CH_2-CH	1.53	$7.1500e \times 10^6$
CH-C	1.53	$7.1500e \times 10^6$
C-O	1.25	$1.3400e \times 10^7$
C=O	1.23	$1.6600e \times 10^7$

C-OH	1.36	$1.0200e \times 10^7$
O-H	1.00	$1.5700e \times 10^7$
C-NT	1.33	$1.0600e \times 10^7$
NT-H	1.00	$1.8700e \times 10^7$

Angle Parameters

angle type	degree [deg]	force constant [kJ/(mol·rad^2)]
CH_2-CH-CH_2	111.0	530
CH_2-CH-C	111.0	530
CH-C-O	117.0	635
O-C-O	126.0	770
CH-C=O	121.0	685
CH-C-OH	115.0	610
O=C-OH	124.0	730
C-O-H	109.5	450
H-NT-H	120.0	445

Proper Torsional Potential

Dihedral type	force constant [kJ/mol]	Degree [Deg]	n
CH-CH_2-CH-C	5.92	0	3
CH_2-CH-C-O (carboxylate)	1	0	6
CH_2-CH-C-O (carboxylic acid)	1	0	6
CH-C-O-H	16.7	180	2
CH_1-CH-NT-H	33.5	180	2

Ryckaert-Bellmans

CH$_2$-CH-CH$_2$-CH	C$_0$=8.397, C$_1$=16.785, C$_2$=1.134, C$_4$=0, C$_5$=0

Table A.2 20 monomers isotatic PAA chain with random deprotonation

Monomer	Tacticity	Charge density					
		$f = 0$	$f = 0.2$	$f = 0.4$	$f = 0.6$	$f = 0.8$	$f = 1$
1	Up	COOH	COOH	COOH	COOH	COO$^-$	COO$^-$
2	Up	COOH	COOH	COOH	COOH	COO$^-$	COO$^-$
3	Up	COOH	COOH	COOH	COO$^-$	COO$^-$	COO$^-$
4	Up	COOH	COO$^-$	COOH	COO$^-$	COO$^-$	COO$^-$
5	Up	COOH	COO$^-$	COO$^-$	COOH	COO$^-$	COO$^-$
6	Up	COOH	COOH	COOH	COOH	COO$^-$	COO$^-$
7	Up	COOH	COOH	COO$^-$	COOH	COOH	COO$^-$
8	Up	COOH	COOH	COO$^-$	COO$^-$	COO$^-$	COO$^-$
9	Up	COOH	COOH	COO$^-$	COOH	COOH	COO$^-$
10	Up	COOH	COOH	COO$^-$	COO$^-$	COO$^-$	COO$^-$
11	Up	COOH	COOH	COO$^-$	COO$^-$	COO$^-$	COO$^-$
12	Up	COOH	COOH	COOH	COO$^-$	COO$^-$	COO$^-$
13	Up	COOH	COOH	COOH	COO$^-$	COO$^-$	COO$^-$
14	Up	COOH	COOH	COOH	COO$^-$	COO$^-$	COO$^-$
15	Up	COOH	COO$^-$	COOH	COOH	COO$^-$	COO$^-$
16	Up	COOH	COOH	COO$^-$	COOH	COO$^-$	COO$^-$
17	Up	COOH	COOH	COOH	COO$^-$	COOH	COO$^-$
18	Up	COOH	COOH	COOH	COO$^-$	COO$^-$	COO$^-$
19	Up	COOH	COO$^-$	COOH	COO$^-$	COO$^-$	COO$^-$
20	Up	COOH	COOH	COO$^-$	COO$^-$	COOH	COO$^-$

Table A.3 20 monomers syndiotactic PAA chain with random deprotonation

Monomer	Tacticity	Charge density

		f = 0	f = 0.2	f = 0.4	f = 0.6	f = 0.8	f = 1
1	Up	COOH	COOH	COOH	COOH	COO$^-$	COO$^-$
2	Down	COOH	COOH	COOH	COOH	COO$^-$	COO$^-$
3	Up	COOH	COOH	COOH	COO$^-$	COO$^-$	COO$^-$
4	Down	COOH	COO$^-$	COOH	COO$^-$	COO$^-$	COO$^-$
5	Up	COOH	COO$^-$	COO$^-$	COOH	COO$^-$	COO$^-$
6	Down	COOH	COOH	COOH	COOH	COO$^-$	COO$^-$
7	Up	COOH	COOH	COO$^-$	COOH	COOH	COO$^-$
8	Down	COOH	COOH	COO$^-$	COO$^-$	COO$^-$	COO$^-$
9	Up	COOH	COOH	COO$^-$	COOH	COOH	COO$^-$
10	Down	COOH	COOH	COO$^-$	COO$^-$	COO$^-$	COO$^-$
11	Up	COOH	COOH	COO$^-$	COO$^-$	COO$^-$	COO$^-$
12	Down	COOH	COOH	COOH	COO$^-$	COO$^-$	COO$^-$
13	Up	COOH	COOH	COOH	COO$^-$	COO$^-$	COO$^-$
14	Down	COOH	COOH	COOH	COO$^-$	COO$^-$	COO$^-$
15	Up	COOH	COO$^-$	COOH	COOH	COO$^-$	COO$^-$
16	Down	COOH	COOH	COO$^-$	COOH	COO$^-$	COO$^-$
17	Up	COOH	COOH	COOH	COO$^-$	COOH	COO$^-$
18	Down	COOH	COOH	COOH	COO$^-$	COO$^-$	COO$^-$
19	Up	COOH	COO$^-$	COOH	COO$^-$	COO$^-$	COO$^-$
20	Down	COOH	COOH	COO$^-$	COO$^-$	COOH	COO$^-$

Table A.4 20 monomers atactic PAA chain with random deprotonation

Monomer	Tacticity	Charge density					
		f = 0	f = 0.2	f = 0.4	f = 0.6	f = 0.8	f = 1
1	Down	COOH	COOH	COOH	COOH	COO$^-$	COO$^-$
2	Up	COOH	COOH	COOH	COOH	COO$^-$	COO$^-$
3	Down	COOH	COOH	COOH	COO$^-$	COO$^-$	COO$^-$

4	Up	COOH	COO⁻	COOH	COO⁻	COO⁻	COO⁻
5	Down	COOH	COO⁻	COO⁻	COOH	COO⁻	COO⁻
6	Up	COOH	COOH	COOH	COOH	COO⁻	COO⁻
7	Down	COOH	COOH	COO⁻	COOH	COOH	COO⁻
8	Up	COOH	COOH	COO⁻	COO⁻	COO⁻	COO⁻
9	Down	COOH	COOH	COO⁻	COOH	COOH	COO⁻
10	Up	COOH	COOH	COO⁻	COO⁻	COO⁻	COO⁻
11	Down	COOH	COOH	COO⁻	COO⁻	COO⁻	COO⁻
12	Up	COOH	COOH	COOH	COO⁻	COO⁻	COO⁻
13	Down	COOH	COOH	COOH	COO⁻	COO⁻	COO⁻
14	Up	COOH	COOH	COOH	COO⁻	COO⁻	COO⁻
15	Up	COOH	COO⁻	COOH	COOH	COO⁻	COO⁻
16	Up	COOH	COOH	COO⁻	COOH	COO⁻	COO⁻
17	Up	COOH	COOH	COOH	COO⁻	COOH	COO⁻
18	Up	COOH	COOH	COOH	COO⁻	COO⁻	COO⁻
19	Down	COOH	COO⁻	COOH	COO⁻	COO⁻	COO⁻
20	Up	COOH	COOH	COO⁻	COO⁻	COOH	COO⁻

Table A.5 20 monomers isotatic HPAM chain with random deprotonation

Monomer	Tacticity	Charge density				
		f = 0	f = 0.25	f = 0.5	f = 0.75	f = 1
1	Up	$CONH_2$	$CONH_2$	COO⁻	COO⁻	COO⁻
2	Up	$CONH_2$	COO⁻	$CONH_2$	COO⁻	COO⁻
3	Up	$CONH_2$	$CONH_2$	COO⁻	COO⁻	COO⁻
4	Up	$CONH_2$	$CONH_2$	COO⁻	$CONH_2$	COO⁻
5	Up	$CONH_2$	$CONH_2$	$CONH_2$	COO⁻	COO⁻
6	Up	$CONH_2$	$CONH_2$	$CONH_2$	COO⁻	COO⁻
7	Up	$CONH_2$	COO⁻	COO⁻	COO⁻	COO⁻

8	Up	CONH$_2$	COO$^-$	COO$^-$	COO$^-$	COO$^-$
9	Up	CONH$_2$	CONH$_2$	COO$^-$	COO$^-$	COO$^-$
10	Up	CONH$_2$	COO$^-$	COO$^-$	COO$^-$	COO$^-$
11	Up	CONH$_2$	COO$^-$	COO$^-$	COO$^-$	COO$^-$
12	Up	CONH$_2$	CONH$_2$	CONH$_2$	COO$^-$	COO$^-$
13	Up	CONH$_2$	CONH$_2$	CONH$_2$	COO$^-$	COO$^-$
14	Up	CONH$_2$	CONH$_2$	CONH$_2$	CONH$_2$	COO$^-$
15	Up	CONH$_2$	CONH$_2$	COO$^-$	COO$^-$	COO$^-$
16	Up	CONH$_2$	CONH$_2$	COO$^-$	COO$^-$	COO$^-$
17	Up	CONH$_2$	CONH$_2$	CONH$_2$	COO$^-$	COO$^-$
18	Up	CONH$_2$	CONH$_2$	CONH$_2$	CONH$_2$	COO$^-$
19	Up	CONH$_2$	CONH$_2$	COO$^-$	CONH$_2$	COO$^-$
20	Up	CONH$_2$	CONH$_2$	COO$^-$	CONH$_2$	COO$^-$

Appendix B
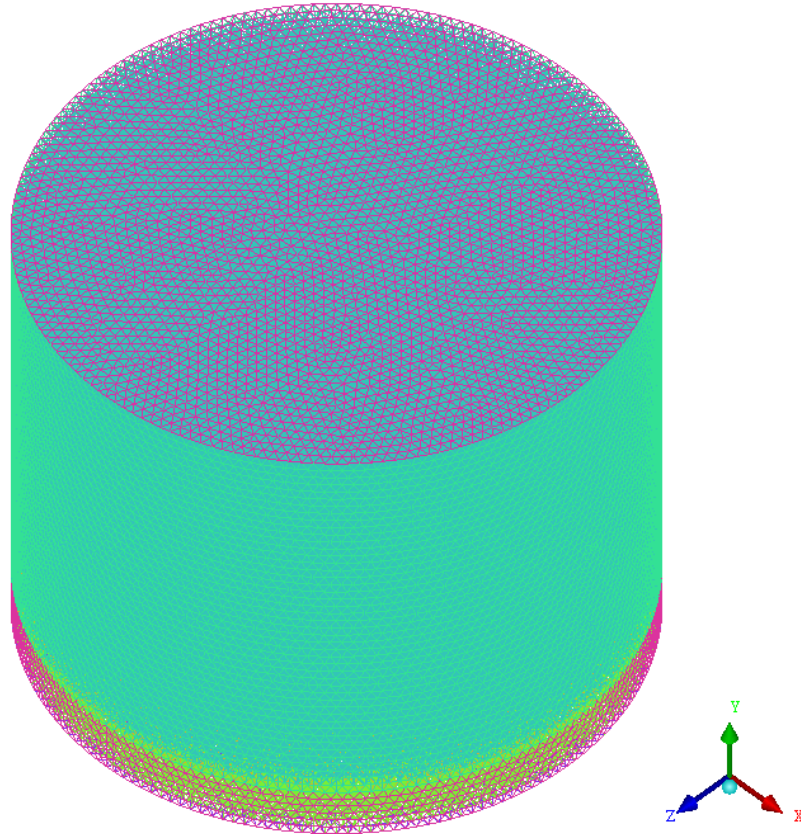# CFD simulation for sucrose solution

B.1 Physical model

Figure B.1 Physical model for the CFD simulation

The details of structure parameters are consistent with the experimental rig described in the manuscript except the side wall is insulting and has no thickness. The upper plate is rotating with different speed set.

B.2 Assumptions

1. To simplify the simulation, the following assumptions were made:
2. Steady and laminar flow;
3. The thermal conductivity and heat specific capacity of solution were set as the value at 15 °C;
4. Fluid is incompressible, Newtonian and viscous;
5. No velocity-slip at the walls.

B.3 Boundary conditions

The boundary conditions were conducted based on the experimental set-up. The outer wall of the bottom is set as constant temperature of 5.4 °C (this is based on the experimental result). The side wall is thermal isolation. The top wall is rotating with some heat convection with atmosphere (air). The heat coefficient determination will be discussed later. The initial temperature and the temperature of the atmosphere are set 23 °C.

B.4. Simulation details

Simulations were conducted separately by changing the rotation speed from 0 to 10 rpm. The time step is 1 s and the overall simulation time is 20000 s based on the Fig. B.2. The system has already fully equilibrated after 20000 s.
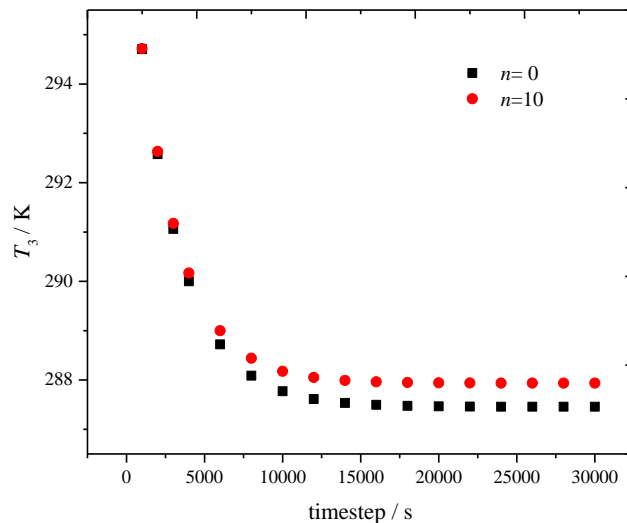
Figure B.2 The temperature at the position around T_3 varies with simulation time

B.5. Convective heat transfer determination for top surface

The convective heat transfer of the upper plate, h_{upper} is difficult to measure. Therefore the value was determined at $n=0$, where the temperature profiles are similar with experimental result. Indeed, since the distribution of temperature within bulk is in layers, the heat transfer performance is mainly

dependent on the thermal conductivity of the fluid and shows independent relationship on the heat transfer coefficient of the upper plate as shown in Fig. B.4. The latter only influences the amount of heat flux removal and the temperature value of the liquid but no effects on the temperature differences between liquid and wall. In this study, h_{upper} = 50 was selected due to similar temperature profiles.
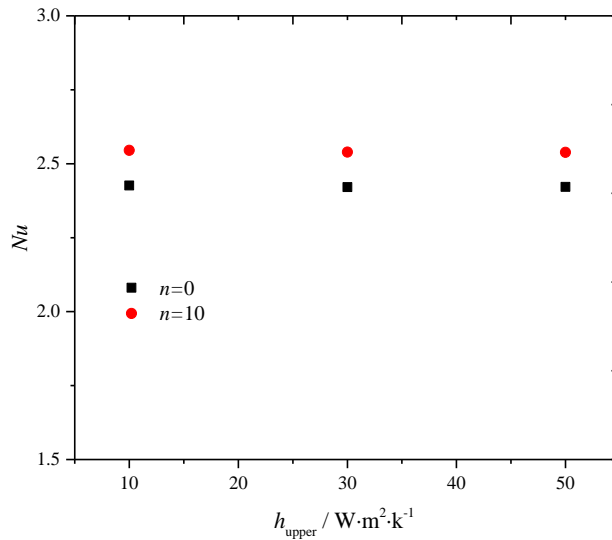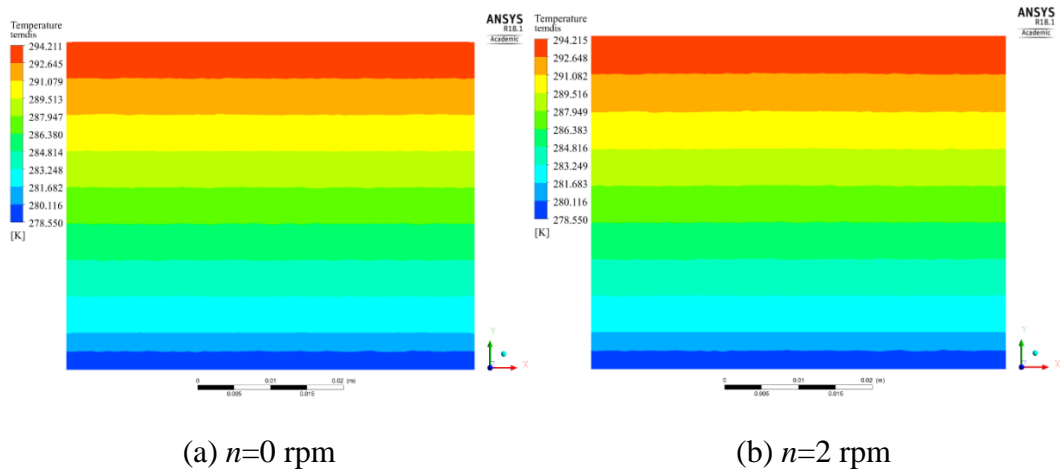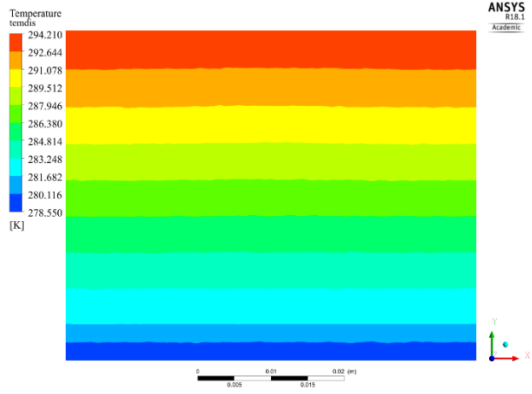

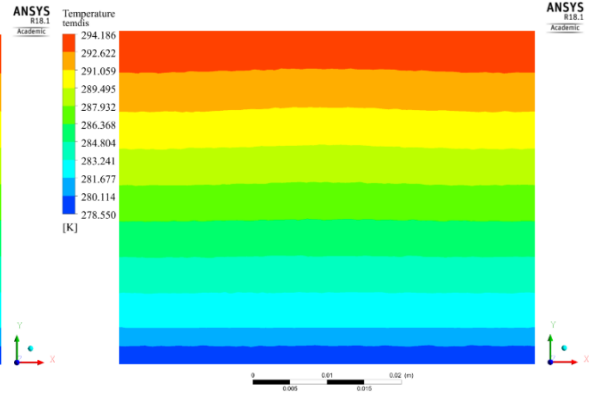**Figure B.3** **Dependence of *Nu* on the heat transfer coefficient of rotating wall**
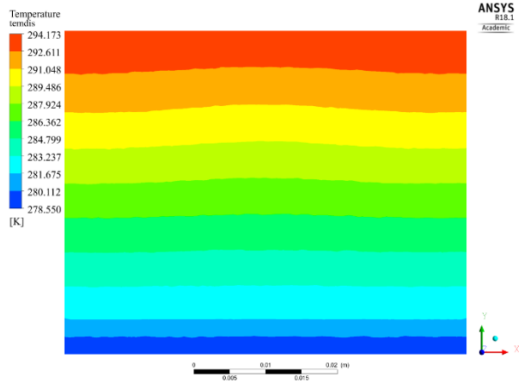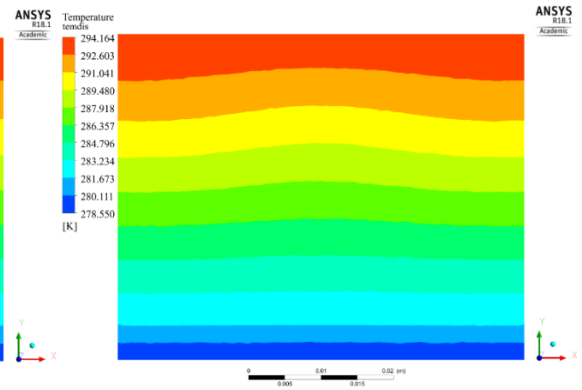

(a) *n*=0 rpm   (b) *n*=2 rpm

(c) *n*=3 rpm

(d) *n*=5 rpm

(e) *n*=7 rpm

(f) *n*=10 rpm

Figure B.4 Temperature distribution along the vertical direction in the axial plane at various rotation speed

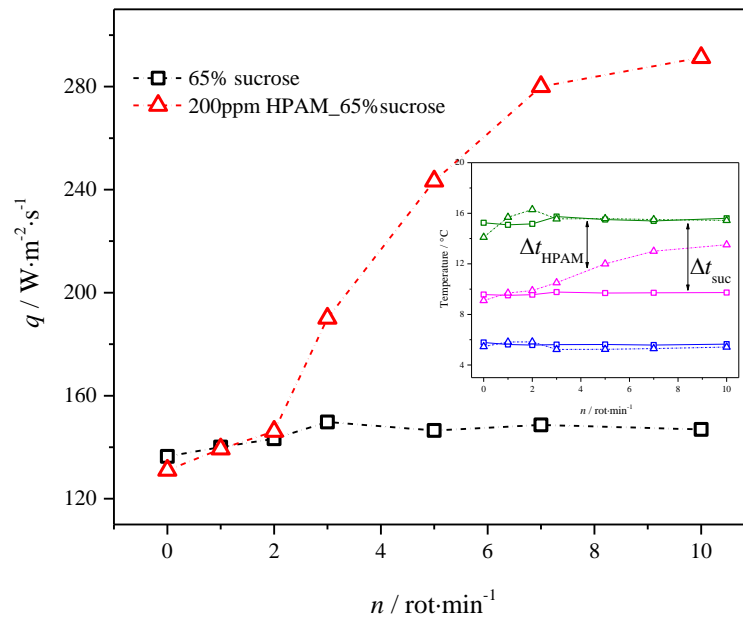## B.6 Heat flux profiles during experiments

Figure B.5 The variations of heat flux density with the degree of rotation; the inserted figure shows the measurements of average temperature of inner wall, out wall and whole bulk. The curves with triangle symbol and square symbol present the HPAM solution and sucrose solution, respectively. The average temperature of the bulk, inner wall and the outer wall are presented by green, pink and blue curves, respectively

The heat flux performances for the sucrose solution and HPAM solution are compared in Fig. B.5. As mentioned above, adding small amount polymer inside concentrated sucrose solution does not significant change the thermal properties of the base fluid. Therefore, before the onset of elastic instability, the heat removal of both working fluids are consistent well and slightly increasing along with the rotating speed. Such increase in mainly due to the rotation of the top plate makes small additional heat transferred between the experimental system and the atmosphere. However, this slight incremental does not influence the global heat transfer performance.